

In situ strain & cure monitoring in liquid composite moulding by fibre Bragg grating sensors

Proefschrift

ter verkrijging van de graad van doctor
aan de Technische Universiteit Delft,
op gezag van de Rector Magnificus prof.ir. K.C.A.M. Luyben,
voorzitter van het College voor Promoties,
in het openbaar te verdedigen op vrijdag 28 maart 2014 om 15:00 uur

door

Johannes Mattheus BALVERS

Ingenieur luchtvaart en ruimtevaart
geboren te Alkmaar

Dit proefschrift is goedgekeurd door de promotor:

Prof.ir. A. Beukers.

Copromotor:

Dr.ir. H.E.N. Bersee.

Samenstelling promotiecommissie:

Rector Magnificus,	voorzitter
Prof.ir. A. Beukers,	Technische Universiteit Delft, promotor
Dr.ir. H.E.N. Bersee,	Technische Universiteit Delft, copromotor
Prof.dr. S.J. Picken,	Technische Universiteit Delft
Prof.dr. V. Michaud,	École Polytechnique Fédérale de Lausanne, Zwitserland
Prof.dr. P. Hubert,	McGill University, Montreal, Canada
Prof.dr. G. Fernando,	University of Birmingham, Verenigd Koninkrijk
Prof.dr.ir. J. Degrieck,	Universiteit Gent, België
Prof.dr.ir. R. Benedictus,	Technische Universiteit Delft, reservelid

The research described in this thesis was partially funded by AgentschapNL (formerly NIVR), Stork SP Aerospace B.V., Stork Fokker AESP B.V. (all located in the Netherlands) and FOS&S (Belgium).

ISBN: 978-90-8891-832-2

Copyright © 2014: J.M. Balvers.

All rights reserved.

No part of the material protected by this copyright notice may be reproduced or utilised in any form or by any means, electronic or mechanical, including photocopying, recording or by any information storage retrieval system, without prior permission of the author.

Cover design & photography: J.M. Balvers

Printed in the Netherlands by Uitgeverij BOXPress || Proefschriftmaken.nl

Keep your dreams alive. Understand to achieve anything requires faith and belief in yourself, vision, hard work, determination, and dedication. Remember all things are possible for those who believe.

GAIL DEVERS

In situ strain & cure monitoring in liquid composite moulding by fibre Bragg grating sensors

Summary

For future airframe weight saving, it is no longer sufficient to look solely at replacing thin-walled metallics by fibre reinforced plastics. Solutions are required for 'thicker' structural parts, e.g. the landing gear rib of a wing assembly, as well. Thanks to its inherent capability of producing complex geometries and being an acceptable out-of-autoclave alternative, the process Liquid Composite Moulding (LCM) would lend itself perfectly to it. Though, conventional curing is not always appropriate. The part's structural integrity may become affected by the build up of process-induced strains arising from thermal gradients. To suppress these negative effects optimisation is considered essential in defining new cure strategies.

Unfortunately, the simulated strains in 'thick' LCM-ed parts are hardly verified due to a fundamental lack in experimental data. Supplementing with online and *in situ* process monitoring by fibre optics is promising. Despite of being still in its infancy, the Fibre Bragg Grating (FBG) sensing technique shows high potential. Maturing it and developing a consistent procedure may close this gap. The question is, however, whether this method is an effective method for online strain monitoring.

In this context, state-of-the-art overviews are provided for the manufacturing of 'thick' advanced composite structures and for online and *in situ* monitoring by FBG sensors. The understanding of the Bragg response is enriched through experimental investigation of its sensitivity to two typical LCM processes: Resin Transfer Moulding (RTM) and Vacuum Infusion (VI). Finally, the effect of the cure cycle on strain formation is studied. It is shown that:

- To support the evaluation of the process-induced strains, knowledge about the resin's cure kinetics and the woven fabric's compaction behaviour is helpful. Preliminary tests defined the best-practice in-lab sensors' fixation. They revealed also a negligible influence of the embedded sensor's coating.
- To put the measured process-induced strains into more perspective, a secondary experimental method, based on thermal annealing, was developed using either surface-mounted or embedded FBG sensors. Introduction of the Line of Zero Stress (LoZS) for the reinforcement lets its residual strain state compare to the process-induced one. Though, the scatter in measured Coefficient of Thermal

Expansion (CTE) of the reinforcement can contribute to a significant error.

- For thin flat VI-ed laminates, the combination of the two methods revealed that the preform can expand in a nearly stress-free state. Furthermore, the higher the cure temperature (until the ultimate glass transition temperature) the more residual strain built up in the reinforcing fibres.
- Two disturbing factors in determining the actual strain state were pre-cure tool-part interaction and resin infusion. By different mechanisms, both influenced the reference point/line.
- Thin flat RTM-ed laminates behaved for low fibre content similarly. Higher volume fractions led to in-plane tensile strains during compaction and subsequent heating. The occurrence of stick-slip hindered, however, the evaluation.
- The analysis of 'thicker' laminates was even more complicated. Here, the expansion of the dry/impregnated preform was no longer 'stress-free', but occurred in a 'compressive' state. Bending of the assembly during cooling can be another source affecting proper CTE and strain evaluation. Scatter and signal's peak splitting troubled the detection of through-thickness strain differences.

Overall, it can be concluded that the high precision and sensitivity of FBG sensors form a threat when coupled to multiphysical processes such as LCM. The contribution of each process step/parameter must be deliberately weighted to quantify the measured strain. This so-called decision-based analysis asks for a multi-field expert-level operator. On the other hand, when the operator is still at beginner's level, monitoring by means of FBG sensors is an excellent method to let him/her familiarise with the designated manufacturing process. Though, jumping too fast to conclusions can be lurking at that level.

That the LoZS-method helps in improving the determination of process-induced and residual strains in flat laminates was successfully illustrated here. The approach is, nevertheless, still open for further improvement. A set of rules (knowledge-based driven) derived from these simpler cases needs to be developed to interpret data for more complex-shaped parts. Future researchers are encouraged to continue along this path such that, eventually, a hybrid solution can be formed for online process monitoring, *i.e.* measuring strain by FBG sensors, in combination with cure modelling, *i.e.* simulating temperature (and degree of conversion).

In situ rek- & uithardingscontrole in vloeibare composietvorming door in glasvezel aangebrachte Bragg tralie sensoren

Samenvatting

Voor toekomstige gewichtsbesparing in vliegtuigcasco's, is het niet langer voldoende alleen naar het vervangen van dunwandige metalen door vezelversterkte kunststoffen te kijken. Oplossingen zijn ook nodig voor 'dikkere' bouwdelen, bijv. het landingsgestelrib in een vleugel. Dankzij zijn inherente bekwaamheid in het vervaardigen van complexe geometriën en het zijn van een acceptabele alternatief voor de autoclaaf, leent het proces 'Liquid Composite Moulding' (LCM) zich perfect ervoor. Conventioneel uitharden is echter niet altijd passend. De integriteit van de structuur kan door de opbouw van proces-geïnduceerde rekken, die uit thermische gradiënten voortvloeien, worden beïnvloed. Om deze negativiteiten te onderdrukken is optimalisatie essentieel voor het definiëren van nieuwe uithardingsstrategieën.

De nagebootste rekken in 'dikke' LCM-delen zijn helaas door een grondig gebrek aan experimentele data nauwelijks geverifieerd. Aanvullen met online en *in situ* processcontrole door optische vezels is veelbelovend. Ondanks nog staand in kinderschoenen hebben in glasvezel aangebrachte Bragg tralie (engels: fibre Bragg grating (FBG)) sensoren hoge potentie. Dichting van de kloof zou door rijping en procedure ontwikkeling mogelijk zijn. Het is echter nog de vraag of deze methode effectief is voor online rekcontrole.

In dit verband is de huidige stand voor zowel het vervaardigen van 'dikke' composieten als ook de online en *in situ* controle door FBG sensoren bepaald. De kennis ten aanzien van de Bragg uitvoer is door middel van een experimenteel onderzoek naar de gevoeligheid voor twee typische LCM-processen verrijkt. Deze zijn 'Resin Transfer Moulding' (RTM) en vacuüm infusie (VI). Tenslotte is het effect van de uithardingscyclus op de rekvorming bestudeerd. Het volgende werd aangetoond:

- Om de evaluatie van proces-geïnduceerde rekken te ondersteunen, is kennis van de harskinetiek en weefselverdichting nuttig. Vooronderzoek leverde een goede methode voor sensorbevestiging. Tevens onthulde deze een minimale rol voor de bekleding van ingebedde sensoren.
- Om de gemeten proces-geïnduceerde rekken in perspectief te plaatsen, werd een tweede experimentele methode, gebaseerd op thermisch gloeien, voor opgelegde en ingebedde FBG sensoren ontwikkeld. De nulspanningslijn (engels: Line of

Zero Stress (LoZS)) van het weefsel laat de restrek met de proces-geïnduceerde rek vergelijken. De verstrooiing in de gemeten thermische uitzettingscoëfficiënt van het weefsel kan echter significant aan de meetfout bijdragen.

- Voor dunne vlakke VI laminaten liet de combinatie van de twee methoden zien dat het weefselpakket in een bijna spanningsvrije toestand uitzette. Verder zorgde een hogere uithardingstemperatuur (tot aan de maximale glasovergangstemperatuur) voor meer restrek in de vezels.
- Twee versturende factoren in de rekbepaling waren de harsinfusie en de interactie tussen mal en bouwdeel voor de uitharding. Door verschillende mechanismen beïnvloedden beiden het/de referentiepunt/-lijn.
- Vlakke RTM laminaten gedroegen zich gelijk voor lage vezelinhoud. Hogere vezelinhoud leidde tot positieve rek gedurende de verdichting en de daaropvolgende opwarming. Het plak-glij voorval belemmerde echter de evaluatie.
- Gecompliceerder was de analyse van 'dikkere' laminaten. Expansie van het droge/benatte weefselpakket was hier niet langer 'spanningsvrij', maar verkeerde in een druktoestand. Buiging van het pakket tijdens afkoelen werd als bron geïdentificeerd, die de berekening van de uitzettingscoëfficiënt en rek bemoeilijkte. Strooiing en pieksplitsing van het signaal zorgden voor problemen in de bepaling van rekverschillen door de dikte heen.

Globaal gezien kan worden geconcludeerd dat een hoge nauwkeurigheid en gevoeligheid van FBG sensoren een bedreiging vormen wanneer ze aan multifysische processen zoals LCM gekoppeld worden. De bijdrage per stap/parameter moet weloverwogen afgewogen worden om de gemeten rek te kwantificeren. Deze zogenaamde beslissingsanalyse vraagt om een expert in meerdere bereiken. Anderzijds kan de meetmethode op basis van FBG sensoren een beginneling helpen zich met het aangewezen vervaardigingsproces vertrouwd te maken. Het te haastig tot een conclusie komen blijft dan echter op de loer liggen.

Dat de LoZS-methode helpt in het verbeteren van de bepaling van proces-geïnduceerde en restrekken voor vlakke laminaten was hier succesvol aangetoond. De benadering is desalniettemin voor verbetering nog vatbaar. Zo zouden regels (op kennis gedreven), welke van zulke simpelere gevallen afgeleid dienen te worden, opgesteld moeten worden ter interpretatie van complexere bouwdeelen. Toekomstige onderzoekers worden gevraagd dit pad te bewandelen, zodat uiteindelijk een hybride oplossing beschikbaar komt, die online procescontrole, d.w.z. rekmeting, met modellering van de uitharding, d.w.z. simulatie van temperatuur (en uithardingsgraad), koppelt.

CONTENTS

Summary	v
Samenvatting	vii
1 Introduction	1
1.1 From 'thin' to 'thicker' composite parts	1
1.2 Complex shapes - liquid composite moulding	2
1.3 Optimisation leads to new cure strategies	4
1.4 The need for online process monitoring	6
1.5 Problem statement and research goals	6
1.6 Scope of the study	7
2 'Thick' Composites Manufacturing	
<i>An Overview of Cure Modelling & Optimisation</i>	11
2.1 Introduction	11
2.2 Manufacturing hurdles and alternatives	12
2.3 Brief overview of achievements	16
2.4 Cure modelling - from thermochemical behaviour onwards	19
2.5 Simulation-based cure cycle design & online controlling	28
2.6 Experimental validation by online monitoring and post-manufacturing evaluation	34
2.7 Concluding remark	36
3 Process Monitoring - A Literature Survey on Fibre Bragg Grating Sen- sors	39
3.1 Introduction	39
3.2 Brief history, applications, pros and cons	40

3.3	Theory of FBG sensing	42
3.4	A variety of FBG sensors	45
3.5	Discrimination between strain and thermal effects	47
3.6	Monitoring composites manufacturing processes	51
3.7	Shortcomings and practical issues	58
3.8	Concluding remarks	61
4	Materials, Processes, and Instrumentation	63
4.1	Introduction	63
4.2	Selection of composite materials	64
4.3	Material characterisation	65
4.4	Choice of manufacturing processes	71
4.5	Instrumentation for process monitoring	74
4.6	Summary	80
5	Thermal Annealing as a Technique for Verifying Strain Formation during Processing	83
5.1	Introduction	83
5.2	In search of a secondary experimental technique	84
5.3	Explanatory information about thermal annealing	85
5.4	Configuration I: surface-mounted FBG sensors	86
5.5	Configuration II: embedded FBG sensors	91
5.6	Discussion and concluding remarks	95
6	Effect of the Cure Regime on the Formation of Strains in VI Laminates	97
6.1	Introduction	97
6.2	Experimental procedures and data analysis	98
6.3	Selection of the initial reference point	99
6.4	Illustrative example 1: GFR EP04908	101
6.5	Illustrative example 2: GFR RTM6	106
6.6	Effect of the cure regime	113
6.7	Some other experimental results	123
6.8	Effectiveness of the LoZS-method	126
6.9	Conclusions	127
7	Pre-cure Tool-part Interaction	131
7.1	Introduction	131

7.2	Experimental setups and procedures	132
7.3	Effect of the resin flow	133
7.4	Alternative explanation: pre-cure tool-part interaction	134
7.5	Experimental underpinning	137
7.6	Pre-cure tool-part interaction in thicker preforms	146
7.7	Discussion and concluding remarks	146
8	Resin Flow: A Disturbing Factor	149
8.1	Introduction	149
8.2	Motivation for digital image correlation	150
8.3	Experimental	151
8.4	Results and discussion	152
8.5	Conclusions	160
9	Effect of the Fibre Volume Fraction on the Formation of Strains in RTM Laminates	161
9.1	Introduction	161
9.2	Experimental	162
9.3	Results	164
9.4	Conclusions	178
10	Exploratory Investigation of Strains in Thicker Laminates	181
10.1	Introduction	181
10.2	Intermezzo: degree of cure at gelation	182
10.3	Cure of a thick GFR EP04908 laminate	184
10.4	Cure of thicker GFR RTM6 laminates - thickness effect	188
10.5	Concluding remarks	197
11	Conclusions and Recommendations	199
11.1	Introduction	199
11.2	Conclusions: background	199
11.3	Conclusions: applicability of FBG sensors in LCM	201
11.4	Conclusions: determination of process-induced and residual strains	202
11.5	Recommendations - conceptual foundation to proceed	205
A	Responses of gratings in different optical fibres	209

B Effect of wrong RTM6 resin mixture	215
C Reproducibility: vacuum-infused GFR RTM6 laminates	219
References	223
Nomenclature	a
Acknowledgements	e
About the Author	g
Publications	h

1

INTRODUCTION

1.1 From 'thin' to 'thicker' composite parts

In the aerospace industry modern synthetic composite materials have slowly replaced their metallic competitors (aluminium, steel and titanium) because of their higher specific strength and stiffness. Starting in the 80s with aircraft such as the Airbus A310 and A320 and Boeing 757 and 767 having only a few percent of composites in structural weight, engineers of the new generation of wide-body jet airliners, the Boeing 787 Dreamliner and Airbus A350, have realised a significant share of composites. The 787 airframe, for instance, has a weight saving of 20 percent compared to the more conventional aluminium designs [1]. The lower airframe weight cuts the operator fuel costs, which was about 30 to 40 percent of the Direct Operating Costs (DOCs) in 2007. Certainly in times of higher jet fuel prices, the more the structural weight is reduced, the greater the saving on DOCs becomes. Hence, weight saving from the use of composites is an important pillar in fuel saving and thus fuel-efficient flying [2].

In 2005 the multi-platform Advanced Low-Cost Aircraft Structures (ALCAS) project was initiated to maintain and to enhance the competitive position of the European aerospace industry. The aim has been to reduce the operating costs while saving simultaneously weight through the cost-effective, full application of carbon fibre composites to primary aircraft structures of both business jets (Dassault Aviation) and large civil airliners (Airbus) [3]. One of the technical platforms covers the design, the manufacturing and the testing of a full composite inner wing and centre box of a large civil airliner. It has been targeted for a weight saving of 20% with zero increase in recurring cost against a reference state-of-the-art metallic wing. In achieving the

goal, attention has been paid to out-of-autoclave processes because of their cost-effectiveness [4]. In order to realise these weight savings, replacing solely thin-walled metallic Structural Significant Items (SSIs) by composite equivalents is no longer sufficient. Solutions are also needed for thicker metallic structural parts, because their conversion may contribute significantly to the weight saving. To achieve the goals of the ALCAS lateral wing platform, additional weight saving is obtained by integrating highly loaded areas such as the landing gear and pylon into the lateral wing structure. In this context, the 'thick' composite SSIs are the landing gear rib, the side stay and the rear spar, *i.e.* the section closest to the root. The thickness of these parts is in the order of 60 to 100 *mm*. To give an impression of the weights¹ involved, the composite gear rib has a gross weight of 205 *kg* [5], and the rear spar weighs about 280 *kg* [6]. In case of the side stay, a weight benefit of 6% is estimated for the prototype. Further optimisation of the geometry may enlarge the weight benefit to 19% [7].

Hence, future weight saving in the aerospace industry requires thicker structural parts to be made of composites as well. But how should these, often complex, SSIs be manufactured and what are the limitations thereof?

1.2 Complex shapes - liquid composite moulding

For years, the aerospace industry has relied on the autoclave curing process for the manufacturing of composite parts. Because of the consistent part quality and high fibre volume fractions reached with prepreg laminates, no other composites manufacturing process was capable of competing with these high standards. Autoclave processing is, however, rather expensive. Capital costs are high for autoclaves. Maintenance and operating costs tend also to be higher compared to standard ovens and hot presses. Besides, having processing times of hours, extending the production volume from low to medium or even higher requires a series of autoclaves or larger interior volumes. Hence, even more money has to be invested to keep up with growing production rates [8].

To date, Liquid Composite Moulding (LCM) is an acceptable alternative in out-of-autoclave composites manufacturing [8]. LCM is a generic term for several processes including Resin Transfer Moulding (RTM), Vacuum Infusion (VI) and Seemann

¹A better approach is to compare the weight for the entire assembly. By the time of writing, the last data regarding weight saving have been collated from the partners, but an initial estimate cannot be given.

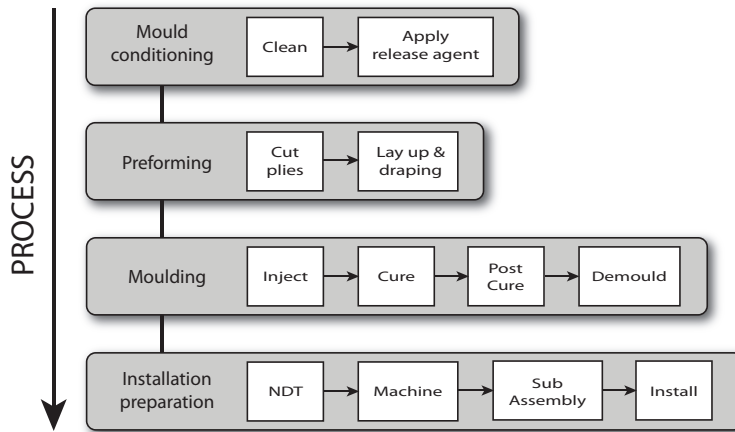


Figure 1.1: Steps in a generic LCM process.

Composites Resin Infusion Moulding Process (SCRIMP™). Four main process steps, between material delivery and operational use of the composite part, can be distinguished in a generic LCM process: (i) mould conditioning, (ii) preforming, (iii) moulding, and (iv) installation preparation (Fig. 1.1). To ensure proper demoulding, mould cleaning and the application of a release agent on the tooling surfaces are prerequisites. Plies of any type of fibrous reinforcement are then draped and stacked to form the dry preform. After closing the mould system, resin is injected into the mould cavity and conventionally cured according to the Manufacturer's Recommended Cure Cycle (MRCC). To enhance mechanical properties, the curing step may be succeeded by an in-mould or, after demoulding, a free-standing post cure at an elevated temperature. Non Destructive Testing (NDT) services provide the quality control. The part is then machined, e.g. hole drilling and/or edge milling. Subcomponents such as bushings are part-to-part assembled before installation of the composite part.

According to Berenberg [8], the sine-wave spars of the Lockheed Martin F/A 22 were probably the first structural applications of RTM composite parts in an aircraft. Since then many more 'thin' composite SSIs have proven the concept of LCM in the aerospace industry. Parts range from simple, e.g. brackets, to highly sophisticated such as the rear pressure bulkhead of the Boeing 787. This one-piece dome measures 4.3 m by 4.6 m and is made by vacuum-assisted RTM [9].

Thanks to its inherent capability of producing these complex geometries, LCM would

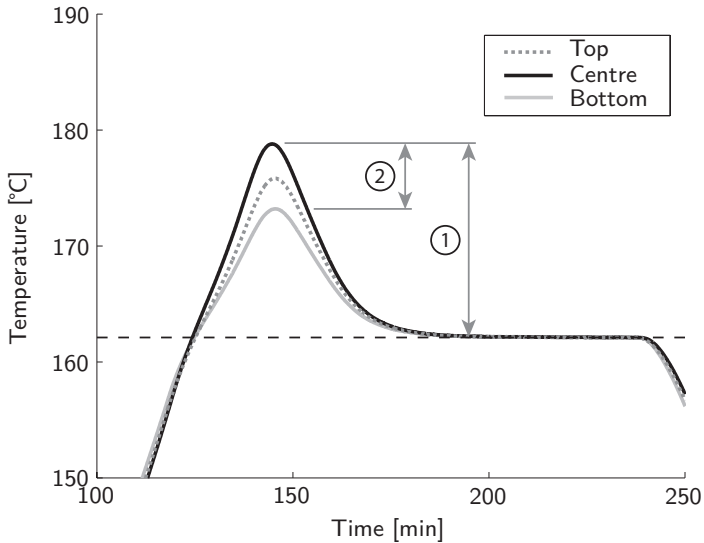


Figure 1.2: Temperature overshoot of 17 °C in a conventionally cured 10-*mm*-thick 43% GFR epoxy plate.

lend itself perfectly to the fabrication of even ‘thicker’ structural parts. In comparison with ‘thin’ composite parts the manufacturing of ‘thicker’ composites is not as straightforward. By implication, curing a ‘thick’ composite part conventionally may result in excessively high localised temperatures (see Fig. 1.2). This can be attributed to the exothermic behaviour of the thermosetting resin system and low thermal conductivities of the constituents. In this way, process-induced strains, which may affect the structural integrity, are built up due to the through-thickness thermal gradients.

1.3 Optimisation leads to new cure strategies

To suppress the negative effects in curing ‘thicker’ composite parts an optimisation technique is considered essential, because a trial-and-error approach would be time-consuming and expensive [10, 11]. The generic steps in cure modelling are schematically shown on the left-hand side of Fig. 1.3. After having established the input parameters such as the lay-up of the plies, rheological properties of the resin system and tooling temperature, the first three steps determine the instantaneous cure state, *i.e.* temperature and degree of cure, to which all other material properties are linked. Executing these steps in an optimisation routine is sufficient for minimising

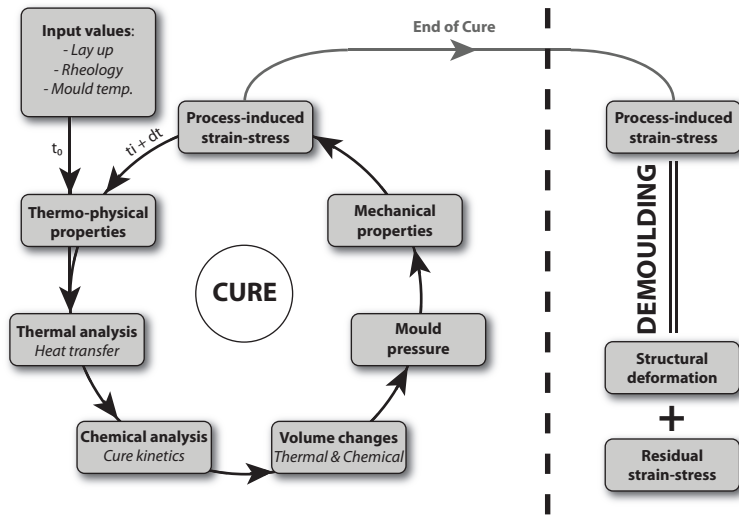


Figure 1.3: Scheme for analysing process-induced strains (adapted from [11]).

the exothermic peak temperature. Several studies have revealed that local temperature overshoots can be minimised effectively by adapting the cure cycle² (Chapter 2). An extra dwell period between the filling temperature and the cure temperature is a common tactic and actually adopted in the manufacturing of the gear rib and the side stay [5, 7].

In studying the influence of the cure cycle on the formation of process-induced strains, substantially more knowledge about the behaviour of the involved materials is needed. Information is required on volume changes caused by thermal expansion/contraction and chemical shrinkage. These volume changes affect the pressure on the tooling system. Mechanical properties, dependent on the cure state and the bulk pressure, are then derived before the process-induced strains can be computed. Most of these submodels are empirically based and therefore susceptible to inconsistencies. The interrelation of these submodels may lead to the accumulation of errors. In general, the quality of the error can be assessed by comparing the simulation output with experimental data. Unfortunately, the simulated process-induced strains are hardly verified because of a fundamental lack in experimental studies on the formation of strains in 'thick' composite parts manufactured by LCM processes [13].

²The cure cycle represents all processing conditions used in manufacturing a composite part [12].

1.4 The need for online process monitoring

On one hand, the process-induced strains can lead to structural deformation upon demoulding (see right-hand side of Fig. 1.3). Spring-in and warpage are some of the possible deformations as well as delaminations between adjacent plies and micro-cracking at the interface of the matrix and the reinforcing fibres [11]. These structural defects may affect the mechanical performance of the composite structure. On the other hand, process-induced strains that are not released upon demoulding are so-called residual strains. Consequently, composite structures with residual strains are prestrained before external loading. Strains due to mechanical loading should be superimposed on the residual strain state in order to determine the correct overall strain state. Ignoring the presence of residual strains may cause the composite structure to fail prematurely. The evaluation of these residual strains becomes therefore an important factor in failure predictions [14].

In order to study the formation of process-induced strains in more detail, the existing simulation tools should be supplemented with experimental data obtained from online and *in situ* monitoring of these composites manufacturing processes. To date the most adequate or promising technique for online and *in situ* process monitoring of composite structures is based on fibre optics [15–17]. In respect of this and from the authors' point of view, the Fibre Bragg Grating (FBG) sensing technique has a high potential in deriving these process-induced strains (see Chapter 3).

1.5 Problem statement and research goals

As illustrated in the introductory paragraphs, several problems are associated with the manufacturing of 'thick' composite parts. Optimisation of the process parameters is the key to solve these issues, but a lack of experimental studies on the formation of process-induced strains troubles the interpretation of the results. Despite of being still in its infancy, the FBG technique seems to be a promising tool to gather experimental data on the formation of process-induced strains. Based on these observations the following research question is formulated:

Is the FBG sensing technique an effective method for online monitoring of the formation of process-induced strains in LCM processes such that, eventually, the gap in verification can be closed that is caused by a lack of experimental studies on the formation of these strains in 'thicker' composite parts?

In order to give an answer to this question, several research goals are defined *a priori*:

- provide an overview of the current status of manufacturing of 'thick' advanced composite structures and the *in situ* process monitoring thereof using FBG sensors;
- enrich the understanding of the Bragg response through experimentally investigating the sensitivity of fibre Bragg grating sensors to LCM processes such as RTM and VI;
- characterise material properties to enhance and validate models simulating the cure behaviour in thick composites;
- manufacture 'thick' composites for studying the effect of the cure cycle on the formation of process-induced strains;
- (develop a hybrid solution for on-line process monitoring that is based on simultaneously simulating the cure behaviour in composites and *in situ* monitoring of the manufacturing process using FBG sensors).

By achieving most of the goals³, this dissertation will contribute to an improved understanding of experimentally measuring the formation of process-induced strains in both 'thin' and 'thick' LCM-ed composite parts by using the FBG sensing technique.

1.6 Scope of the study

After this brief introduction, two overviews are presented. The manufacturing of 'thick' composite parts is discussed by focusing, in particular, on cure modelling and optimal cure cycle design. Attention is paid to the experimental validation of the numerical results as well (Chapter 2). A look is then taken at the current state of the FBG sensing technique in composites manufacturing processes (Chapter 3). Based on the conclusions at the end of these overviews, boundaries are set for the workspace. Short descriptions are given for the experimental setups, procedures and materials used throughout this research study. The embedding procedure for the optical fibres is highlighted as well (Chapter 4). As can be seen in Fig. 1.4, knowledge is first

³As will become clear in the remaining part, the third goal involved more effort than initially foreseen. Hence, the development of a hybrid solution became optional.

gained by monitoring the manufacturing of 'thin' laminates. A secondary technique is introduced that brings the measured process-induced and residual strains into perspective (Chapter 5). The effect of the cure regime on the formation of these strains is then studied for a typical VI process. The discovery of interesting artefacts requires further analyses on pre-cure tool-part interaction and resin flow (Chapter 7 and 8, respectively). The section about analysing 'thin' laminates concludes with a study on the effect of the fibre volume fraction on the formation of process-induced strains in a vacuum-assisted RTM process (Chapter 9). All preceding steps will help in analysing the cure behaviour in 'thick' laminates as monitored by FBG sensors. The approach concludes therefore with an exploratory investigation of process-induced strains in thick laminates subjected to one-step curing only (Chapter 10). Last, but not least, this study ends with the lessons learned and conclusions drawn. Recommendations are given to support future work (Chapter 11).

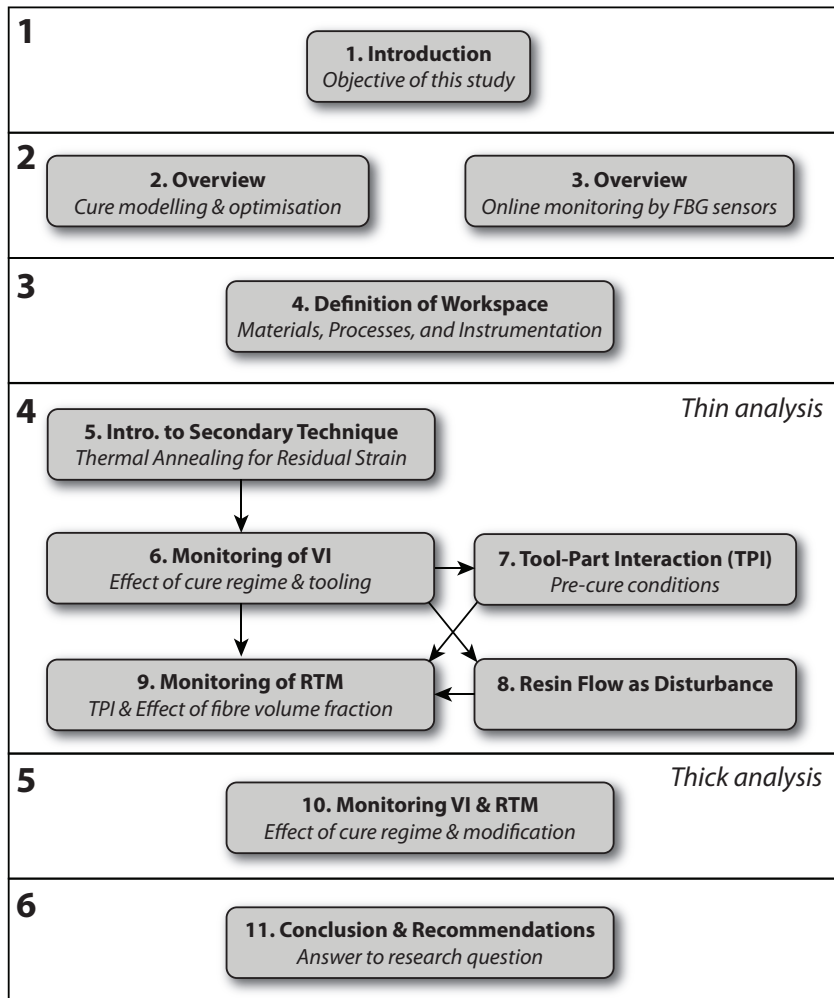


Figure 1.4: Structure of this dissertation.

2

'THICK' COMPOSITES MANUFACTURING AN OVERVIEW OF CURE MODELLING & OPTIMISATION

2.1 Introduction

Research in composite manufacturing processes is an interdisciplinary activity that involves multiphysical phenomena such as cure kinetics, heat transfer, fluid dynamics and mechanics [18]. Presenting basic topics on composite manufacturing would, of course, aid the reader in forming background knowledge, but he (or she) is referred to other literature [19–21]. This overview continues the discussion started in Section 1.3 about cure modelling of 'thick' composite parts¹.

The primary focus of this chapter is threefold: elaborating on cure modelling of 'thick' composite parts by discussing the achievements according to the three mainstreams and by presenting the mathematical approaches (Sections 2.3 and 2.4), showing the trends in simulation-based cure cycle design and online controlling (Sec-

¹Before the rise of LCM processes, autoclaving of prepregs had been the common solution to manufacture 'thicker' composite parts. Early work in cure modelling had almost entirely been dominated by this manufacturing process [22–30]. Filament winding and pultrusion were sometimes used in studies on 'thick' cylindrical and extruded composite parts [31–33]. The leitmotiv of this overview is nevertheless formed by studies that challenged the manufacturing of 'thick' composite parts by LCM processes [34–38] (among others) (see also Section 1.2). When necessary or as a supplement, side steps in the survey are made to discuss results from other composite manufacturing processes.

tion 2.5), and emphasizing the necessity of online experimental validation (Section 2.6). Precedingly, common issues in curing 'thick' composite parts are summarised and manufacturing alternatives are put forward (Section 2.2).

2.2 Manufacturing hurdles and alternatives

2.2.1 Manufacturing hurdles

As mentioned in the opening chapter, the conventional cure cycle is not recommended for manufacturing 'thicker' composite structures. Several critical points pave the way to a cure behaviour similar to the one as depicted in Fig. 1.2. These are:

- the high level of energy released by the exothermic reaction;
- the low thermal conductivity of the thermosetting resin system;
- and the poor convective heat transfer at the tooling surface.

The amount of heat released by the exothermic reaction, often expressed as Joule per gram of material, depends on the type of thermosetting resin system and can vary significantly. In [18] two examples, separated by a factor of four, are given: (i) a polyester resin (168.6 J/g) on the low end of the spectrum and (ii) styrene (646.6 J/g) on the high end. In conjunction with the type of thermosetting resin system, its kinetics reaction time should also be considered. In the automotive industry, a short cure cycle, in the order of minutes, is common to achieve high production rates. On the contrary, process cycles may lengthen to a day in blade manufacturing for wind turbines. In the latter, the heat is released over a longer time span.

Instead of an extended cycle time, conduction may suppress thermal spiking as well. Thermosetting resin systems are, however, known for their rather low thermal conductivity in comparison to metals (500 times lower than aluminium [18]). In case of an Arrhenius² type of reaction, the higher internal temperature due to entrapped heat accelerates the reaction even more. In an adiabatic situation, colder zones would eventually heat up by the thermal energy transferred away from these hot spots. In practice, the tooling may provide a pathway to dissipate the accumulated heat. In RTM processes, the thermal energy may easily dissipate into the (metallic) tooling. On the contrary, the heat flux between composite and air is limited in processes such

²The rate constants in chemical reactions depend on the reaction temperature and activation energy.

as autoclaving and VI due to the vacuum bag acting as an insulator and the rather low heat capacity of air. Hence, thermal spiking is more severe in case of the latter.

When the reaction becomes out-of-control, material degradation is an ever present possibility [39]. For most modern epoxy-based resin systems, the degradation temperature is higher than the glass transition temperature in a fully-cured state [40]. Evaporation of volatiles can occur at higher temperatures [18]. Local 'overcuring' may lead to burning and, in the worst case, even to an explosion [41]. The onset of degradation/evaporation counts therefore as an important constraint in the processing window.

Furthermore, the non-uniform development of the cure reaction results in gradients in the composite part. Propagation of the through-thickness curing front can be described by three basic scenarios: (a) outside-in, (b) inside-out, and (c) one-side curing (Fig. 2.1). The first scenario, observed frequently in conventionally curing 'thick' composite parts, may result in entrapped voids, volatile by-products of the curing, and delaminations, because the fully cured exterior region constrains the interior region [23, 38, 42]. It is characterised by a high thermal spike due to fast curing of the core. Lowering the cure temperature turns the curing front from progressing outside-in to inside-out (second scenario). The core gels and vitrifies before the exterior surface. The thermal spike is generally lower. The disadvantages are a longer processing time to cure the composite part and lower mechanical properties due to incomplete cure³. In the third scenario, the through-thickness curing front moves from one side to the other. This can be triggered by imposing different temperatures on the upper and lower mould surfaces or giving insulating properties to one of the sides. Unsymmetrical curing, which may lead to geometric distortion, seems to make this scenario less favourable. No matter which scenario is followed, the thermal and cure gradients give rise to process-induced strains, for which their associated problems during demoulding and in the part's operational phase have already been highlighted in Section 1.4.

2.2.2 Intermezzo: definition of a 'thick' composite part

Up to now, the word 'thick' has been placed between quotation marks. The critical points mentioned above emphasize, however, that a theoretical basis is lacking in categorising composite parts as 'thick' by simply referring to their physical thickness.

³To reach the same degree of cure, it takes longer when curing at lower temperatures. Vitrification lowers, however, also the final degree of cure that can be reached.

situations, coupling of the filling and curing stages are essential for proper cure modelling.

In [38] a non-dimensional number called the gelling ratio:

$$Ge = \frac{\text{Filling time}}{\text{Reaction time}} \quad (2.2)$$

is, however, defined that allows for stage-decoupling when $Ge \ll 1$. As the main interest of this study is the monitoring of process-induced strains in slow curing resin systems for which the filling occurs in a near isothermal state, it is assumed that stage-decoupling can be applied⁵. Non-isothermal coupling of the resin flow and curing is therefore excluded from this overview⁶.

On a smaller scale, thermal expansion of the constituents or consolidation may still lead to resin flow in the curing stage. The latter, sometimes referred as a squeezing sponge effect [47], is observed in composites manufacturing processes with flexible tooling. Although some included a flow or compaction model in their cure analyses of thick composite parts [22, 39, 47–54], the problem is often simplified by neglecting the effect of convective heat transfer [36, 55, 56]. In practice, this constant resin-content situation would apply to fully compacted prepreg lay-ups or no bleed-processing in autoclaving and fully impregnated preforms in the RTM process [27, 56].

2.2.4 Alternatives

Skirting around the problems of manufacturing thick composite parts, several alternatives have been developed in recent years. As the geometrical shape is often set beforehand, solutions are sought in the two other fundamental aspects of the design trinity⁷: materials and processes [34].

Selecting an equivalent thermosetting resin system that generates less heat is an obvious solution of the former. Adding low profile additives⁸ and cure retarders may also be counted among this group. In [59] and [60] an attractive technique is presented to manufacture thick polyester- and vinylester-based laminates using pre-catalysed

⁵In this study, two resin systems are selected that have substantially long curing times (Chapter 4).

Both resin systems are assumed to remain in a quasi-steady unreacted state during mould filling. Moreover, the impregnated preform is supposed to be in thermal equilibrium at the end of the filling stage.

⁶Interesting literature on this topic can be found in [45].

⁷See Section 1.3 in [57] for an explanation of the design trinity.

⁸Adding additives can reduce the severity of cracking in thick composite cylinders [58].

glass fabric. Expensive certification procedures, especially in the aerospace industry, put, however, stringent requirements on the selection/adaptation of materials.

Altering the manufacturing process is then another option. In manufacturing the side-stay, smaller stacks were partially cured before building up the entire composite part. In this manner, a thickness of 60-90 *mm* was achieved without significant thermal spiking [7]. This so-called staged curing^{9,10} is first discussed in [61]. The method relies on releasing some of the exothermic energy while curing the thinner stacks. Instead of heating the composite part via the surrounding air (oven and autoclave) or tooling, alternative heating methods such as internal resistive heating [62], microwave curing [63, 64] and electron beam curing [65, 66] have been investigated as well. Despite promising results, some of the solutions are still considered exotic.

However, the mainstream has focused on developing methodologies to optimise processing conditions for existing materials and manufacturing configurations [11, 12, 34, 35, 38, 67, 68] (among others) (see also Section 2.5).

2.3 Brief overview of achievements

In early work, the encountering of various undesirable effects during prepreg autoclaving asked for understanding the curing process on a more fundamental level [23]. Being the first in 1983, Loos and Springer [22] developed a comprehensive one-dimensional cure simulation of a flat uni-directional (UD) graphite/epoxy laminate using an implicit finite difference method. The simulation included thermochemical, flow, void, and stress models. Their 'CURE' model is now, in various forms, widely used. Concerning the cure modelling of thick composites, three topics can be distinguished in literature¹¹:

- presenting methodologies for solving the cure model (more efficiently) [23, 41, 48, 55, 56, 74, 76–81];
- expanding the cure model by incorporating more physical phenomena/details and/or investigating their effects through parametric studies [23, 24, 28, 30,

⁹Staged curing does not affect the mode I interlaminar fracture toughness and shear strength [61].

¹⁰Similarly to staged curing, 'wind and cure' steps are frequently used in manufacturing composite flywheels to control the radial temperature [31].

¹¹Most of the studies cited here are based on the autoclave process [10, 22–28, 30, 39, 41, 42, 47–56, 69–73]. The sparse literature on cure modelling of thick composite parts manufactured by LCM processes [11, 12, 34–38, 58, 67, 68, 74, 75] opens the possibility to discuss them as well.

33, 36, 37, 39, 47, 50–53, 55, 58, 71, 72, 75, 82];

- optimising the conventional cure cycle to meet objectives set by thick composite manufacturing [10–12, 25–27, 31, 34, 35, 38, 41, 42, 49, 54, 67–70, 73, 83].

2.3.1 Solving the cure model using different methodologies

As the era of computer technology had just started, introducing methods for solving more efficiently the set of governing equations, *i.e.* reducing the computational effort, became one of the first interests. Researchers developed initially special-purpose numerical packages based on finite difference schemes to analyse their cure models [23, 27, 30, 48, 69, 73]. In these studies, convergence issues related to mesh density and time stepping was one of the topics addressed regularly. At the arrival of the new millennium, special-purpose numerical packages based on the Finite Element (FE) formulations set slowly in [39, 41, 45, 74, 76, 77, 80, 81]. Analyses were no longer limited to one- or two-dimensional case studies. It was, however, soon realised that switching to general-purpose numerical package was even more beneficial because of the well-developed pre- and post-processors. By adding appropriate subroutines, cure models have been implemented in ANSYS [55], LUSAS [56], ABAQUS [82] and COMSOL Multiphysics™ [79].

2.3.2 Expanding the cure model and analysing effects by parametric studies

The basis of all cure modelling is formed by the thermochemical analysis in which the energy balance (thermal) is coupled to the cure kinetics (chemical). Solving this transient problem gives the instantaneous cure state. In [45], the necessity of the two-phase model¹² when dealing with the non-isothermal mould filling by fast reacting resin systems. In the decoupled analysis, this initial value problem, *i.e.* the initial temperature and degree of cure distributions, was studied in [28] and [68]. Others incorporated physical phenomena such as consolidation, resin flow and viscosity (mostly in autoclaving) [39, 47–50, 52–54], and the inhibitor decomposition [36, 75]. Submodels improved the representation of the thermophysical properties such as density, specific heat capacity, and thermal conductivity [30, 33, 37, 52, 79]. Parametric studies concentrated on the effect of the thickness [23–25, 28, 47, 48, 69, 71], the processing history *e.g.* different cure schedules or part of the cure cycle such as the

¹²The reinforcing fibres and the resin system are treated separately by setting up two energy balances.

heating ramp or dwell temperature [23, 24, 47, 48, 50, 82], the boundary conditions, e.g. the effective heat transfer coefficient, unsymmetric curing, tooling geometry, bleeder thickness [23, 24, 51, 55, 69, 75] on the cure state.

In only a few researches cure modelling was extended to derive effective mechanical properties and process-induced and residual stresses in thick composite parts [24, 31, 38, 58, 72, 82]. Bogetti and Gillespie [24] were the first that conducted a fundamental study of process-induced residual stresses in thick-sectioned thermosetting composites [72]. In their study, a one-dimensional cure simulation was coupled to an incremental stress analysis. Others introduced a viscoelastic material model to analyse process-induced stresses in unidirectional and cross-ply laminates [38, 72] or implemented a woven fabric micromechanics model [82]. In another study [58], a one-dimensional radial heat transfer model was coupled to a thick cylindrical shrinkage model to investigate the mechanisms of interlaminar cracking in a composite cylinder. The simplified stress-strain relationships showed that differential shrinkage can cause interlaminar cracking. A similar approach is reported in [31].

2.3.3 Optimising the cure cycle

The last topic is covered by research groups that have been developing routines for optimal cure cycle design for thick composite parts. Studies fall in either one of the three categories: (i) simulation-based cure cycle design [11, 25–27, 30, 34, 38, 41, 49, 54, 67–69, 73], (ii) online controlling of the curing process [31, 84], and (iii) simulation-based design with event-based control [10, 12, 35, 42, 73, 83]. The latter, which is in fact a coupled version of the first two categories, is particularly useful when dealing with batch-to-batch variations and fluctuations in heating rates of the equipment [12]. Sensors detect online these differences and the optimisation routine defines then offline a new cure strategy (see Fig. 2.2). For the purpose of optimal cure cycle design, global optimisation techniques such as random walk and evolutionary strategies (genetic algorithms) [11, 12, 35, 38, 49, 67, 68], gradient-based optimisation techniques [34, 41, 54, 83], and expert-based systems [10, 31, 42, 73] have been used. In a comparison between three different global optimisation techniques, *i.e.* random walk, simulated annealing, and evolutionary strategies, a similar optimal cure cycle was found, but with different variances and fitnesses [12]. Trial-and-error approaches in the search for optimal curing are reported in [25–27, 30, 69, 70]. Most common objective functions are: obeying maximum temperature constraint to prevent material degradation, lowering through-thickness thermal gradients, and minimising processing time. In general, optimal cure cycle design directed towards two alternatives: either introducing additional dwell periods or performing rapid cooling and reheating.

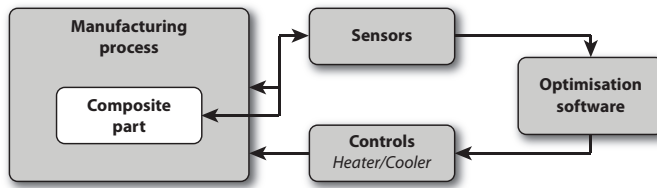


Figure 2.2: Scheme of smart cure cycle control system (based on [31]).

In this experimental study, the first topic, solving the cure model efficiently, is of less importance. More interesting are the trends observed in defining the cure model, the second topic, and designing the optimal cure cycle, the third topic. Section 2.4 continues therefore with an overview of the mathematical submodels in cure modelling. Section 2.5 will focus on the influence of the objective function on the optimal cure cycle.

2.4 Cure modelling - from thermochemical behaviour onwards

Traditional analyses of process-induced strains in thin laminates are based on the mismatch in Coefficient of Thermal Expansions (CTEs) between adjacent plies, homogeneous temperature difference between ambient and cure temperature, and no stress development prior to the end of the cure. The cure temperature is then the stress-free temperature. These analyses are not appropriate for thick composite parts. In isotropic thermosetting resin systems, thermal and cure gradients significantly influence strain development before the fully cured state is reached. Combined with the volumetric shrinkage of the resin system, they should be accounted for in studying the evolution of process-induced strains in thick composite parts [24, 72].

This section elaborates on the mathematical approaches that physically describe the curing of thick composite parts. As already introduced before, the energy balance(s) (thermal) and the cure kinetics (chemical) form the core in modelling the cure behaviour. As the majority of the publications centred around this thermochemical model, details of the governing equations are presented in the first place. Metaphorically speaking, this can be seen as the first stage in a two-stage rocket. In the second stage, the process-induced strains are derived. Sparse literature on modelling

this stage for thick composite parts limits the discussion. Only a global introduction is given to the modelling of the instantaneous effective mechanical properties and incremental process-induced strains.

2.4.1 First stage - thermochemical analysis

Heat transfer

Two approaches can be distinguished in modelling the heat transfer in composites manufacturing processes: (i) the less commonly used two-phase model and (ii) the more frequently applied local equilibrium (or lumped) model. In the two-phase model, the energy balance equations are separately averaged for the matrix and the reinforcing fibres. The heat transfer coefficient h_{rf} couples both two equations. Fast reaction or rapid changes in temperature, e.g. during non-isothermal mould filling, are best described by this model. The lumped approach can be adopted when the resin flow is slow (or even stagnant) and/or the heat transfer coefficient between the two phases is large (equal temperature). Experimental determination of the heat transfer coefficient is no longer needed, but, as a bargain, the single energy balance equation requires the thermophysical properties of both phases to be homogenised effectively [45, 85].

The vast majority of the studies determined only through-thickness profiles using one-dimensional energy balances [11, 24, 34, 36] (among others). Some researchers modelled the heat transfer in cross-sectional [23, 48] or even three-dimensional geometries [39, 56, 73, 74]. Cylindrical geometries were analysed in a polar coordinate system [26, 31, 58]. Scaling of the energy balance equations was applied for in trend analyses [34, 41, 48, 54]. In general, the three-dimensional Fourier's law of heat conduction can be expressed in a Cartesian coordinate system as [85]:

- Two-phase model:

1. Energy balance in the matrix:

$$\phi \rho_r c_{p,r} \frac{\partial T_r}{\partial t} + \rho_r c_{p,r} (\vec{V} \cdot \nabla T_r) = \phi \nabla \cdot k_r \nabla T_r + \phi h_{rf} (T_r - T_f) + \phi \dot{Q} \quad (2.3)$$

2. Energy balance in the reinforcing fibres:

$$(1 - \phi) \rho_f c_{p,f} \frac{\partial T_f}{\partial t} = (1 - \phi) \nabla \cdot k_f \nabla T_f + \phi h_{rf} (T_f - T_r) \quad (2.4)$$

- Local equilibrium model:

$$\rho_c c_{p,c} \frac{\partial T}{\partial t} + \rho_r c_{p,r} (\vec{V} \cdot \nabla T) = \phi \nabla \cdot k_c \nabla T_r + \phi \dot{Q} \quad (2.5)$$

where ρ , c_p , and k are density, specific heat capacity, and thermal conductivity, respectively. The terms T , ϕ , and \vec{V} represent the temperature, the porosity, and the velocity field, respectively. In these equations, the heat source, expressed by \dot{Q} , relates proportionally to the rate of reaction R_α of the thermosetting resin system:

$$\dot{Q} = \rho_r H_u R_\alpha \quad (2.6)$$

in which H_u is the ultimate enthalpy, *i.e.* the total heat of reaction, of the thermosetting resin system. The subscripts r , f , and c refer to resin, fibre, and composite, respectively.

These equations are based on assumptions such as (i) constant thermophysical properties, (ii) a Newtonian flow, and (iii) an incompressible fluid [85]. Effects due to thermal and molecular dispersion may be important in certain situations, but are not considered here [45, 86]. The use of the porosity ϕ implies the ideal, void-free, situation [34, 48]. In practice, the initial presence of voids or the formation thereof during curing lowers the resin volume fraction ($v_r < \phi$). The underlined convection terms can be dropped on the assumption of negligible resin flow [24, 55].

The generalised temperature boundary condition is formulated as:

$$a \frac{\partial T_s}{\partial n} + b[T_s - T(t)] = 0 \quad \text{on the domain boundary} \quad (2.7)$$

and allows for either prescribed, convective, or insulated temperature boundary conditions (Table 2.1). The coefficients a and b define the effective heat transfer across the domain boundaries [23, 24]. The cure cycle, *i.e.* the temperature profile, may be imposed (read: prescribed) directly onto the surfaces of the composite part. This approach works for tooling acting as a heat sink. In vacuum bagging, the thermal resistance of the foil and poor air convection can result in an increased surface temperature [75]. Another boundary condition, in the form of an effective heat transfer coefficient (a combination of convection to the surroundings and conduction by the tooling), is then applied¹³. The boundary condition can also be relocated to the tooling surface by establishing an additional energy balance equation for the tooling [34, 58]. Consumables such as Teflon film, bleeder, and vacuum bag may also be specified as these influence the heat transfer [55]. The third boundary condition in Table 2.1 describes the adiabatic situation, *e.g.* a situation in which the bleeder is considered an excellent insulator [30]. In the decoupled analysis of the cure stage, the starting temperature of the cure cycle is normally selected as the initial value.

¹³A higher coefficient permits a more rapid heat transfer into the laminate such that it heats up and cures faster. Excessive heat can easier escape keeping an overall lower exotherm [23].

Table 2.1: Generalised boundary condition [23].

Type	Coefficient a	Coefficient b
Prescribed	0	1
Convective	1	$h_{eff}/k_{eff} > 0$
Insulated	1	0

Cure kinetics

In cure kinetics, the rate of reaction is obtained from a species mass balance equation:

$$\frac{\partial \alpha}{\partial t} + \underline{\vec{V}} \cdot \underline{\nabla} \alpha = R_{\alpha} \quad (2.8)$$

in which the underlined term, advection of the degree of cure, is mostly omitted because of a negligible velocity field [85]. The term R_{α} is a function of the degree of cure and the temperature, $f(\alpha, T)$. In the decoupled analysis of the cure stage for thick composite parts, the initial degree of cure is usually set to zero, *i.e.* $\alpha_0 = 0$, implying the unreacted state¹⁴. The rate of reaction changes proportionally to the heat source:

$$\dot{Q} = \frac{dQ}{dt} \propto \frac{d\alpha}{dt} = R_{\alpha} \quad (2.9)$$

There are two strategies in modelling the cure kinetics, *i.e.* deriving the function $f(\alpha, T)$ from testing samples: either mechanistic or semi-empirical (phenomenological). Semi-empirical models fit an overall reaction order. The cure kinetics of commercial resin systems are mainly modelled in this fashion due to the lack of knowledge about the constituents [36]. On the contrary, the kinetic mechanisms that describe reactions such as initiation, inhibition, radical concentration, and propagation in polymerisation are individually modelled in the mechanistic approach. Although models in the mechanistic form give a better representation of the cure kinetics, they require detailed analyses of the concentration of reactants, intermediates, and products [87]. In studies on curing thick composites, the mechanistic approach forms the smallest group in modelling the in-house characterised cure kinetics¹⁵.

¹⁴In practice, a value close to zero, *e.g.* 10^{-7} [83], is used in order to circumvent problems in solving the set of equations.

¹⁵Many of the numerical studies relied on cure kinetics models (both semi-empirical and mechanistic) that had been developed earlier by others. The cure kinetics of an epoxy resin system, modelled back in 1982 [88], has reappeared in many other studies [23–26, 39, 47–49, 73, 74].

Table 2.2: Semi-empirical cure kinetic models for thermosetting resin systems [89].

Model	Equation	Equation number
n^{th} order reaction	$\frac{d\alpha}{dt} = k(1 - \alpha)^n$	(i)
Autocatalytic reaction	$\frac{d\alpha}{dt} = k\alpha^m(1 - \alpha)^n$	(ii)
n^{th} order + autocatalytic reaction	$\frac{d\alpha}{dt} = (k_1 + k_2\alpha^m)(1 - \alpha)^n$	(iii)
General complex reaction model	$\left. \frac{d\alpha}{dt} \right _{\text{overall}} = \sum_{i=1}^j g_i A_i e^{-\frac{E_i}{RT}} f_i(\alpha_i)$	(iv)
Arrhenius dependence of rate constant	$k_i(T) = A_i e^{-\frac{E_i}{RT}}$	(v)

In here, m, n are reaction orders, R is the universal gas constant, and j is the number of independent reactions. In the Arrhenius equation, A_i and E_i are the pre-exponential factor and activation energy of the i^{th} reaction. The reaction function and normalised weighting factor of the i^{th} reaction are represented by $f_i(\alpha_i)$ and g_i .

Different formulations of R_α have been proposed for a wide variety of thermosetting resin systems. The commonly used semi-empirical models can be found in Table 2.2. Popular in modelling the cure kinetics of epoxies is the n^{th} order + autocatalytic reaction; the Kamal-Sourour equation [10, 36, 58]. A more detailed overview of both semi-empirical and mechanistic cure kinetics models can be found in [87].

In the phenomenological models presented in Table 2.2 the conversion reaches eventually unity. In actual fact, vitrification changes the reaction from chemically-controlled to diffusion-controlled¹⁶ [90]. In the glassy state, the reduced mobility of the polymer chains causes the reaction to slow down significantly such that the final degree of cure does not reach unity. This phenomenon was hardly addressed in early studies [83]. In some recent studies, solutions are put forward in modelling this phenomenon by introducing: (i) $R_\alpha = 0$ at the moment of vitrification [30], (ii) a maximum degree of cure as a function of temperature [36, 38, 82], or (iii) a ratio between isothermal heat of reaction as a function of cure temperature and the total heat of reaction [25]. Other solutions may be found in studies that focus particularly on the cure kinetics of thermosetting resin systems [90]. Including vitrification in the cure kinetics may require a model, e.g. the DiBenedetto equation [30], for the instantaneous glass transition temperature:

$$T_g = T_{g,0} + \frac{(T_{g,\infty} - T_{g,0})\lambda\alpha}{1 - (1 - \lambda)\alpha} \quad (2.10)$$

where $T_{g,0}$ and $T_{g,\infty}$ are the glass transition temperatures of the unreacted and fully-cured resin system. The structural parameter λ represents theoretically the ratio

¹⁶Vitrification occurs when the instantaneous glass transition temperature surpasses the cure temperature.

of the heat capacities between the glassy and rubbery state for the fully cured and unreacted resin [89].

Thermophysical properties

For the constituents, three thermophysical properties are required as input for the energy balance(s). These are: density, specific heat capacity, and thermal conductivity. Despite their temperature and degree of cure dependency¹⁷ [48, 58], they are generally treated as constants in cure modelling of thick composite parts [23, 34, 36, 55, 74] (among others). Some used, however, functions such as:

$$f(T, \alpha) = c_1 + (c_2T + c_3)\alpha \quad (2.11)$$

$$= c_4 + (c_5\alpha + c_6)T + c_7\alpha \quad (2.12)$$

to represent the thermophysical properties [30, 33, 52]. In here, c_i are fitting parameters. The minimal impact of variable thermophysical properties is demonstrated by a sensitivity analysis using linear relations between the unreacted and fully-cured state of the resin system in [75]. Similarly, the assumption that changes in the resin thermophysical properties at gelation are relatively unimportant is verified in [28]. On the contrary, others concluded that the prediction of the through-thickness temperature distribution improves when the simulation is based on variable resin properties [52]. In [58] the resin's specific heat capacity was determined as a function of the cure state, but not included in the cure model. In [78] and [37] cure simulations are performed with thermophysical properties modelled as a function of temperature and degree of cure. The latter used even higher order polynomials in curve fitting. A comparison between simulations with constant and variable material properties was, however, not performed in these studies. In general, more accurate submodels may improve the overall cure modelling, but require more effort in material characterisation.

In the local equilibrium model (Eq. 2.5), these thermophysical properties have to be effectively homogenised. The composite's volumetric heat capacity is derived from the simplest micromechanical model: the rule of mixture (= parallel model) [39]. The effective thermal conductivity tensor of the composite material depends on the geometry of the medium. Approximating its values by the weighted arithmetic mean, as is done by the rule of mixture, may not be appropriate for all principal material directions¹⁸ [48]. In a search for improvement, more sophisticated models have

¹⁷Dependence on degree of cure counts for the matrix properties only.

¹⁸The weighted harmonic mean is applied more often, even in studies on woven and cross-ply laminates, to represent the transverse thermal conductivity [73].

been used such as the Tsai-Halpin¹⁹ [55] and Springer-Tsai²⁰ [27, 39, 47] relations or even others [74]. The Springer-Tsai model (original [92], but here in corrected formulation [39]) predicts the transverse thermal conductivities, k_{yy} and k_{zz} , in UD compositions as a function of fibre volume fraction v_f via:

$$\frac{k_{yy}}{k_r} = \frac{k_{zz}}{k_r} = 1 - 2\sqrt{\frac{v_f}{\pi}} + \frac{1}{B} \left[\pi - \frac{4}{\sqrt{1-C}} \tan^{-1} \frac{\sqrt{1-C}}{1 + B\sqrt{v_f/\pi}} \right] \quad (2.13)$$

where

$$B = 2 \left(\frac{k_r}{k_f} - 1 \right) \quad C = B^2 \frac{v_f}{\pi} \quad (2.14)$$

Despite its complicated appearance, it still relies on the same input as for the weighted arithmetic means. The wide variety of approaches illustrates, however, that estimating the composite's thermal conductivity tensor forms a major issue in cure modelling of (thick) composite parts on a macroscopic level²¹

2.4.2 Second stage - process-induced strain analysis

The Classical Lamination Theory (CLT) forms the theoretical basis in analysing the process-induced and residual stresses [24, 38, 82]. In [24] and [82] the one-dimensional cure simulation is coupled to the incremental laminated plate theory in an elastic modelling approach. Others considered the cure-dependent viscoelastic behaviour of the material critical when examining the process-induced stresses [38, 72, 94]. In [72] the variation of potential energy is applied. In [31] and [58] simplified global stress-strain relationships are introduced for thick cylinders despite their incorrectness for low degree of cure.

To the author's knowledge, these are the few studies on modelling the process-induced and residual stresses in thick composite parts. The second stage in cure modelling is therefore revisited briefly according to the flow diagram in [24]. That is, the temperature and degree of cure distributions are used to compute the instantaneous effective mechanical properties and incremental process-induced strains before the effective plate loads, deformations and ply strains are determined by CLT. In a

¹⁹The Tsai-Halpin model represents an judicious interpolation between the series and parallel models [91].

²⁰The Springer-Tsai model has an analogy with shear loading [92].

²¹Not directly related, but worthwhile to mention here, is the work performed in [93] in which the accuracy and validity of various micromechanical models for the calculation of the effective thermal conductivities of laminated composites are investigated.

backward approach, these steps are described below²².

Using the principle of superposition, the strains $[\epsilon]_{x,y}^k$ in lamina k within the laminate equals the sum of the strains produced by existing stresses in the lamina, $[\sigma]_{x,y}^k$, and the hygrothermochemical strains of the lamina. Inverted to stresses, the stress-strain relation can be expressed as:

$$\begin{bmatrix} \sigma_x \\ \sigma_y \\ \sigma_{xy} \end{bmatrix}_k = \begin{bmatrix} Q_{xx} & Q_{xy} & Q_{xs} \\ Q_{yx} & Q_{yy} & Q_{ys} \\ Q_{sx} & Q_{sy} & Q_{ss} \end{bmatrix}_k \begin{bmatrix} \epsilon_x - e_x \\ \epsilon_y - e_y \\ \epsilon_s - e_s \end{bmatrix}_k \quad (2.15)$$

where $[Q]_{x,y}$ is the reduced stiffness matrix and $[e]_{x,y}$ are the transformed, but unrestrained, hygrothermochemical strains of the lamina. The summation of the integrated stresses across the thickness of each lamina gives then the force resultants. In the absence of curvatures and externally applied mechanical forces and moments, the hygrothermochemical relations for a symmetric laminate are given by:

$$\begin{bmatrix} N_x^{HTC} \\ N_y^{HTC} \\ N_{xy}^{HTC} \end{bmatrix} = \begin{bmatrix} A_{xx} & A_{xy} & A_{xs} \\ A_{yx} & A_{yy} & A_{ys} \\ A_{sx} & A_{sy} & A_{ss} \end{bmatrix} \begin{bmatrix} \epsilon_x^o \\ \epsilon_y^o \\ \epsilon_s^o \end{bmatrix} \quad (2.16)$$

where $[N^{HTC}]$ is the hygrothermochemical force and $[A]$ is the laminate stiffness matrix. The reference plain strains $[\epsilon^o]$ relate to the effective CTE $[\bar{\alpha}]_{xy}$, the moisture expansion coefficient $[\bar{\beta}]_{xy}$, and the chemical expansion coefficient $[\bar{\gamma}]_{xy}$:

$$\begin{bmatrix} \epsilon_x^o \\ \epsilon_y^o \\ \epsilon_s^o \end{bmatrix} = \begin{bmatrix} \bar{\alpha}_x \\ \bar{\alpha}_y \\ \bar{\alpha}_{xy} \end{bmatrix} \Delta T + \begin{bmatrix} \bar{\beta}_x \\ \bar{\beta}_y \\ \bar{\beta}_{xy} \end{bmatrix} \Delta c + \begin{bmatrix} \bar{\gamma}_x \\ \bar{\gamma}_y \\ \bar{\gamma}_{xy} \end{bmatrix} \Delta \alpha \quad (2.17)$$

The parameters ΔT , Δc , and $\Delta \alpha$, are the changes in temperature, moisture concentration, and degree of cure, respectively [91].

To solve the set of equations, the incremental stress-free macroscopic process-induced strains have to be computed for each lamina²³. Referring to the principal material axes of the lamina, these strains are given by:

$$e_1 = e_1^{th} + e_1^{hy} + e_1^{ch} = \alpha_1 \Delta T + \beta_1 \Delta c + \gamma_1 \Delta \alpha \quad (2.18)$$

$$e_2 = e_2^{th} + e_2^{hy} + e_2^{ch} = \alpha_2 \Delta T + \beta_2 \Delta c + \gamma_2 \Delta \alpha \quad (2.19)$$

²²The consequences of demoulding are not ventilated here.

²³In [24] this term is used to denote the hygrothermochemical strain in the lamina. In [72] these are called the nonmechanical strains.

Early cure models ignored the chemically induced strains. However, their importance is recognised for the internal loading in thick laminates [24]. Only moisture effects have not been taken into account [72]. The total process-induced strains is thus computed by superimposing the thermally and chemically induced strains. Using transformation matrices, the thermochemical strains can be referred to the (x, y) -coordinate system of the laminate.

The last step in this explanation, but the first after the thermochemical analysis is the determination of the instantaneous effective mechanical properties, *i.e.* the engineering constants of the lamina. In a similar manner to the thermophysical properties, mechanical properties of the reinforcing fibres and matrix have to be homogenised effectively. In this respect, mechanical properties of the reinforcing fibres are considered constant, *i.e.* independent of temperature and degree of cure [24, 38]. The resin characteristics change, however, dramatically during cure. Initially, the resin behaves as a viscous fluid, but turns into a (visco)elastic solid towards the end of cure. Hence, the mechanical properties of the resin cannot be considered constant. Some simple approaches use an α -mixing rule model²⁴ of the unreacted (at the After Gel Point (AGP)) and the fully cured resin moduli [24] or coupled the instantaneous modulus of the resin directly to the final resin modulus through the instantaneous degree of cure [82]. However, characterisation of the resin helps in finding more elaborate and descriptive representations [94]. By assuming a constant Poisson's ratio, the moduli of elasticity in tension and shear can be linked via the classical relationship for isotropic materials. Another approach is to assume a constant plain strain bulk modulus. A slight difference in Poisson's ratio is then introduced at low degree of cure, but this does hardly effect the process-induced strains [24, 38].

For modelling the cure-dependent viscoelastic behaviour a modified power law is considered in [94] to model the stress relaxation curve for the thermorheologically simple material, whereas a series of exponential functions is used in [72] to model the time-dependent stiffness of the matrix.

A self-consistent field micromechanics model can be used to compute the effective mechanical properties [24], but this may lead to an overestimation of the in-plane effective moduli near the rubber-to-glass transition in particular cases [38]. For the

²⁴Although in [24] a term is included in the α -mixing rule model to quantify the competing mechanisms between stress relaxation and chemical hardening of the resin, its coefficient is set to zero in their analysis. In this way, the elastic modelling approach provides only upper bounds for the process-induced stresses.

thermally induced strain, the CTE along the principal material axes of the lamina are derived by micromechanics as well [24, 38]. For uniform strain contraction, the isotropic shrinkage strain equals:

$$\Delta\epsilon_r^{\text{chemical}} = \sqrt[3]{1 + \Delta v_r} - 1 \quad (2.20)$$

where the incremental specific volume resin shrinkage Δv_r is the total chemical shrinkage for the fully cured resin multiplied by the instantaneous degree of cure $\lambda_{chem}\alpha$. In micromechanics, the reinforcing fibres act as constraints such that the chemical shrinkage may vanish almost completely in the fibre longitudinal direction due to the stiffening effect of the reinforcing fibres [24, 38, 58].

The author recognises that the overview is limited in some aspects. However, the intention was to give the reader a feeling of the complexity in cure modelling due to the wide variety of consecutive steps.

2.5 Simulation-based cure cycle design & online controlling

The manufacturing hurdles in conventional curing thick composite parts ask for an alternative cure cycle. Studies on optimal cure cycle design fall into three different categories. Whether simulation-based, online controlled, or a combination thereof, the approaches aim at the same goal: optimising the processing procedures while maintaining the quality in thick composite parts.

2.5.1 Sub-objectives and constraints

Optimisation algorithms (or controlling strategies) search for appropriate parameters (design variables) that satisfy the given objective function (or rules). This objective function, or fitness function, can consist of several (competing) criteria. Quality may be defined by the sub-objectives present in the fitness function. Optimising the fitness function results in the 'best' quality. Unfortunately, quality applies then only

to the criteria present in the fitness function ²⁵. Incorrect modelling of the occurring physical phenomena and/or incorrect values for the parameters are other sources that may influence the final quality [42].

In [11], seven of these competing sub-objectives are identified for reducing the process-induced stresses and the cycle time in LCM processes for thick composite parts. In other studies on optimal cure cycle design, similar criteria can be found. For instance, minimisation of time required to reach a user-defined minimum degree of cure is applied as one of the sub-objectives in [41, 83]. Effectively seen, this is a merge of the second and third item of the following list of sub-objectives:

- Minimisation/limit of the exothermic peak temperature to avoid material degradation [10, 11, 25–27, 30, 41, 42, 49, 54, 67, 69];
- Minimisation of the processing time [10–12, 25, 27, 35, 41, 42, 49, 54, 67, 83];
- Maximisation of the final degree of cure (complete cure) to improve mechanical properties [10, 11, 41, 42, 54, 67, 83];
- Minimisation of the thermal gradients
 1. throughout the whole cure cycle [31, 49, 68, 73, 83];
 2. after the instant the resin gels [34, 35];
- Minimisation of the process-induced²⁶ strains [11, 12, 31, 42, 67, 70]²⁷;
- Achieving a constant through-thickness degree of cure at AGP level [11, 67];
- Minimisation of the through-thickness cure gradients after AGP level [11, 35, 67].

²⁵In [41], for instance, a gradient-based optimisation technique was used to determine the optimal cure cycle for an autoclave process. The objective was minimisation of processing time, while obeying the maximum temperature constraint. A reduction of 66% in processing time was achieved by introducing multiple dwell periods. Consolidation was, however, not considered in finding the fast-curing cycle. In a follow-up study [54], it was theoretically proven that a 40 mm thick composite part does not fully consolidate for the given cure cycle. The optimal cure cycle did satisfy the prescribed criteria, but the quality would still have been poor due to failed assumptions in the model and fitness function.

²⁶A distinction is made between curing internal stresses and cooling stresses in [11, 67].

²⁷The extent of cure cross-over is used in [12]. A low value indicates that the composite cures primarily inside-out. Residual stresses are then expected to be minimal.

For optimal curing in autoclave processes, sub-objectives based on consolidation [25, 26, 49, 54] and having a void-free²⁸ evenly distributed resin [48] can be added to the list. Void minimisation is, however, a sub-objective in optimising the filling strategy for LCM processes [95, 96]. Modelling the consolidation has, in general, not been considered for LCM processes. These sub-objectives are therefore left out.

In the fitness function, the importance of each sub-objective can be quantified by weighting coefficients [11, 49, 68]. The analyst can thus influence the degree of success of a set of design variables by his/her choice of weighting coefficients. The shape of the fitness function itself is important for the speed of convergence [11, 12].

The design variables represent the adjustable parameters of the problem. In optimal cure cycle design, the design variables describe the temperature profile of the autoclave/oven or tooling. The temperature profile can be discretised into a small series of steps/linear functions [11]. Giving the initial system temperature, a one-step conventional curing is then characterised by two parameters: a heating ramp, Q_1 , and a dwell time, dt_2 (see Fig. 2.3a). Complex curves, *e.g.* multi-step cure cycles, can be created by increasing the number of linear functions. For a constant time interval only the ramps have to be determined [27, 49]. Non-linear control of the autoclave temperature is even proposed in [73]. In online controlling, the MRCC dictates the initial temperature path [10, 73, 83]. Whether these temperature profiles are feasible depend on the dynamics of the manufacturing process and constraints. In some studies the design variables are therefore constrained by physical and practical limitations, *e.g.* minimum and maximum heating and cooling capacities, of the manufacturing process [27, 40, 49, 67]. Time-delay constraints reflect the time required by the system to change the temperature [41].

2.5.2 Trends in optimal cure cycles

Most of the research work on optimal cure cycle design has been focused on the first three sub-objectives. As the studies dealt with a wide range of part thickness and a variety of material models, only the major trends in the optimised cure cycles can be distilled on this level of discussion. Optimal cure cycles for minimisation of process-induced and residual strains are discussed at the end of this section.

²⁸Voids reduce the strength-bearing capabilities, create stress risers and can affect the surface finishing [43, 48].

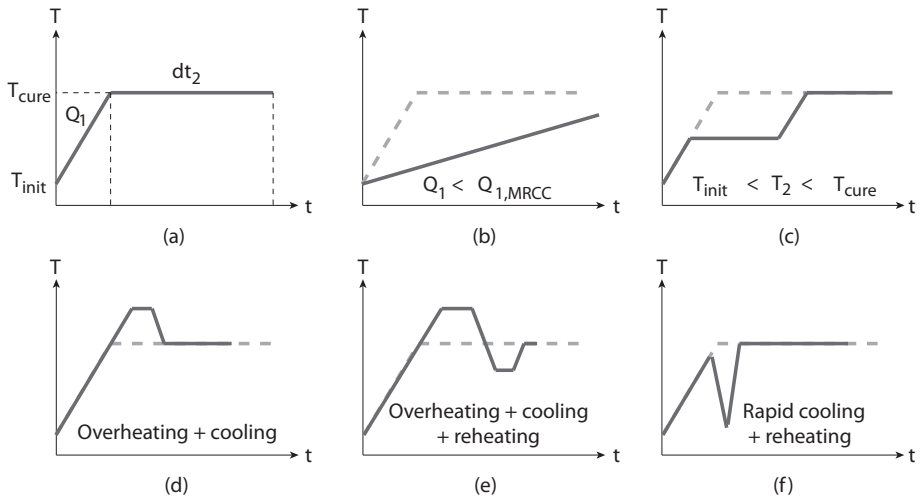


Figure 2.3: Generic cure schedules (without cooling down) in optimal cure cycle design - (a) conventional curing (MRCC); (b) traditional curing by slow heating; (c) curing with an intermediate dwell; (d) two-step curing with overheating and cooling; (e) three-step curing with overheating, cooling, and reheating; (f) curing with rapid cooling and reheating.

Traditionally, the solution to overcome thermal spiking has been to slowly heat the composite part (see Fig. 2.3b). The cure is then automatically executed over a longer timespan [42]. In optimal cure cycle design, this trend is observed when minimisation of processing time is not part of the objective function [25, 26, 30]. In online controlling, a similar trend is found when the initial temperature path is defined by the MRCC [10, 73, 83]. Controlling rules adapt constantly the heating rate to prevent material degradation. As the initial temperature path is based on the one-step conventional cure cycle, which is too fast for thicker laminates, the heating rate decreases when the cure temperature is approached resulting in a longer processing time.

Cost motives and desired production rates makes this solution less suitable for industrial applications. The remedy is to change the optimal one-step conventional cure cycle for thin laminates into a two-step cycle by introducing an intermediate dwell

period²⁹ (Fig. 2.3c) [27]. Time is allowed for heat conduction through the laminate thickness at temperatures where the cure rate is still low. Hence, an inside-out cure is promoted [97]. Although the maximum temperature can indeed be reduced by the two-step cure cycle, the cycle time extends because of a lower cure temperature that slows down the reaction [27]. Two-step cure cycles are nonetheless seen as serious options in designing the optimal cure cycle³⁰.

The optimal cure cycle may be further improved by increasing the number of dwells [41]. In [41] three cases are analysed: single dwell, two-dwell, and three-dwell cure cycles. The design centres around minimisation of processing time, while obeying the maximum temperature constraint. The single dwell cure cycle stretches the processing time, because the cure temperature is lower. The cure time reduces by about 25% for the two-dwell cycle. Instead of an intermediate dwell period such as in the two-step cure cycle, the first dwell is now at a higher temperature for a short time to speed up the reaction. Once started, the tooling temperature is reduced to avoid over-heating (Fig. 2.3d). In the optimal three-dwell cure schedule the second dwell temperature is lower than the final cure temperature in order to compensate for the longer first dwell (Fig. 2.3e). Compared to the single dwell cure schedule, more degrees of freedom can reduce the cure time, but improvements become less significant with more dwells [54]. The strategy of cooling and reheating appears in several other optimal cure cycle designs [12, 27, 50, 51, 69].

As noticed correctly in [41], a uniform temperature distribution must also be considered. In fact, through-thickness thermal gradients contribute to process-induced and residual strains [34]. Thus, rapid curing by introducing 'cooling-and-reheating' steps in the cure schedule may no longer be appropriate. In hot-pressing of prepregs, a non-linear model-based methodology is proposed to control the cure cycle online [83]. Minimisation of the temperature difference between centre and surface of the composite part is added as a sub-objective to the fitness function. For a one-step MRCC as input, the control method that combines a dynamic inversion controller, state observer, and a gradient-based optimisation algorithm, steers to traditional solution of slow heating³¹. Also in [49], it is demonstrated that the influence of optimising for minimal thermal gradients can be significant on the optimal cure cycle. Without

²⁹Note that autoclaving is already characterised by a two-step curing cycle because of the consolidation stage. A third dwell may therefore be recommended by the manufacturer in curing thick parts [28, 50, 70].

³⁰The effect of batch-to-batch variations in online controlling of the desired two-step cure cycle is investigated in [42].

³¹Whether the optimisation or the feedback dictated the solution is an interesting question.

the sub-objective, the optimised cure cycle points towards the 'cooling-and-reheating' strategy. In the new situation, a two-step cure cycle replaces the less favourable 'cooling-and-reheating' strategy at the cost of a longer processing time. Though, thermal gradients do not have to be minimised for the complete cycle [34]. The instant the resin gels can be selected as the starting point for minimising the through-thickness thermal gradients. The methodology, which is based on the rate of energy balance principle, reduces substantially the through-thickness thermal gradients by introducing an intermediate dwell. The plateau divides the cure regime into a conduction zone (insignificant reaction) and a heat generation zone (uniform curing). Faster heating to a higher cure temperature at the start of the heat generation zone results theoretically in a reduction of the cycle time and thermal gradients.

In the two control strategies developed in [31], the sub-objective of uniform temperature distribution is considered a necessary condition in order to minimise residual stresses in thick composite filament wound structures. Both control strategies lower indeed the radial residual stresses and strains, but at the cost of quintupling the processing time. On the contrary, others show that the residual stresses in thick-wound composite cylinders can be reduced without increasing the processing time [70]. This smart cure method relies on abrupt cooling (quenching) during the conventional cure cycle and, subsequent, reheating to complete the cure reaction. Despite a single experiment, the result is found remarkably because of the statement about thermal gradients and their relation to residual strains.

Perhaps the most comprehensive thermal optimisation methodology for the curing stage in LCM processes is described in [11, 67]. Herein, two approaches are considered to reduce curing stresses: (i) minimisation of thermal gradients in the through-thickness direction and (ii) evaluation of internal stresses developed during cure. The former tends to produce the slowest cure cycle available (see also [31]). The latter permits higher thermal gradients in the rubbery state. To this end, two other sub-objectives are considered in the fitness function to minimise cure gradients. First of all, the progression of the curing front is controlled by assuring that the cross-over point was close to the AGP level. The other sub-objective insists on uniform through-the-thickness development of the chemical shrinkage. Figure 2.4 shows the effect of modelling with elastic properties, viscoelastic properties, and without stress analysis on the optimised cure cycle for a thick composite part³². Including the processing stresses in the fitness function increases the processing time. Furthermore, the time required for stress relaxation decreases the slope of the last cooling ramp. Minimisa-

³²The shape of the optimised cure cycle is established prior to the actual optimisation.

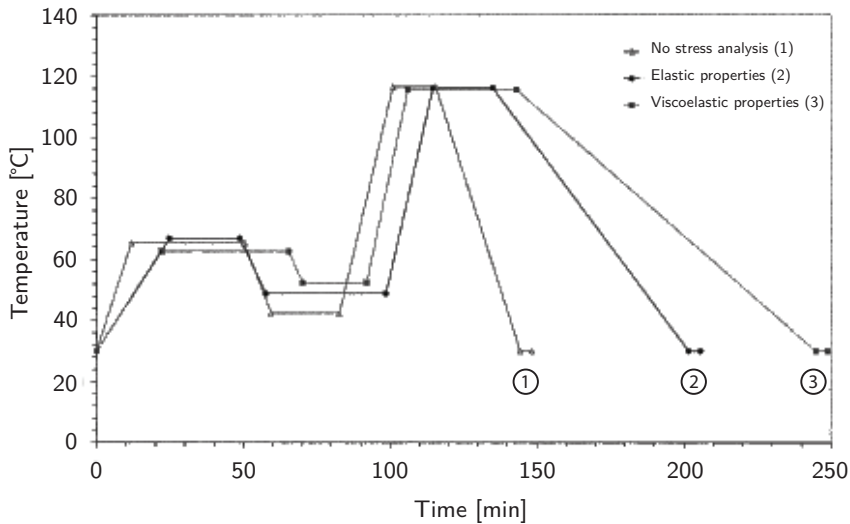


Figure 2.4: Optimised temperature profiles - effect of modelling with elastic properties, viscoelastic properties, and without stress analysis [67].

tion of the cure gradients is therefore insufficient in optimal cure cycle design. The evolution of the processing stresses must be considered as well.

2.6 Experimental validation by online monitoring and post-manufacturing evaluation

Creating models seems a must to capture the understanding of the physical processes in composites manufacturing processes. Loos and Springer [22] did already so in studying the issues of manufacturing thick composite parts by autoclaving back in the 80s. However, reliability of the cure simulation should be an important concern, as the thermomechanical parameters of a composite part can be difficult to predict due to its heterogeneous nature. Generally, only semi-empirical submodels, e.g. for the cure kinetics, are available [12]. Validation by experimental testing becomes a necessity for the (simplified) cure simulations. In this sense, a systematic set of reliable experimental data has to be generated in order to evaluate existing and future cure simulations [25, 38].

Some research work on cure modelling and optimisation lacks the underpinning by

proper experimental testing [26, 30, 34, 39, 41, 46–49, 54, 68, 71, 72, 74, 78, 80, 82]. In developing methodologies for solving the cure model (more efficiently), comparative analyses have often been carried out using analytical/numerical solutions (from other studies) [28, 56, 74, 78, 80]. Numerical case studies are found in studies in which a proof was given of a newly developed methodology [11, 26, 34, 38, 46, 47, 49, 56, 67, 82]. In optimal cure cycle design, numerical simulations have highlighted the benefits of the optimised cure cycle over the conventional one (often the standard MRCC for thin laminates) [31, 41, 54]. Hence, the optimised cure cycles may become unrealistic or infeasible³³. The costs of operating an experimental setup can be another motive to step away from experimental correlation. Some studies rely therefore solely on experimental data that was published earlier by other research groups [27, 39, 48, 53, 56, 73, 74, 76–78, 80].

In case of experimental testing, correlation/validation has often been limited to a few tests in which the temperature distributions are acquired by embedded thermocouples [10, 12, 22, 23, 25, 27, 33, 35–37, 42, 43, 50–52, 55, 58, 69, 75, 83, 97]. Others sensors in online process monitoring of thick composites are: heat flux sensors [12, 75], pressure and thickness gauges [25], dielectric sensors [25, 50] and Extrinsic Fabry-Perot Interferometry (EFPI) sensors [10]. The EFPI sensors can be used to determine the end of cure by monitoring the chemical shrinkage, whereas the dielectric sensors follow continuously the extent of cure.

In these studies, some show a 'good' agreement between the predicted temperature distributions and the actual ones [22, 23, 27, 35, 51, 52, 55, 58, 97]. Though, the definition of a 'good' agreement seems researcher dependent. Trial-and-error fitting is sometimes applied in order to improve the agreement between numerical and experimental results. This so-called backwards technique can be used to set some of the heat transfer properties [75]. In [37] a correction factor in the cure kinetics model is introduced to address batch-to-batch differences. Even the wide range in measured and published data allows to fine tune the cure model to fit the experimental data [55, 58]. In these particular cases, validation by the experimental testing is questionable.

On the contrary, others observed temperature discrepancies for which a manifold of reasons can be presented. These discrepancies may be caused by treating the thermophysical properties such as density, specific heat capacity, and thermal conductivity, as constants [27, 55, 69]. An inaccurate cure kinetics model may be another source

³³In [34], heating of the RTM tooling by a ramp of about 150 °C/min is proposed in order to suppress thermal gradients during resin polymerisation.

as well as the wrongful determination of the effective heat transfer coefficient and/or the effective transverse thermal conductivity [27, 33, 36, 69, 75]. Thermal contact at the interfaces and batch-to-batch differences are listed in [37]. Changes in the ratio of constituents and part thickness and heat transport due to resin flow are mentioned in [55]. Furthermore, experimentally determined temperature distributions may not represent the one-dimensional through-thickness cure simulation due to heat transfer through the edges of the finite laminate [12]. The processing temperature may also vary along the tooling surface due to inhomogeneous heating. In combination with high sensitivity of the resin reaction, this can have a profound effect on the temperature distribution [45, 75].

Experimental results have been scarce for process-induced and residual strains. Approaches rely on either pre- [24, 38] or post-manufacturing [31, 70, 83] evaluation. In case of the former, experimental validation of the proposed thermomechanical model is provided indirectly by tests performed on thin laminates. That is, 'stop-curing' results from UD and unsymmetrical laminates are reported in [24], whereas results from the longitudinal plate curvature of unbalanced laminates are used in [38]. In post-manufacturing evaluation, the residual stress distribution is measured by destructive testing of the composite part. In order to relieve stresses, either holes have been drilled [83] or cut-outs have been made [31, 70]. In case of the latter, it is shown that both a 'cooling + reheating' cure cycle [70] and cure strategies that keep a uniform temperature distribution, *i.e.* slow curing [31], can reduce the residual stresses in thick cylinders³⁴. The traditional way of slow curing, which suppresses the thermal gradients, gives a residual strain profile that is closer to the envelope generated by the ASTM standard for determining residual stresses by the hole-drilling strain-gauge method than conventional curing [83].

2.7 Concluding remark

In studies about simulation-based cure cycle design and online controlling, a wide variety of optimised cure cycles have been proposed for thick composite parts. The objective function seems to have a large influence on the shape of the cure cycle. When minimisation of processing time is not considered, the traditional way of slow curing appears as the solution to avoid material degradation while still achieving a complete cure. Including this sub-objective results in optimal cure cycles with multiple

³⁴Only a few tests have been performed to confirm this statement in both studies.

dwells. Typical are the cycles with a 'cooling + reheating' step and an intermediate dwell. The latter is more convenient when minimisation of thermal gradients is also considered. Fulfilling the objective function would nevertheless result in the 'best' quality. Failed assumptions in the model and fitness function, incorrect modelling of the occurring physical phenomena, and/or incorrect values for the parameters, can be sources that affect the quality. At this point, experimental verification becomes essential to verify whether optimised cure cycles are indeed optimal and even feasible in practice. Although some studies compared the predicted temperature distributions with the actual ones from embedded thermocouples, the limited number of tests does not contribute to a better understanding of the requirements in modelling and optimising the curing stage for thick composite parts. In this respect, monitoring the evolution of process-induced and residual strains during cure has not even been considered yet.

In conclusion, more effort has to be put in further development of testing methods for thick composite parts in order to supplement simulation-based cure cycle design and online controlling.

3

PROCESS MONITORING - A LITERATURE SURVEY ON FIBRE BRAGG GRATING SENSORS

3.1 Introduction

One of the key issues in manufacturing advanced composites, both thin and thick, is the in-mould segment time. Studies to shorten this have been performed (Section 2.5). A shorter cure cycle may be economically advantageous, but it may also affect material properties adversely. Real-time monitoring of the curing process turns therefore into an attractive solution [98]. In this respect, fibre optics are promising tools that may ultimately lead to shorter qualification times for new structures, improvements in quality of manufacturing, and reduction of rejected parts [15–17, 99]. Optical fibre-based sensing techniques such as Raman, interferometry (Michelson, Fabry-Perot), intensity, polarisation, Bragg gratings, Brillouin etc. are capable of monitoring a wide variety of parameters (strain, temperature, flow, pressure, chemical concentration etc.) [100]. FBG and EFPI sensing are two of these techniques that can measure simultaneously temperature and the formation of process-induced strains. The disciplinary group Design and Production of Composite Structures (DPCS)¹ at the Faculty of Aerospace Engineering introduced the former in their research a few years ago [13].

In this chapter an overview is presented of the current state of monitoring composites manufacturing processes by FBG sensors². Precedingly, the reader is introduced

¹<http://www.dpcs.lr.tudelft.nl>

²The overview is based on articles that have been published over the last 10-15 years.

to the concept of FBG sensing by a brief overview of major milestones, the applications in other industries/research areas, and pros and cons (Section 3.2). The theoretical working principles are summarised and extended to the field of monitoring composites manufacturing processes (Section 3.3). Different types of gratings and the discrimination between strain and temperature are discussed in Sections 3.4 and 3.5. Section 3.6 lists the main achievements in monitoring composites manufacturing processes according to: (i) flow monitoring, (ii) curing of neat resin systems, and (iii) fabrication of fibre reinforced plastics. Shortcomings and practical issues are presented in Section 3.7. Finally, Section 3.8 presents some concluding remarks.

3.2 Brief history, applications, pros and cons

In 1978 Hill *et al.* discovered by chance that photosensitivity increases the refractive index of the core of the optical fibre [101]. This early FBG is formed by exciting an optical fibre with a laser. As such, a standing wave pattern is established that forms the periodic perturbation of the refractive index. Long production times, variation in strength along the optical fibre and the fact that the filter reflects only wavelengths near the one of the laser limits the usefulness of these gratings³ [102]. More than ten years later the ultraviolet transverse holographic technique was introduced [103]. Two intersecting coherent ultraviolet laser beams irradiates now the optical fibre from the side. As the intersecting angle of the two beams defines the grating period, the operating wavelength range gets extended. This technique was superseded by the invention of the phase mask technique in 1993 [104]. The corrugated surface relief of the silica phase mask diffracts the laser light into 0, +1, and -1 orders. The +1 and -1 orders produce the periodic pattern needed for the inscription of a grating in the optical fibre. The grating period does not depend on the wavelength of the writing laser, but is constrained by the phase-mask period [102]. These fabrication methods are, however, labour intensive and time-consuming. Repeatability and mechanical strength are other limiting factors. Since then, the industries have pushed towards reel-to-reel and draw tower fabrication processes that allow for writing multiple FBGs in a continuous single fibre spool. Improved tolerances, higher yields and lower production costs are the main advantages [105]. In 1995 the first gratings were commercially produced. Initially these FBGs were applied in optical communications devices for dense wavelength division multiplexing, dispersion compensation, laser stabilisation, and erbium amplifier gain flattening. After the collapse of the telecom-

³The grating is thus the periodic perturbation of the refractive index.

munications bubble at the end of the 90s, many players in the industry shifted to sensing applications [105].

Because of their intrinsic capability to monitor a multitude of measurands, a wide variety of mechanical sensing applications of FBG sensors have been developed for different fields and industries. Examples are the monitoring of civil structures such as concrete bridges and domes for gust loads and tunnels for long-term deformation. Soil pressure FBG sensors monitor earthwork structures and innovative FBG-based sensors measure seismic activities. Applications related to Structural Health Monitoring (SHM) are found in both aerospace and wind-energy industries. FBG sensors have also been applied in health monitoring of oil rigs and transportation infrastructure [99, 102, 105]. Last but not least, FBG sensors are applied in online and *in situ* monitoring of composites manufacturing processes⁴.

That FBG sensors are present in many different fields arises from their advantages over other sensing techniques such as foil strain gauges. FBG sensors are totally passive and have a small size⁵. Hence, they can easily be embedded and do not require local power or show resistive heating. The narrowband signal favours multiplexing⁶ in the wide wavelength operating range of the C-band (1525-1565 nm). Moreover, the non-conducting FBG sensors are immune to electromagnetic interference and can operate in harsh environments. Due to low loss of signal in the C-band region, optical fibres with FBG sensors are highly suitable for remote sensing. The parameters are directly encoded into the Bragg wavelength and are therefore independent of fluctuations in light intensity, source power, and connector losses [109]. Despite the relevant advantages of FBG sensors over foil strain gauges, some disadvantages have to be mentioned here. FBG sensors are sensitive to thermal disturbances and transverse strain. Careless handling may easily result in fibre breaking. Secondly, a lack of standards exists for the application of FBG sensors as process monitoring tools and the costs are still high because of the manufacturing procedure and the limited number of suppliers. And, with respect to composite manufacturing processes, the embedded optical fibres may affect fatigue and compressive properties during the operational lifetime [100, 105, 110].

⁴At the end of the 90s the first articles were published in journals that can be related to this field [106, 107]

⁵A standard Single Mode (SM) telecommunication optical fibre has an outer diameter of 125 μm and a core diameter of 7-12 μm [100].

⁶Multiplexing enable engineers to create multi-point sensing arrays that act as a nervous system in their designs [108].

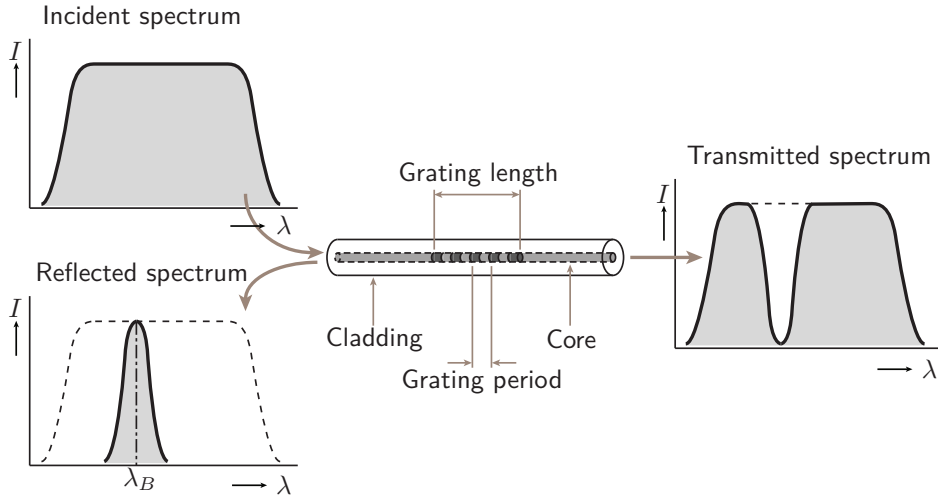


Figure 3.1: Working principle of the uncoated FBG sensor (based on [98]).

3.3 Theory of FBG sensing

3.3.1 General working principles

Briefly explained, a Bragg grating in an optical fibre, which is illuminated by a broadband spectrum light, reflects a narrow-band optical signal, satisfying the Bragg condition at a particular wavelength, *i.e.* the Bragg wavelength λ_B , whereas all other wavelengths of the broadband spectrum light are transmitted. This reflection is caused by the periodic modulation of the refractive index at the so-called grating (see Fig. 3.1).

The Bragg wavelength itself is defined as the centre wavelength of the reflected narrow-band optical signal and is a function of the effective refractive index n_{eff} and the grating period Λ . That is,

$$\lambda_B = 2n_{eff}\Lambda \tag{3.1}$$

According to this expression, a shift of the Bragg wavelength is observed when either the effective refractive index or the grating period changes. Strain and thermal effects that modify the physical or geometric properties of the grating are thus recorded by monitoring this shift [15]. As a function of axial strain⁷ ϵ_1 and temperature T , the shift of the Bragg wavelength is determined by differentiating Eq. 3.1 with respect to

⁷Strain along the principal axis of the optical fibre is denoted by subscript 1.

these parameters. To this end, a linear relation⁸ between the gauge length L of the sensor and the grating period is used. Since this derivation can be found in a number of books [13, 111, 112], the resulting equation is presented here directly:

$$\frac{\Delta\lambda_B}{\lambda_B} = (1 - P)\Delta\epsilon_1 + (\alpha_n + \alpha_f)\Delta T \quad (3.2)$$

where P , α_n and α_f are the effective photo-elastic coefficient, the thermo-optic coefficient and the CTE of the optical fibre, respectively. The equation can be rewritten using strain and thermal sensitivities:

$$\frac{\Delta\lambda_B}{\lambda_B} = S_\epsilon\Delta\epsilon_1 + S_T\Delta T \quad (3.3)$$

Please note that the thermal sensitivity of the Bragg wavelength arises from both a change in grating period due to thermal expansion of the fibre and a change in effective refractive index caused by the thermo-optic effect. The strain sensitivity arises from a change in the grating period as well as a change in effective refractive index due to the strain-optic coefficient [113].

3.3.2 Terminology

In Fig. 3.2 some definitions are given with respect to the optical fibre and the reflected spectrum. The longitudinal axis of an optical fibre is denoted by x or 1, whereas its transverse axes are y and z or 2 and 3, respectively. When embedded between plies of a laminate, the transverse axis y corresponds to an in-plane direction. Hence, the z -axis represents then the out-of-plane direction.

Besides the Bragg wavelength, some other parameters are of interest in analysing the reflected spectrum. The Full Width at Half Maximum (FWHM) represents the width of the reflected spectrum at half of the intensity level. When loading an optical fibre, broadening of the reflected spectrum (an increase in FWHM) may be observed in addition to the wavelength shift. Extensive broadening results occasionally in peak splitting. At the sides of the reflected spectrum lobes may be present. These are artefacts of the inscription process and can be suppressed by changing its settings.

3.3.3 Principles for composites process monitoring

In some studies, the experimental process data are analysed using Eqs. 3.2 or 3.3 [98, 106–108, 114–137]. However, when an FBG sensor is bonded to or embedded in a host

⁸ $\partial\epsilon_1 = \partial L/L = \partial\Lambda/\Lambda$.

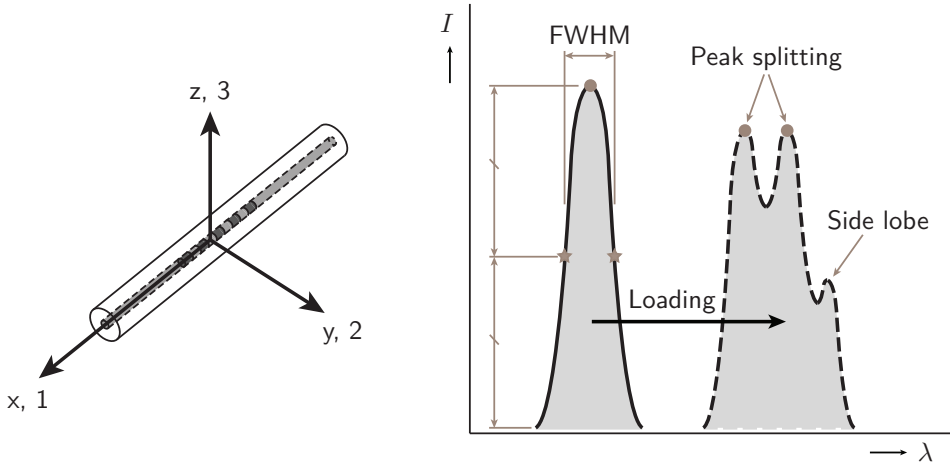


Figure 3.2: Principal axes of optical fibre and definitions in reflected spectrum.

structure, the mismatch between the CTEs of the optical fibre and host structure can result in additional straining [15, 138–145]. Consequently, Eq. 3.2 should be modified to:

$$\frac{\Delta\lambda_B}{\lambda_B} = (1 - P)[\Delta\epsilon_1 + (\alpha_H - \alpha_f)\Delta T] + (\alpha_n + \alpha_f)\Delta T \quad (3.4)$$

and Eq. 3.3 becomes:

$$\frac{\Delta\lambda_B}{\lambda_B} = S_\epsilon[\Delta\epsilon_1 + (\alpha_H - \alpha_f)\Delta T] + S_T\Delta T \quad (3.5)$$

where α_H is the host's CTE. For an embedded FBG sensor in an unconstrainedly curing neat resin system the host's CTE may be split up into [142]:

$$\alpha_H = \begin{cases} \alpha_{H,liq} & \text{when matrix is liquid,} \\ \alpha_{H,gel} & \text{when matrix has passed its gelation point,} \\ \alpha_{H,vit} & \text{when matrix has vitrified.} \end{cases} \quad (3.6)$$

Not only the mismatch in CTEs would contribute to the formation of process-induced strains, but also the chemical shrinkage of the neat resin system. This behaviour may be captured by an additional term in Eq. 3.4:

$$\frac{\Delta\lambda_B}{\lambda_B} = S_\epsilon[\Delta\epsilon_1 + (\alpha_H - \alpha_f)\Delta T + \gamma_{chem}\Delta\alpha] + S_T\Delta T \quad (3.7)$$

in which γ_{chem} and α represent the chemical shrinkage coefficient and degree of cure after a given cycle, respectively [142, 143]. For a fully cured isotropic resin system

having an initial volume of uncured material V_0 , the chemical shrinkage coefficient is estimated by:

$$\gamma_{chem} = \left(\frac{\Delta V}{V_0} + 1 \right)^{1/3} - 1 \quad (3.8)$$

where ΔV is the change in volume [143].

Process-induced strains in constrainedly curing neat resin systems can be influenced by the tooling. Perfect adhesion may result in a CTE of the host structure that represents the tooling material. The tooling may also prevent the formation of chemical shrinkage-induced strains [115]. Similarly, the presence of reinforcing fibres influence the behaviour of the host structure as well.

In conclusion, the interpretation of the host structure depends totally on the process to be investigated. The host structure can simply be the coating of the optical fibre, the resin system, the reinforcing fibres, or the tooling material or a combination thereof. It gets even more complicated when adhesion between the different materials is not ideal.

Two other phenomena that may be included in the equations are the resin flow and the hydrostatic pressure. In a fully saturated preform, liquid resin may flow when it is thermally expanding/contracting. In [142], it is stated that the resin flow generates a non-negligible tensional state of stress within the matrix. A flux term ϵ_{flux} is therefore introduced in Eqs. 3.4 and 3.5. The FBG sensor responds also to differences in hydrostatic pressure Δp . Although Eqs. 3.4 and 3.5 should include the term $S_p \Delta p$ on the right-hand side, it is found that, up to 0.7 MPa, the hydrostatic pressure has a negligible influence [127].

3.4 A variety of FBG sensors

Fibre optic sensors can be categorised in several manners. The most important categorisations classify either (i) by the structure, *i.e.* intrinsic versus extrinsic, of the fibre optic sensor, or (ii) by the applied modulation type, *i.e.* intensimetric, polarimetric, interferometric, or spectroscopic, or (iii) by the spatial implementation, *i.e.* point, integrated, distributed, or multiplexed.

Single FBG sensors in an optical fibre are structurally seen as intrinsic sensors. Two types of modulation can be assigned: either interferometry or spectroscopy. The measurement principle of the latter is based on changes in the reflected spectrum. In the former, the basis lies at the measurement of differences in optical path length. Both are valid for FBG sensors. Finally, FBG sensors act as discrete point sensors despite the fact that the reflected spectrum represents an integrated value over the

grating length [109, 112].

FBG sensors themselves can also be grouped [109]. As mentioned in Section 3.2, FBG sensors are produced by a wide variety of fabrication methods. Generally speaking, these techniques change the spectral characteristic of the optical fibre by controlling numerous physical parameters such as induced index change, period chirp, and fringe tilt [146]. A positive step-index profile creates an induced index change uniformly along the longitudinal axis of the optical fibre. This type of grating is uniform and is mostly applied in monitoring composites manufacturing processes [15, 98, 106–108, 110, 114–139, 141–145, 147–155]. More complex refractive index modulation profiles results in apodised, chirped, tilted, phase shift and long period FBGs [109, 146]. Changing from a SM optical fibre to a High Birefringence (HiBi) optical fibre as signal carrier affects the reflected spectrum too [17]. Strong apodisation is combined with others to suppress the side-lobes in the reflected peak [140, 152].

Besides the uniform FBG sensor, some of these grating types have been used in monitoring composites manufacturing processes. For chirped gratings, which have a linear change in period, each wavelength of the reflected spectrum is associated with a fixed position along the gauge length ($\lambda_B(x) = 2n_{eff}(x)\lambda(x)$). It has the ability to link changes in the reflected spectrum directly to a position in the grating [140]. However, the analysis of the spectral response depends upon on an assumed strain profile [130].

Gratings inscribed in SM optical fibres have the inability to discriminate between the contribution of the transverse strain to the wavelength shift and the longitudinal strain contribution. A solution to this problem of multi-axial strain sensing is based on the inscription of a grating in a HiBi optical fibre. The reflected spectrum of such a HiBi FBG sensor shows two distinct Bragg peaks corresponding to the two polarisation axes. The equations describing now the change in wavelength in the so-called fast and slow axes of the fibre are a function of the axial strain, the two transverse strains (in the slow and fast axes, ϵ_s and ϵ_f , respectively), and temperature. Upon compensating for the thermally induced shift, the HiBi FBG sensors can determine the effective transverse strain⁹:

$$\epsilon_f - \epsilon_s = f\left(\frac{\Delta\lambda_{B,f}}{\lambda_{B,f}} - \frac{\Delta\lambda_{B,s}}{\lambda_{B,s}}\right) \quad (3.9)$$

Hence, information is given about the effective transverse strains at the expense of the longitudinal strain. The latter is lost after mutual subtraction of the two equations [17, 129].

⁹The shear strain and cross-sensitivity are neglected

3.5 Discrimination between strain and thermal effects

As mentioned in Section 3.3, local changes in strain and temperature affect the Bragg response simultaneously. For a single FBG sensor, discriminating between these two parameters is difficult. The Bragg equation (Eq. 3.10) has two unknowns and therefore infinitely many solutions. Only the compensation for one leads to the identification of the other. As demonstrated in this section, multiple approaches have been applied in the monitoring of composites manufacturing processes.

$$\frac{\Delta\lambda_1}{\lambda_{B1}} = \begin{bmatrix} S_{T1} & S_{\epsilon 1} \end{bmatrix} \begin{bmatrix} \Delta T \\ \Delta \epsilon \end{bmatrix} \quad (3.10)$$

3.5.1 Thermocouples for temperature compensation

The most easy-to-apply method compensates for the thermally induced shift in Bragg response, $S_{T1}\Delta T$, by means of a thermocouple positioned near the FBG sensor [15, 17, 98, 106, 108, 115–118, 120, 123–125, 128, 129, 135, 138, 139, 141, 143, 153]. Assuming that there is no thermal difference between the two sensor locations, the thermocouple measures the same local temperature, $\Delta T = \Delta T_{TC}$. Multiplication of the measured temperature by the calibrated thermal sensitivity S_{T1} of the optical fibre gives the thermally induced shift in the Bragg response. The process-induced strain is then derived from Eq. 3.11. Due to the thermocouple's intrusiveness, this concept is not yet suitable for out-of-lab applications.

$$\Delta \epsilon = \frac{1}{S_{\epsilon 1}} \left(\frac{\Delta\lambda_1}{\lambda_{B1}} - S_{T1}\Delta T_{TC} \right) \quad (3.11)$$

3.5.2 Dual-grating methods with FBG as optical thermometer

Another differential method compensates directly for the thermally induced shift by using two identical FBG sensors: an internal one, *i.e.* embedded in or bonded to the specimen, and an external (reference) one acting as a strain-free optical thermometer ($S_{\epsilon 2} = 0$) [106, 107, 143]. When both are subjected to the same thermal environment ($\Delta T_1 = \Delta T_2 = \Delta T$), factors other than the applied strain that are affecting the response of the internal FBG sensor can be ruled out. No additional measurements are needed for determination of the thermal sensitivity because of identical properties

($S_{T2} = S_{T1}$). The system of two Bragg equations:

$$\begin{bmatrix} \frac{\Delta\lambda_1}{\lambda_{B1}} \\ \frac{\Delta\lambda_2}{\lambda_{B2}} \end{bmatrix} = \begin{bmatrix} S_{T1} & S_{\epsilon1} \\ S_{T2} & S_{\epsilon2} \end{bmatrix} \begin{bmatrix} \Delta T \\ \Delta\epsilon \end{bmatrix} \quad (3.12)$$

reduces then to:

$$\begin{bmatrix} \frac{\Delta\lambda_1}{\lambda_{B1}} \\ \frac{\Delta\lambda_2}{\lambda_{B2}} \end{bmatrix} = \begin{bmatrix} S_{T1} & S_{\epsilon1} \\ S_{T1} & 0 \end{bmatrix} \begin{bmatrix} \Delta T \\ \Delta\epsilon \end{bmatrix} \quad \Rightarrow \quad \Delta\epsilon = \frac{1}{S_{\epsilon1}} \left(\frac{\Delta\lambda_1}{\lambda_{B1}} - \frac{\Delta\lambda_2}{\lambda_{B2}} \right) \quad (3.13)$$

It is often mistakenly assumed that the thermal effect contributes only reversibly to the shift in Bragg wavelength. Performing an annealing step prior to the actual experiment reveals irreversible changes in Bragg response that can be attributed to permanent changes in coating properties and/or refractive index modulation [17]. Without taking this treatment into account, misinterpretation of the residual strain is bound to happen (see also Chapter 4). With aforementioned concept the treatment may not be necessary (although still advisable), because both sensors are subjected simultaneously to these irreversible thermal effects [106].

That thermal variations can exist between the location of the internal sensor and its surroundings, in which the reference sensor operates, is more than plausible¹⁰. To minimise the thermal difference between the two FBG sensors it is favourable to embed both of them at a certain distance d from each other¹¹. The reference sensor, which should still operate as a strain-free optical thermometer, should then be encapsulated¹² (Fig. 3.3) [99, 114, 122, 126, 127, 132, 142, 154]. This configuration has the same advantage, but at a reduced chance of thermal variations¹³. Careful preparation is essential to prevent leaking and friction between the misaligned optical fibre and the inner wall of the capillary tube. Local stress concentrations may occur at the transition from the bare optical fibre to the capillary. Difficulties may also arise

¹⁰Especially in thicker composites, the exothermic reaction may lead to local temperature overshooting, which is not seen by the reference sensor [142].

¹¹Foreign bodies in composite parts, e.g. thermocouples, can influence locally the mechanical properties. Having these close to the FBG sensor may result in strain readings that are no longer representative. A distance d between the sensors needs to be defined that acts as a lower limit bound.

¹²The capillary tubes, sealed with a high-temperature epoxy of silicon, can be made of silica or steel. Outer diameters in the range of 0.3-1.4 mm have been used in [99, 114, 122, 131, 142]. Better performance is achieved with steel capillary tubes [142].

¹³The use of smaller capillary tubes prevent the slowing down of the sensor's response due to the thermal cushion created by the air inside the cavity.

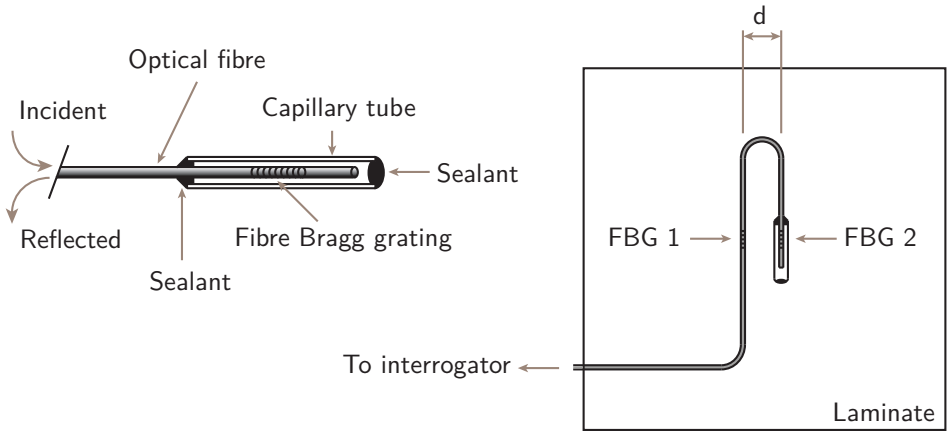


Figure 3.3: An encapsulated FBG sensor and its positioning.

when encapsulated FBG sensors have to be embedded in complex-shaped structures. Mould closing may introduce such a large force that the capillary tube deforms plastically or even breaks [156].

3.5.3 Hybrid solutions with different sensor types

The two concepts mentioned in the previous paragraph use the ability of multiplexing to create multiple FBG sensors in a single optical fibre. Fortunately, multiplexing is not restricted to one type of fibre optic sensors. Discriminating between the two parameters can also be achieved when an FBG sensor is coupled to an EFPI sensor (Fig. 3.4). In EFPI of length L , the total strain ϵ_{tot} in the host structure is a function of the cavity length d , *i.e.* the distance between the ends of two encapsulated in-line optical fibres, and the thermal strain of these internal optical fibres $\epsilon_{f,T}$ [100, 118, 131, 132, 156]. That is,

$$\epsilon_{tot} = \frac{\Delta d}{L} + \epsilon_{f,T} = \frac{\Delta d}{L} + \frac{L - d_0}{L} \alpha_f \Delta T \quad (3.14)$$

where d_0 is the initial cavity length. The temperature dependency is solved for by combining the EFPI sensor with an FBG sensor that acts as a strain-free optical thermometer. The equation changes to:

$$\epsilon_{tot} = \frac{\Delta d}{L} + \frac{L - d_0}{L} \frac{\alpha_f}{S_T} \frac{\Delta \lambda}{\lambda_B} \quad (3.15)$$

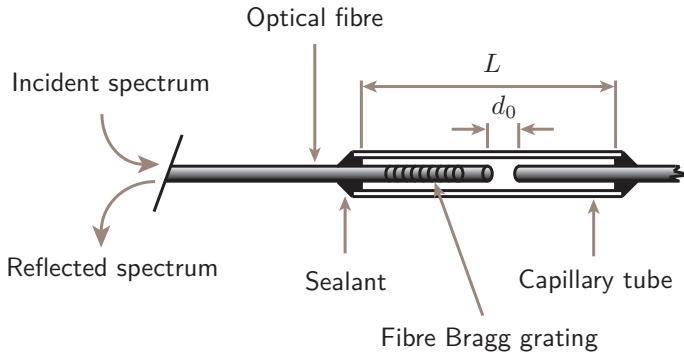


Figure 3.4: An FBG/EFPI hybrid sensor (adapted from [131]).

Accurate measurements of the initial cavity and gauge lengths are, however, critical for this concept [131, 132].

A slightly different type of the FBG/EFPI hybrid sensor is demonstrated in monitoring simultaneously the strain and temperature in a cantilever composite beam [157]. A silica capillary with the same outer diameter as the optical fibre is spliced to an in-line FBG sensor to create an EFPI sensor with a gauge length equalling the cavity length. This EFPI sensor is sensitive to only axial strain and has a relatively small intrinsic thermal response. The measured strain is then subtracted from the Bragg response to retrieve the local temperature.

3.5.4 Dual-grating concepts with low condition numbers

For identical properties of two FBG sensors ($1 = 2$), the sensitivity matrix has the following entries:

$$[S] = \begin{bmatrix} S_T & S_\epsilon \\ S_T & S_\epsilon \end{bmatrix} \quad (3.16)$$

The condition number, $C(S) = \|S\| \|S^{-1}\|$, of this sensitivity matrix indicates how well the matrix is conditioned. That is, the closer the value gets to unity the less sensitive the solution of this system of linear equations is to errors in the data. The aforementioned sensitivity matrix has an infinite condition number, *i.e.* is ill-conditioned¹⁴. The concept of two identical FBG sensors is thus incapable of simultaneous determination of the two parameters. When one of the entries is set to zero, the condition number becomes finite and a solution can be obtained (applied to previous concepts).

¹⁴An infinite condition number indicates that the matrix is singular.

A difference in sensitivities may also be created by changing the core dopants and their relative concentrations. In this way, a pair of different optical fibres with similar FBG sensors can be selected that provides a low condition number¹⁵. Instead of changing the material properties of the optical fibres, the grating type may also be varied [158]. An application of the latter in monitoring a composites manufacturing process has not been presented yet. A list of candidates for these two dual-grating concepts can be found in [121]. A drawback is, however, the mechanically weakening by splicing, which affects the operating range.

3.5.5 Chirped FBG sensor as self-temperature referenced strain sensor

The last concept to be discussed here is based on a chirped FBG sensor operating as a self-temperature referenced strain sensor [140]. By partially embedding the chirped FBG sensor, the internal part is subjected to both process-induced strains and temperature while the external/reference part is in a strain-free condition. The change in bandwidth becomes the key parameter instead of the Bragg wavelength. For this purpose, the left, L , and right, R , edge wavelength at 50% of the maximum reflectivity is recorded. Equation 3.10 still holds and the process-induced strain is found by solving:

$$\Delta\epsilon = \frac{1}{S_{\epsilon 1}} \left(\frac{\Delta\lambda_L}{\lambda_{B,L}} - \frac{\Delta\lambda_R}{\lambda_{B,R}} \right) \quad (3.17)$$

where the left-edge wavelength comes from the internal part of the chirped FBG sensor. The procedure for embedding makes this concept, however, less attractive.

3.6 Monitoring composites manufacturing processes

The capabilities in measuring the process-induced strains motivates the use of FBG sensors in composites manufacturing processes. In Section 3.6.2 the monitoring of neat resin systems is discussed, whereas Section 3.6.3 focuses on continuous fibre composites. FBG sensors can, however, also be employed for another purpose: the detection of resin arrival during mould filling 3.6.1.

¹⁵Temperature and strain variations should be kept small and the gauge length should not become too long [121].

3.6.1 Resin arrival and flow front propagation

Long-gauge (100 *mm*) FBG sensors can detect flow-front propagation under both isothermal and non-isothermal mould filling conditions in VI processes [154]. In this approach, the sensors are linked to a technique called Optical Frequency Domain Reflectometry (OFDR). The combination allows for measuring the Bragg wavelength at an arbitrary position along the gauge length at a high spatial resolution of sub-millimetre order. In non-isothermal mould filling the thermal difference between the resin and the optical fibre forms the trigger. In isothermal mould filling, the flow-front can be determined by measuring the changes in compressive strain. The former method is, however, less suitable for large composite parts due to diminishing temperature differences over time. In the latter, changes in compressive strain may be close to the strain resolution, which makes it again hard to localise the flow front.

Similar conclusions are drawn in monitoring the injection of an aircraft propeller blade manufactured by RTM [99]. Lacking a thermally induced effect, a strain threshold was defined in order to identify the interaction of the resin flow with the sensors. Minor changes in Bragg response were measured due to the tightly packed preform. Only after careful post-processing valuable results regarding the resin flow were obtained.

3.6.2 Cure behaviour of neat resin systems

The first step towards monitoring the formation of process-induced strains in composites manufacturing processes is studying the cure behaviour of single fibre reinforced resin systems. In here, the FBG sensor is the actual reinforcing fibre that sense the effects of ongoing cross-linking. Sample geometries vary from blocks [130] and cylinders [98, 110, 115, 116, 126, 130, 133, 143, 144] to flat beams [15, 138–140, 153] and a small square plate [17]. Issues that have been dealt with are briefly summarised below.

1. Influence of the cure regime;

The cure regime has a profound effect on the formation of process-induced strains in unconstrained curing. There are less compressive strains for extended dwell times¹⁶ and lower heating. Heating the liquid resin results in a steeper build up of strain between gelation and vitrification. Up to vitrification, the strain development is influenced by the cure kinetics. Higher cure temperatures

¹⁶Here, the dwell time resembles the time course of the resin staying at filling temperature conditions.

have less influence unless the curing is started at isothermal conditions. The latter results in less compressive strains for higher cure temperatures [98, 116].

2. Curing under (un)constrained conditions;

Unconstrained curing¹⁷ results in isotropically stress-free shrinking of the resin system. In both directions (radially and along the longitudinal axis of the cylinder) compressive strain levels are comparable [115]. Roughening of the mould wall introduces inner stresses due to the adhesion of the resin to the mould wall. Material flux occurs then mostly in the direction in which the resin is contact-free. Compressive strains can be three times larger compared to the unconstrained condition for this direction [115]. In [138], the experimentally measured process-induced strains are taken as input for a two-dimensional stress model. Only after preliminary fitting of essential parameters, the model shows that the choice of tooling material (and thus differences in CTEs) can have a significant effect on the formation of process-induced strains. Demoulding influences the measured strain as well. The balancing forces exerted by the tooling are released, which may cause a shift in the Bragg wavelength [139].

3. Formation of transverse strains and edge effect;

Linear regression has shown a high correlation between the effective transverse strain (Eq. 3.9) and degree of cure for a partially constrained flat resin specimen [17]. In combination with Optical Low-Coherence Reflectometry (OLCR) and a back-scattering technique called layer-peeling, long gratings can capture the residual strain distribution along their gauge length in cured epoxy¹⁸. Similar residual strain distributions have been obtained along the centre line for blocks and cylinders of equal lengths. In these samples, the edge causes a non-homogeneous parabolic strain distribution in the optical fibre. The central zones remain in a state of plain strain. Cylinders with a reduced length show a lower maximum compressive strain level [110, 130, 133, 143].

¹⁷Free movement of the sample, *i.e.* no bonding to the tool, can be obtained by coating the mould wall with a thin layer of silicon oil [98], Teflon [15] or by sandwiching between Teflon sheets [17].

¹⁸The proposed technique works solely for cured resin samples due to the low frequency of scanning.

4. Assigning resin characteristics to the Bragg response;

Chemical shrinkage in the liquid resin does not cause straining. The first detectable strain is linked to the onset of gelation [98, 115, 116, 126, 138, 139]. This can be verified by rheological measurements in which the gel point should be linked to the crossover of the shear storage and loss moduli [115, 116]. When the resin is in its rubbery state, strains develop by means of the reaction-induced shrinkage. The vitrification point is identified as a local minimum in measured strain [98]. After vitrification, the formation of process-induced strain is dictated by the CTE of the host structure [98, 126]. Chemical shrinkage can be determined by comparing the Bragg wavelength before and after polymerisation, but be aware that it represents only the shrinkage after gelation [144].

5. Proof of concepts for FBG sensors;

A proof of concept is conducted for 7-cm chirped FBG sensor (strongly apodised and partially embedded) acting as a self-temperature referenced strain sensor (Section 3.5.5). This type can also determine the onset of gelation [140]. A dual-function optical fibre consisting of an FBG sensor and a refractometer can also extend the possibilities of process monitoring. Besides the detection of the onset of gelation and the formation of process-induced strains, the refractometer can give insight into the degree of cure [15, 153].

6. Thermal cycling/post-curing.

Post-curing affects the strain level. Some measured a strain release [126, 139], whereas others observed compression of the optical fibre [110, 130, 133, 143]. After post-curing, subsequent thermal cycling does not result in significant changes in strain [126, 139]. However, a multitude of parameters such as the strain-free temperature [126], the glass transition temperature [116, 126], and the CTEs below and above the glass transition point [116, 126, 139, 144] can be revealed. The latter two have been verified by Differential Scanning Calorimetry (DSC) and dilatometry tests on a Thermal Mechanical Analyser (TMA), respectively [116, 126, 144]. Through mathematical operations on the Bragg response of differently sized cylinders, the modulus of elasticity can be estimated as well [144].

3.6.3 Continuous fibre composites

Most studies have been based on both thermosetting and thermoplastic continuous fibre (carbon, glass, or aramid) composites. Besides UD coupons [17, 106, 121–123, 127, 128, 131, 134, 141], plates have been manufactured having stacking sequences such as crossply [108, 114, 122, 131, 132, 135, 141, 145, 152], angle-ply [134], quasi-isotropic [129, 134, 148, 155], multidirectional [136, 142, 151] or have been composed of fabrics [131, 150, 151, 154] or braided [117, 118]. In addition, attention has been paid to the processing of Fibre Metal Laminates (FMLs) [119, 134], sandwich structures [107, 120, 147], filament wound pressure tanks/cylinders [124, 125, 149] and a braided cylinder [117]. Fabrication involved most of the common composites manufacturing processes such as hand lay-up + vacuum bagging [136, 142], prepreg + oven curing [106], prepreg + autoclaving [107, 121–123, 127, 129, 131, 132, 141, 145, 150], LCM [117, 118, 147, 151, 154], hot pressing [17, 108, 114, 119, 120, 128, 134, 135, 148, 152, 155], and filament winding [124, 125, 149].

Two strategies can be distinguished for the determination of process-induced strains: (i) by comparing Bragg wavelengths before and after fabrication [110, 119, 130, 133, 134, 143, 144, 147, 149, 151, 154, 155] and (ii) by online monitoring of the manufacturing process [15, 98, 106–108, 114–118, 120, 121, 123–129, 131, 132, 135, 137–142, 148, 150, 152]. The first method is perhaps the easiest to carry out, because it assumes that the shift in Bragg wavelength contributes entirely to the formation of process-induced strain. On the other hand, observing the manufacturing process reveals that many actions/process steps influence the Bragg response. The uncertainty in interpreting the Bragg response led to the reporting of only the cooling strains. Below are the main points/achievements summarised:

1. The first experimental results were published in 1998. Simultaneous monitoring by thermocouples, dielectric sensors, and FBG sensors in a three-stage oven-cured UD coupon demonstrated that a combination of these techniques may optimise the cure cycle for minimum residual strain [106].
2. The anisotropy in UD laminates leads to distinct differences in compressive cooling strains in the two in-plane material axes. While cooling down, the laminate contracts more in the transverse direction. Hence, larger compressive strains are observed in this direction. In the direction of the reinforcing fibres, the compressive cooling strain is minimal. In Glass Fibre Reinforced (GFR) crossply (both symmetric and unsymmetrical) and fabric laminates the compressive strains are similar in the orthogonal directions and in between the values mea-

sured for the UD laminate [131]. The increase in number of plies results in more compressive strain accumulated within Glass Fibre Reinforced Plastic (GFRP) laminates [142]. In filament wound cylinders, negative strains are developed while curing in the axial direction, whereas hardly any change is observed in the circumferential direction [124, 125].

3. Thermal strains govern mostly the formation of process-induced strains [118]. Intermediate cooling between curing and post-curing can significantly influence the formation of process-induced strains [121, 123], but a detailed study on the influence of the cure regime has not been reported yet.
4. In two studies on the cure behaviour of (un)damaged laminates opposing conclusions are found. The first study indicates that FBG sensors are not very sensitive to artificially created delaminations [108, 135]. This is in contrast with the second investigation in which delaminations are detected in Carbon Fibre Reinforced Plastic (CFRP) laminates [137]. The distance between the sensor and the delamination may have played a role, but a lack of details prevents further commenting.
5. Tooling material affects significantly the build-up of process-induced strains in CFRP laminates. The results show that (i) tooling having a higher CTE produces higher process-induced strains, (ii) FBG sensors are capable of detecting the debonding of the laminate from the tooling, and (iii) the compaction pressure improves adhesion of the laminates to the tooling's surface in autoclaving [125, 127, 141]. In a numerical study, the importance of the tool-part interface is addressed by illustrating the differences between unconstrained and constrained models, *i.e.* free and perfectly bonded to the tooling, respectively [128]. Releasing the compaction pressure and opening of the mould can also change the process-induced strain level [117, 128].
6. The concept of dual-grating sensing in which the external FBG sensor acts as an optical thermometer is demonstrated in autoclave curing of glued GFRP skins onto a foam core for the first time [107]. In other works, similar conclusions are drawn for temperature compensation by the concept of FBG/EFPI hybrid sensor [131, 132] and dual-grating concept with encapsulated FBG sensor [114, 136, 142]. The dual-grating concept with low condition number based on different optical fibres resulted in 6% difference in temperature in comparison with a surface-mounted thermocouple [121]. Independently operating EFPI and FBG sensors should measure similar process-induced strains. A deviation in re-

sponses due to different effective stiffness is observed in [118]. A less significant difference is, however, noted by other studies [108, 135].

7. Interesting points such as the glass transition and the melting were detected in monitoring hot pressing of UD thermoplastic laminates [128]. In compression moulding of a sandwich structure consisting of thermoplastic FML skins and an aluminium-foam core, both the onset of melting and the onset and completion of the solidification process were sensed by FBG sensors. These transitions can be verified by DSC measurements [120].
8. A source of peak-splitting in SM optical fibres is birefringence induced by transverse stresses. From a theoretical model, it is found that the evolution of the lowest Bragg wavelength depends essentially on the axial strain ϵ_1 . The gap between the peaks relates to the effective transverse strain [148]. This contradicts, however, with experimental work, in which the centre wavelength at FWHM agrees well with the response of strain gauges in compression testing of a braided cylinder [117]. Measurements with HiBi FBG sensors embedded in UD GFRPs show that the effective transverse strain is more pronounced in case the sensor is orthogonal to the reinforcing fibres. In both directions, parallel and orthogonal, the effective thermal strains develop linearly with increasing degree of cure. In the initial stage, in which the reaction is slow, the effective transverse strain is dominated by thermal expansion, whereas it stabilises after vitrification [17]. The gap width remains, however, constant in the tool removal step [128].
9. The role of the coating and the gauge length is investigated in hot pressing quasi-isotropic laminates. Less spectral variations are obtained for shorter gauge lengths and polyimide coating. Polyimide coating provides better adhesion and a higher interfacial strength [155]. (Re)coated FBG sensors keep the unique Bragg condition and behave as transverse insensitive gratings [150]. Smaller diameter optical fibres are less susceptible to transverse strains [152].
10. The laminate's CTE can be determined by thermal cycling in an oven [122, 136]. The measured values have been compared with output from resisting foil gauges, a dilatometer and a linear finite element method. In UD laminates strain gauges may give erroneous results due to transverse effects. FBG results are seems better, but they may differ in thermal strain amplitude with dilatometer tests¹⁹.

¹⁹Moisture absorption and/or scaling effect are probably causes for this difference.

Good agreement exists for cross-ply laminates. Though, dilatometer tests may show again different behaviour [114, 131].

3.7 Shortcomings and practical issues

Since the FBG sensing technique is still in its infancy for monitoring composites manufacturing processes, most of the attention has been focused on the so-called 'bugs' in the system. Identifying (the causes of) the problems helps in preventing misinterpretation and to understand the limitations of this sensing technique. In the following, the problems that have been reported so far are organised into four categories.

1. Misinterpretation of the Bragg response to actions/process steps;

Not all of the changes may contribute to the formation of process-induced strains. Changes may relate to mould closing, stick-slip behaviour of the optical fibre, compaction pressure (both underpressure and overpressure), volume changes, chemical shrinkage, gelation, glass transition, melting, and resin flow [106, 107, 114, 117, 126–128, 131, 142, 155]. In crystalline thermoplastics, the presence of an optical fibre has also a significant effect on the formation of crystalline regions at the sensor/host interface region during the cooling phase [120]. The ones that do not contribute to the formation of process-induced strains and are not filtered out by thermal correction make it difficult to reproduce experiments (see, for example, Fig. 3.5) [125, 128, 141].

2. Unfavourable changes in spectral characteristics;

By mechanical testing it is proven that perturbing influences on the Bragg response may arise from local point-wise indentation, transverse loading and micro-bending. Point-wise loading occurs when the optical fibre is not aligned with the adjacent reinforcing fibres. Upon compaction, localised radial loading by crossing reinforcing fibres deforms the gauge length non-uniformly (Fig. 3.6). Consequently, the grating period is not constant and the reflected spectrum broadens, *i.e.* the FWHM increases, leading occasionally to peak-splitting [134, 151]. Broadening of the reflected spectrum and, eventually, peak splitting occurs also in case of birefringence caused by transverse loading. This phenomena can be observed while compacting the preform and during the cooling down

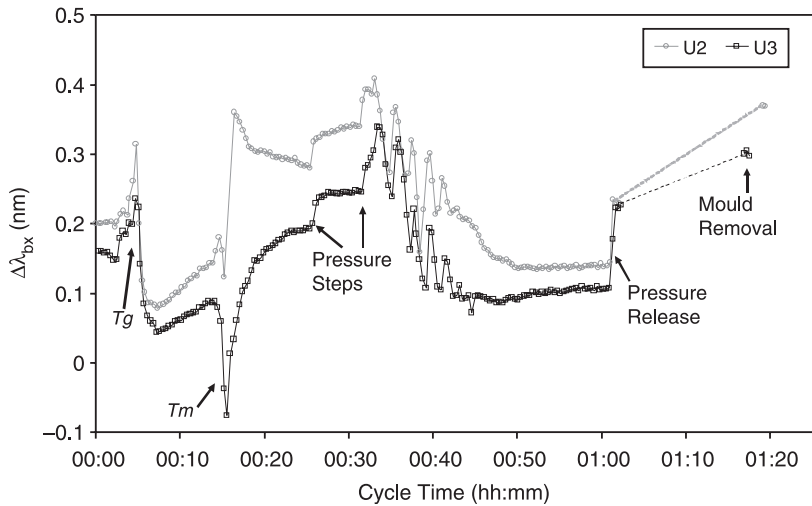


Figure 3.5: Change in Bragg wavelength while hot-pressing two thermoplastic CFR UD laminates [128].

stage due to differences in thermal contraction along the principal axes of the laminate. In the presence of a transverse stress field²⁰, the circular cross-section of the optical fibre deforms into an ellipse. Two distinct light-travelling axes are found, which reflect their own spectra [122, 134, 141, 148, 150, 152]. Spectrum analysis helps to differentiate between non-uniform straining along the gauge length and birefringence. To this end, the FBG sensor needs to be illuminated through linearly polarised light at 0° and 90° . The reflected spectrum remains unchanged in case of the former. The latter shows two distinct spectra corresponding to the two polarisation axes (Fig. 3.7) [141, 150]. Nevertheless, to prevent these signal disturbances, limits are required for transverse and point-wise loading [151]. Micro-bending results in a loss in optical power [107].

3. Coating influences;

The coating on the optical fibre may influence the measurement of the process-

²⁰When the transverse strains are large relative to the longitudinal strain, the simplification of the strain-optic coefficient P produces a significant error in the measured strain ϵ_1 , because the Poisson's ratio relationship ($\epsilon_2 \neq \epsilon_3 \neq -\nu\epsilon_1$) is no longer followed [128].

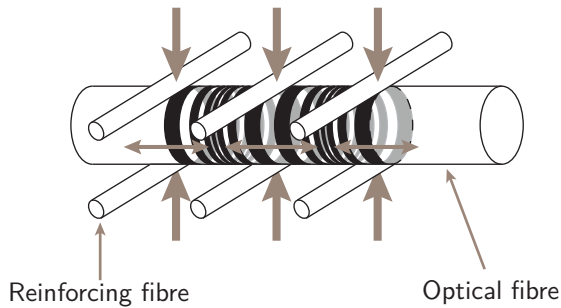


Figure 3.6: Deformation of the grating by adjacent fibres (adapted from [134].)

induced strains²¹. The coating can be removed by chemical or mechanical stripping [15, 110, 120, 123, 128, 130, 138–141, 143, 145, 147]. The direct contact improves the mechanical bonding [147]. However, the optical fibres become more fragile and tend to break easier. The reflected spectrum is more prone to spectral variations. To enhance the reliability of an embedded optical fibre a coating seems thus vital, but a certain level of adhesion is needed for an efficient load transfer [159]. Poor adhesion may induce stick-slip behaviour [126]. Silane sizing on the optical fibre is seen as one of the possible surface treatments [110, 123, 128].

4. Embedding optical fibres and their survivability.

With respect to survivability, the following is noted: (i) hydrogen loaded optical fibres have worse mechanical properties, (ii) splicing has to be avoided when forming arrays of FBG sensors, (iii) ingress/egress points are preferred on both sides of the embedded optical fibre, (iv) recoating prevents fibre breaking while embedding [149]. Cobraiding of an exchangeable nylon fibre and replacing afterwards by the optical fibre can be a technique to prevent damaging in less dense preforms [117]. Weak ingress/egress points can be strengthened/protected by Teflon tubing [119, 128, 134, 141] or by encasing the optical fibre by a plastic sheath [147]. The latter makes online process monitoring, however, impossible. Embedding the optical fibre perpendicular to the adjacent reinforcing fibres can lead to resin-rich regions, which may cause a non-uniform strain along the grating length. Although smaller gauge lengths are more effective under strain

²¹Besides the coating, a difference in the Young's moduli of the optical fibre and the reinforcing fibres may affect the process-induced strains as well due to the stiffening effect on the matrix [142].

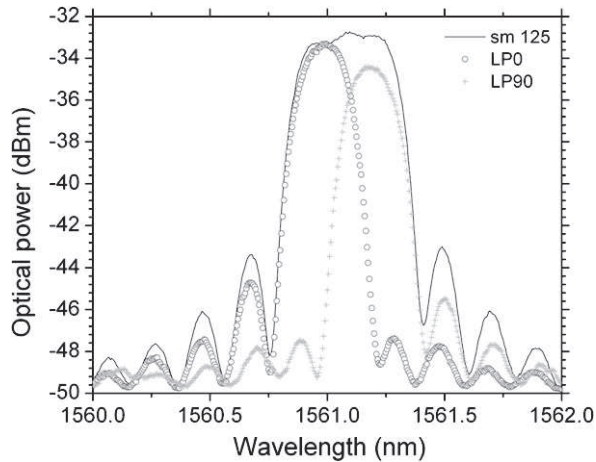


Figure 3.7: Broadening of spectrum as a result of birefringence (sm 125 = quasi unpolarised, LP0 = polarised at 0° , LP90 = polarised at 90°) [141].

gradients [149, 160], resin-rich pockets have a more pronounced effect on the Bragg response [117]. Prestraining may reduce these transversal effects [145]. Unfortunately, the only descriptive and illustrative procedures that help engineers with practical issues such as optical fibre alignment, orientation, and permanent affixing are reported in [147] for sandwich structures and in [124] for filament wound cylinders.

3.8 Concluding remarks

In brief, lots of studies demonstrate the potential of FBG sensors by discussing results for a wide variety of neat resin and composite specimens and manufacturing techniques. Main conclusions drawn from these studies in this overview are:

- Numerous parameters/process steps, *e.g.* cure regime and tooling material, influence the Bragg response. Careful interpretation is essential in order to correctly define the process-induced strains and to reproduce experiments. A thermo-elastic response diagram may help to understand the Bragg response.
- The choice of the gauge length for the FBG sensor should depend on the application. Whenever possible, the optical fibre should be aligned with adjacent reinforcing fibres. Cross-over of fibres may deform the FBG non-uniformly or

apply a transverse stress field that lead to birefringence in the reflected spectrum. Coating attenuates these effects and prevents fibre breaking. However, its presence may impact the Bragg response.

- Compensation of the thermally induced strain by thermocouples is the easiest concept for in-lab applications. Though, calibrations have to be performed *a priori* to determine the thermal sensitivity of the optical fibre and the distance between sensors should be minimised such that both are subjected to the same thermal environment.
- Last but not least, not much attention has been paid to verify the experimentally obtained process-induced strains by other means. Some tried numerical modelling for which extensive knowledge of material properties is required. Others compared the output from an experimental EFPI sensor to the Bragg response. Both approaches result in some thoughts, but the investigations have been on such a small-scale base that results are debatable.

4

MATERIALS, PROCESSES, AND INSTRUMENTATION

4.1 Introduction

As stated by Percival Lowell¹, who was the astronomer that initiated the search operation for dwarf planet Pluto in the beginning of the twentieth century, learning and precision are vital for starting any investigation. Chapters 2 and 3 formed here the learning by passing in review the basics of manufacturing thick laminates and process monitoring by FBG sensors. An important lesson learnt is that FBG sensors are sensitive to almost every composite manufacturing step. Each composites manufacturing process step leaves a distinct trace behind in the Bragg response history. This chapter defines the workspace for this study by giving precise descriptions and motives underlying the selection of composite materials, manufacturing processes, and instrumentation. It helps the reader in understanding the results to be presented in subsequent chapters.

¹“Imagination is as vital to any advance in science as learning and precision are essential for starting points.”

4.2 Selection of composite materials

4.2.1 Matrices

As the baseline for this study, the epoxy-based HexFlow[®] RTM6² produced by Hexcel, France, is selected. This high-performance thermosetting resin system is the current standard for LCM processes in the European aerospace industry. It is produced in two variants: either as a monocomponent system (RTM6-1) or as the newer bicomponent equivalent (RTM6-2). The latter was developed and launched officially in 2010 in order to overcome transport restrictions of the former. The manufacturer claims that both resin systems have an identical cure behaviour [161]. Details on mixing RTM6-2 can be found in the Product Data Sheet (PDS) [162]. The MRCC prescribes the pre-heating of the resin system to 80 °C, whereas the tooling should be at 120 °C. Filling should be done under low pressure (2-3 *bar*). The cure temperature and time are 160 °C and 75 minutes, respectively. A free-standing post-cure of 120 minutes at 180 °C with a ramp of 1 °C/*min* is recommended. Most of the experiments described here are based on the RTM6-2 resin system. Whenever RTM6 is mentioned in the text, it refers to the RTM6-2 resin system. The sparse moments that the monocomponent RTM6 resin system is involved are indicated by referring to the RTM6-1 resin system in the text.

As the (post-)cure temperature of RTM6 is near the pre-set upper limit for the coated optical fibres, the decision is taken to include a second epoxy-based resin system in this study. This bicomponent resin system has a lower processing temperature and an extended pot life at room temperature. Hexion[™] Specialty Chemicals, Germany, produced this resin system and hardener under the trade names of EPIKOTE[™] 04908 and EPIKURE[™] Curing Agent 04908, respectively^{3,4}. The mixing ratio is 100 parts by weight for the resin and 30 parts by weight for the curing agent. The processing temperature ranges from Room Temperature (RT) to 80 °C with dwell times of eight hours to several days [163].

²In the remaining part of this dissertation this resin system is abbreviated to RTM6.

³In the remaining part of this dissertation this resin system is abbreviated to EP04908.

⁴In this study, the resin's manufacturer modified the chemical composition. Impregnation became problematic due to an increased viscosity. Not much later the resin system has even been taken off the market. The limited amount placed at disposal restricts the number of LCM experiments.

4.2.2 Reinforcement

RTM6 resin system is mainly applied in Carbon Fibre Reinforced (CFR) aerospace structures. Carbon would thus be an appropriate but also an expensive choice as material for the reinforcing fibres. The extensive material consumption for thicker composites is seen as a convincing argument to change to a cheaper glass fabric. An additional advantage is its translucency that allows to visually inspect the embedded optical fibre after manufacturing. However, researchers seem reserved in using woven fabrics in combination with online process monitoring by FBG sensors. Upon preform compaction, localised radial loading by crossing reinforcing fibres may deform the gauge length non-uniformly [134]. To reduce the effect of microbending an 8-harness satin weave E-glass fabric (HexForce[®] G-300-7581) supplied by Hexcel, France, is selected that has a high count of yarns (about 20) per centimetre in both warp and weft directions. The fabric has a dry weight of 303 g/m^2 and its ply thickness is 0.23 mm . The epoxy-compatible finish is Z6040.

4.3 Material characterisation

4.3.1 Cure kinetics

Experimental procedures

Two DSC procedures have been adopted in determining the degree of conversion as a function of reaction temperature. In Procedure A, both dynamic and isothermal scans are performed under nitrogen purge on an obsolete modulated DSC 2920, TA Instruments. Sample weights are in the order of 10 mg . Dynamic scans are done at the heating rates: 0.25, 0.5, 1, 2, 5, 10, 15, and 20 $^{\circ}C/min$. The temperature range is set to -50 to 330-350 $^{\circ}C$. For each sample, the total heat of reaction is derived according to the procedure reported in [89]. In total, five isothermal scans are performed: 140, 150, 160, 170, and 180 $^{\circ}C$, for which the initial ramp is set to 25 $^{\circ}C/min$. The baseline is constructed by rescanning the cured sample. As such, the degree of cure can be computed as a function of cycle time and test temperature.

In Procedure B, the cure kinetics of RTM6-2 is studied more thoroughly on a modulated DSC of the Q1000 series, TA Instruments [164, 165]. As such, the glass transition temperature is determined as well. Ten samples of unreacted resin, weighing about 10 mg , are tested in the dynamic scanning mode at the following heating rates: 2, 4, 5, 6, 8, 10, 12, 15, 18, and 20 $^{\circ}C/min$, in order to determine the total heat

of reaction. The starting point is changed to RT conditions, whereas the upper limit is kept similar. A series of samples are then isothermally cured at four different test temperatures: 140, 150, 160, and 180 °C for a certain amount of time. To reach the test temperature the ramp is set to 100 °C/min. Cooling after the isothermal dwell is done at a rate of 30 °C/min. The latter is assumed to be sufficient to ‘freeze’ the reaction instantaneously. Samples are then dynamically scanned at a heating rate of 10 °C/min to determine both the residual heat of reaction and the instantaneous glass transition temperature. The fractional conversion of the partially cured samples is derived from the ratio between residual and total heat of reaction.

Experimental results

In Procedure A, the total heat of reaction is $396 \pm 15 \text{ J/g}$. For Procedure B, the total heat of reaction for each sample is listed in Table 4.1. The average is $430 \pm 19 \text{ J/g}$. The latter agrees with the total heat of reaction of the RTM6-1 resin system: $436.5 \pm 2.9 \text{ J/g}$ in [89]. As the same resin batch is used for the two procedures, the difference between the two procedures is most likely due to the difference in equipment state. The evolution of the degree of cure, left-hand side of Fig. 4.1, is found almost identical. That the isothermal cure conditions are not reached instantly in Procedure A may explain the horizontal shift. This fault has an increasing effect, when the cure temperature gets lower. On the right-hand side of the same figure, the instantaneous glass transition temperature is given as a function of the fractional degree of cure for the samples of Procedure B.

Model development

In this study, the so-called Kamal-Sourour equation is adopted (Eq. *iii* in Table 2.2). For modelling RTM6-1, a modification of the kinetic rate constants $k_{i,c}$ by introducing a diffusion rate constant k_d is proposed in [89]. The true kinetic rate constants k_i are given by:

$$k_i = \frac{k_{i,c}k_d}{k_{i,c} + k_d} \quad \text{for } i = 1, 2 \quad (4.1)$$

Table 4.1: Total heat of reaction of RTM6 resin at different heating rates - Procedure B.

Heating rate [°C/min]	2	4	5	6	8	10	12	15	18	20
Total heat of reaction [J/g]	447.5	451.9	409.1	411.4	424.6	409.2	454.5	450.9	420.9	416.3

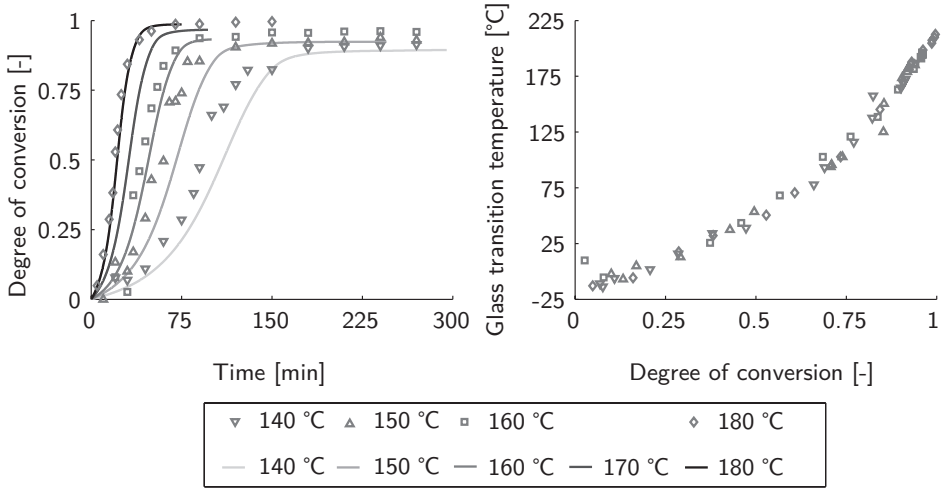


Figure 4.1: Cure kinetics of RTM6-2 resin system. LHS: degree of conversion for isothermal cure at different cure temperatures (solid lines correspond to Procedure A) - RHS: Relationship between glass transition temperature and degree of conversion.

Hence, the modified Kamal-Sourour equation is then represented by:

$$\frac{d\alpha}{dt} = \left(\frac{k_{1,c}k_d}{k_{1,c} + k_d} + \frac{k_{2,c}k_d}{k_{2,c} + k_d} \alpha^m \right) (1 - \alpha)^n \quad (4.2)$$

where m and n are reaction orders. The kinetic and diffusion rate constants are expressed as:

$$k_{i,c} = A_i \exp\left(\frac{-E_i}{RT}\right) \quad \text{for } i = 1, 2 \quad (4.3)$$

and:

$$k_d = A_d \exp\left(\frac{-E_d}{RT}\right) \exp\left(\frac{-b}{0.00048(T - T_g) + 0.025}\right) \quad (4.4)$$

in which E is the activation energy, A is the pre-exponential factor, R is the universal gas constant. The second exponential factor relates to the equilibrium fractional free volume, in which the instantaneous glass transition temperature is obtained from the DiBenedetto equation (Eq. 2.10).

Table 4.2: Estimated parameters of DiBenedetto equation (Eq. 2.10) - Procedure B.

Parameter	$T_{g,0}$	$T_{g,inf}$	λ
	[°C]	[°C]	[-]
Value	-14.9	217.8	0.39

Table 4.3: Estimated parameters of kinetic models (Eqs. 4.2 to 4.4) - Procedure B.

Parameter	E_1	A_1	E_2	A_2	m	n	E_d	A_d	b
	[kJ/mol]	[1/s]	[kJ/mol]	[1/s]			[1/s]	[kJ/mol]	
Value	73.3	3.61×10^4	57.5	1.76×10^4	1.18	1.19	207.3	4.98×10^{26}	0.16

The approach described in [89] is adopted to find $k_{1,c}$ for the isothermal runs of Procedure A⁵. The other parameters are fitted by an unconstrained non-linear optimisation (Nelder-Mead simplex direct search algorithm), for which a randomiser is added to vary the initial values of the scalar function to avoid trapping in local minima. In the second step the regression analysis is continued for fitting the parameters of the diffusion rate constant for the diffusion-controlled region. A proper fit is obtained, but the stabilisation issue mentioned before makes the use of this experimental data set questionable. For Procedure B, only the three time-dependent pre-exponential factors are refitted. Rerunning the regression analysis results in the best fit as shown in Fig. 4.2. Tables 4.2 and 4.3 summarise the optimal parameters for Procedure B. Up to $\alpha \approx 0.75$ the fit follows the RTM6-1 cure kinetics model. Although the latter is in good agreement with experimental data presented in [89], the difference in final degree of conversion is remarkable⁶. The best fit of the DiBenedetto equation describes well the development of the glass transition temperature (right-hand side (RHS) of Fig. 4.2). Though, it differs slightly with the RTM6-1 model [89]. A closer look at these differences is definitely required, because subsequent cure modelling may affect the prediction of the true mechanical properties. There is, however, no priority given to clarify the differences within this study.

⁵This constant is equal to the initial reaction rate for zero conversion. A plot of the natural logarithm of this constant versus the inverse of the cure temperature results in a linear dependence in which the slope and intercept are equal to $-E_1/R$ and $\ln(A_1)$, respectively.

⁶In [166] a similar behaviour is observed for RTM6-1.

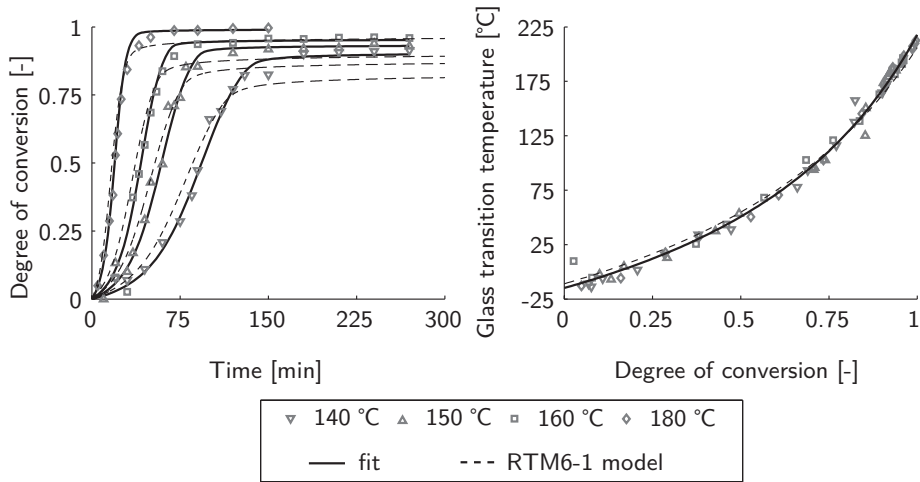


Figure 4.2: Cure kinetics model of RTM6-2 resin system and comparison with RTM6-1 model [89, 167, 168]. LHS: degree of conversion versus time - RHS: Relationship between glass transition temperature and degree of conversion.

4.3.2 Compaction behaviour

Procedure

Simple compaction tests have been performed for the fabric on a hot press (JOOS hydraulic 100 tonnes press, United States of America)⁷. Although the closing speed may have an influence on the compaction [170], its value is fixed by the settings of the hot press. After the press reaches a pre-set limit and waiting for ten minutes, the gap distance is measured manually using a calliper. The average gap distance is determined from six measurements for different pressures. At reaching the maximum set pressure of 4 *bar*, the press is opened and a new cycle is started. Three different stacks are used: two times a 30-ply preform and a 122-ply preform⁸. In literature, it is shown that for a small number of plies (ten or more) the average compaction per ply is fairly constant [171]. Since the measurements are done manually, having

⁷The absence of a dedicated machine such as in [169] does not induce problems in investigating the compaction behaviour on this level.

⁸The latter corresponds to a preform that would be used in manufacturing 25-*mm*-thick RTM laminates with the set-up described in Section 4.4.2.

more plies would lead to a better estimation of the average ply thickness. The plies of the stacks measure $290\text{ mm} \times 290\text{ mm}$, which is similar to the dimensions used in the vacuum-assisted RTM tests (see Section 4.4.2). Due to the limitations and shortcomings in performing compaction tests using the hot press, wet compaction is not considered. To determine the fibre volume fraction the following expression is used:

$$v_f = \frac{A_w n}{\rho_f t} \quad (4.5)$$

where A_w is the areal weight of a single ply, n is the number of plies, ρ is the density of the fibre, and t is the thickness of the preform [170, 172].

Results

In Fig. 4.3 the compaction pressure is plotted as a function of the calculated fibre volume fraction. The observed trend is found in accordance with literature for other fabrics and mats [169, 173]. Only the 30-ply preforms are subjected to consecutive cycles. Debulking causes a shift of the curve: less compaction pressure is required to achieve the same fibre volume fraction. In [174], a two-parameter power law model is suggested to describe the relationship between the fibre volume fraction and the compaction pressure:

$$v_f = Ap^B \quad (4.6)$$

where A and B are the fitting parameters. As the first compaction cycle is of major concern, the best fit obtained for A and B is shown for this case only. The values belonging to the best fit are 0.469 and 0.162, respectively. It is recognised here that extrapolation to lower fibre volume fractions would give erroneous results. Fitting to a more sophisticated model such as the constitutive law presented in [175] is not investigated here⁹.

As will be mentioned in Chapter 9, three different fibre volume fractions are studied in the vacuum-assisted RTM set-up. That is, the preforms consist of 8, 10, or 12 plies. Burn-off tests on cured specimens reveal average fibre volume fractions of 0.48, 0.59, and 0.66, respectively. According to the power law model, the compaction pressures that have been applied to achieve these fractions are then 1.2, 4.1, and 8.3 *bar* respectively.

⁹A brief summation of models for predicting the compaction behaviour of fibrous materials can be found in [176].

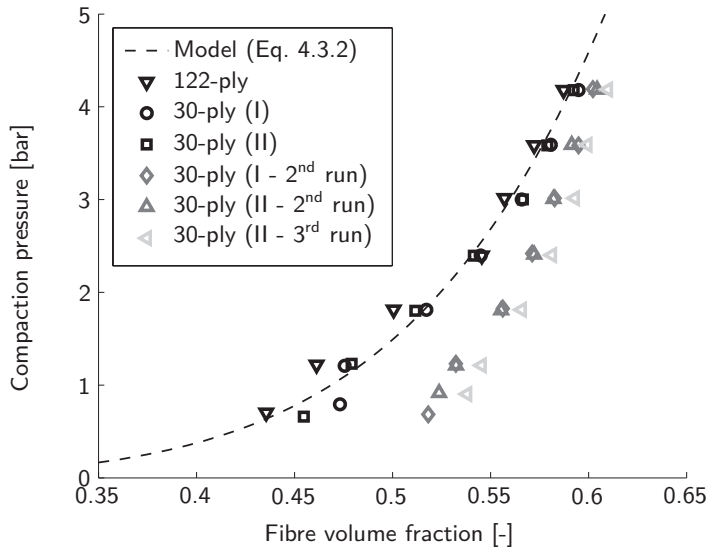


Figure 4.3: Step compaction of dry multiply preforms.

4.4 Choice of manufacturing processes

In Section 1.2 the group of LCM processes was introduced as an alternative to the expensive autoclave curing process. This study focuses in particular on two of these: VI and vacuum-assisted RTM. For both processes, the tooling surfaces have been carefully prepared according to the three-step WaterWorks Aerospace Release System of Zyxax Inc., United States of America [177]. Between consecutive manufacturing cycles the tooling is cleaned with demineralised water before reapplying a single layer of release agent¹⁰. The complete procedure is repeated after 5-10 manufacturing cycles. The geometry of the laminates are restricted to flat plates. Exploring more complex geometries falls beyond the scope of this investigation. Having two different LCM processes and an adjustable thickness of the laminates is already sufficient to form a picture of the capabilities of FBG sensors in determining process-induced strains. In the following, the experimental set-ups are explained in detail.

¹⁰Cleaning with a solvent such as PF-QD Quick Dry Industrial Solvent from PT Technologies Europe, Ireland, affects adversely the performance of this release layer [178].

4.4.1 Experimental set-up for VI

In general, VI requires a single-sided tooling with sufficient stiffness. In case of flat laminates, a metallic plate can already serve this goal. A vacuum bag encloses then the tooling plate and ensures that the preform is stabilised against the plate. In this study, the preform is laid on top of a 3-*mm*-thick aluminium 6082 base plate (Fig. 4.4). The dimensions of the base plate, 500 *mm* × 500 *mm*, are bounded by the inner dimensions of the oven, a VTU 60/60 from Vötsch Industrietechnik GmbH, Germany. The preform is composed of several plies of the glass fabric. The dimensions of these plies are set to 300 *mm* × 200 *mm*. A caul plate (similar material and thickness as the base plate) covers the preform. The caul plate is kept smaller in order to minimise race-tracking of the resin along the edges. The addition of the caul plate reduces the unsymmetry in curing and gives a moulded surface. The stacking sequence is kept simple, *i.e.* $[0/90]_{x,s}$, in which x is half of the number of plies (4 for a thin preform). The fibre volume fraction, determined by burn-off tests, is 43% at a compaction pressure of 0.5 *bar*. By positioning the inlet and vent distribution coils/tubing along the short sides of the preform, a line infusion is created (see arrow in Fig. 4.4). The dry stack is then vacuum bagged and tested for leakages before placing the assembly in the oven (Fig. 4.5). Outside the oven, the vent tubing is connected to a resin trap and vacuum pump, whereas the end of the inlet tubing is submerged in / connected to a resin pot. In case of EP04908 this is simply a polypropylene mixing cup. For RTM6, the resin is contained in a metallic canister that is preheated to 80 °C by an electric hot plate with controller (IKATHERM® HCT + IKA® ETS-D4 fuzzy, IKA®, Germany).

For the RT infusion of EP04908, the absolute pressure level, as indicated by a digital barometer (GDH 200, GREISINGER electronic GmbH, Germany) on the vent line, is set to 50 *mbar*. At this condition, the infusion time is roughly 30 *min*. As soon as the resin reaches the vent line, the absolute pressure level is raised to 500 *mbar*. Resin is flushed to reduce the number of voids. The same approach is adopted for RTM6. Though, the absolute pressure level is maintained at 750 *mbar* throughout the filling stage because of the lower viscosity. Filling time is about 10 *min*. Directly after the isothermal cure, the laminate is cooled to RT conditions and demoulded. The mechanical removal of the distribution coils is the last step. The edges of the laminate are not machined to avoid breaking of the optical fibre. The cured laminate is now ready for further investigation.

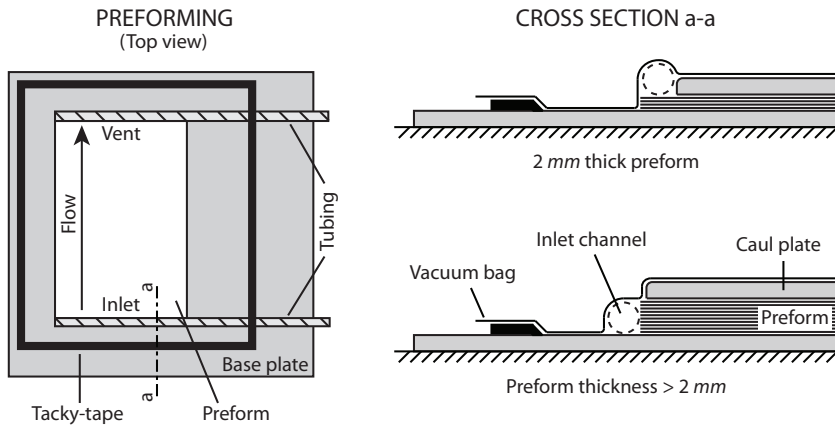


Figure 4.4: Details of vacuum infusion set-up (the caul plate is not shown in the top view).



Figure 4.5: Position of vacuum bagged mould in the oven.

4.4.2 Experimental set-up for vacuum-assisted RTM

For this study, custom-built steel tooling, consisting of upper and lower mould halves, is designed and manufactured in-house by DEMO, the Electronic and Mechanical Support Division, of the Delft University of Technology. In closed state (using twenty bolts), the square mould cavity¹¹ measures $300\text{ mm} \times 300\text{ mm} \times 2\text{ mm}$. The left-hand side of Fig. 4.6 resembles the state directly after opening. It shows a GFR RTM6 laminate clanged to the lower mould part. The in-plane dimensions of the preform

¹¹Picture frames can be inserted to achieve laminate thicknesses of 25, 50, or 100 mm.

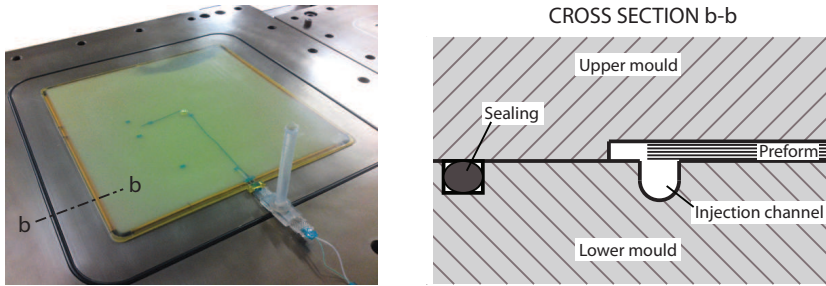


Figure 4.6: Details of the vacuum-assisted RTM test set-up.

are smaller ($290\text{ mm} \times 290\text{ mm}$) to avoid jamming of reinforcing fibres. Considering the injection strategy, a peripheral flow is chosen to minimise race-tracking. Details are schematically illustrated on the right-hand side of Fig. 4.6. The vent port, located in the centre, is integrated in the upper mould half. Filling is performed using a custom-built 10-dm^3 RTM injection unit from Isojet Équipements, France. The 'moving piston' concept allows to control both pressure and flow-rate. For safety reasons, the auto-transition mode is selected. That is, the machine switches automatically to a pressure-driven injection, when the set pressure is reached for constant flow rate. The injection is assisted by vacuum at the vent port. After filling, purging is done to reduce the number of air bubbles. The injection pressure is maintained during cure by leaving the inlet port open. Heating and cooling is done by an oil heating unit (TT-380 with controller MP-694, TOOL-TEMP Ag, Switzerland) which is connected to both mould halves, in which oil circuits are integrated, by two pair of heating hoses. An in-house developed LabVIEW user program handles the steering. The feedback is obtained from thermocouples integrated in the tooling. After cooling, careful releasing of the laminate is necessary to prevent breaking of the optical fibre(s) and thermocouple(s) at the egress point. The curved laminate is machined afterwards by cutting off the 1-cm resin-rich edges on a Secotom-10 machine from Struers, Denmark. The laminate becomes flat and is then ready for further investigation.

4.5 Instrumentation for process monitoring

In the introductory paragraph of Chapter 3 the reader was informed about the FBG sensing technique being introduced by the disciplinary group of DPCS several years ago. In a preceding study [13], a ready-to-use Commercial Off-The-Shelf (COTS)

instrumentation package was bought from FOS&S, Belgium. This purchase implies, however, that there is less freedom for modification.

4.5.1 Interrogator and software

For data retrieval, a 16-channel FBG interrogator and matching software is used. Each channel requires one second for evaluation. The number of connected optical fibres determines therefore the minimum cycle time. The optical source operates in the C-band wavelength. Depending on the type of experiment, the initial Bragg wavelength of the FBG sensor should be chosen such that the Bragg response remains within the optical source domain. In the experiments performed here, the Bragg response is continuously monitored. Snapshots of the reflected spectrum are taken as well. This cannot be done, while saving the peak wavelength(s). . Settings for peak evaluation are default [179].

4.5.2 Optical fibres

As in almost all preceding studies (Section 3.4), this study uses also a FBG sensor with a uniform grating type. The grating is inscribed by a lithographic process, while drawing the single mode optical fibre (125 μm) from a tower. Hence, this is a so-called Draw Tower Grating (DTG[®]s)¹². The optical fibre itself is made of fused silica with a germanium doped core for high photosensitivity. A 35 μe coating of an organically modified ceramic (Ormocer[®]) is applied to improve the mechanical properties (ultimate strain of 5-6%). FBGS-Technologies GmbH, Germany, is responsible for the manufacturing. After delivery, the optical fibre is spliced to a pigtail using a FITEL S121 fusion splicer (Furukawa Electric. Co., Ltd., Japan).

The grating length, the initial Bragg wavelength, and the mutual distance between FBG sensors in a single optical fibre, are the only eligible parameters. The latter is set to 100 mm such that two FBG sensors can be positioned side-by-side without severely bending the optical fibre. The initial Bragg wavelength of the FBG sensor is 1542, 1546, or 1550 nm . In an array, the 4 nm wavelength difference guarantees that intermingling of the Bragg responses in the reflected spectrum are minimal. A grating length of 4 mm is chosen in conjunction with the fibrous reinforcement. As about 9 yarns cross the FBG sensor in both weft and warp directions, effects from

¹²In subsequent chapters FBGs will refer to these DTG[®]s.

Table 4.4: Coefficients for describing behaviour of free-standing optical fibres.

Type	No. of experiments	Coefficients	
		$a \times 10^{-3} [\mu\epsilon/^\circ\text{C}^2]$	$b [\mu\epsilon/^\circ\text{C}]$
Coated	24	9.61 (0.254)	7.41 (0.041)
Uncoated	3	13.48 (0.366)	6.12 (0.057)

microbending should become constant on laminate level¹³.

Thermal treatment

Prior to usage, the optical fibres are thermally treated (in 3 hours to 190 °C followed by a 1 hour dwell) in an oven to stabilise the coating. Temperature is recorded by a K-type thermocouple. For double-checking purposes, the thermal cycle is performed twice. In Figure 4.7, the normalised change in Bragg wavelength, *i.e.* $\Delta\lambda_B/\lambda_B$, is plotted as a function of temperature. Overlaying the second cycle shows that the optical fibre is stabilised after the thermal treatment. The drop measures 5.76×10^{-5} at RT conditions (25 °C). Dividing this value by $1 - P$ ($= 0.796$ [180]) results in a strain of about 70 $\mu\epsilon$ (see Eq. 3.2). This value is consistent for treating these type of coated FBG sensors in such a fashion. According to Eq. 3.2, the slope is a combination of the CTE and thermo-optic coefficient of the coated optical fibre. The slope is best described by a first-order polynomial, $y = aT + b$. The mean and standard deviation of both coefficients are listed in Table 4.4. The properties of the stable uncoated optical fibre are characterised as well, but difficulties in stripping the Ormocer[®] coating limited the set to three samples. Figure 4.8 illustrates the effect of the coating on the measured Bragg response. Herein, the theoretical Bragg response of an uncoated FBG sensor, *i.e.* α_n ($= 5.9 \mu\epsilon/^\circ\text{C}$) and α_f ($= 0.55 \mu\epsilon/^\circ\text{C}$) are constant [180]), is shown as well. On average, the response of the coated FBG sensor is 11% higher than the one for an uncoated FBG sensor for the given temperature range. Furthermore, the relative error between the measured and theoretical response of the uncoated FBG sensor is already 5% at 71 °C. Taking at least the non-linearity into account is thus inevitable in high temperature applications.

¹³A short grating length is preferred to let the FBG sensor act as a point sensor. Though, microbending by the adjacent reinforcing fibres may become a dominant factor when the grating length is too short.

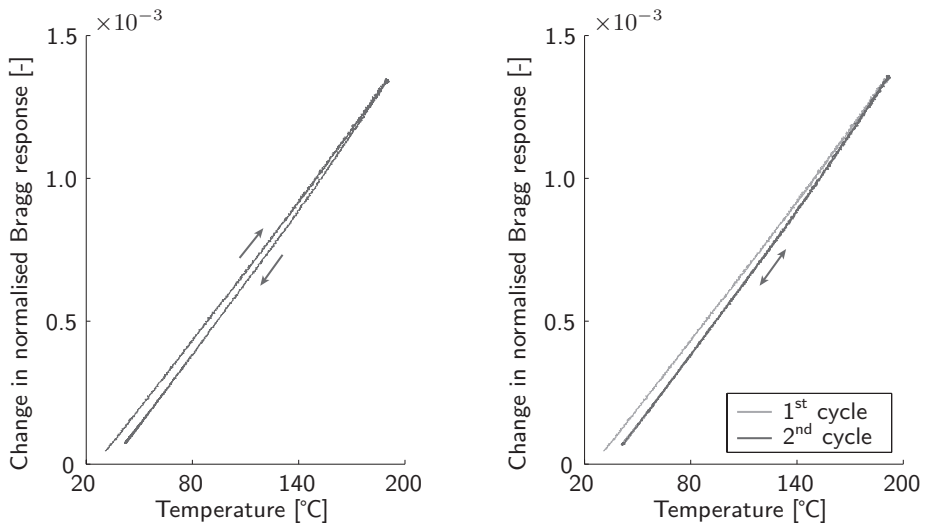


Figure 4.7: Typical Bragg response to thermal treatment - Left: effect of treatment, right: proof of stabilisation.

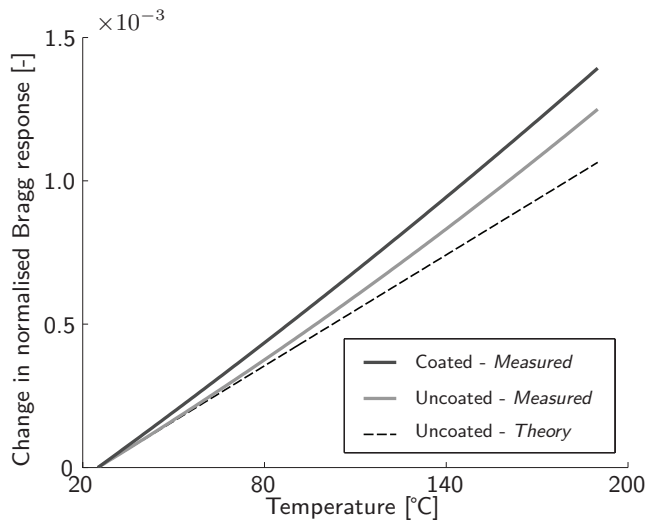


Figure 4.8: Effect of the coating on the output of free-standing FBG sensors (measured responses are based on coefficients listed in Table 4.4).

Correction for thermal contribution

Two parameters, strain and temperature, define theoretically the Bragg response in Eqs. 3.2 and 3.4. In order to determine the process-induced and residual strains in laminates, the Bragg response has to be corrected for the thermal contribution. In Chapter 3 five methods were introduced. In this study, thermocouples are seen as the only viable solution to compensate for the thermally induced strain. To this end, commercially available K-type thermocouple lead with a small diameter (about 1 mm) is used. Data is collected by a 2701 ethernet multimeter/data acquisition system (Keithley, United States of America).

4.5.3 Embedment procedures

Optical fibres

For neat resin systems, it has been proven theoretically that the effective behaviour of the polymer/fibre assembly is essentially governed by the polymer as the effect of the fibre gradually decreases for increasing specimen diameter [144]. If this theory extends to laminates, a similar behaviour may be assumed in which the role of the coating can be neglected.

This may be proven in an experimental study in which the responses of two embedded FBG sensors are simultaneously recorded while heating up an 8-ply dry preform prepared for VI (Section 4.4.1). The two FBG sensors in a single optical fibre are embedded in the middle of the stack and parallel to the weft direction (short side of the preform). The coating is removed for the FBG sensor at the end of the string. For different compacting pressures, the temperature is increased from RT to 180 °C. In both cases, the CTE of the host material is determined by Eq. 3.4 using the coefficients for the uncoated optical fibre (Table 4.4) and the factor $1 - P = 0.796$ [180] in the range of 45-165 °C. As shown in Table 4.5, which lists the measured CTEs, the relative error is less than 1%. This seems to imply that the Ormocer® coating can be ignored in the analysis. Stripping of the coating is, therefore no longer considered necessary in further testing¹⁴.

An important rule for embedding is that the optical fibre's path between an FBG sensor and transition points in thickness, e.g. egress points and ply drop-off regions, should

¹⁴Difficulties in mechanically stripping, the fragility of the bare optical fibre lowering the success rate of embedding, and birefringence problems (see experiment described in Appendix A), do outweigh the choice of stripping even more.

Table 4.5: Coated versus uncoated: measured CTE of the host material.

Compacting pressure [mbar]	CTE of host structure [$\mu\epsilon/^\circ\text{C}$]		Relative error
	Uncoated	Coated	
Ambient - 50	5.711	5.755	0.78%
Ambient - 250	5.633	5.661	0.48%
Ambient - 500	5.654	5.648	-0.11%
Ambient - 750	5.488 ¹	5.532	0.80%
Ambient - 950	-	5.546	-

¹ Up to 140 °C due to fibre slipping.

never be a straight line. This should prevent that local events occurring elsewhere are transferred to the FBG sensor [181]. Figure 4.9 shows two typical arrangements. The arrows point to the positions of the FBG sensors ¹⁵. The FBG sensor is taped on both sides to the underlying ply to ensure proper alignment and to prevent slipping of the optical fibre^{16,17}. In this in-lab environment, the influence of the tapes (Airtech International Inc., United States of America) are assumed negligible. Investigating other ways of attaching/placing is not considered. At the egress point, Teflon tubing (outer diameter of 1 mm) protects the optical fibre¹⁸.

In some tests, the reinforcing fibres of the adjacent plies that are perpendicular to the longitudinal axis of the FBG sensor are cut out by making two parallel incisions (Fig. 4.10). A slit of about 25 mm × 4 mm is created. As such, the FBG sensor is only surrounded by parallel-oriented reinforcing fibres (Fig. 4.11). In this manner, the effect of microbending is studied.

¹⁵A simple hot wire set-up can help locating the exact position of the FBG sensor.

¹⁶In the previously mentioned short study on the effect of the coating, the uncoated FBG sensor was fixed at one side only. The free movement of the FBG sensor led to fibre slipping at low compacting pressures. Estimating the CTE of the host structure was therefore impossible at the lowest compacting pressure (see Table 4.5).

¹⁷That fibre slipping is observed ensures that the FBG sensor follows actually the behaviour of the host structure in case the optical fibre is properly fixed.

¹⁸At the mould sealing (tacky-tape in VI or the cast silicon plug in vacuum-assisted RTM (see left-hand side of Fig. 4.6 in which the plug can be seen in the bottom right quadrant of the picture)) 10 mm of the optical fibre remains unprotected to prevent leaking of air/resin through the Teflon tubing.

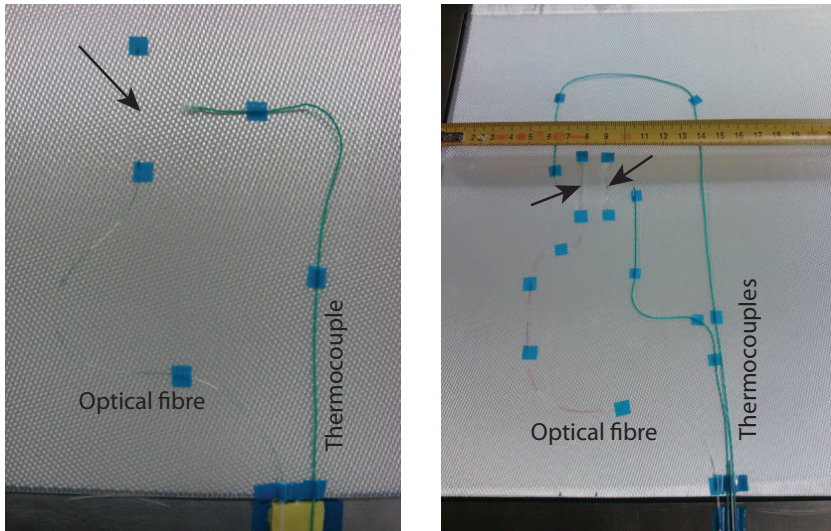


Figure 4.9: Two typical arrangements of FBG sensors and thermocouples.

Thermocouples

The thermocouples are positioned in a similar fashion as the optical fibres (see Fig. 4.9). The distance between the thermocouple point and the FBG sensor ranges between 15-25 *mm*. Differences in temperature are assumed negligible over this distance. The presence of the thermocouple is ignored in evaluating the process-induced strains.

4.6 Summary

A precise description of the materials, processes, and the instrumentation involved in this study is presented in this chapter. The following points summarises briefly this chapter.

- With respect to the materials, two epoxy-based resin systems are selected: RTM6 (high temperature) and EP04908 (low temperature). The latter allows a more efficient use of the operating window of the FBG sensor (up to ≈ 200 °C). The flat-shaped preforms are formed by stacking symmetrically plies of a glass fabric (HexForce® G-300-7581). The effect of microbending on the 4-*mm* FBG sensor is assumed to be constant for this type of fabric.

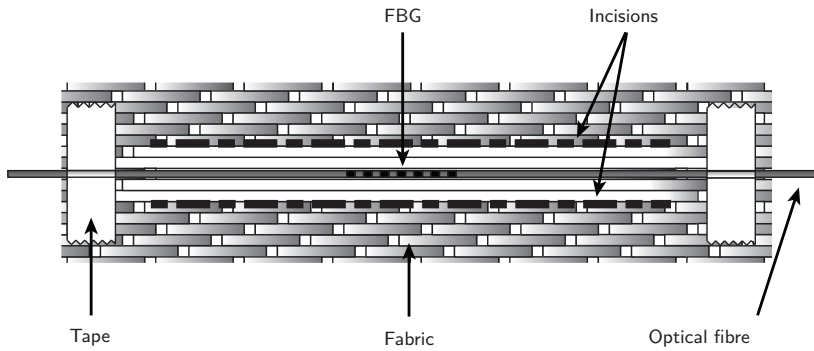


Figure 4.10: Placement of optical fibre.

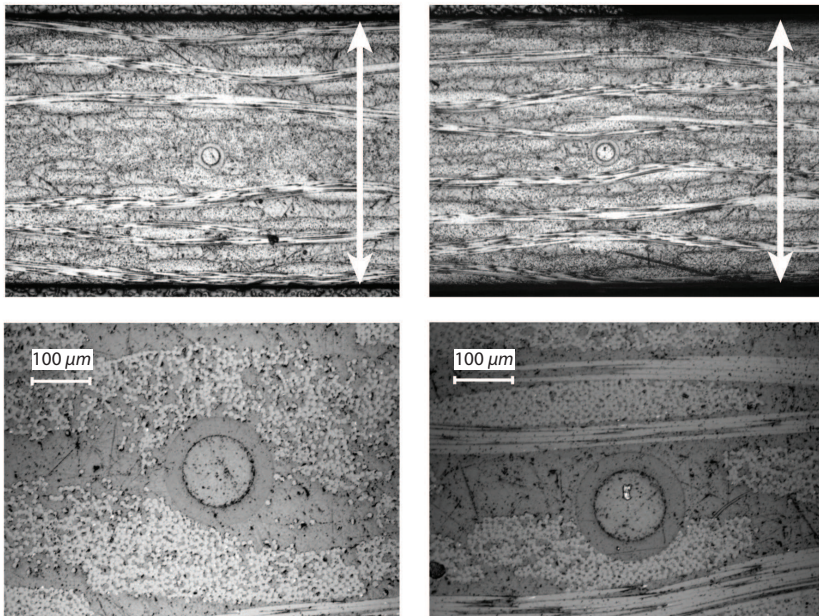


Figure 4.11: Microscopy of samples obtained from a thin VI laminate (thickness of $\approx 1.9\text{mm}$ (indicated by the double arrow lines)) - top: cross-sections of laminate, bottom: enlarged views, left: with fibres removed, right: without fibre removal.

- To support the analyses in subsequent chapters, the cure kinetics of RTM6-2 and the compaction behaviour of the fabric are determined. Compared to the

Table 4.6: Details of both manufacturing processes.

Manufacturing process	VI	Vacuum-assisted RTM
Preform size	300 mm × 200 mm	290 mm × 290 mm
Minimum thickness	8 plies (≈ 2 mm)	2 mm
Flow strategy	line infusion	peripheral injection
Curing	oven	oil-heated tool
Post-processing	removal of distribution coils	removal of resin-rich edges

RTM6-1 cure kinetics models listed in literature, vitrification of RTM6-2 seems to occur at a higher degree of cure.

- For the manufacturing of the laminates, two processes are selected: VI and vacuum-assisted RTM. Table 4.6 summarises the details of each process.
- To follow the formation of process-induced strains, two types of sensors are embedded in the preform: optical fibres with 4-mm uniform FBG sensors and K-type thermocouples. The latter is used for compensating the thermal contribution. The optical fibre has an Ormocer[®] coating that is not removed before processing. A short study seems to indicate that the coating has a negligible influence. Both sensors are fixated by tape to prevent fibre slipping and misalignment. The presence of the thermocouple is assumed negligible on the formation of process-induced strains.

5

THERMAL ANNEALING AS A TECHNIQUE FOR VERIFYING STRAIN FORMATION DURING PROCESSING

5.1 Introduction

As mentioned in the opening chapter, predicting adequately the failure of composite parts relies on knowing the residual strain state after manufacturing. To date, tools for simulating composite manufacturing processes help to identify the process-induced strains. Experimental validation of these simulation tools is, however, scarce for LCM processes - especially concerning thicker composite parts (Chapter 2). Research groups believe that fibre optics based on FBG sensors can fill up this gap. Their potential has already been demonstrated in several studies on curing neat and fibre reinforced resin systems (Chapter 3). Though, a secondary experimental technique to verify the strains measured by FBG sensors is still missing. This chapter identifies such an experimental technique, which could be the key for advancing in online monitoring by FBG sensors.

5.2 In search of a secondary experimental technique

In an earlier study [182], post-manufacturing techniques were reviewed for evaluating the residual strain state in composite parts. These techniques fall into two categories: either destructive or non-destructive. Destructive techniques such as layer removal, blind-hole drilling and successive grooving analyse laminate strains, *i.e.* on a global scale, by measuring the response of the composite part. In general, the lack of accuracy is noted as a drawback for these successive material removal techniques. Non-destructive techniques such as photo-elasticity, Raman spectroscopy and embedded strain gauges, determine mainly intraply and interply stresses, *i.e.* stresses on microscopic and laminar scales, respectively. Some of these put stringent requirements on the specimen, whereas others give limited information or are inaccurate.

In a study on the residual strains in (un)constrained plies of GFRPs, a similar conclusion is drawn [183]. None of the techniques met the requirements. A novel experimental method was therefore introduced, in which the strains can be continuously monitored during a thermal annealing¹ step in a non-contact dilatometer assembly. Afterwards, the measured strains were converted to a temperature-dependent residual strain state within the reinforcing fibres. Based on the rule of mixture and Hooke's law, the residual stress state in the matrix can be determined as well.

The aforementioned experimental technique is appraised for its simplicity. There is no need for taking into account plasticity and viscous effects of the matrix. Moreover, it surpasses other techniques by its capability to measure strains in unconstrained GFRPs. Only thermal lagging between assembly jig and specimen may be seen as an issue, but that can be accounted for by heating up gradually. For this reason, the secondary experimental technique in this study is based on this thermal annealing approach (Fig. 5.1). Instead of measuring the strains by a non-contact dilatometer assembly [183], the FBG sensing technique is proposed. In this way, results from on-line process monitoring and post-manufacturing evaluation can directly be compared. The same sensing technique makes mutual calibration of instrumentation needless. Another advantage is the absence of misalignment problems with the embedded FBG sensor. Monitoring the thermal annealing of GFRPs by FBG sensors is, however, not a proven technique yet.

¹The term annealing refers to a heat treatment in which a material is exposed to an elevated temperature for an extended time period and then slowly cooled [184]. In [183], the term annealing is used to describe the novel experimental method in which UD laminates are slowly heated up.

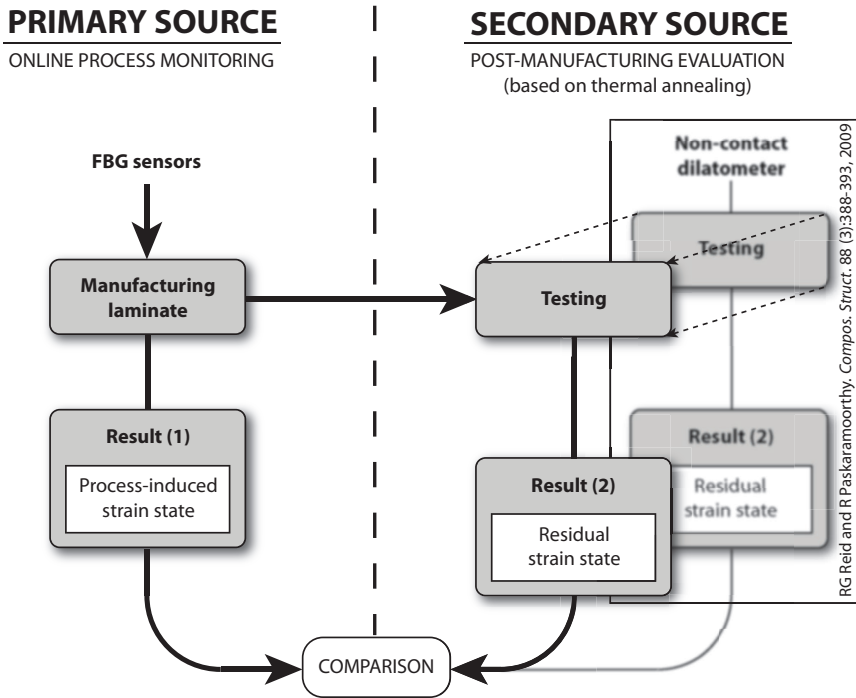


Figure 5.1: Scheme to clarify position of secondary technique based on thermal annealing using FBG sensors.

5.3 Explanatory information about thermal annealing

When a thermosetting resin system passes its glass transition temperature, its modulus of elasticity drops. The modulus above the glass-to-rubber transition zone depends on the cross-link density of the thermosetting resin; the lower the cross-link density the larger the drop [185]. In Fig. 5.2 the modulus of elasticity of neat EP04908 (cured at 60 °C for 16 hrs) is plotted as a function of temperature for two identical tests (standard tension Dynamic Mechanical Analyser (DMA) on a Perkin Elmer Pyris Diamond DMA, United States of America). The loss in stiffness measures about 99%. A similar behaviour is assumed for RTM6. In this situation, loads can no longer be transferred by the matrix. Hence, the laminate's thermal expansion is represented by the stress-free expanding of the reinforcing fibres. Extrapolating this stress-free state back to RT conditions yields the Line of Zero Stress (LoZS) of the reinforcing fibres. The residual strain in the reinforcing fibres is then retrieved by subtracting the LoZS

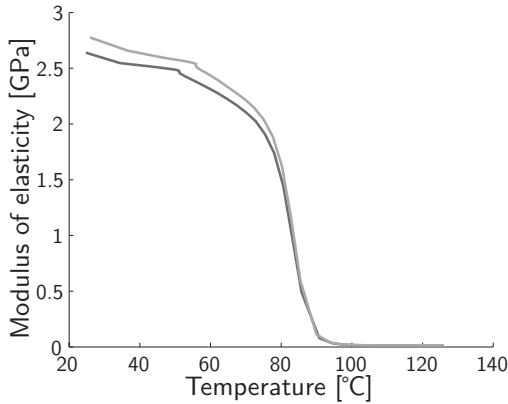


Figure 5.2: Modulus of elasticity of neat EP04908.

from the measured strain [183]. These basics are summarised in Figure 5.3. The end of the glass-to-rubber transition zone marks the borderline between the two segments: (i) in which the resin contributes to the expansion (laminates) and (ii) in which the resin does not contribute anymore (reinforcing fibres). According to this figure, the reinforcing fibres are thus under compression at low temperatures.

5.4 Configuration I: surface-mounted FBG sensors

In the following, two different configurations, *i.e.* surface-mounted and embedded, for the test specimens are discussed. Through experimental work, the pros and cons of both configurations are identified. One of the early lessons learned is that a step back, *i.e.* from thick to thin laminates, seems inevitable to gain a more comprehensive understanding of process monitoring by FBG sensors. In this section, the first configuration is addressed, in which only surface-mounted FBG sensors are considered. In this manner, a picture is quickly formed of the suitability of this experimental technique.

5.4.1 Specimens and experimental setup

Figure 5.4 shows schematically a prepared specimen ($135 \text{ mm} \times 15 \text{ mm}$). The specimens are cut (Unitom cut-off machine) from several GFR RTM6-1 and GFR EP04908 laminates manufactured according to the VI procedure (Section 4.4.1). The orientation of the specimens with respect to the laminate coordinate system is kept

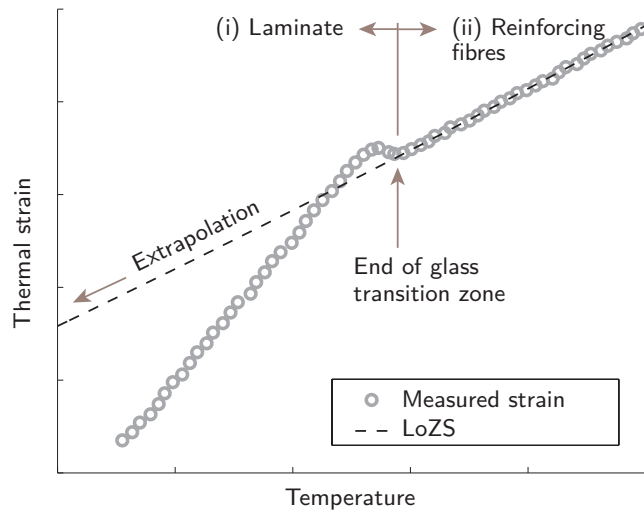


Figure 5.3: Extrapolation of LoZS for determination of the residual strain in the reinforcing fibres.

constant, *i.e.* all align with the short side. The best method found so far for mounting the optical fibre to the specimen is mechanical clamping. Glueing is not an option. The mismatch in CTEs between the glue and the laminate may disturb the readings. A lower glass transition temperature of the glue could also cause early strain relaxation in the optical fibre. By using a glue that is identical to the matrix these problems could be solved, but a second cure cycle would then be required. Clamping the optical fibre to the specimen by using two pair of strips ($35\text{ mm} \times 10\text{ mm}$) is seen as the best method. Strips of other material such as aluminium are discarded because of the mismatch in CTEs. The FBG sensor is located within the 70-mm measurement section. A thermocouple is attached as well. After preparing a batch (up to four specimens), the specimens are hanged vertically in the oven by clamping the upper part, which is called the 'clamping zone' in the figure, to a grid. The type of clamping allow the specimens to swing freely.

5.4.2 Procedure

After installing the specimens, a predefined program is ran by the JUMO dTRON 304 controller of the oven. A heating ramp of about $17\text{ }^\circ\text{C/hr}$ brings them from RT to a final temperature well above the ultimate glass transition temperature. In

case of RTM6-1, the final temperature is set to 250 °C. The limit for EP04908 is set 100 °C lower. A slow heating rate is preferred in order to have a quasi-homogeneous temperature distribution in the specimen. The absence of a mounting jig allows for a higher heating rate compared to the one in [183].

5.4.3 Data analysis

By using Eq. 3.4, which is arranged to:

$$\Delta\epsilon_1 + \alpha_H\Delta T = \frac{1}{1-P} \left[\frac{\Delta\lambda_B}{\lambda_B} - (\alpha_n + \alpha_f)\Delta T \right] + \alpha_f\Delta T \quad (5.1)$$

the Bragg response is converted to the in-plane thermal strain, $\alpha_H\Delta T$. Any additional strain, which cannot be related to thermal expansion or contraction of the host structure, should be captured by the term $\Delta\epsilon_1$. In the analysis, $\Delta\epsilon_1$ is set to zero. The term $(\alpha_n + \alpha_f)\Delta T$ is replaced by the function describing the behaviour of the free-standing uncoated optical fibre (see Table 4.4). The factors α_f and $(1-P)$ are set to 0.55 $\mu\epsilon/^\circ\text{C}$ and 0.794, respectively, [180].

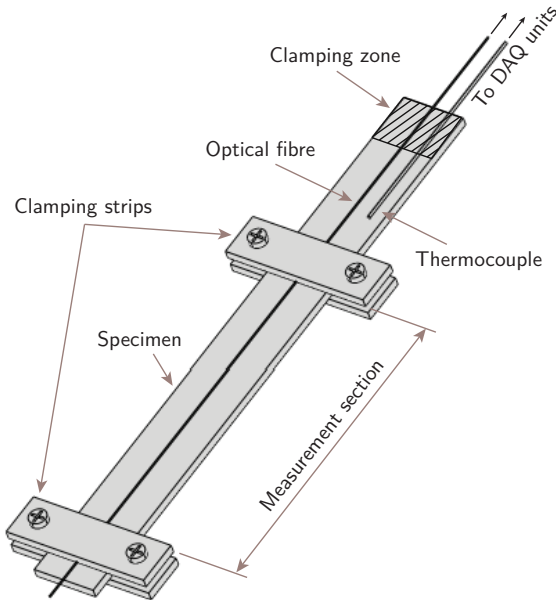


Figure 5.4: Schematic illustration of specimen with surface mounted sensors.

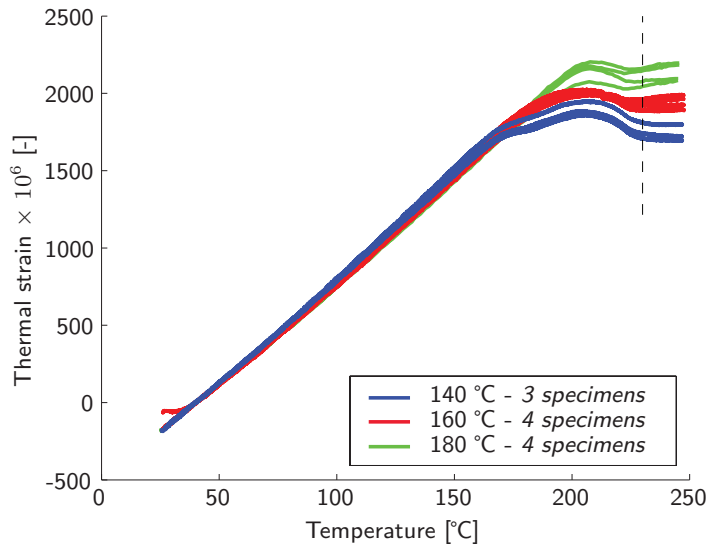


Figure 5.5: Surface-mounted optical fibres: thermal strain in GFR RTM6-1 specimens ($T_{ref} = 40\text{ °C}$).

5.4.4 Results

GFR RTM6-1

The first results correspond to thermal annealing the GFR RTM6-1 specimens (see Fig. 5.5). In this figure, the reference point for the thermal strain is set to 40 °C. Up to the lowest cure temperature the curves coincide. As a lower cure temperature yields a lower glass transition temperature due to incomplete cure [186], specimens cured at a set temperature of 140 °C enter the glass-to-rubber transition zone earlier than the other two. The end temperature of the glass-to-rubber transition zone is, however, nearly identical for all cure temperatures. Post-curing increases the glass transition temperature. The matrix remains stiff enough to transfer strains. Upon reaching the ultimate glass transition temperature ($\approx 206\text{ °C}$ for RTM6-1 [89]), the glass-to-rubber transition zone is finally abandoned. Only the experimental data above about 230 °C, marked by the dashed line in the figure, seems useful for constructing the LoZS of the reinforcing fibres. At this point, some considerations have to be made:

- The domain for curve fitting ranges from approximately 230 to 250 °C. This is only about 10% of the total domain. Hence, the extrapolation of the LoZS to lower temperatures may result in a large scatter in residual strain due to

leverage.

- RTM6-1 is said to be in its rubber state when the temperature is above 220-230 °C. Above this temperature degradation occurs as well, as illustrated by the carbonised specimens. The assumption of stress-free expansion of the reinforcing fibres needs to be reconsidered. However, the material degradation does not allow the domain for curve fitting to be enlarged by bringing the specimens to a higher temperature.
- The optical fibres are not treated for temperatures higher than 200 °C. Additional coating stabilisation may, however, be marginal (Section 4.5.3).

RTM6, the baseline resin system in this study, has thus its limitations in evaluating this post-manufacturing technique.

GFR EP04908

EP04908 seems more suitable because of its ultimate glass transition temperature of about 89 °C [163]. In this manner, the domain for curve fitting can be enlarged both absolutely and relatively. Figure 5.6 shows the thermal strain in the GFR EP04908 laminates. Additional curing, as observed in the GFR RTM6-1 specimens, seems not to affect the measured strain during thermal annealing. The domain is set from 110 °C (the dashed line in the figure) to 150 °C (about one third of the total domain) for fitting the LoZS. Equal domains give a fair comparison of the LoZS for each laminate because of the expected temperature dependency of the CTE. The average slope and its standard deviation of all eleven specimens together is 4.47 $\mu\epsilon/^\circ\text{C}$ and 0.51 $\mu\epsilon/^\circ\text{C}$, respectively. The standard deviation drops to 0.14-0.18 $\mu\epsilon/^\circ\text{C}$ when averaging the LoZS for each laminate individually. Misalignment while cutting the specimens might be the cause of this anomaly. The averaged slope is nevertheless close to the lower bound of the range of CTEs values quoted for E-glass: 4.7 - 5.4 $\times 10^{-6}$ $\mu\epsilon/^\circ\text{C}$ [183].

Remarkable is the offset between the measured strains in equally cured specimens after passing the glass-to-rubber transition zone (see arrows in the figure). A reduction in the clamping force may be the cause, because the strips suffer also from the glass-to-rubber transition. A typical stick-slip behaviour is, however, not observed. A redistribution of some of the prestrain due to mounting may be another cause. The limited number of tests restricts the formulation of a clear answer for this offset. To circumvent the problems associated to this offset, the cure temperature is used to define the initial stress-free point in the analysis [187]. The thermal strain in each

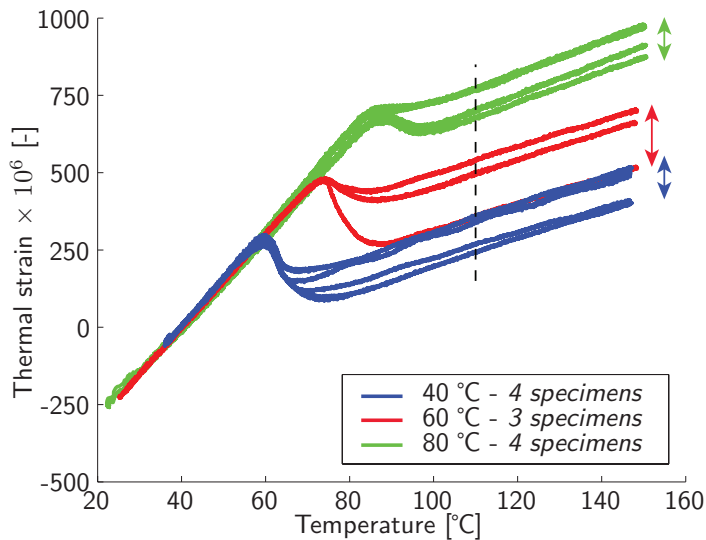


Figure 5.6: Surface-mounted optical fibres: thermal strain in GFR EP04908 specimens ($T_{ref} = 40\text{ }^{\circ}\text{C}$).

specimen is corrected for the LoZS and then referenced to the cure temperature² (Fig. 5.7). In general, the curves are similar to the data presented in [183]. A higher cure temperature results in more residual strain in the reinforcing fibres at RT conditions. Though, the residual strain values above the glass-to-rubber transition should be interpreted carefully for the aforementioned reasons.

5.5 Configuration II: embedded FBG sensors

The previous study with the first configuration demonstrated the potential of FBG sensors in thermal annealing as a post-manufacturing technique to evaluate the residual strain state. In the second configuration, the FBG sensors are embedded. In this case, the cured resin would 'freeze' the position of the FBG sensor. A direct comparison between the process-induced and residual strains is thus offered without risking misalignment of the FBG sensors.

²It should be noted that 40, 60, and 80 °C in Fig. 5.7 refer to the set temperature of the oven. The actual cure temperature is about 4-5 °C higher.

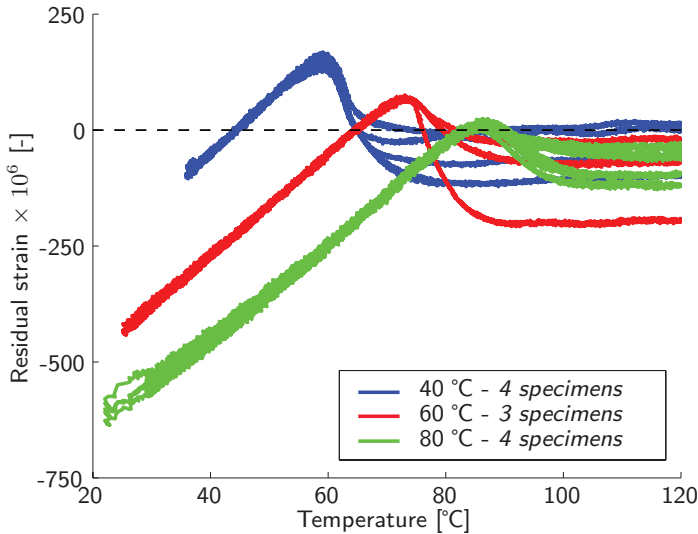


Figure 5.7: Surface-mounted optical fibres: residual strain in reinforcing fibres of GFR EP04908 specimens.

5.5.1 Specimens, setup, procedure and data analysis

The procedure for manufacturing the thin laminates is explained in Section 4.4.1. In total, five GFR EP04908 laminates are cured at different set temperatures (40, 60, 80, 90, and 100 °C)³. The last two are added to study the effect of curing above the ultimate glass transition temperature. The sensors are embedded between the fourth and fifth ply of the preform (see Section 4.5.3). Afterwards, the laminates are, one by one, thermally annealed in the same oven. The laminates are hanged vertically with the sensors' egress points pointing upwards in the oven. A sliding-joint assembly should allow free expansion. The thermal programme shows similarities with the one used for testing the first configuration. The temperature is initially increased from RT to 150 °C in about 7.5 hrs (≈ 17 °C/hr). The ramp is then followed by a dwell period of 1 hr before cooling down to RT conditions at the same rate. Again, Eq. 5.1 is used to convert the Bragg responses (see Section 5.4.3).

³For the reasons mentioned in Section 5.4.4, GFR RTM6 laminates are not analysed here.

Table 5.1: LoZS - measured slopes for laminates cured at different isotherms.

Cure temperature [°C]	40	60	80	90	100	Average
Slope [$\mu\epsilon/^\circ\text{C}$]	4.88	5.21	5.63	5.72	5.80	5.45 (0.35)
Ratio [-]	0.84	0.90	0.97	0.99	1	-

5.5.2 Results

Figure 5.8 shows the residual strain in the reinforcing fibres after subtracting the LoZS. Table 5.1 lists the measured slopes of the individual LoZSs. These slopes are determined by curve fitting using a first-order polynomial. Considering the glassy state only, the results seem to agree fairly well with the ones obtained by the surface-mounted FBG sensors (Fig. 5.7). The assumption that the initial stress-free point is dictated by the cure temperature seems to hold. In general, the increase in compressive residual strain in the reinforcing fibres is found proportional to the cure temperature until the cure temperature reaches the ultimate glass transition temperature. No significant increase in compressive residual strain is observed for cure temperatures above this transition. The curve fitting results show a significant difference in the measured slopes for the LoZS. The ratio seems to indicate that the slope approaches asymptotically a maximum value when the cure temperature increases. The slopes for the two lowest cure temperatures are still in the range of CTE values quoted for E-glass: $4.7 - 5.4 \times 10^{-6} \mu\epsilon/^\circ\text{C}$ [183]. In case of the higher cure temperatures, a slight overestimation is noted. Figure 5.2 showed that the resin modulus of elasticity drops by 99% in the rubber state. Micromechanical models combined with CLT predict a CTE that is almost entirely dominated by the properties of the reinforcing fibres [91]. Hence, a difference in degree of cure cannot explain the occurrence. Though, the difference in measured slopes could simply be within the scatter of the collected data. After all, the average value of the slopes is close to the upper bound of the range of CTE values given earlier for E-glass. That the surface-mounted FBG sensors measured an average value that approaches the lower bound may be explained by some of the problems mentioned earlier. More testing would be needed to be more conclusive.

As opposed to RTM6 (see Fig. 5.5), the EP04908 matrix does not regain its stiffness upon entering the glass-to-rubber transition zone. The instantaneous glass transition temperature does, however, built up as proven by the results from cooling down (Fig. 5.9). In spite of some minor anomalies, the thermal annealing brings the reinforcing fibres in the same residual strain state afterwards. The two laminates cured

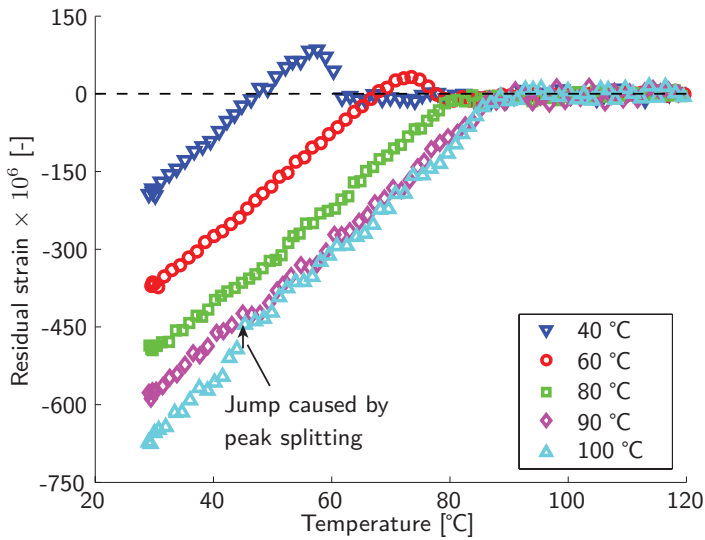


Figure 5.8: Embedded optical fibres: residual strain in reinforcing fibres of GFR EP04908 laminates.

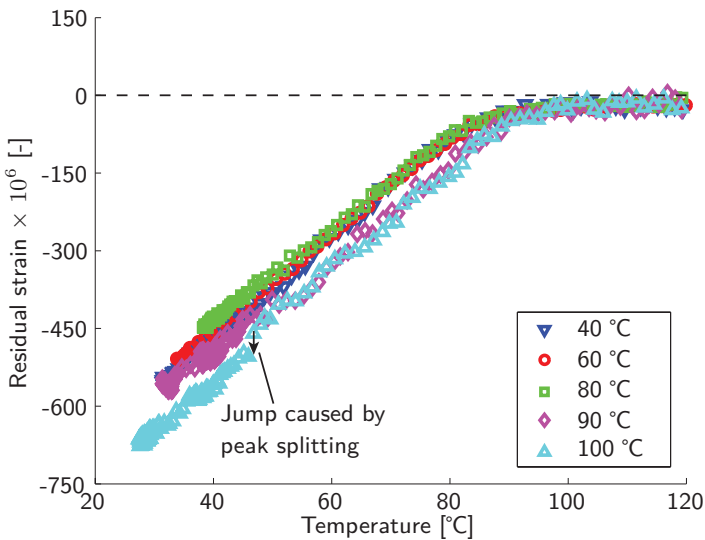


Figure 5.9: Embedded optical fibres: residual strain in reinforcing fibres of GFR EP04908 laminates (after thermal annealing).

at 90 and 100 °C seem to pass the rubber-to-glass transition at a slightly higher temperature for yet unknown reasons. Furthermore, peak-splitting remains present in the response of the FBG sensor embedded in the 100 °C-cured laminate. A more quantitative analysis is presented in the next chapter, in which this post-manufacturing evaluation technique is coupled to the online monitoring of the VI process for thin laminates.

5.6 Discussion and concluding remarks

A secondary experimental technique for strain determination has been evaluated in this chapter. The basis of this technique is found in [183] and relies on thermal annealing. Instead of using their non-contact dilatometer assembly, FBG sensors are used to monitor the thermal strain. By introducing the LoZS, the residual strain state in the reinforcing fibres can be determined. In an experimental study, two different configurations have been tested: (i) smaller composite specimens equipped with surface-mounted FBG sensors and (ii) laminates with embedded FBG sensors. Despite some anomalies, thermal annealing is seen as a promising post-manufacturing evaluation technique for the derivation of the residual strain state. Some remarks are:

- By fixating the FBG sensor, it monitors intentionally the behaviour of the reinforcing fibres in the manufacturing process. As thermal annealing as a post-manufacturing technique determines the residual strain in the reinforcing fibres, combining the experimental data seems fruitful.
- Two ideas for monitoring have been worked out: by means of surface-mounted and embedded FBG sensors. The former saves costs by reusing the optical fibres, but sliding of the optical fibre and misalignment problems are risks. Embedded FBG sensors have the advantage that a direct comparison can be made with online process monitoring.
- As a quasi-homogeneous temperature distribution is preferred, a low heating rate is needed. In the absence of an assembly jig for the instrumentation, the heating rate is can be tripled compared to the one used in [183]). Though, some improvements may still be gained on reducing the cycle time.
- The thermal annealing technique requires the specimens to be heated up well above the glass-to-rubber transition in order to fit properly the LoZS. In combination with the operational limits set for the optical fibre and the unknown consequences of material degradation, GFR RTM6 samples cannot be evaluated

properly. The secondary resin system EP04908 is therefore analysed in parallel. Rules created for the latter should then be applied to the former.

- In [183], the analysis continues with the calculation of the stresses in the reinforcing fibres using Hooke's law. The stress state in the matrix can be determined by using the ratio of volume fractions. These steps are not yet considered here.
- Since the FBG sensor should perform online monitoring of the manufacturing process, the thermal annealing step can not be considered an independent technique by the way it is performed here. A correlation with other measuring methods such as the non-contact dilatometer assembly in [183] or digital image correlation (see description in Chapter 8) is thus still necessary.

6

EFFECT OF THE CURE REGIME ON THE FORMATION OF STRAINS IN VI LAMINATES

6.1 Introduction

Now that thermal annealing has been introduced as a secondary/post-manufacturing evaluation technique to determine the residual strain state in the reinforcing fibres, a closer look can be taken at the actual monitoring of the VI process (Section 4.4). Adding step by step more complexity is seen as the best strategy in deciphering the Bragg response, finding the limitations of the FBG sensing technique, and avoiding jumping to conclusions. On the hand of two examples, the usefulness of coupling the two approaches is demonstrated for thin laminates. The chapter continues then with a study on the effect of the cure regime on the formation of process-induced strains. So far, this parameter has hardly been addressed in any of the previous studies related to monitoring in continuous fibre composite manufacturing processes by FBG sensors. The thermal history has, however, a profound effect on the formation of process-induced strains in neat resin systems (Section 3.6.2). The only remark concerning the cure regime for continuous fibre composites is found in a study on adaptive composite materials. Intermediate cooling between curing and post-curing instead of direct heating seems to have influenced the formation of the process-induced strain (Section 3.6.3).

The aim of this chapter is therefore twofold: explaining the approach on the basis of experimental data from the two examples and studying the effect of the cure regime

on the formation of process-induced strains in thin VI laminates¹.

6.2 Experimental procedures and data analysis

In addition to the experimental procedures described in Chapters 4 and 5, this section highlights some facts concerning the test sequence as depicted in Fig. 6.1.

6.2.1 Vacuum infusion

Two groups of laminates are manufactured according to the method described in Section 4.4.1. The procedure, as explained in Section 4.5.3, is followed to embed both types of sensors in the mid-plane of an eight-ply stack. The orientation of the FBG sensor is always parallel to the short side of the preform². The first group of experiments, consisting of five GFR EP04908 laminates, are subjected to a one-step cure cycle. A $1\text{ }^{\circ}\text{C}/\text{min}$ ramp is selected for heating and cooling³. The selected cure temperatures are 40, 60, 80, 90 and $100\text{ }^{\circ}\text{C}$ with dwell times of 32, 16, 8, 8 and 8 hours, respectively. Multi-sensor optical fibres are available for the laminates cured at the three lowest temperatures. The additional FBG sensors would give more insight into the presence of cure-induced strains and microbending effects by embedding them according to the scheme in Fig. 4.10. Similar experiments are performed in the second group consisting of GFR RTM6 laminates. The first three laminates are cured isothermally at 140, 160, and $180\text{ }^{\circ}\text{C}$ for 200, 75, and 100 minutes, respectively. For the fourth laminate, the heating rate is lowered to $0.25\text{ }^{\circ}\text{C}/\text{min}$ to study the effect of early gelation. In additional testing, the reproducibility and the effect of different tooling materials is addressed as well.

6.2.2 Thermal annealing

The procedure for thermal annealing is described in Section 5.5.1. The maximum temperature for GFR RTM6 laminates is lowered to $190\text{ }^{\circ}\text{C}$ due to the initially unknown consequences of degradation of the optical fibre's coating as well as the RTM6 matrix at temperatures higher than $200\text{ }^{\circ}\text{C}$. As the complete laminates are thermally annealed, no material is saved for other testing purposes.

¹Results from online monitoring the RTM process are discussed in Chapter 9. Chapter 10 presents the results for thicker laminates.

²In keeping the number of variables low, the other principal direction has not been investigated yet.

³Maintaining the cooling rate of $1\text{ }^{\circ}\text{C}/\text{min}$ is not possible near ambient conditions.

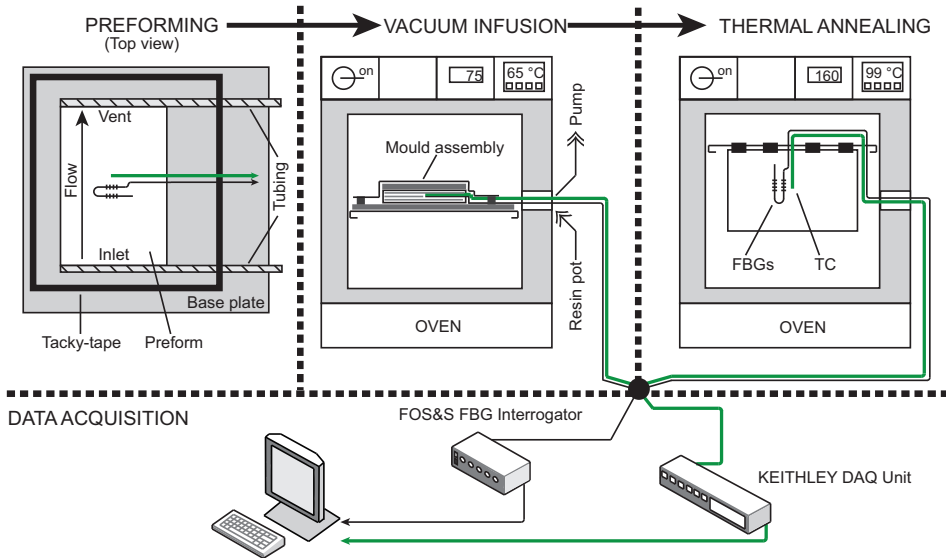


Figure 6.1: The test sequence schematised.

6.2.3 Data analysis

Equation 5.1 is used to convert the Bragg responses to strains (see Section 5.4.3).

6.3 Selection of the initial reference point

A generic VI process consists of several processing steps (Fig. 1.1). As the optical fibres are embedded in the preforming stage, all subsequent steps may influence the Bragg response. Prior to curing, three actions can be identified that affect the Bragg response: (i) the actual placement of the optical fibre, (ii) debulking, and (iii) the impregnation of the preform. With respect to the first point, straightening of the optical fibre between the FBG sensor's fixation points causes a bit of tensile straining (see Fig. 4.9). The small value is, however, ignored here. In a preliminary study [188], debulking is found to increase the Bragg wavelength. The compaction pressure results generally in a larger shift in the Bragg wavelength. Reproducing the debulking tests is, however, difficult. Local phenomena such as nesting between adjacent plies, deformation and compaction of adjacent yarn cross-sections, and flattening of the yarn waveform seem sources for the scatter. Difficulties in controlling manually the orientations of the plies with respect to the FBG sensor's axis is another contribution

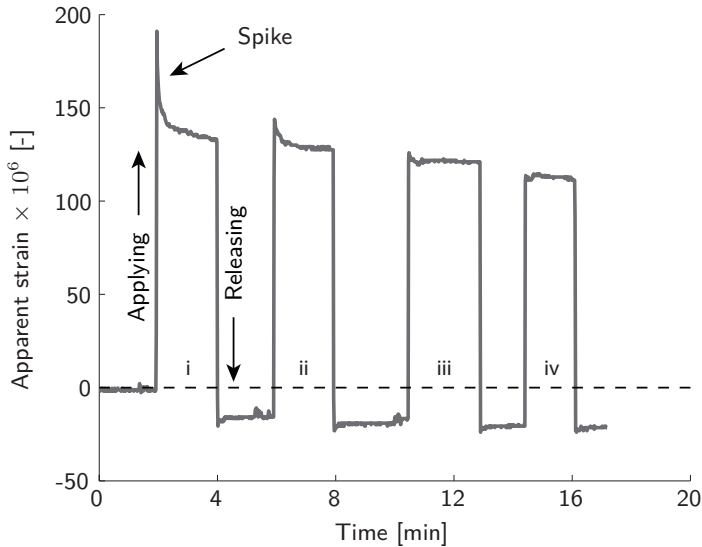


Figure 6.2: Typical response of an embedded FBG sensor to a number of debulking cycles.

that makes the prediction of the Bragg response to debulking cumbersome. Though, a strong correlation is assumed between the out-of-plane displacement/deformation while debulking and the settling of the FBG sensor and its accompanying response⁴. Figure 6.2 shows such a typical Bragg response of an embedded FBG sensor to four consecutive debulking cycles (*i-iv*). The compacting pressure is about 250 *mbar*. The preform is debulked four times by instantly applying vacuum. In this example, the apparent strain measures roughly 150 $\mu\epsilon$. The spike may be related to the relaxation in the preform [190]. As consecutive cycling seems to stabilise the Bragg response, it is decided to perform three or four debulking cycles prior to filling to improve uniformity amongst the experimental data. A similar conclusion is drawn with respect to filling at RT conditions. Although Chapter 8 will go into more detail, the Bragg response is found to correlate well with the out-of-plane displacement/deformation of the preform. Consequently, the initial reference point for both EP04908 and RTM6 is chosen to coincide with the start of the heating cycle⁵.

⁴Comparing the Bragg response directly to the compression behaviour of preforms such as experimentally determined by Kelly *et al.* [189] may be an option to verify this assumption.

⁵In case of RTM6, the Bragg response to the filling remains thus present in the experimental data.

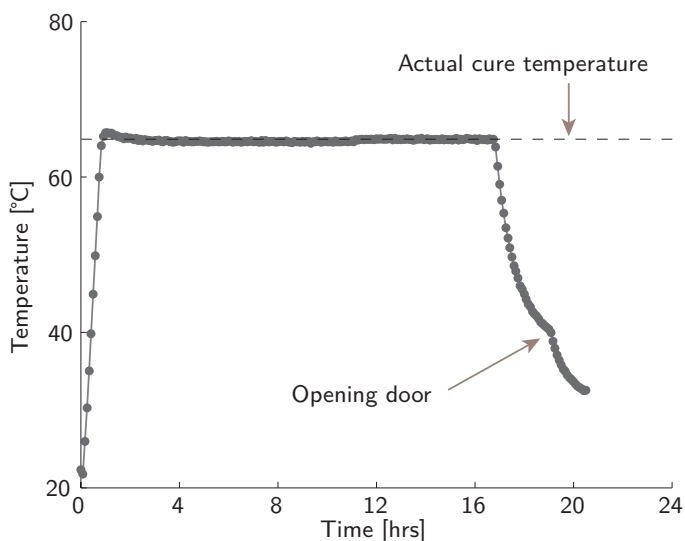


Figure 6.3: Cure temperature profile of GFR EP04908 laminate cured at 60 °C.

6.4 Illustrative example 1: GFR EP04908

In this section, the coupling of online monitoring of the manufacturing to thermal annealing, the post-manufacturing technique described in the previous chapter, is demonstrated on the basis of experimental data obtained from a 16-hours 60 °C-cured GFR EP04908 laminate.

6.4.1 Results: monitoring of the manufacturing

Figure 6.3 shows the mid-plane temperature profile as measured by the embedded thermocouple. The set temperature of 60 °C resulted in a measured cure temperature of 65 °C in the laminate⁶. The thermal strain is plotted as a function of the noise-reduced⁷ temperature in Fig. 6.4. The data between points *I-IV* resemble the cure cycle. Point *V* describes the state of the laminate after demoulding. In total, four stages can be distinguished:

⁶The cause of this offset is likely the positional difference between the steering thermocouple of the oven and the embedded one in the laminate in combination with a disturbed heat flow due to the tooling.

⁷The noise in the thermocouple readings is reduced by Savitzky-Golay smoothing.

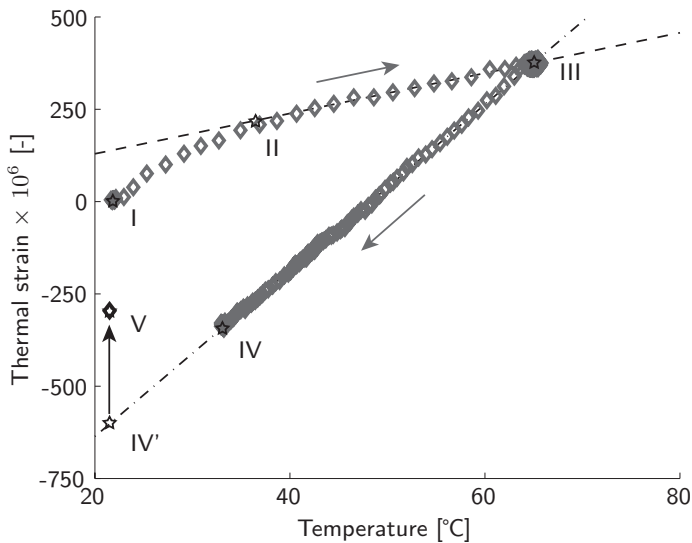


Figure 6.4: Online monitoring of the curing of a GFR EP04908 laminate at 60 °C.

- **Stage I-II:** Non-linear increase in strain due to the thermal expansion of the host structure. This behaviour is linked to a combined effect of: (i) tool-part interaction caused by friction between the tooling and the preform and the plies of the preform mutually and (ii) yarn straightening in the woven fabric. Since this explanation differs from literature [142], a proof of this pre-cure tool-part interaction is presented in Chapter 7.
- **Stage II-III:** Linear increase in strain due to the thermal expansion of the host structure. At point II the yarns are no longer stretched, because friction between the aluminium plates and preform is overcome by the force originating from the mismatch in thermal expansion. The slope (with 95% confidence bounds) is approximated by fitting a first order polynomial (dashed line): $5.47 (5.383, 5.547) \mu\epsilon / ^\circ\text{C}$ (R^2 is 0.9857). The value is close to the range of CTEs quoted for E-glass: $4.7 - 5.4 \mu\epsilon / ^\circ\text{C}$ [183]. The dynamic friction coefficient seems sufficiently low such that the contribution of the tooling can be neglected.
- **Stage III-IV:** Linear decrease in strain due to the thermal contraction of the host structure while cooling down. The slope of the best fit (dash-dotted line) measures $22.49 (22.45, 22.53) \mu\epsilon / ^\circ\text{C}$ (R^2 is = 0.9984). This is found close to $23.4 \mu\epsilon / ^\circ\text{C}$, the CTE stated for the aluminium alloy [191]. The tooling plates dictates thus the thermal strain in the laminate in this stage.

- **Stage IV'-V:** Increase in measured strain as a result of demoulding. The mismatch in CTEs of the tooling and the laminate causes an additional build-up of thermal strain during cooling. Due to the tool-removal step, an increase of $307 \mu\epsilon$ at $21.5 \text{ }^\circ\text{C}$, represented by the arrow in Fig. 6.4, is found implying that the in-plane CTE of the symmetric laminate must be smaller compared to the aluminium alloy.

Curing of the EP04908 resin system seems not to affect the measured strain⁸. The absence of a thermal spike may clarify the difference with [142] (see also Section 6.7.1). Whether the difference between points **I** and **V** represents then the residual strain is discussed in the following section.

6.4.2 Results: monitoring of the thermal annealing

In Fig. 6.5 the strain curve from thermal annealing, discussed before in Chapter 5, is overlaid onto the one from online monitoring the manufacturing process using the same initial reference point. The following is deduced:

- As the dash-dotted line, representing the thermal expansion of the laminate, intersects with the strain reading just after release from the tooling (represented by the black marker), there is no permanent change in the Bragg response during the 12 hours waiting time.
- As the LoZS (dashed line) aligns well with the linear increase in process-induced strain due to the expansion of the impregnated preform (stage **II-III** in Fig. 6.4), the influence of the tooling seems negligible. Since the matrix has also a marginal influence⁹, the impregnated preform is said to be in a stress-free state.
- The extrapolated LoZS diverts from the process-induced strain below $40 \text{ }^\circ\text{C}$. It is believed that the effect of yarn straightening in combination with friction causes the 'new' stress-free state in the preform. Upon curing, the reinforcing fibres are 'locked' in their new position by the matrix.
- The initial stress-free temperature, defined here as the intersection of the LoZS (dashed line) and the line describing the expansion behaviour of the laminate (dash-dotted line), of $67.9 \text{ }^\circ\text{C}$ is close to the cure temperature of $65.0 \text{ }^\circ\text{C}$.

From the fourth point it can be concluded that the strain due to the pre-cure tool-part interaction should be ignored in the residual strain analysis. In Fig. 6.6 the residual

⁸Point **III** in Fig. 6.4 resembles the complete dwell period.

⁹A proof of this statement is given in Chapter 7).

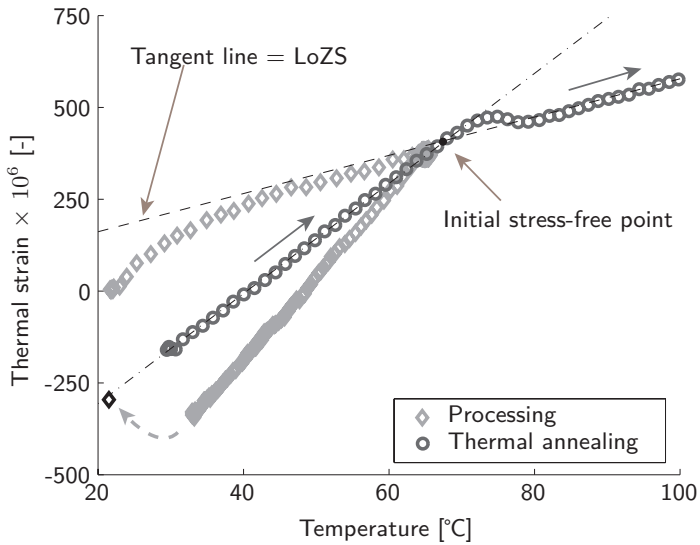


Figure 6.5: Comparison between monitoring process and thermal annealing of GFR EP04908 laminate cured at 60 °C (note that data from thermal annealing extended originally to 150 °C).

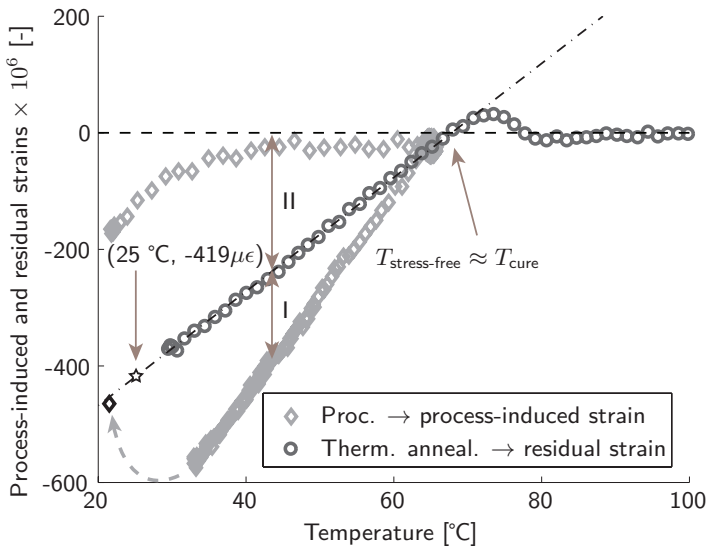


Figure 6.6: Process-induced and residual strains of GFR EP04908 laminate cured at 60 °C.

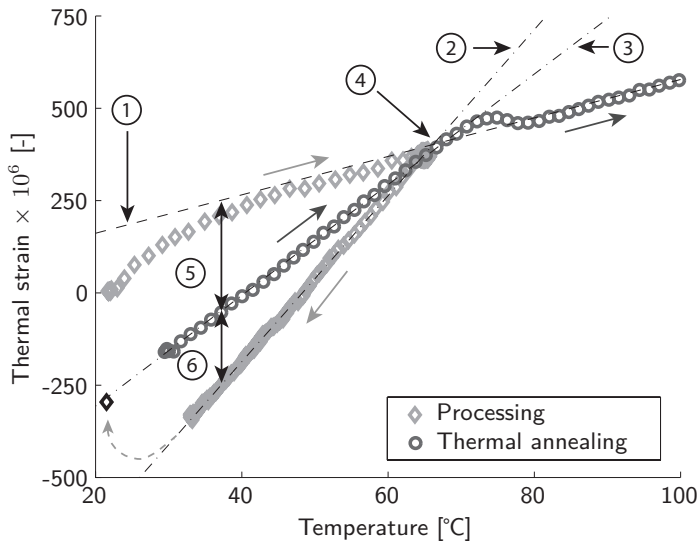


Figure 6.7: Process monitoring and thermal annealing for laminate cured at 60 °C (see Table 6.1).

strain is plotted as a function of temperature. To this end, the LoZS is subtracted from the measured strain. In addition, the process-induced strain is shown after LoZS-correction. The effect of the tooling, *i.e.* a compressive strain in the reinforcing fibres of $292 \mu\epsilon$ at 25 °C, on the thermal contraction of the laminate is indicated by difference I. The remaining, indicated by difference II and measuring $-419 \mu\epsilon$ at 25 °C, is the residual strain in the reinforcing fibres. Hence, the difference between points **I**, *i.e.* start of process monitoring, and **V**, *i.e.* after demoulding, in Fig. 6.4 would have underestimated the residual strain by $121 \mu\epsilon$ (29%) at 25 °C.

The combination of monitoring the manufacturing and thermal annealing gives thus more insight in the cure behaviour. Besides the near stress-free state of the impregnated preform during the second part of the heating stage (stage **II-III** in Fig. 6.4), other features are indicated in Figs. 6.7 and 6.8. Their definitions are listed in Table 6.1. These features are used later on in studying the effect of the cure regime on the formation of strains.

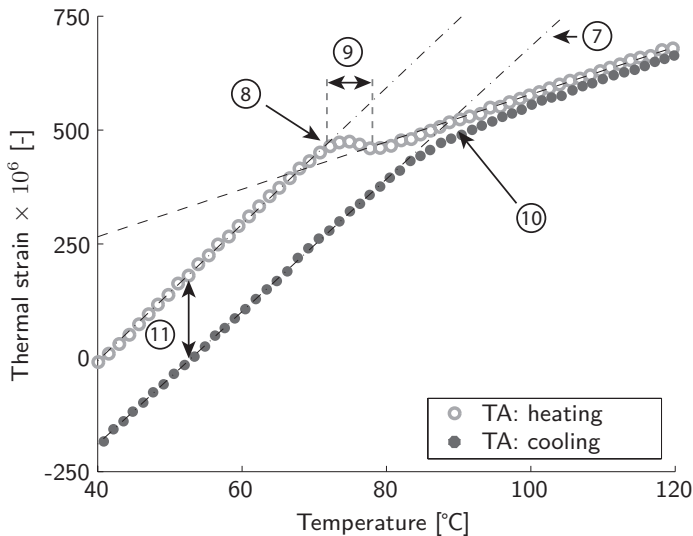


Figure 6.8: Thermal annealing: heating up and cooling down for laminate cured at 60 °C (see Table 6.1).

6.5 Illustrative example 2: GFR RTM6

In this section, observations such as the stress-free expansion of the impregnated GFR EP04908 preform are used to illustrate the cure behaviour in a GFR RTM6 laminate.

6.5.1 Results: monitoring of the manufacturing

Figure 6.9 shows the mid-plane temperature profile as measured by the embedded thermocouple. The cure schedule can be split up into five zones: two heating segments (1 & 3), two dwell periods (2 & 4), and a cooling segment (5). The small drop in temperature in zone 2 is associated with the non-isothermal infusion, whereas the small thermal spike in zone 4 is caused by the exothermic reaction.

Figures 6.10 and 6.11 present the thermal strain as a function of temperature. In essence, a similar behaviour is observed compared to the GFR EP04908 laminate (Fig. 6.4). Point 1 in Fig. 6.11a shows a permanent change in thermal strain of 42 $\mu\epsilon$ occurring at resin arrival. In Fig. 6.12 this is visualised once more by plotting both the temperature and the thermal strain as a function of time. The arrows indicate the main differences. The following is considered in finding a proper explanation:

- The effect of the local change in temperature due to non-isothermal filling on

Table 6.1: Data extracted for specimen: VI @ 60 °C.

Definition	Value	Units
1 - CTE of glass fabric	5.21	$\mu\epsilon/^\circ\text{C}$
2 - CTE of laminate sandwiched between aluminium tooling	22.49	$\mu\epsilon/^\circ\text{C}$
3 - CTE of laminate	14.99	$\mu\epsilon/^\circ\text{C}$
4 - Initial stress-free temperature	67.9	$^\circ\text{C}$
5 - Residual strain	-419	$\mu\epsilon$
6 - Strain due to tool-part interaction	-292	$\mu\epsilon$
7 - CTE of thermally annealed laminate	14.55	$\mu\epsilon/^\circ\text{C}$
8 - Onset of transition zone	69.7	$^\circ\text{C}$
9 - Length of transition zone	8.7	$^\circ\text{C}$
10 - Ultimate glass transition point	88.7	$^\circ\text{C}$
11 - Change in strain after thermal annealing	-176	$\mu\epsilon$

the thermal strain is assumed reversible. As no net temperature difference exists over the filling time span, a permanent change in measured strain is thus not expected from this source.

- As the flow-front propagates, the local fluid pressure starts to increase and affect the compaction. Since this is opposed to debulking (Section 6.3), a decrease in thermal strain is expected.
- As the FBG sensor is attached to the ply underneath, the mismatch in CTEs forces the optical fibre to expand more than it would naturally do. A sudden change in compacting conditions due to resin arrival may have led to contraction of the optical fibre.

This suggests that the drop in thermal strain is best interpreted as a shift of the reference point. Though, the sudden contraction of the optical fibre may have affected the (local) strain state in the adjacent reinforcing fibres. Despite the absence of a conclusive answer, the impact of the decision on the residual strain can be considered marginal (about 3% at RT conditions).

In zone 5, debonding from the two aluminium plates occurred while cooling down (points 2 and 3 in Fig. 6.11). At point 2, debonding results in a jump of 70 $\mu\epsilon$, whereas 149 $\mu\epsilon$ is recorded at the second debonding. A similar behaviour is found for cooling down a flat CFRP laminate in a steel matched-mould system in [192]. In there, an estimate is even given for the maximum shear stress that can be sustained by the laminate just before debonding. From point 3 onwards, the tooling seems

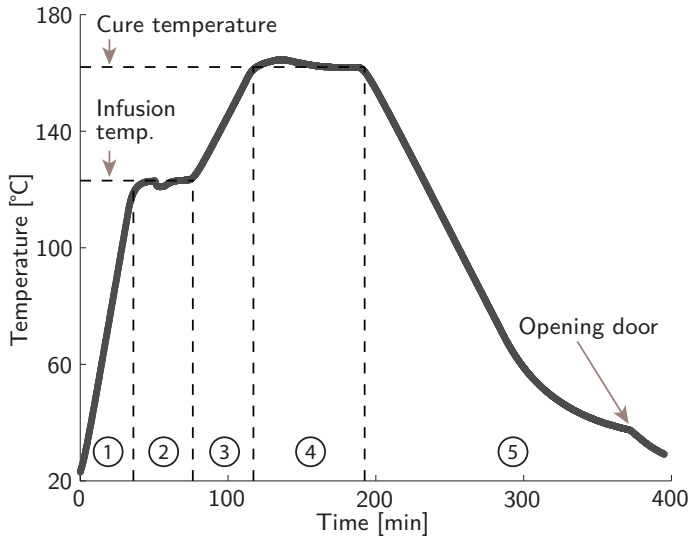


Figure 6.9: Cure temperature profile of GFR RTM6 laminate cured at 160 °C.

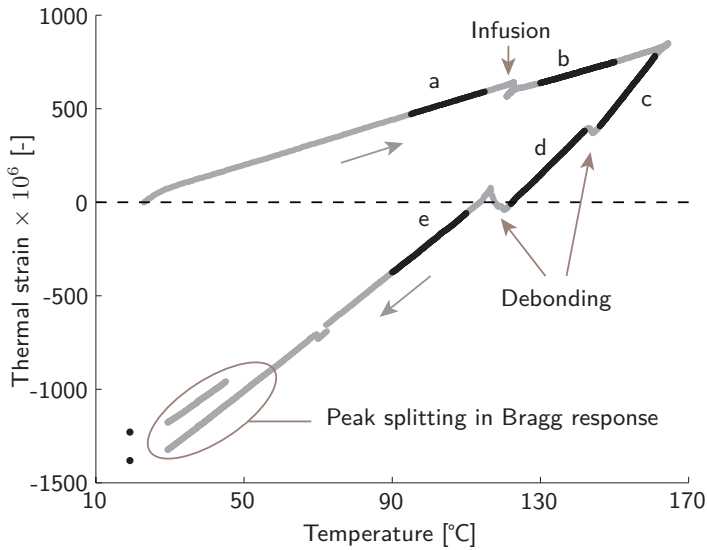


Figure 6.10: Process monitoring of a GFR RTM6 laminate cured at 160 °C.

no longer to influence the CTE of the host structure. Peak splitting in the Bragg response, see encircled area in Fig. 6.10, is likely caused by the presence of transverse stresses, which troubles the determination of the true in-plane strains. Some thermal

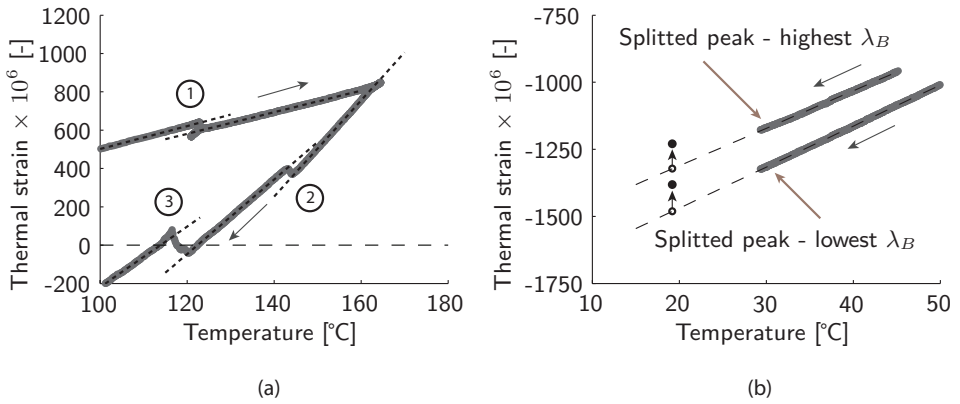


Figure 6.11: Zoom on (a) resin infusion and debonding and (b) demoulding.

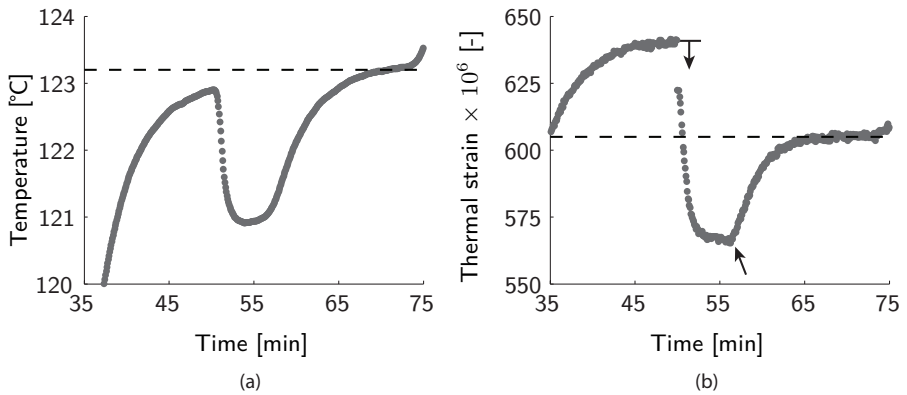


Figure 6.12: Infusion zone - (a) temperature and (b) thermal strain.

strains are still released in demoulding (see Fig. 6.11b). A plausible explanation is that the friction between the tooling and the laminate may have prohibited the full release of the accumulated strain related to tool-part interaction during debonding.

6.5.2 Intermezzo: traditional overestimation of the CTE and cooling strains

Table 6.2 lists the slopes that correspond to the zones zones *a-e* in Fig. 6.10 as estimations of the CTEs of the host structure. Traditionally, constant values for α_n and α_f are used (second column). As mentioned in Section 4.5.3, the term $(\alpha_n + \alpha_f)\Delta T$ is, however, replaced by the function $6.74 \cdot 10^{-9} \times (T - T_{\text{ref}})^2 + 6.12 \cdot 10^{-6} \times (T - T_{\text{ref}})$ [$\mu\epsilon/^\circ\text{C}$] in Eq. 5.1 (third column). In line with the observation for the GFR EP04908 laminate, the third-column values corresponding to the CTE of E-glass are, however, slightly higher than quoted in literature (fourth column). Nevertheless, an analysis based on constant properties of the optical fibre leads to a significant overestimate of the CTE of the host structure. That in zone *c*, in which the laminate is still bonded to both tooling plates, the slope is lower than the value given by literature can be explained by the fact that expansion is not entirely dominated by the aluminium tooling. The laminate resembles about one-quarter of the total thickness of the assembly. In combination with its mechanical properties and a lower CTE, a thermomechanical sum reveals that the measured slope has to be slightly lower than the CTE of the aluminium alloy.

Deriving the thermal strain as a function of temperature is an intermediate step in the analysis presented here. That is, the LoZS needs to be subtracted from the measured strain to obtain the process-induced and residual strains. Hence, this step neutralises the effect of the α_n and α_f values on these strains. On the contrary, cooling strains that are not referenced against the LoZS would be overestimated as well.

6.5.3 Results: monitoring of the thermal annealing

In Fig. 6.13, the experimental data from thermal annealing are overlaid onto the manufacturing data. The dash-dotted line represents the LoZS as obtained from analysing the GFR EP04908 laminate (see previous section). Clearly visible is its offset with the line describing the expansion of the preform. Stage **I-II** appears to be less pronounced due to a lower compaction pressure (Section 6.4). Apparently, the yarns are not straightened as much.

In the analysis, the figurative road ends now in a T-junction: either the expansion of non-fully straightened yarns can occur in a stress-free state or the LoZS for fully straightened yarns should be taken as the reference. Bringing the GFR RTM6

Table 6.2: Linear fitting to curves a-e in Fig. 6.10.

Zone	Temp. range [°C]	Slope (const. values) [$\mu\epsilon/^\circ\text{C}$]	Slope (lin. function) [$\mu\epsilon/^\circ\text{C}$]	Literature [$\mu\epsilon/^\circ\text{C}$]	Description of the host structure
a	95-115	7.35	5.98	4.7-5.4 [183]	Dry preform ¹
b	130-150	7.60	5.64	-	Impregnated preform ²
c	146-161	27.28	25.09	25.6 [191]	Laminate + two mould plates ³
d	122-142	21.31	19.48	-	Laminate + one mould plate
e	90-110	17.09	15.81	-	Laminate

¹ Effect of tooling is assumed negligible (see Section 6.4.2).

² Effect of tooling and resin is assumed negligible (see Section 6.4.2).

³ The CTE value quoted in literature is based on the average between RT and 300 °C for a different aluminium alloy of the 6xxx series, *i.e.* aluminium 6060.

laminate above the ultimate glass transition temperature is, however, discouraged for the reasons mentioned in Section 5.4.4. A test with a wrongly mixed batch of RTM6, discussed in Appendix B, gives some additional insight. As the ultimate glass transition temperature gets lower, thermal annealing becomes again effective for post-manufacturing evaluation. The LoZS appears to be above the line describing the thermal expansion of the impregnated preform. This may point towards the second option in which the LoZS of the fully straightened yarns should be the reference. The difference, indicated by 2 in Fig. B.2, seems to agree also with the drop in strain due to the filling. The latter may then be interpreted as a correcting measure. Finally, scatter can be a source as well. Hence, the answer remains inconclusive for this small series of tests.

In this study, it is decided to reference the process-induced strains against the apparent LoZS of the impregnated reinforcing fibres. The possible error:

$$\text{Error} = \frac{1}{(\alpha_c - \alpha_f)\Delta T / \Delta\epsilon - 1} \quad (6.1)$$

on the residual strain state at RT conditions would be small for high temperature applications. In this expression, α_c and α_f reflect the CTEs of the laminate and reinforcing fibres, respectively. The parameter $\Delta\epsilon$ represents the difference in strain between the apparent LoZS and the LoZS for the fully straightened reinforcing fibres. Assuming a difference in strain of about 50 $\mu\epsilon$, a temperature difference of about 140 °C and values for the CTEs as presented later on in Table 6.7, the error is less than 4%. The error increases, however, for a lower cure temperature.

Figure 6.14 shows the process-induced and residual strain states after correcting for

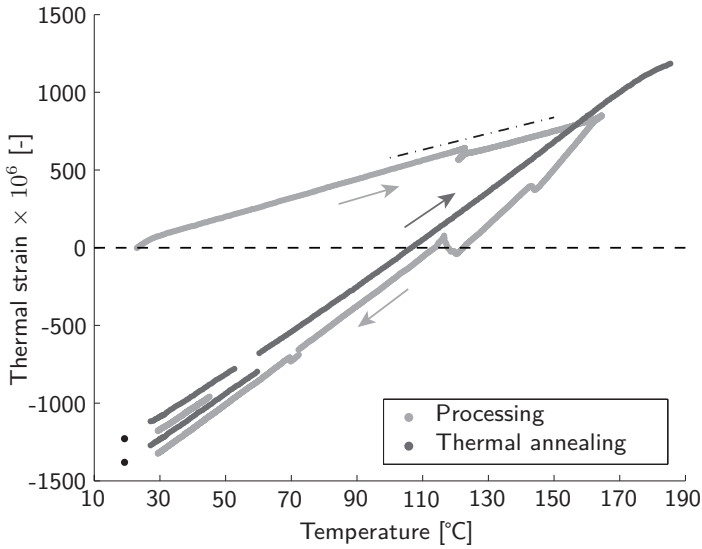


Figure 6.13: Process monitoring and thermal annealing for GFR RTM6 laminate cured at 160°C .

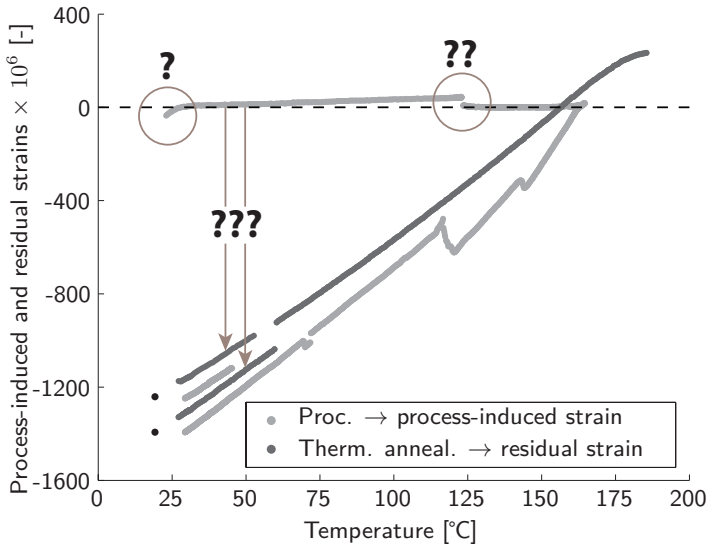


Figure 6.14: Estimated process-induced and residual strains of GFR RTM6 laminate cured at 160°C .

the apparent LoZS. Pre-cure tool-part interaction and filling have already been noted as interesting points (see question marks in the figure). Peak splitting of the Bragg response is the third interesting point, because it obscures the analysis on the process-induced and residual strains. To find the origin of these multiple peaks a closer look can be taken on the polarisation dependence of the reflected spectrum [128]. In absence of suitable equipment, the study performed in [150] is used to conclude that the peak splitting is most likely caused by strain-induced birefringence. In Appendix A, a comparative study is shown in which the cure behaviour of a GFR EP04908 laminate is analysed. Three FBG sensors in three different optical fibres are embedded in the laminate. Only the uncoated FBG sensor shows peak splitting while cooling down (Fig. A.4). As the lower Bragg wavelength of the two peaks agrees well with the the single-peak responses of the two coated FBG sensors, it may be a good indicator for the process-induced and residual strains. This is in accordance with the theoretical prediction in [148]. Though, Fig. 5.8 seems to contradict this statement. As literature is scarce on this subject, it is decided to perform only trend analysis for strains in GFR RTM6 laminates.

6.6 Effect of the cure regime

The latter of the two illustrative examples demonstrates that simply extrapolating the knowledge to a higher temperature application is not that straightforward. Several phenomena such as pre-cure tool-part interaction and resin arrival require further analysis. More experiments have to be performed in order to be more concise. To this end, the effect of the cure regime is investigated.

6.6.1 GFR EP04908: varying the cure temperature

As mentioned in Section 6.2.1, the manufacturing and thermal annealing of five GFR EP04908 laminates are online monitored. The subplots in Figure 6.15 present the combined results for the laminates that have not been discussed yet. For trend analysis, the effect of cure temperature is better highlighted by treating the results from manufacturing and thermal annealing separately. Figure 6.16 shows the process-induced strains, whereas Figs. 6.17 and 6.18, which are duplicates of Figs. 5.8 and 5.9, focus on the residual strains before and after thermal annealing. The slopes for the individual LoZSs, determined in the previous chapter, are listed in the second column of Table 6.3. All behave more or less similarly. The initial non-linear straining is followed by a stage in which the impregnated preforms expand in a stress-free state.

In all tests, cure-induced straining is not observed. The aluminium tooling governs the thermal contraction during cooling. Debonding occurs for the laminates cured at a higher temperature (see, for instance, the encircled data in the subplot of the 80 °C-cured laminate in Fig. 6.15). A distinct difference is observed for the laminates cured at 90 and 100 °C. Referring to Figure 6.16 and the second column in Table 6.6, the process-induced strain seems to reach a maximum regardless of the increase in cure temperature. At 92 °C the impregnated preforms expand no longer in a stress-free state, but follow the expansion of the tooling. The matrix becomes thus capable of transferring shear loads. In curing a neat resin system, the onset is attributed to the gelation [138]. That this behaviour occurs at 92 °C can be linked to the heating ramp of 1 °C/min (see Section 6.6.2). The tensile straining hardly affects the residual strain state in the reinforcing fibres, because the matrix remains in its gelled state during the isothermal dwelling. The reinforcing fibres return first to their original condition, *i.e.* the stress-free state, before further cooling introduces the compressive strains as the matrix vitrifies.

Estimated coefficients of thermal expansion

In Table 6.3 the estimated CTEs are listed for the different materials. For this particular fabric, the average CTE is slightly above the range of CTEs stated for E-glass: 4.7 - 5.4 $\mu\epsilon/^\circ\text{C}$ [183]. The average CTE of the combined system, *i.e.* tooling + laminate, is close to 23.4 $\mu\epsilon/^\circ\text{C}$, the CTE stated for this aluminium alloy¹⁰ [191]. The measured CTEs for the laminates are consistent except for the laminate cured at 100 °C. Speculations seem to point towards peak-splitting and side-lobe formation in the reflected spectrum as disturbing factors in the Bragg response (see Fig. 3.2). As literature values are unavailable and experimental testing is beyond the scope, a theoretical value is calculated by using approximate micromechanical relations and CLT [91, 193]. Table 6.4 lists the material properties used in the analysis. The fabric is approximated by a cross-ply. For the range of CTE values stated for E-glass, the theoretical CTE of the laminate ranges then between 14.75 and 15.33 $\mu\epsilon/^\circ\text{C}$. Knowing that the experimental average of the CTE of E-glass is close to the upper limit, the experimental values of the laminate's CTE before thermal cycling seems to agree well with the theoretical prediction. After thermal cycling an average drop of 5% is observed in the laminate's CTE. Ongoing curing does change the thermomechanical properties, but the trend is present in both the fully-cured and partially cured lami-

¹⁰An explanation for the underestimation is presented in Section 6.5.2.

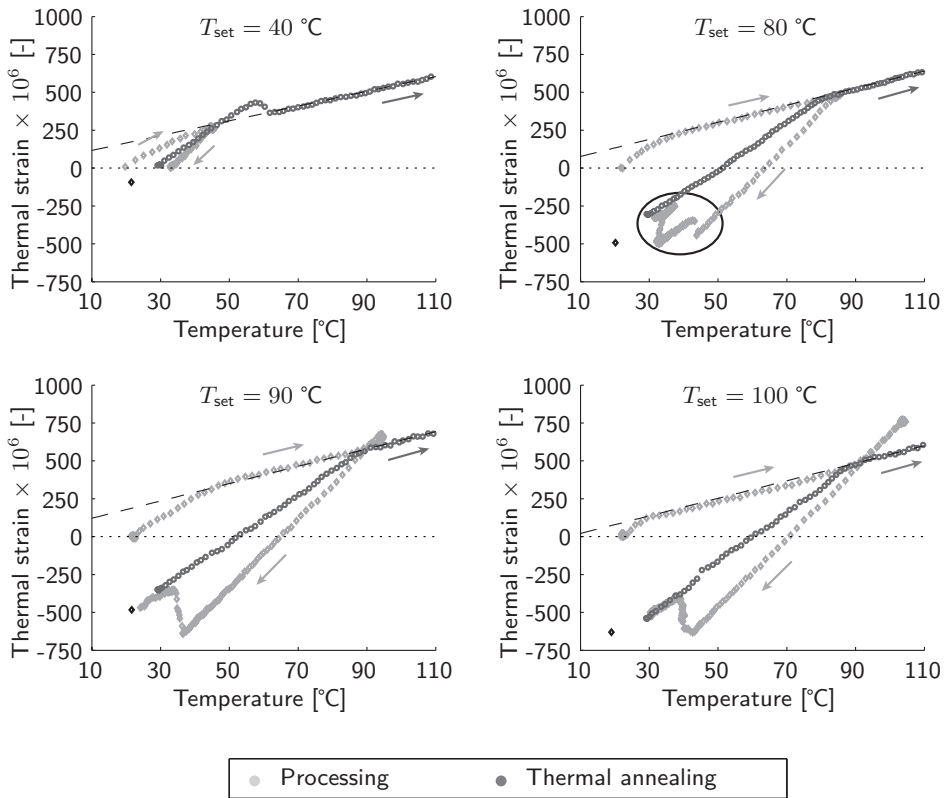


Figure 6.15: Overview of thermal strains for different curing conditions.

nates. It is believed that the glass-to-rubber transition may have affected the amount of microbending.

Cure temperature, stress-free temperature and onset of glass transition

The initial stress-free temperature, which is defined by the intersection of the LoZS and the line describing the thermal expansion of the laminate (point 4 in Fig. 6.7), is close to the actual cure temperature for the laminates cured below the ultimate glass transition temperature (Table 6.5). Curing at a higher temperature results in a stress-free temperature that approaches this glass transition temperature. It remains, however, unclear what causes the slight overestimation.

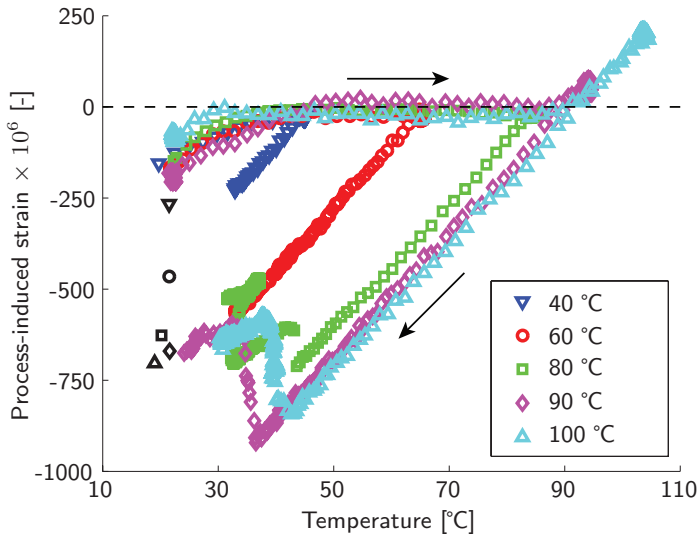


Figure 6.16: Process-induced strain in reinforcing fibres for GFR EP04908 laminates cured at different conditions. The black markers resemble the state after demoulding.

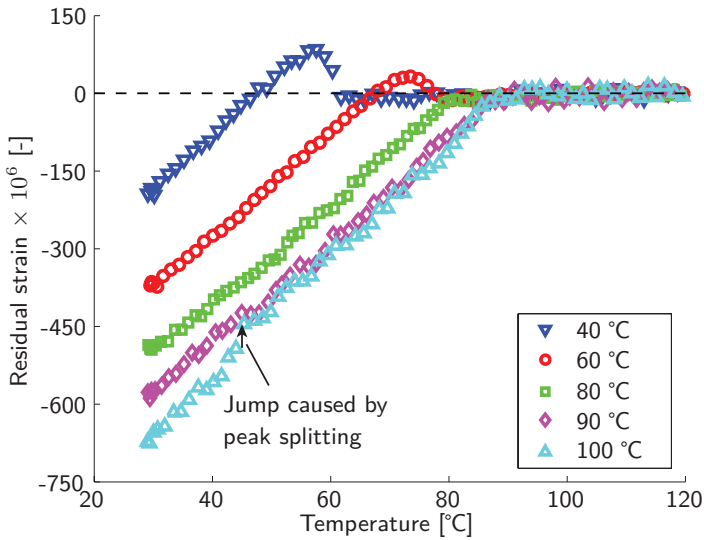


Figure 6.17: Residual strain in the reinforcing fibres of GFR EP04908 laminates (before thermal annealing).

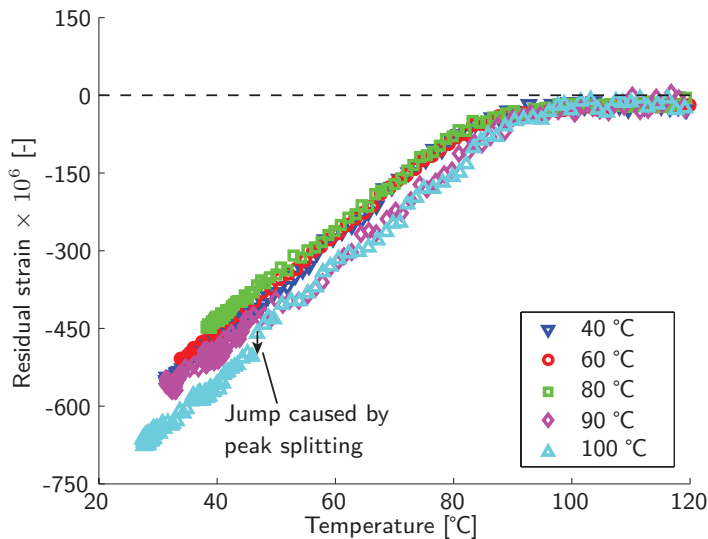


Figure 6.18: Residual strain in reinforcing fibres of GFR EP04908 laminates (after thermal annealing).

Measured strains

Table 6.6 lists the measured strains derived for RT conditions. In general, a higher cure temperature leads to more compressive process-induced strains. For the given heating rate, the maximum is defined by the gelation temperature of the matrix and is about $-1100 \mu\epsilon$. Tool-part interaction is accountable for about $480 \mu\epsilon$ (43%). These strains disappear through debonding and/or demoulding¹¹. The remaining is the residual strain in the reinforcing fibres. On an absolute scale, less residual strain is found in laminates for which the initial stress-free temperature is lower than the ultimate glass transition temperature. As shown in Fig. 6.18 thermal cycling restores this difference. In fact, the sum of the residual strain and the strain due to thermal cycling is found to be merely constant.

¹¹A similar percentage can be found by evaluating: $1 - (\alpha_{\text{laminat}} - \alpha_{\text{fabric}}) / (\alpha_{\text{tooling}} - \alpha_{\text{fabric}})$. Taking the average values for the CTEs as listed in Table 6.3 a value of 41% is derived.

Table 6.3: Estimated coefficients of thermal expansion.

Name	Coefficients of thermal expansion [$\mu\epsilon/^\circ\text{C}$]			
	<i>Fabric</i>	<i>Tooling</i> ¹	<i>Laminate (before)</i>	<i>Laminate (after)</i>
40 °C	4.88	22.03	15.45	14.73
60 °C	5.21	22.54	14.99	14.57
80 °C	5.63	22.44	15.12	14.48
90 °C	5.72	22.63	15.39	14.44
100 °C	5.80	22.80	16.44	15.21
<i>Average</i>	5.45	22.49	15.48	14.69

¹ In practice, these values represents a combined effect of tooling and laminate. The former dictates, however, the thermal contraction. Hence, the heading refers to tooling only.

Table 6.4: Material parameters used in theoretical predicting the CTE of the GFR EP04908 laminate.

Constituent	Modulus of elasticity	CTE	Poisson's ratio	Volume fraction
	[GPa]	[$\mu\epsilon/^\circ\text{C}$]	[-]	[-]
Reinforcing fibres	73 ¹	4.7-5.4 [183]	0.23 ¹	0.43 ²
Matrix	2.9 [163]	63.1 [194]	0.35 ¹	0.57 ²

¹ Generic values obtained from Ref. [91]. ² Obtained via matrix burn-off tests [195].

6.6.2 GFR RTM6: varying the cure temperature and the heating rate

Cure temperature

In Figs. 6.19 and 6.20 the combined results are shown for the laminates cured at 140 and 180 °C, respectively. The curves for the process-induced and residual strains are presented separately in Figs. 6.21 and 6.22, respectively. Both the heating and cooling paths of the thermal cycle are shown in the residual strain plot. All three laminates behave in a similar manner. The non-linear expansion in stage I-II and the drop in strain due to filling are present. Furthermore, debonding and peak-splitting in the Bragg response are observed as well. Similar to the GFR EP04908 laminates, more process-induced strains is found for higher cure temperature. In case of the 180 °C-cured laminate, the gelation moves the reinforcing fibres away from their apparent stress-free state before reaching the actual cure temperature. The lower peak temperature, see Fig. 6.23, is another confirmation that the cure has

Table 6.5: Cure, stress-free and glass transition temperatures/zones.

Name	Temperatures [°C]			
	<i>Cure</i>	<i>Initial stress-free</i>	<i>Onset of initial glass transition (Glass-rubber transition zone)</i>	<i>Ultimate glass transition</i>
40 °C	44.6	47.5	55.7 (6.7)	87.7
60 °C	65.0	67.9	69.7 (8.7)	88.7
80 °C	84.2	82.4	82.4 (-)	88.7
90 °C	94.1	89.7	89.7 (-)	96.4
100 °C	103.8	89.4	89.4 (-)	95.2

Table 6.6: Measured strains at room temperature conditions ($T = 25$ °C).

Name	Strains $\times 10^6$ [-]			
	<i>Process-induced</i>	<i>Tool-part interaction</i>	<i>Residual</i>	<i>Change due to thermal annealing</i>
40 °C	-363	-126	-237	-381
60 °C	-711	-292	-419	-176
80 °C	-1024	-480	-545	-19
90 °C	-1111	-486	-625	2
100 °C	-1142	-456	-685	25

already advanced significantly in the second heating stage.

In accordance with the analysis in Section 6.5, the CTEs for the different heating and cooling stages are approximated by linear fitting (Table 6.7). The estimates for the dry and impregnated preform, *i.e.* zones *a* and *b*, respectively, show some fluctuations. A source may be the changing conditions during filling (see Chapter 8). The initial stress-free temperature seems to be lower than the cure temperature (Table 6.8). The former is determined using the apparent LoZS, which may explain the difference compared to the GFR EP04908 laminates. The early gelation in the 180 °C-cured laminate may also have influenced the initial stress-free point. The drop in strain due to the filling is more or less constant and about $40 \mu\epsilon$ (Table 6.9). Thermal annealing affects the residual strain state due to additional curing. The largest increase in compressive residual strain is observed for the laminate cured at the lowest cure temperature. That the residual strain states of the laminates do not coincide after thermal annealing in such a way as observed for the GFR EP04908 laminates (Fig. 5.9) can be explained by the additional curing and the limit set for the maximum temperature.

Heating rate

For the 180 °C-cured laminate, the ramp of 1 °C/min causes the matrix to gelate before reaching the cure temperature. The gelation occurs at about 178 °C. Figure 6.24

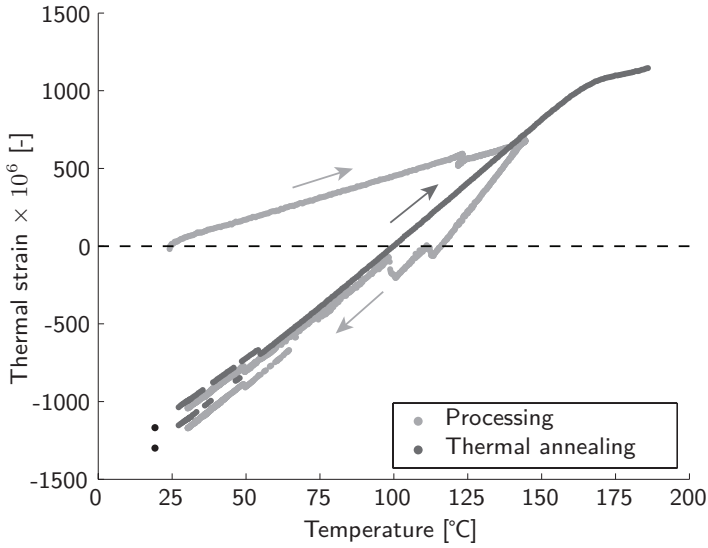


Figure 6.19: Manufacturing and thermal cycling of the 140 °C-cured GFR RTM6 laminate.

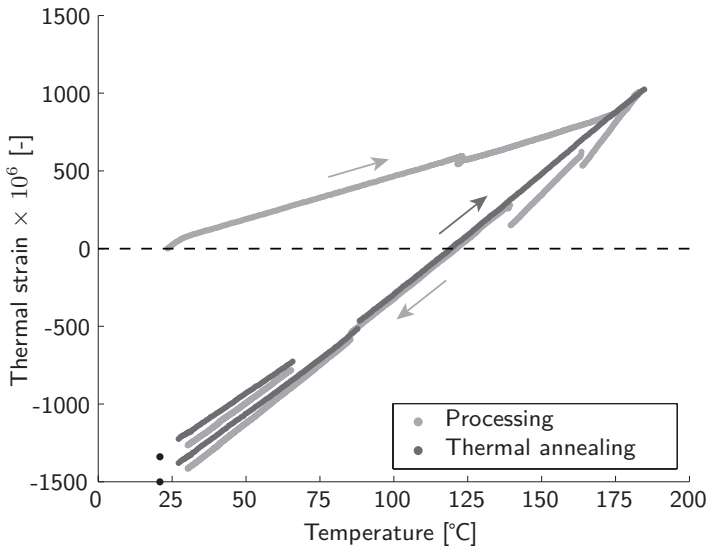


Figure 6.20: Manufacturing and thermal cycling of the 180 °C-cured GFR RTM6 laminate.

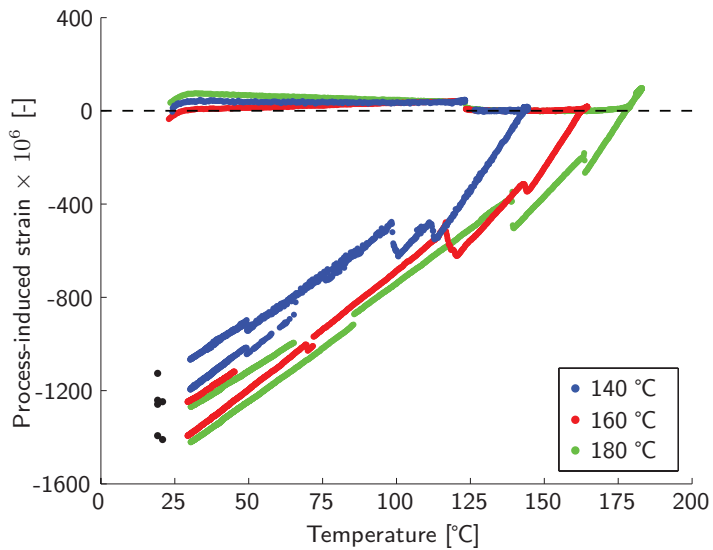


Figure 6.21: Process-induced strains in GFR RTM6 laminate cured at different temperatures.

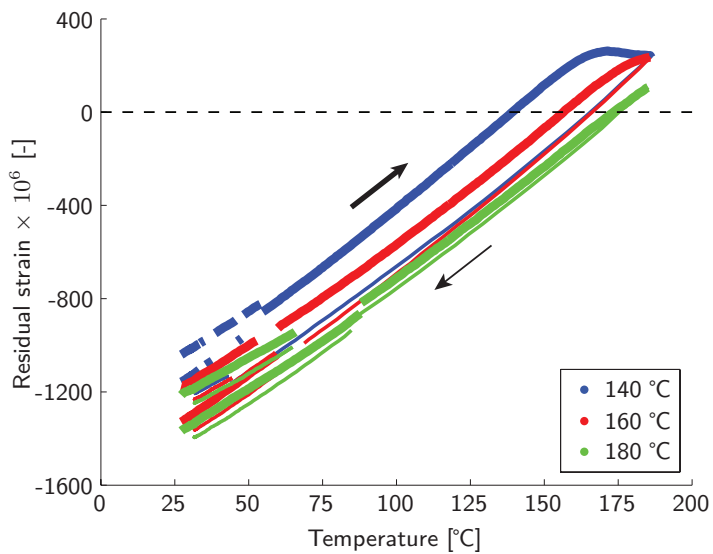


Figure 6.22: Residual strains in GFR RTM6 laminate cured at different temperatures.

illustrates the effect of changing the heating rate, *i.e.* 0.25 instead of 1 °C/*min*, on the formation of process-induced and residual strains in GFR RTM6 laminates cured

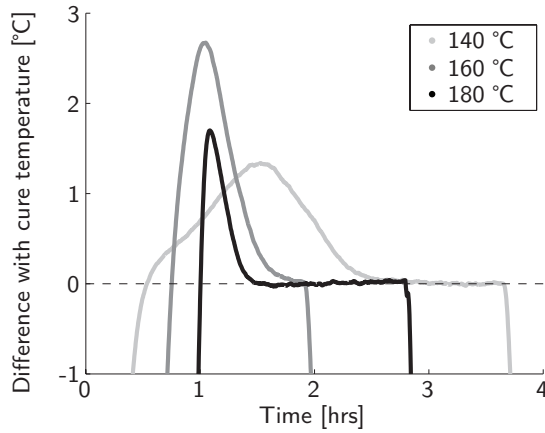


Figure 6.23: Thermal spiking in GFR RTM6 laminates cured at different temperatures. Time corresponded to the start of the second heating stage.

Table 6.7: Linear fitting to curves *a-e* (defined in Fig. 6.10) for laminates cured at different temperatures.

Name	Estimated CTE [$\mu\epsilon/^\circ\text{C}$] for temperature zone [$^\circ\text{C}$]				
	<i>a</i>	<i>b</i>	<i>c</i>	<i>d</i>	<i>e</i>
GFR RTM6 140 °C	(95-115)	(130-140)	(140-120)	(111-101)	(98-78)
	5.74	5.65	24.21	19.38	15.71
GFR RTM6 160 °C	(95-115)	(130-150)	(161-146)	(142-122)	(110-90)
	5.98	5.64	25.09	19.48	15.81
GFR RTM6 180 °C	(95-115)	(140-160)	(178-164)	(162-142)	(136-116)
	5.47	5.92	25.20	19.18	15.78

Table 6.8: Cure temperature and initial stress-free temperature.

Parameter	GFR RTM6 140 °C	GFR RTM6 160 °C	GFR RTM6 180 °C
Cure temperature [$^\circ\text{C}$]	143.1	161.8	181.3
Initial stress-free temperature ¹ [$^\circ\text{C}$]	139.2	156.5	173.4

¹ Based on the apparent LoZS.

at 160 °C. The lower ramp shifts the gelation point to 152 °C¹². A clear difference exists in the process-induced strains. On the contrary, the residual strain state seems

¹²When coupled to the cure kinetics model of RTM6, the associated degree of cure can be determined (see Chapter 10).

Table 6.9: Drop in strain due to resin arrival at FBG sensors and thermal cycling.

Name	Infusion temperature [°C]	Drop in process-induced strain at infusion [$\mu\epsilon$]	Averaged drop in residual strain due to thermal annealing [$\mu\epsilon$] ¹
GFR RTM6 140 °C	123	37	280 (4.6)
GFR RTM6 160 °C	123	42	111 (1.7)
GFR RTM6 180 °C	123	36	38 (1.2)

¹ Temperature range between 140 and 160 °C (stepsize of 5 °C).

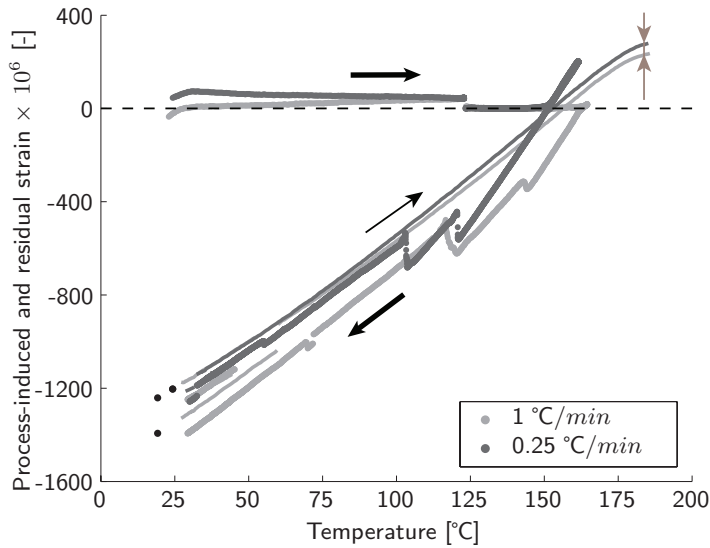


Figure 6.24: Effect of heating rate on the formation of strains.

hardly affected. Only a small offset is noted at higher temperatures. The difference in slopes of the individual LoZS may, however, have obscured this result (Table 6.10), but the difference is believed to remain marginal compared to the overall residual strain state (see Chapter 9).

6.7 Some other experimental results

6.7.1 Effect of fibre removal - cure-induced strain

The initial idea of removing adjacent reinforcing fibres perpendicular to the optical fibre was to reduce the effects of microbending and transverse stresses upon debulking

Table 6.10: Linear fitting to curves a-e (defined in Fig. 6.10) for laminates cured at different heating rates.

Name	Estimated CTE [$\mu\epsilon/^\circ\text{C}$] for temperature zone [$^\circ\text{C}$]				
	<i>a</i>	<i>b</i>	<i>c</i>	<i>d</i>	<i>e</i>
GFR RTM6 160 $^\circ\text{C}$ 1.0 $^\circ\text{C}/\text{min}$	(95-115)	(130-150)	(161-146)	(142-122)	(110-90)
	5.98	5.64	25.09	19.48	15.81
GFR RTM6 160 $^\circ\text{C}$ 0.25 $^\circ\text{C}/\text{min}$	(95-115)	(130-145)	(155-135)	(117-106)	(100-80)
	5.66	5.91	24.93	20.19	15.04

Table 6.11: Effect of fibre removal on the LoZS.

Name	Estimated CTE [$\mu\epsilon/^\circ\text{C}$]		Ratio [-]
	<i>Standard</i>	<i>With reinforcing fibres removed</i>	
	GFR EP04908 40 $^\circ\text{C}$	4.88	
GFR EP04908 60 $^\circ\text{C}$	5.21	5.01	0.96
GFR EP04908 80 $^\circ\text{C}$	5.63	5.43	0.96

(see Section 4.5.3). Some minor differences are observed during testing the 40, 60 and 80 $^\circ\text{C}$ -cured laminates. Figure 6.25 shows the change in process-induced strains during the isothermal dwell period of 16 hours for the GFR EP04908 laminate cured at 60 $^\circ\text{C}$. From about one hour onwards, the FBG sensor that is not constrained by the perpendicularly oriented reinforcing fibres measures a continuous decrease in strain (about 30 $\mu\epsilon$), whereas the other remains nearly constant. Cure shrinkage effects are thus more dominant for lower fibre volume fraction (and thus neat resin systems [98]). About 50 $\mu\epsilon$ of compressive strain is found in the 80 $^\circ\text{C}$ -cured laminate, whereas hardly any cure-induced strain is present in the 40 $^\circ\text{C}$ -cured laminate. Whether the cure-induced strain in the optical fibre can be translated on a one-to-one basis to the reinforcing fibres cannot be assessed. The impact on the residual strain state of the reinforcing fibres is minimal. In Table 6.11 the LoZSs are compared for the FBG sensors that are embedded in the three GFR EP04908 laminates cured at 40, 60 and 80 $^\circ\text{C}$ ¹³. Fibre removal seems to reduce the measured CTE by about 5 %. This may be explained by the absence of microbending in the optical fibre.

¹³Standard refers here to the situation in which reinforcing fibres are not removed.

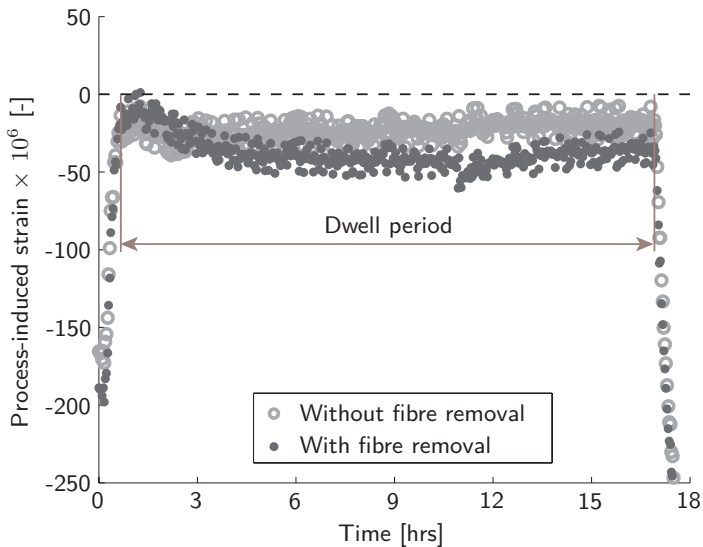


Figure 6.25: Cure-shrinkage-induced strain formed in dwell period.

6.7.2 Effect of tooling material: aluminium vs. steel

As long as the resin does not gelate before the cure temperature is reached, the tooling seems not to influence the process. Only after the cure, the tooling dictates the formation of process-induced strains. It is therefore expected that different tooling material have a minimal effect on the residual strain state in these flat laminates. As a proof, a GFR RTM6 laminate is manufactured using steel plates of similar thickness (Fig. 6.26). Apart from a different infusion temperature, all process settings are identical to the ones used in manufacturing the 160 °C-cured GFR RTM6 laminate between the aluminium tooling plates (Section 6.5). The process-induced strains are indeed different because of the lower CTE value of steel (see Tables 6.7 and 6.12). In case of the steel tooling, debonding does not occur in the cooling stage. Although different behaviour is observed during manufacturing, the residual strains are equal. Hence, the choice of tooling material seems not to matter in this particular case.

Table 6.12: Linear fitting to curves a-e (defined in Fig. 6.10) for steel tooling.

Name	Estimated CTE [$\mu\epsilon/^\circ\text{C}$] for temperature zone [$^\circ\text{C}$]				
	a	b	c		
			(80-100)	(120-140)	(160-140)
GFR RTM6 - steel	5.86	5.74	13.96	13.29	13.01

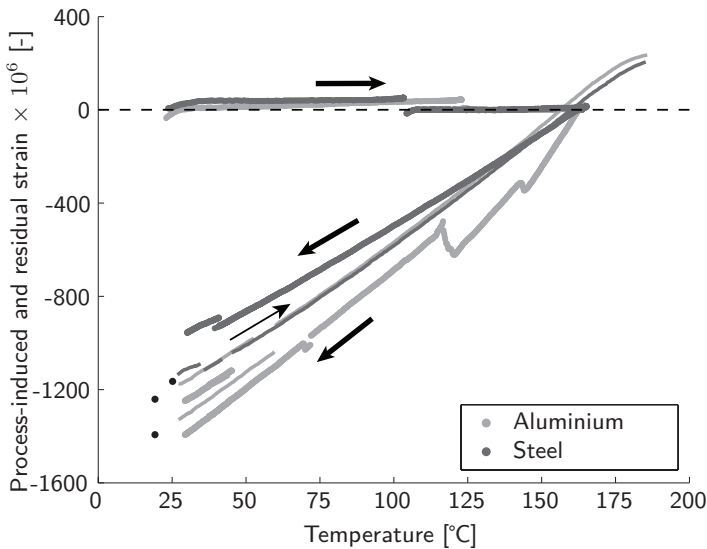


Figure 6.26: Effect of tooling material on the formation of process-induced and residual strains.

6.7.3 Reproducibility of VI experiments - curing at 160 °C

In Appendix C experimental results are shown for three GFR RTM6 laminates cured at 160 °C. The laminate labeled 'GFR RTM6 I' corresponds to the one extensively discussed in Section 6.5. The laminates are manufactured in chronological order. Two remarks can be made: (i) laminate 'GFR RTM6 II' is infused at a lower temperature, but this hardly affected the formation of process-induced strains and (ii) the moment of debonding differs between the laminates. The latter can be related to the degrading condition of the tooling surfaces. The influence on the residual strains is, however, negligible. A slightly larger increase in compressive strain is observed in the 'GFR RTM6 I' laminate after thermal annealing for yet unknown reasons. Overall, it is concluded that experimental results can be reproducible, but scatter may become significant at this level of analysing process-induced and residual strains.

6.8 Effectiveness of the LoZS-method

For EP04908, the actual LoZS is determined by thermal annealing. From the analysis it is deduced that both the tooling and matrix have a negligible influence during the heating stage of the manufacturing process (stage II-III in Fig. 6.4). Hence, the

preform is expanding in a near stress-free state. Results from online monitoring of the manufacturing of the GFR RTM6 laminates are then studied based on this observation. In total, the CTE of the reinforcing fibres has been experimentally determined 36 times in the text discussed before. Figure 6.27 gives an overview of the measured CTEs. In the same graph, the range of values stated in literature (4.7 - 5.4 $\mu\epsilon/^\circ\text{C}$ [183]) is also indicated. In determining the average, only the ninth data series is excluded because of a different optical fibre. The mean μ is 5.61 $\mu\epsilon/^\circ\text{C}$ with a standard deviation σ of 0.31 $\mu\epsilon/^\circ\text{C}$. The mean is slightly higher than the upper limit given by literature and may be caused by thermal effects. The standard deviation is about 5.5 %. A large influence on this standard deviation have the outliers that are mainly present in two data series. These series relate to the actual determination of the LoZS from thermal annealing. Hence, a closer look is definitely needed to identify the source(s) of these outliers. At this point, it is believed that the stiffness of the optical fibre or microbending may have influenced the measurement of the stress-free expansion of the reinforcing fibres. As the determination of the strain depends on the LoZS, the standard deviation affects this value as well. The range can be given by

$$1 \pm \frac{\sigma}{\alpha_H - \mu} \quad (6.2)$$

in which 1 corresponds to the mean. When the host structure is represented by the aluminium tooling (23.4 $\mu\epsilon/^\circ\text{C}$ at RT conditions [191]), a deviation of ± 1.7 % may occur. In case of a GFRP laminate with an in-plane CTE of about 15 $\mu\epsilon/^\circ\text{C}$, the deviation may increase to ± 3.3 %.

6.9 Conclusions

- The LoZS-method, *i.e.* the combination of online monitoring the manufacturing process and subsequent thermal annealing of a laminate, gives insight in both the formation of process-induced and residual strains and the limitations of FBG sensors in thin VI laminates. However, a follow-up study is still required to investigate in more depth this method.
- In ramping the impregnated preform to the desired cure temperature, it is found that the expansion of the reinforcing fibres occurs in a stress-free state. Two points require, however, further analysis (see also Chapters 7 and 8). The stress-free expansion is preceded by a non-linear thermal expansion stage (stage I-II in Fig. 6.4) for which the tooling is held responsible. The brief explanation given in this chapter contradicts, however, with literature, which states that resin flow

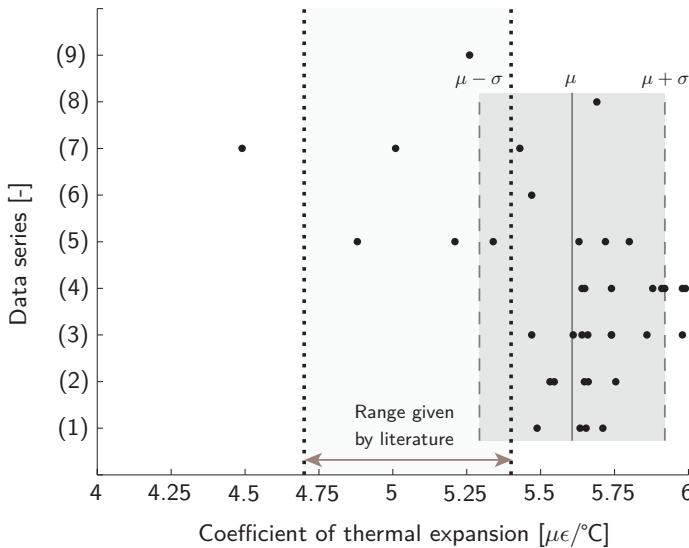


Figure 6.27: Measured CTEs for E-glass : (1) PM - dry fabric, coated FBG sensor (Table 4.5); (2) PM - dry fabric, uncoated FBG sensor (Table 4.5); (3) PM RTM6 - dry fabric (Tables 6.7, 6.10, 6.12, B.1, and C.1); (4) PM RTM6 - impregnated fabric (Tables 6.7, 6.10, 6.12, B.1, C.1); (5) MTA EP04908 (Tables 5.1); (6) PM EP04908 - impregnated fabric (in text of Section 6.4); (7) MTA EP04908 - Fibre removal (Table 6.11), (8) MTA EP04908 - uncoated FBG sensor (Table A.2); (9) MTA EP04908 - differently coated FBG sensor (Table A.2). PM = process monitoring and MTA = monitoring thermal annealing.

causes this phenomenon. The second point is the drop in strain due to non-isothermal filling at an elevated temperature. In a temporary conclusion this drop has been interpreted as a shift of the reference point. Consequently, the apparent LoZS is based on the thermal expansion of the impregnated preform.

- The study on the effect of the cure regime shows that the initial stress-free temperature agrees well with the cure temperature for GFR EP04908. The deviation for GFR RTM6 may be explained by the assumption on the LoZS. Compressive cure-induced strains are only observed when the matrix volume fraction is locally increased by fibre removal. The residual strain state in the reinforcing fibres increases proportional with the cure temperature. By changing the heating rate, it is shown that the tooling can affect the process-induced

strains in case the matrix gels before the cure temperature is reached. The reproducibility is illustrated by curing multiple GFR RTM6 laminates.

- The study on the effect of the cure regime is also used to gather data about the LoZS. Only in the case of EP04908, thermal annealing is used to determine directly the LoZS. Based on the rule that the impregnated preform expands in a stress-free state a apparent LoZS is constructed for the RTM6-based laminates. Based on 36 measurements, it can be concluded that the measured CTE of the reinforcing fibres is slightly higher than the upper limit given by literature. Neglecting its thermal dependence may be the source. As a consequence of the standard deviation of about 5.5 %, the process-induced (for aluminium tooling) and residual strains may deviate by 3.3 and 1.7 %, respectively. The outliers present in the data series related to thermal annealing, which severely impact the standard deviation, makes a comparison with an additional post-manufacturing technique unavoidable.

7

PRE-CURE TOOL-PART INTERACTION

7.1 Introduction

From the previous chapter, the definition of the LoZS in the reinforcing fibres shows to be helpful in determining the in-plane process-induced and residual strains. The impregnated preform appears to be mostly in a stress-free state. Only at the beginning the extrapolated LoZS does not coincide with the measured thermal strain (Fig. 7.1). From rational thinking, the experimental results in this temperature range have been ignored in determining the process-induced and residual strains. In [142] an explanation for the deviation is presented. In the experiments performed in that study, manually impregnated triaxial fabrics were laid up on a base plate and covered by a second plate. The assembly was then vacuum bagged and cured in an oven. Hence, this hand lay-up process has similarities with the VI process used here (Section 4.4.1). In the analysis, the compensated Bragg wavelength¹ of the embedded FBG sensors was plotted versus temperature. Identical behaviour was observed for the initial stage in ramping the impregnated preform to the cure temperature in [142]. It was stated that “resin flow phenomena occurring during the early stage of the cure reaction can generate a not negligible tensional state of stress within the matrix”, for which the motivation was based on fibre motion and loads [196].

But, why would a liquid resin be capable of straining the reinforcing fibres when a gelled resin fails in contributing to the effective thermal expansion of the laminate

¹The Bragg wavelength was compensated for thermal influences by an encapsulated FBG sensor (see Section 3.5).

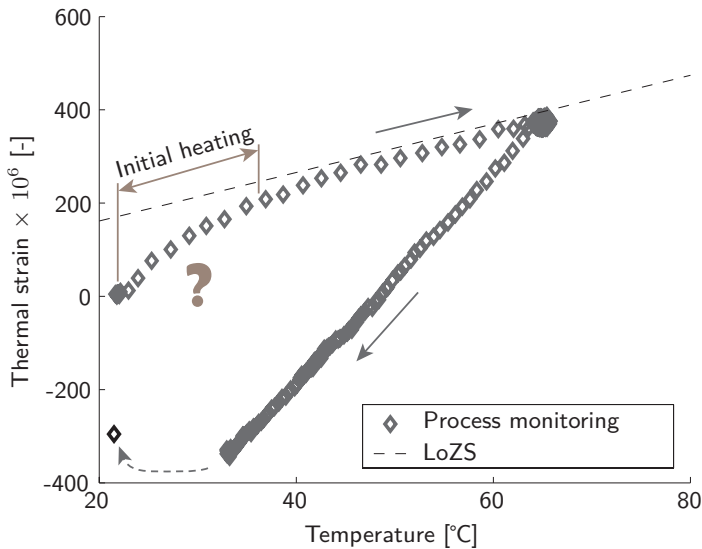


Figure 7.1: Difference between LoZS and measured thermal strain at the beginning of the heating segment (here: process monitoring of GFR EP04908 laminate cured at 60 °C (see also Fig. 6.4)).

(Chapter 5). The aim of this chapter is therefore to study this pre-cure behaviour experimentally.

7.2 Experimental setups and procedures

In order to investigate the role of the EP04908 resin system, two laminates, manufactured according to the procedure for VI (Section 4.4.1), are mutually compared for their heating segments². The first laminate is the one that was extensively discussed in Section 6.4. For the second laminate, the preform is compacted and, without filling, directly subjected to a comparable thermal cycle. That is, the heating rate and compaction pressure are similar, but the cure temperature is set higher (not relevant here). Whether the preform is impregnated or dry is the intentional difference.

As will be demonstrated, the resin flow has a negligible influence on this pre-cure phenomenon for the given compaction settings. Hence, the investigation continues by analysing different tooling concepts, tooling material (aluminium versus steel) and

²Unless it is explicitly stated in the text, the FBG sensor is embedded in the middle of the stack. Its orientation is parallel to the short edge of the preform.

the use of a top plate (testing with or without) for dry preforms. A regulator on the vacuum pump allows to investigate the influence of the compaction pressure as well. The experimental setup needs to be modified in order to study the effect of constraining the preform. To this end, the new assembly is positioned between the platen of the hot press. The latter generates a clamping force acting on two strips of the enlarged preform of $300 \text{ mm} \times 250 \text{ mm}$ (Fig. 7.2). To let the preform follow the thermal expansion of the tooling the applied pressure has to be sufficient to impede slipping. The Teflon sheets and the insulators, having the same stacking and material as the preform, are there to reduce the friction between the assembly and the platen and to limit the heat conduction, respectively.

The aforementioned experiments are carried out for 8-ply preforms only. Whether the same pre-cure behaviour would occur in the RTM process and for thicker preforms is, of course, also of interest. In anticipating Chapter 10 in which the monitoring of thick composite manufacturing is discussed, some of the results are used here for illustrative purposes. The results for the RTM process can be found in Chapter 9.

7.3 Effect of the resin flow

Figure 7.3 shows once more the thermal strain for the $60 \text{ }^\circ\text{C}$ -cured GFR EP04908 laminate. Results from testing the dry preform are shown as well. It should be clear that this simple experiment seems to refute the statement made in [142] for

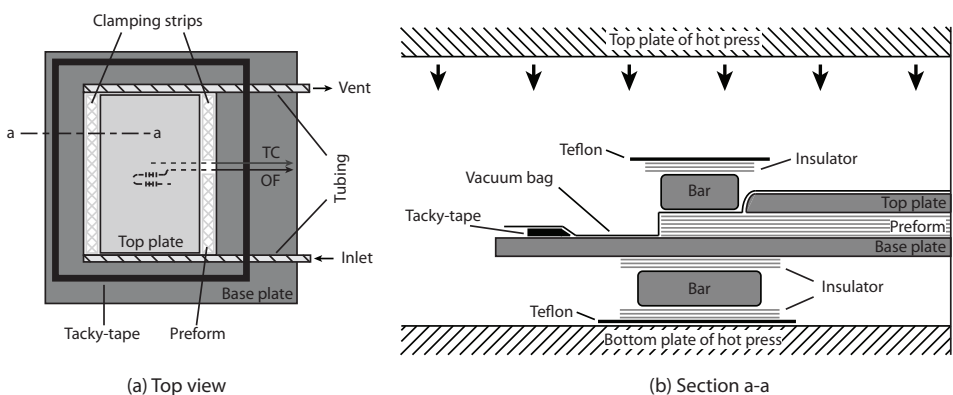


Figure 7.2: Details of the experimental setup in which preform is clamped by the platen of a hot press.

these process settings. Consequently, resin flow is eliminated as a factor that affects this particular pre-cure behaviour. Remarkably, lubrication by the matrix seems also negligible. Another explanation is needed for the occurrence of this phenomenon.

7.4 Alternative explanation: pre-cure tool-part interaction

In Chapter 6 it was shown that the cooling stage of the manufacturing cycle is dictated by the thermal contraction of the tooling (before debonding). The measured CTE in this stage approaches the one stated in literature for the tooling material. As a tangent line fitted to the first data points of the heating segment appears to have a similar slope, tool-part interaction may be the source here. Solid friction resists the relative motion, caused by a mismatch in thermal expansion between the tooling and the preform. Since lubrication is assumed absent, this type of friction would be classified as Coulomb friction. At a certain point, the shear force overcomes the threshold

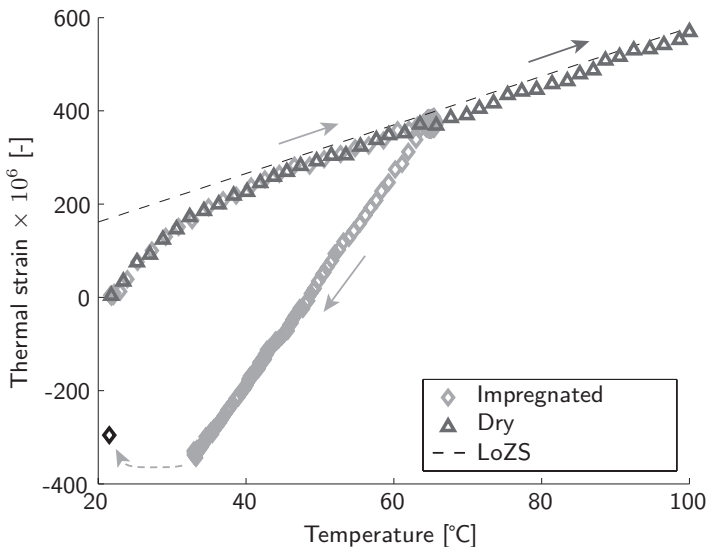


Figure 7.3: Comparison between impregnated (here: process monitoring of GFR EP04908 laminate cured at 60 $^{\circ}\text{C}$ (see Fig. 6.4)) and dry preforms.

and the preform starts sliding between the tooling³. The measured slope drops to the CTE of the impregnated preform. So far, it may sound logically. However, by the way it is explained here, an in-plane tensile strain state in the reinforcing fibres would be expected at the transition. From the analysis in Chapter 6, it was however learnt that the reinforcing fibres are in a stress-free state. A typical stick-slip behaviour, which would be expected for tensioned reinforcing fibres, is also not observed. Hence, the explanation is not yet satisfactory.

In analysing the compaction behaviour of preforms, a general observation is the decrease in thickness per layer with increasing compaction pressure. Main factors contributing to the compaction of fabrics are: yarn cross-section deformation, yarn flattening, yarn bending deformation, void/gap condensation, and nesting [171]. Micro-mechanical models for predicting this compaction behaviour rely on several assumptions. One of the assumptions is that elastic deformation of the fabric takes place in thickness direction only [171]. This can be visualised by supporting the undulated yarn by two rollers with lateral constraints in a simplified micro-mechanical model (Fig. 7.4)⁴. In practice, this may imply that friction at the interface of the tooling and preform prevents in-plane displacement. Compaction increases the proportion of non-undulated yarn in length. Since its original length is longer than the distance between the two wheel supports, the yarn (and thus the reinforcing fibres) has to be under 'compression' in the new situation, *i.e.* at the start of the cure cycle.

This explanation may also clarify why the FBG sensor is in tension after compaction (see Section 6.3). Before applying the compaction pressure, the part of the optical fibre with the FBG sensor forms a straight line between its two fixation points (Fig. 7.4). As the distance between the two supports does not change in compacting and a similar pressure distribution acts on the optical fibre, its path has to increase in order to accommodate with the adjacent fibres. Consequently, the optical fibre gets loaded in tension⁵.

This explanation seems, however, still not sufficient. Besides the Coulomb friction and the effect of yarn flattening on the strain state in the reinforcing fibres, it is speculated

³A better stress transfer at the ply/ply interface is assumed in comparison with the ply/tool interface due to intermingling of the fibres.

⁴In the figure, the contact pressure is uniformly distributed. This has however only illustrative purposes. Resultant compression forces and other distributions such as linear and sinusoidal appeared also in [171]. Regardless of the representation of the lateral forces, the compaction pressure would still flatten the yarn.

⁵This implies that the Bragg response to the compaction has to be interpreted carefully.

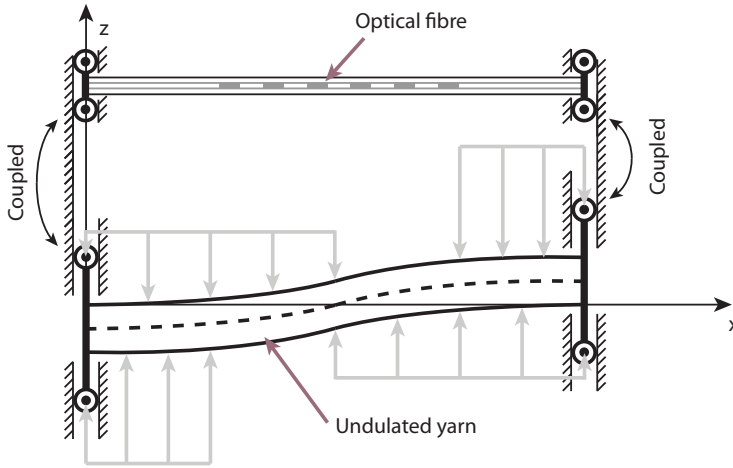


Figure 7.4: Simplified micro-mechanical model of a yarn under compaction (based on the uniform pressure distribution model presented by Chen *et al.* [171]). In the schematics, the optical fibre was also included.

that a third mechanism plays also a role. This mechanism deals with locking in the fabric. A fabric that is subjected to uniaxial tensile testing would first straighten its yarns in the direction of loading before they get actually stretched (Fig. 7.5) [197]. Thermal loading of the assembly in combination with Coulomb friction straightens the yarns. The moment that cross locking sets in a larger force is required to stretch the yarns.

In summary, the following is assumed to occur. Coulomb friction between tooling and preform is sufficient to let 'compressive' strains build up during compaction. These strains are then released via yarn straightening in subsequent thermal loading. This continues until a critical point is reached at which the friction force is no longer capable to straighten/stretch the yarns. The preform is then sliding between the tooling. Whether the yarns are fully locked cannot be assessed, but the reinforcing fibres are in a stress-free state for the given process settings. Based on this hypothesis, the increase in thermal strain cannot be fully accounted to the reinforcing fibres. The kinematics of the preform do not have to affect the strain state in the individual reinforcing fibres. The interpretation of the measured strain needs to be done carefully.

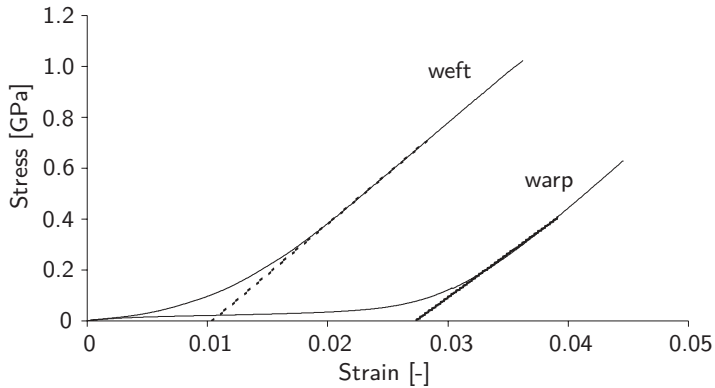


Figure 7.5: Example of uniaxial tensile experimental stress-strain curves for fabric strips in warp and weft directions [197].

7.5 Experimental underpinning

7.5.1 Cyclic behaviour

In Fig. 7.3, only the data from heating the dry preform is used. As tool-part interaction seems to dominate the first stage of the heating segment, it is of interest to include the cooling segment as well. In thermal contraction, the friction force has to flip direction. Figure 7.6 shows the complete thermal cycle for the dry preform. Tool-part interaction reoccurs and seems even reversible. In further analysis, the offset with the LoZS, indicated by the difference $\Delta\epsilon$ in Fig. 7.6, is used to define the change in thermal strain due to this pre-cure tool-part interaction.

7.5.2 Effect of tooling material

As the slope of the tangent line to the first data points of the heating segment is assumed to depend on the tooling material, exchanging the tooling material may prove again the existence of pre-cure tool-part interaction. Figure 7.7 shows two series of thermal loading a dry preform. The first series belongs to aluminium as tooling material and has been discussed before. In the other series⁶ the tooling plates are made of steel. The reference point in plotting the thermal strain is the intersection of the

⁶Please note that the thermal cycle has been shortened in the second series. The maximum temperature is lowered and the heating ramp is changed from 1 to 3 °C/min. Preliminary work points to a marginal influence on the difference $\Delta\epsilon$ for both parameters.

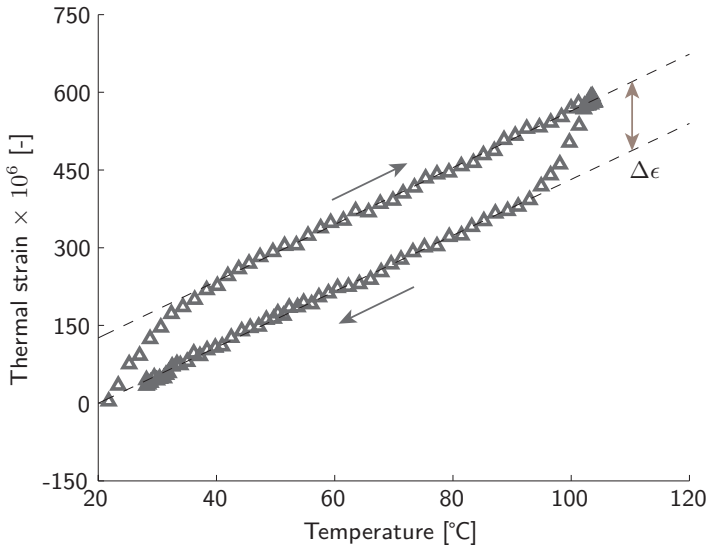


Figure 7.6: Full thermal cycle (heating & cooling) for dry preform.

aforementioned tangent line and the line parallel to the LoZS. The figure illustrates clearly the effect of the different tooling materials. The slope of the tangent line is about 50% for the steel tooling ($CTE_{steel} \approx 0.5 \times CTE_{alu}$). On the contrary, the choice of tooling material does hardly affect $\Delta\epsilon$.

Figure 7.8 shows the thermal loading the preform between the steel tooling plates once more. Four lines are added to this graph. The parallel dash-dotted lines **I-II** and **III-IV** represent the expansion behaviour dictated by the steel tooling, whereas the parallel dashed lines **II-III** and **IV-I** describe the thermal expansion of the preform. These four lines together form a bounding envelope (the path is given as **I-II-III-IV-I**). In comparison with the experimental data, it is observed that during heating, while the assembly expands, the preform has more difficulties in following the ideal path (**I-II-III**) than during cooling down in which the assembly contracts (**III-IV-I**). It is believed that the kinematics of the preform in combination with different heating and cooling rates⁷ influences this behaviour.

⁷The time interval is fixed between two consecutive data points in Fig. 7.8.

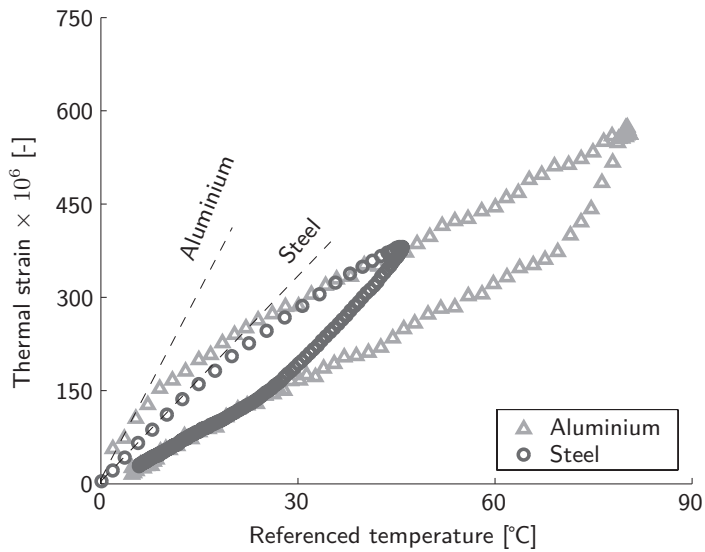


Figure 7.7: Effect of tooling material on the thermal strain.

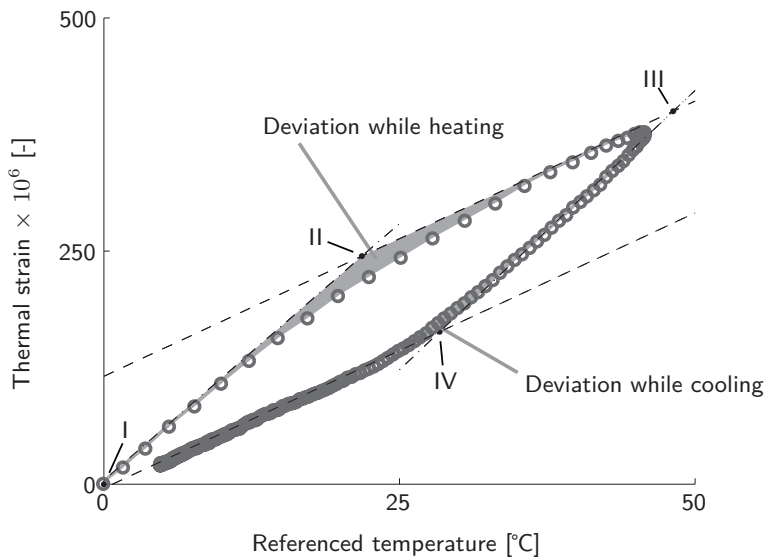


Figure 7.8: Deviation from ideal case.

7.5.3 Effect of tooling concept

In practice, many VI laminates are made on single-sided tooling only. The vacuum bag resembles then the other half of the closed-mould tooling. To extent the study on

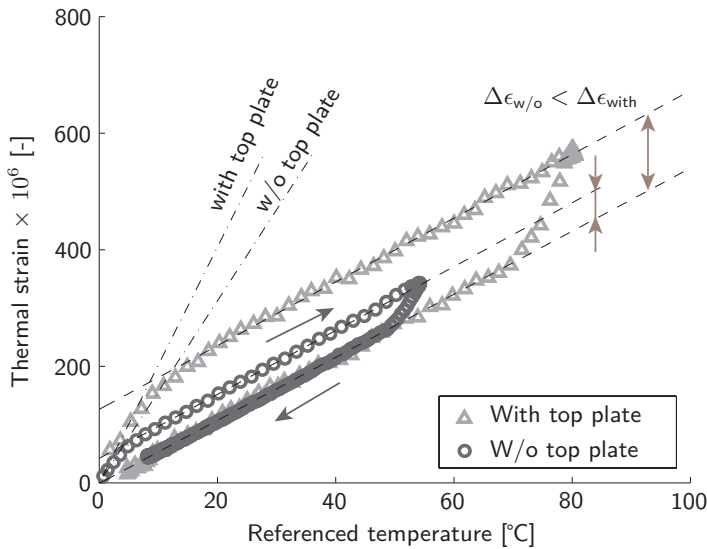


Figure 7.9: Difference between moulding with or without aluminium top plate.

pre-cure tool-part interaction, a series of experiments are therefore performed for the different tooling concepts. Two different cases, with and without (w/o) top plate, are compared. Results for the aluminium tooling are shown in Fig. 7.9. There is a clear difference between the tooling concepts. First of all, the slope of the tangent line decreases for single-sided tooling. Apparently, pre-cure tool-part interaction diminishes in plies further away from the tooling surface. As the plies on the other side of the preform are no longer constrained by the tooling, their expansion can be assumed to be closer to the CTE of E-glass^{8,9}. The strain difference gets about halved. As only one side of the preform is in touch with the aluminium tooling, the total friction force has to drop by a factor two. Sliding of the preform must then occur in an earlier stage. This may imply that the yarns are not as much straightened for the single-sided tooling concept. Whether the line describing the thermal expansion of the preform needs to be interpreted as an apparent LoZS remains an open question for the moment.

⁸The contribution of the vacuum bag is neglected.

⁹In cooling the cured GFR RTM6 laminates, a similar behaviour was noted. Between the first and second debonding, the measured slope lies between the CTEs of the laminate and tooling material (see, for instance, Table 6.2).

7.5.4 Effect of compaction pressure

So far, the compaction pressure has been kept constant at about 500 *mbar*. By assuming Coulomb friction in the hypothesis, it is expected that a change of the normal force, *i.e.* the compaction pressure, would also affect the pre-cure tool-part interaction. To this end, the influence of the compaction pressure is evaluated for four different cases, which are based on the two tooling materials and two concepts. In each case, thermal loading is performed for five different values, randomised beforehand, of the compaction pressure. The compaction pressure is relieved and reapplied three times between consecutive cycles. The thermal cycle is similar to the shortened one, *i.e.* 3 °C/*min* between RT and 80 °C. As output, the difference $\Delta\epsilon$ is determined. In Fig. 7.10 the obtained strain differences are plotted as a function of the absolute pressure. The results for the linear regression are listed in Table 7.1. Four points are observed: (i) an increase in compaction pressure results in a higher strain difference, (ii) the strain difference becomes minimal in the absence of compaction, (iii) the single-sided tooling concept let the strain difference halve, and (iv) there is an offset between cases with similar tooling concepts but having different tooling materials. The first three points can be clarified by the assumption of Coulomb friction. The offset cannot be explained immediately. From preliminary work it was found that consecutive thermal cycling without intermediate releasing and reapplying of compaction pressure would result in a behaviour as shown in Fig. 7.11. The true strain difference may become underestimated in the second cycle. Recovery seems to occur towards the end of the heating segment for yet unknown reasons (see encircled data). Releasing and reapplying the vacuum may not have eliminated completely this unwanted behaviour. Hence, the offset may therefore be smaller or even non-existent in practice. On the contrary, when the offset would exist, the explanation may be found in the difference in the coefficient of friction, which depends on the materials of the two bodies and on the cleanliness of the contacting surfaces [198]. In a second series of experiments, in which only the case 'Aluminium - with' is reproduced, the strain differences are determined at different temperatures once more (Fig. 7.12). Overall, the results agree well with the first series, but fluctuations can be significant.

7.5.5 Effect of clamping

In assess the influence of clamping, two cases are investigated: the press is either closed and thus constraining the preform or the press is left open and the preform

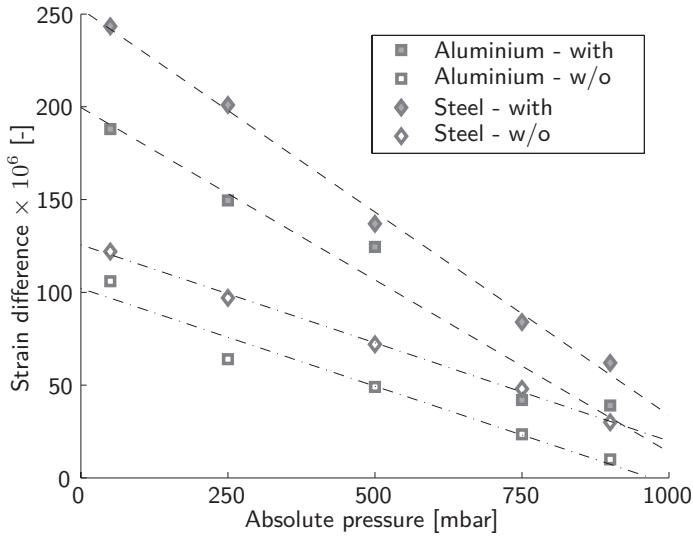


Figure 7.10: Effect of compaction pressure on $\Delta\epsilon$ (dashed and dash-dotted lines are linear fits to the data of experiments carried out with and without top plate, respectively).

Table 7.1: Results of linear regression on experimental data of Fig. 7.10.

Mould system	Linear model
Aluminium with top plate	$\Delta\epsilon = -0.186 \times p + 200$
Aluminium without top plate	$\Delta\epsilon = -0.105 \times p + 102$
Steel with top plate	$\Delta\epsilon = -0.219 \times p + 253$
Steel without top plate	$\Delta\epsilon = -0.106 \times p + 126$

is 'free' to move (the nominal case) for two different compaction pressures¹⁰. Figure 7.13 shows the results for testing at a compaction pressure of 500 *mbar*. Results from the nominal case are found in good agreement with testing in an oven (Fig. 7.6). While heating up the constrained preform, the preform follows the expansion of the aluminium tooling for a longer time. At 60 °C (referenced temperature of 35 °C) the applied force is released by opening the press¹¹. The preform reacts immediately by

¹⁰While testing the clamping condition, it was noted that controlling the applied pressure is difficult due to the low accuracy of the hydraulics of the JOOS press at low forces in combination with the small contact area. Hence, only the cases 'on' and 'off' are investigated.

¹¹The Bragg response is manually corrected for the effect of applying/releasing of the clamping force from the hot press.

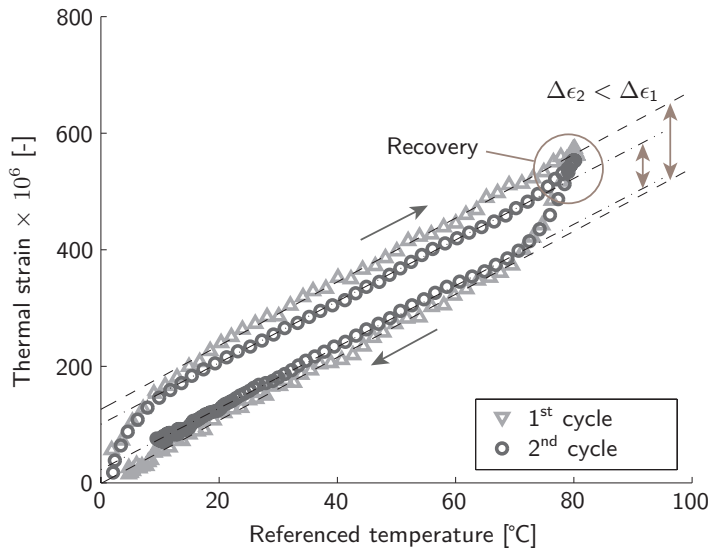


Figure 7.11: Consecutive thermal cycling of dry preform between aluminium tooling.

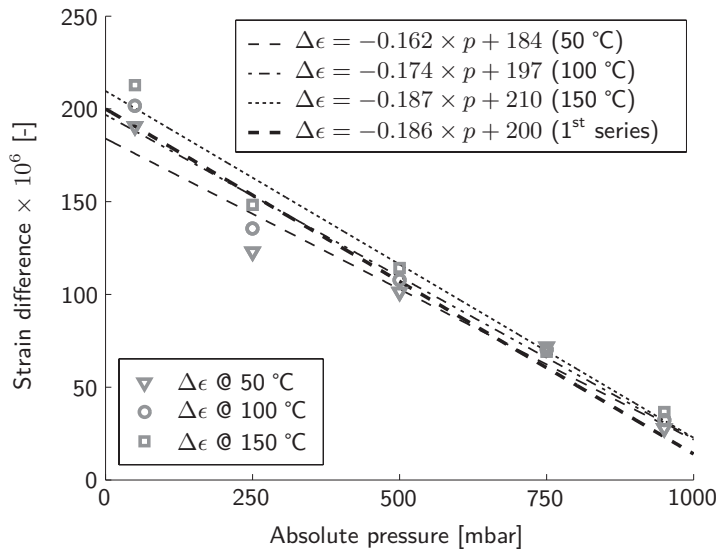


Figure 7.12: Case 'Aluminium - with' reproduced - Strain differences measured at different temperatures.

dropping the accumulated strain. In further heating, the unconstrained preform behaves similar to the nominal case. Exactly the same trend is observed for the preform

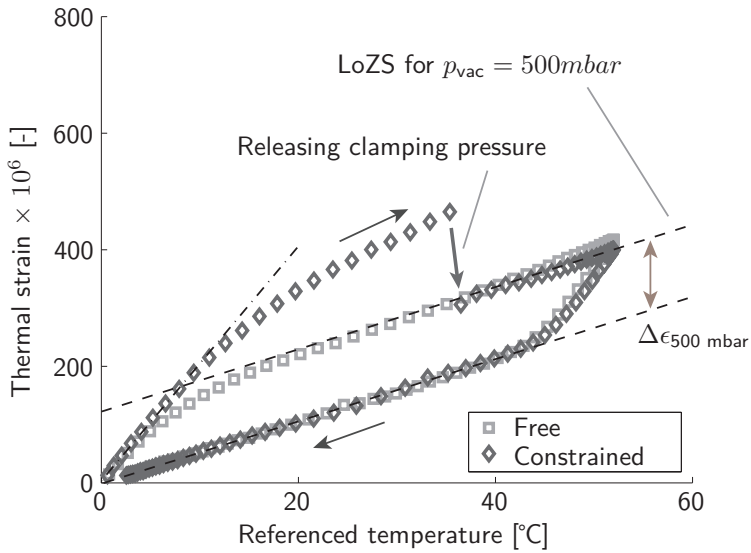


Figure 7.13: Effect of constraining the sides of the preform ($p_{vac} = 500\text{mbar}$).

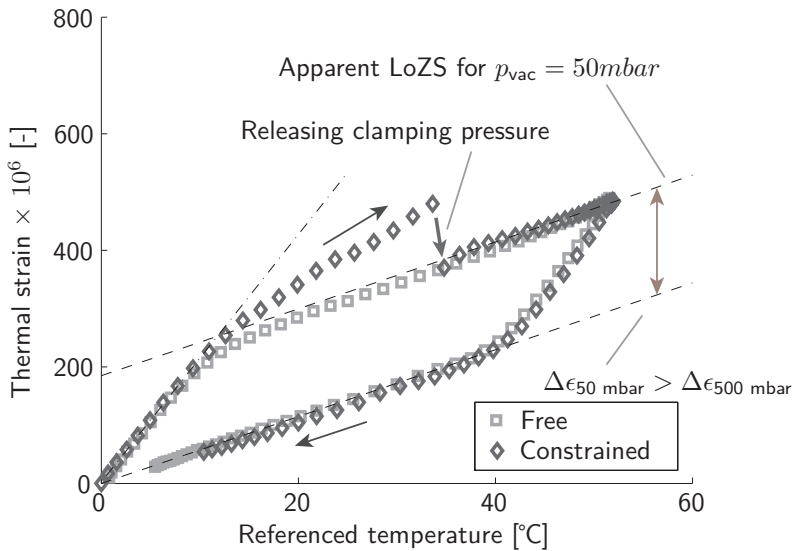


Figure 7.14: Effect of constraining the sides of the preform ($p_{vac} = 50\text{mbar}$).

compacted at an absolute pressure of 50 mbar (Fig. 7.14).

In Fig. 7.10 it was shown that the strain difference, $\Delta\epsilon$, increased with increasing

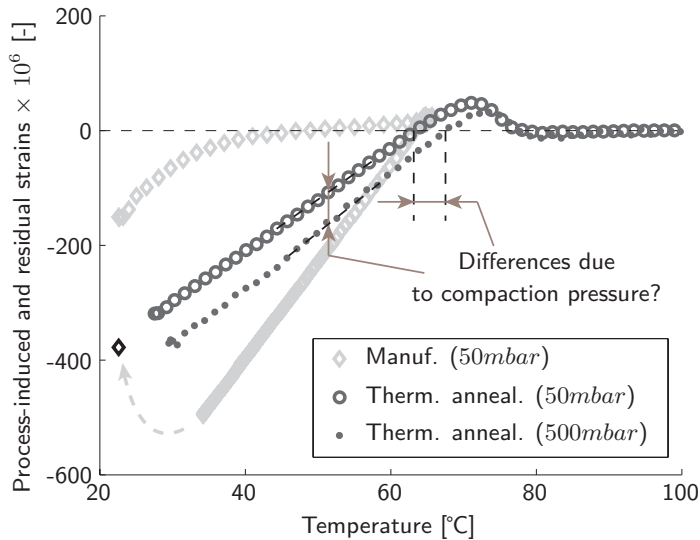


Figure 7.15: Influence of the compaction pressure on the strain formation.

compaction pressure. For an absolute pressure of 50 *mbar*, this strain difference is about 100 $\mu\epsilon$ higher than the standard case of compacting at 500 *mbar*. It is thus of interest to investigate the consequences of curing at different compaction pressures. One of the GFR EP04908 laminates is therefore cured at 60 °C, while keeping the compaction pressure unchanged after filling (Fig. 7.15). At a first glance, compacting at a higher pressure seems to have lowered both the compressive residual strain in the reinforcing fibres and the initial stress-free temperature¹². The former can perhaps be explained by a higher fibre volume content due to a higher compaction pressure, which decreases the effective CTE of the laminate. However, the slopes of the LoZS differ by about 0.19 $\mu\epsilon/^\circ\text{C}$ (5.40 versus 5.21 $\mu\epsilon/^\circ\text{C}$). The difference in residual strain may therefore be overestimated. Furthermore, the pre-cure tool-part interaction is not much different (see for comparison Fig. 6.6). Lubrication may have played a role at the higher compaction pressure, but cannot be proven in this study on dry preforms. That the pre-cure tool-part interaction may even show different behaviour at an equal compaction pressure should be considered as well (see, for instance, Fig. 6.16). A conclusive answer to the influence of compacting on the strain formation is not brought by this single experiment.

¹²The other set of data is from thermal annealing the 60 °C-cured laminate that is compacted at 500 *mbar* (see Fig. 6.6 and the discussion in Section 6.4).

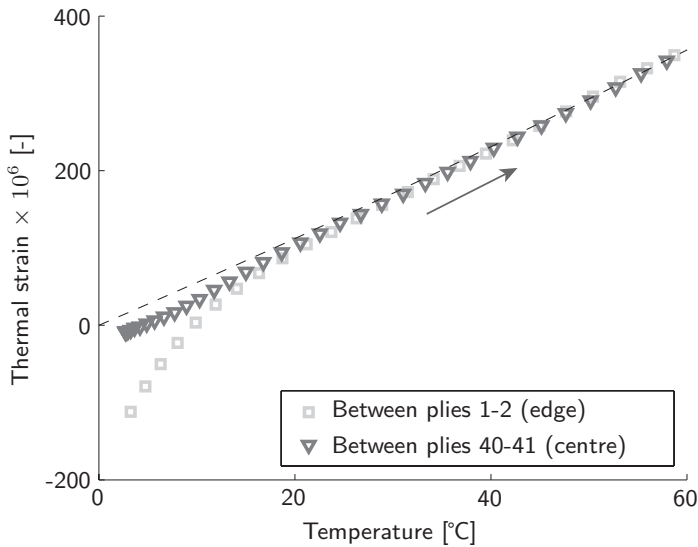


Figure 7.16: Heating up a 20-mm dry preform consisting of 80 plies at a compaction pressure of 50 mbar. The curves are shifted for comparative reasons

7.6 Pre-cure tool-part interaction in thicker preforms

In Fig. 7.16, results are shown for an 80-ply preform in which two optical fibres with a single FBG sensor are embedded. In this example, aluminium tooling is used. As these results belong to an experiment in which the filling is done upon reaching the prescribed tool temperature of 120 °C, the heating segment of the dry preform can only be presented. The FBG sensor closest to the tooling records a similar behaviour as in thin preforms on a single-sided tooling (see Fig. 7.10). Pre-cure tool-part interaction has a limited through-thickness range. It seems plausible that the yarns may not straighten as much in thicker preforms¹³.

7.7 Discussion and concluding remarks

The LoZS-method derives the process-induced and residual strains in the reinforcing fibres by thermal annealing. In the (T, ϵ) -plot, this assumption leads to a difference between the LoZS and the measured strain in the first segment of the heating stage. In Chapter 6 it was shown that the compaction pressure plays a role. In analysing

¹³Similar results are reported in Chapter 10.

the GFR RTM6 laminates in that chapter, an ‘apparent’ LoZSs had to be considered. Despite the small error (about 3% on the residual strain), the aim of this chapter was to study this pre-cure behaviour in more detail, because a better understanding would eventually help in reconstructing the LoZS from online process monitoring only.

In literature, this particular pre-cure behaviour is addressed to resin flow [142]. However, results from thermal loading dry preforms weaken this claim. A hypothesis is therefore formed that attributes this pre-cure behaviour to tool-part interaction in combination with flattening and subsequent straightening/stretching of the yarns in the fabric. An experimental study on dry preforms for both thin and thick laminates points towards this direction by revealing that:

- pre-cure tool-part interaction reverses in cooling. This results in a strain offset between the thermal expansion and contraction of the dry preform. This offset can be characterised by a single number ($\Delta\epsilon$ in the (T, ϵ) -plot (Fig. 7.6)).
- the CTE of the tooling material dictates the slope of the line tangent to the first data points belonging to this pre-cure tool-part interaction in the (T, ϵ) -plot. Its slope is close to the CTE of the tooling material in case of double-sided tooling and thin preforms. Analogous to a single-side bonded laminate, removal of the top plate reduces the slope.
- the tooling concept affects the strain offset. In the single-sided tooling concept the total amount of friction forces is halved compared to the double-sided tooling concept. Consequently, the strain offset is also reduced by a factor two.
- the difference $\Delta\epsilon$ varies linearly with the compaction pressure. In general, the higher the compaction pressure the bigger is the strain offset.
- constrained reinforcing fibres are brought into a tensile strain state by stretching them. Upon removing the clamping forces, these strains are released and the preform continues expanding as if it is unconstrained, *i.e.* the strain offset is dictated by the compaction pressure.
- the influence of the tooling on the thermal expansion behaviour of the plies in the middle of the stack diminishes with increasing preform thickness. At the surface, a similar behaviour is observed compared to single-sided tooling.

Hence, the definition of the difference $\Delta\epsilon$ is helpful in analysing the cure cycle from a theoretical perspective. In practice, its use may still be limited for the prediction of the LoZS in laminates. First of all, this difference can only be determined when the cooling segment is included in the thermal cycle. In fact, the starting point

for curing may not always be on the line that describes the thermal contraction of the dry preform in the (T, ϵ) -plot due to unrecorded temperature fluctuations in the preparation phase (Fig. 6.16). Theoretically, a constant $\Delta\epsilon$ is expected based on the constant compaction pressure (see Table 7.1). In case of aluminium tooling, an unrecorded change of only 1 °C would cause a shift of about 20-25 $\mu\epsilon$.

Different compaction pressures affect also the difference $\Delta\epsilon$. The example with the wrong resin mixture in the previous chapter seems to indicate that there is only one LoZS for this type of fabric regardless of the compaction pressure. Furthermore, the curves of the thermal strain in case of clamping looks similar to the unconstrained ones for the pre-cure tool-part interaction zone. Only the difference $\Delta\epsilon$ is larger. Hence, estimating the amount of tensile strain in the reinforcing fibres is difficult. This implies that localising the LoZS is still considered troublesome when having only data from online process monitoring at one's disposal.

In general, it can be concluded that a reasonable insight is gained in what causes this pre-cure behaviour, but that a fundamental study, including impregnated preforms, is still required in order to clarify some of the observations.

8

RESIN FLOW: A DISTURBING FACTOR

8.1 Introduction

That resin arrival can be detected by the FBG sensor was already discussed in Section 3.6.1. Through thermally induced and strain-induced effects the resin flow can be mapped [99, 154]. The source of the latter is, however, not investigated in these studies. In Chapter 6, it was noted that (non-)isothermal mould filling affects the Bragg response. Figure A.3 shows three different normalised changes in Bragg wavelength to the filling stage of a GFR EP04908 laminate. Using Eq. 3.2 and the assumption of isothermal conditions, this change can be converted in a theoretical strain value, e.g. the FBG sensor closest to the inlet shows a drop in strain of about $65 \mu\epsilon$. The process-induced and residual strains seems, however, unaffected (Figs. A.4 and A.5). For RTM6, the non-isothermal filling creates an offset between the lines describing the thermal expansion of the dry and impregnated preform in the (T, ϵ) -plots (Fig. 6.10). Since the filling takes place at an elevated temperature, the drop complicates the determination of process-induced and residual strains.

Finding a proper explanation on a more fundamental level for the change in Bragg response due to (non-)isothermal mould filling is thus the objective of this chapter. As such, the influence of resin flow on the formation of process-induced and residual strains in the reinforcing fibres can be criticised. To this end, the Bragg response is compared with the output from digital image correlation for measuring the preform thickness. This chapter focuses only on thin VI laminates. The consequences of mould filling in the RTM process are left for the next chapter. The discussion about

the effect on FBG sensors embedded in thicker preforms is reserved for Chapter 10.

8.2 Motivation for digital image correlation

The filling stage can be considered a complex process due to the interaction of different physical phenomena. One of the consequences of this interaction is the local variation in part thickness. As the fluid pressure reduces the compaction stress on the preform, the preform reacts by elastic deformation in through-thickness direction [199]. Somehow, the embedded optical fibre has to follow this displacement. Measuring simultaneously the change in preform thickness may therefore clarify some of the ambiguities in the response of FBG sensors to mould filling.

Several measurement systems are available to measure this displacement. In [200] the change in preform thickness is recorded by multiple dial gauges along the flow path. Others monitored the variation in thickness using laser transducers and LVDTs [189, 201]. For this study, it is decided to use a non-contact full-field measurement technique; digital image correlation¹. This choice does not only confine the interference with the FBG sensing technique to a minimum but enlarges also the area of interest². This technique was demonstrated before for full-field monitoring of the resin flow and laminate properties in [199, 203].

Digital image correlation tracks object deformation by tracking deformation of a random speckle pattern in an image. In Fig. 8.1 the principle of the two-dimensional technique is highlighted by pixelated source and target images. A correlation function is used to find the new location of the subset. To perceive the environment, in this case the preform, two imaging sensors are required. Stereo-triangulation is the process that recovers the 3D environment. Although calibration is needed to establish a common coordinate system, the measuring technique itself is fast and has an excellent accuracy and high spatial resolutions [204].

¹In this study, a commercially available digital image correlation system is used; LIMESS Vic3D (supplied by LIMESS Messtechnik & Software GmbH, Germany [202]).

²Instead of a discrete set of measuring points, the change in preform thickness is measured in a full-field modus.

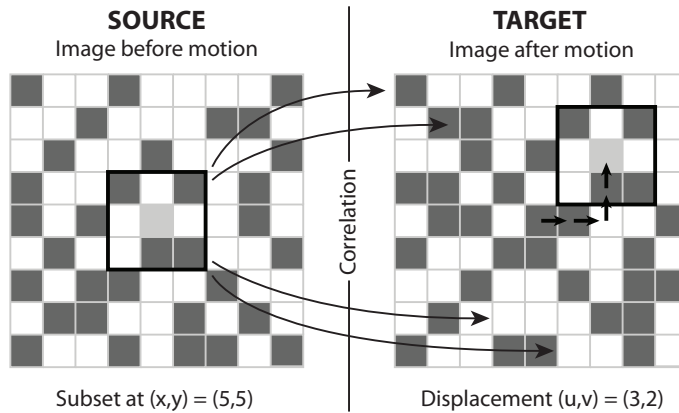


Figure 8.1: Schematical overview of digital image correlation.

8.3 Experimental

The procedure described in Section 4.4.1 is followed to build up the VI assembly. To provide a direct vision on the resin flow by the cameras, the top plate is left out. The speckle pattern is applied manually in a predefined grid drawn on the vacuum bag³. Figure 8.2 shows the setup and an enlargement of the measuring grid completed with the speckle pattern.

Thermocouples and FBG sensors are embedded in the middle of the preform according to the procedure given in Section 4.5.3. Although the filling is done with EP04908 at RT conditions, the thermocouples are used to double-check the local temperature. After installation, the data recording systems are started⁴. Every ten seconds a pair of images is captured by the camera system. Data are recorded during the three segments of the filling stage: (1) resin infusion at an absolute pressure level of 50 *mbar* on the vent line, (2) flushing at an absolute pressure of 500 *mbar*, and (3) stabilisation of the impregnated preform after closing the inlet.

³Spraying a stochastic pattern has been unsuccessful due to correlation problems for the software. Light scatter by the uneven surface of the vacuum bag resulted in darker areas in the images such that the sprayed dots became unrecognisable. A white undercoat may resolve this problem, but is not considered here.

⁴Data synchronisation is manually done afterwards.

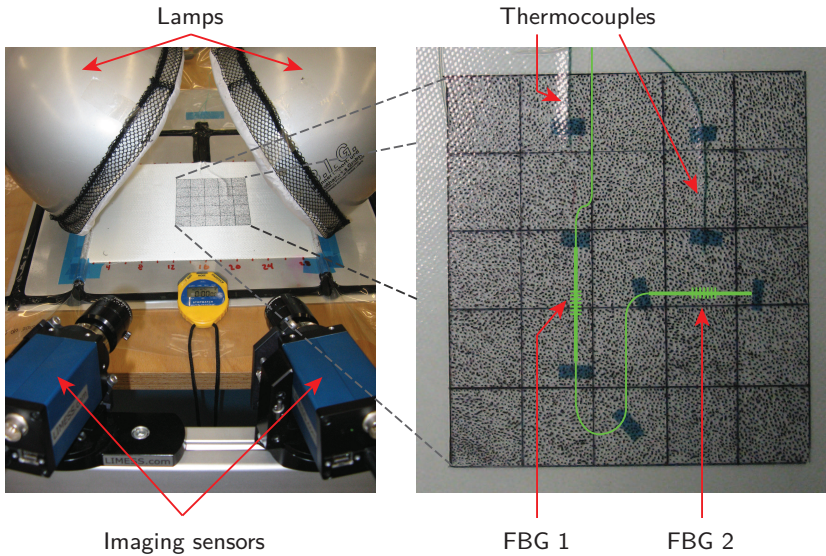


Figure 8.2: LHS: Experimental setup for correlating Bragg response to preform thickness. RHS: Grid with speckle pattern, position of two FBG sensors in a single embedded optical fibre highlighted in green.

8.4 Results and discussion

8.4.1 GFR EP04908: Typical variation in preform thickness and correlation with the Bragg response for the single-sided tooling concept

As mentioned in the previous section, the speckle pattern is applied on the surface of the vacuum bag. Hence, the digital image correlation software calculates the combined displacement of the preform and vacuum bag. By assuming a constant thickness of the vacuum bag, the out-of-plane displacement can be attributed to the change in preform thickness.

Figure 8.3 shows an example of the output of the digital image correlation software. In this particular case, the results comes from testing the experimental setup as shown in Fig. 8.2. In Fig. 8.4 the average variation in preform thickness is shown for the lines 1 and 2. Typical behaviour is observed in which the propagation of the flow front

causes initially a steep drop in the preform thickness. In [200], this effect is attributed to lubrication, which eases the compaction. As the flow front propagates, the fluid pressure increases locally. The manually recorded position of the flow front is found typical for such a 1D flow case, *i.e.* $x \propto \sqrt{t}$ (Darcy's law) [19]. The faster propagation of the flow front at the beginning causes a more rapid build up of fluid pressure such that less time is reserved for the lubrication effect. This is illustrated by results from another test in Fig. 8.5. In here, the FBG sensor (and therefore also the points for computing the variation in preform thickness) is about 5 *cm* from the inlet. The drop in the preform thickness is completely absent. In the same figure, the three segments of the filling stage can be distinguished clearly. In the second segment, the preform relaxes because of a lower compaction pressure. This is then partially cancelled in the third segment in which the inlet is closed. In general, this trend is expected for each preform (see also Fig. 8.8 later on), but a stronger or weaker reaction in either one of the segments could occur due to local differences in compaction.

In Fig. 8.6 the variation in preform thickness as a function of cycle time from Fig. 8.5 is compared to the normalised change in Bragg wavelength. Striking are the similarities between the two curves. When the preform relaxes due to a decrease in compaction pressure, the FBG sensor records a shift in opposite direction. The two data sets correlate negatively for each segment (see right-hand side of Fig. 8.6). Relative movement of the optical fibre with respect to the yarns of the adjacent plies is likely the cause of the slightly different behaviour in each segment. In fact, microbending of the optical fibre is intentionally introduced in this experiment by removing the transverse adjacent reinforcing fibres (Fig. 4.10)⁵. The left-hand side of Fig. 8.7 shows the surface plot of the focal area. The valley is a result of the compaction after fibre removal. The local peak in the preform thickness is caused by the thermocouple (see also Fig. 8.3). On the right-hand side, the effect of compaction after fibre removal on the optical fibre is schematically illustrated. Microbending at the drop-off, which occurs on both sides of the FBG sensor, may have prestrained the optical fibre. Since this is between the two fixation points, any change to this condition affects the FBG sensor as well.

In Fig. 8.8 the variations in the preform thickness and the normalised changes in Bragg wavelength are shown for the two FBG sensors of the first illustrative example. The variation in preform thickness is again typical for the three-segment filling stage. Apart from the drop in thickness due to the lubrication effect, the FBG sensors

⁵Before this kind of experiments was performed, it had been found that microbending stretches the optical fibre. A positive shift in the Bragg response can still be observed even when the FBG sensor itself is shielded by a capillary [188].

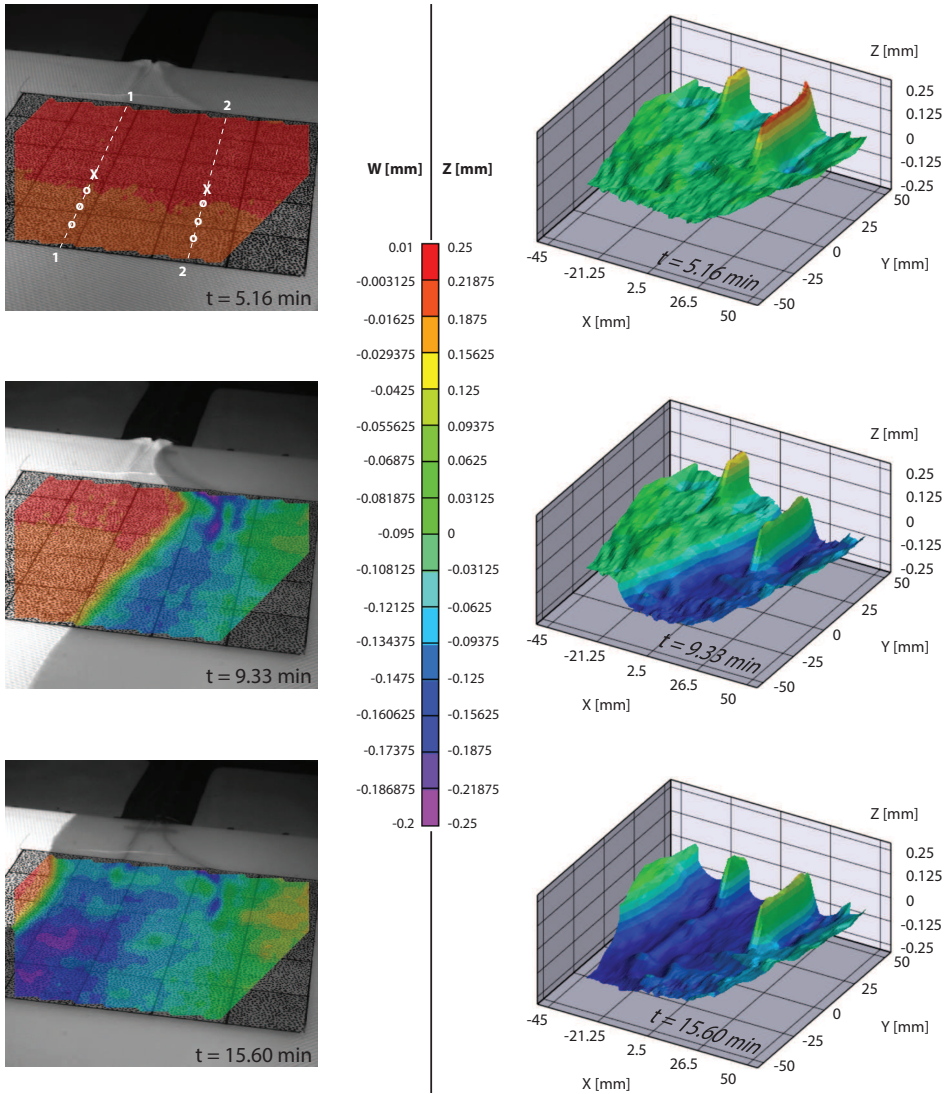


Figure 8.3: LHS: 2D overview of out-of-plane displacement w [mm]. RHS: 3D overview of the thickness z [mm]. For the upperleft figure: the marker 'o' and 'x' are points for data collection and the position of the FBG sensor (see also Fig. 8.2, respectively).

seem less sensitive to the variation in preform thickness, because fibre removal was not considered here. The negative correlation of the two parameters is less perfect.

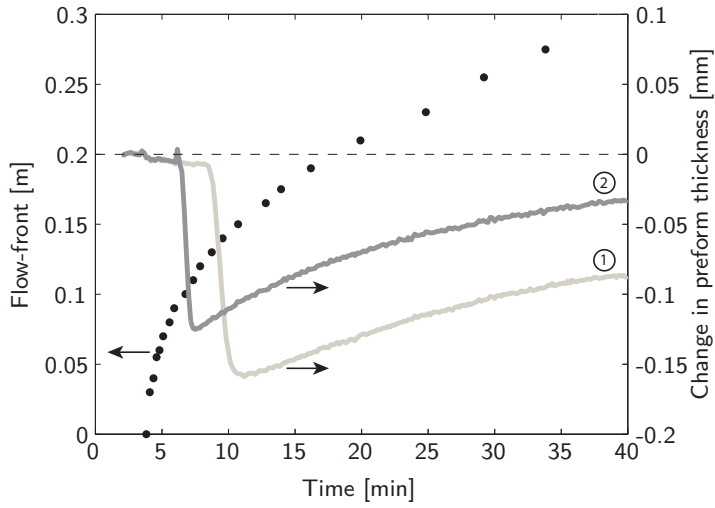


Figure 8.4: Flow-front propagation and average out-of-plane displacement for lines 1 and 2 (see Fig. 8.3).

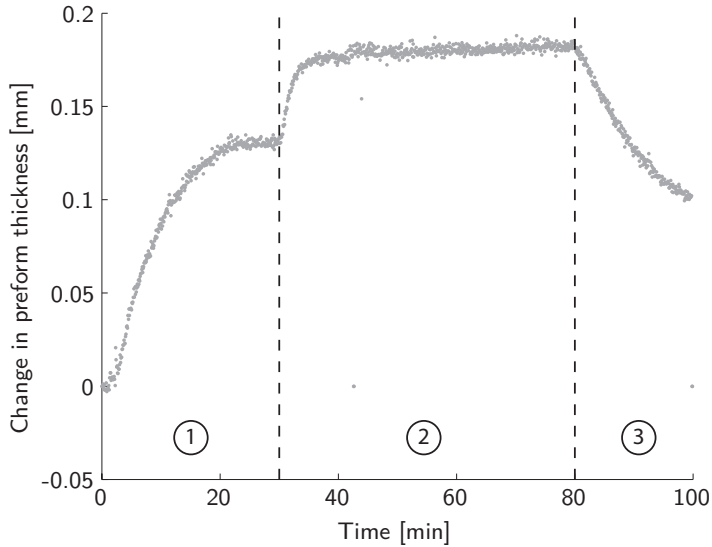


Figure 8.5: Three zones in the filling stage: (1) infusion at absolute pressure of 50 *mbar*, (2) flushing at 500 *mbar*, (3) preform stabilisation after closing inlet.

Other effects seem to have influenced the Bragg response as well. The thermocouple readings show an increase of about 2 °C over the filling time. The sudden change

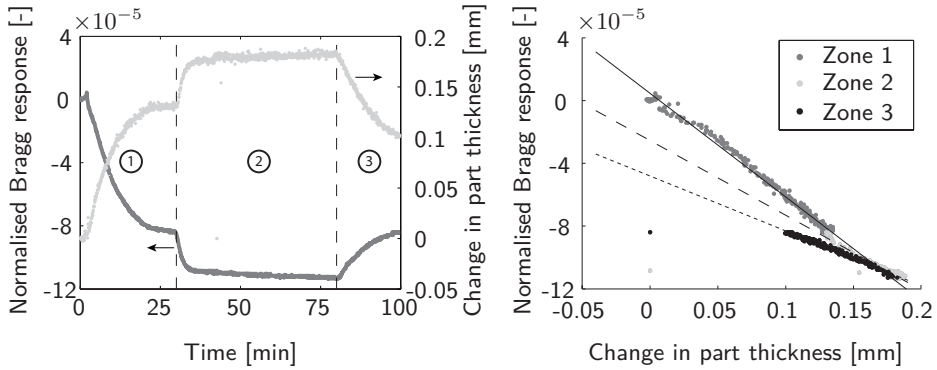


Figure 8.6: Normalised Bragg responses and variation in part thickness. LHS: both parameters as a function of time. RHS: correlation between the two parameters.

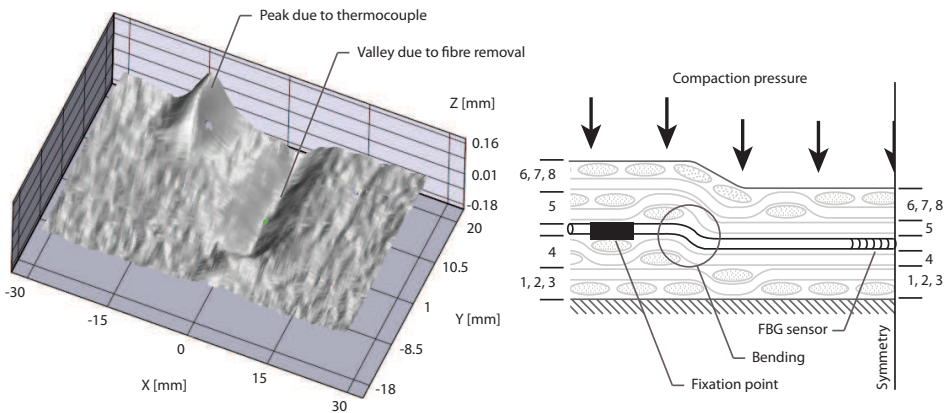


Figure 8.7: LHS: three-dimensional overview of surface, z [mm], of preform. RHS: bending of optical fibre enhances Bragg response to resin infusion.

in Bragg response due to the drop in preform thickness cannot be explained at the moment. The orientation of the FBG sensor with respect to the flow-front may be important. Though, it is still believed that the sudden change in Bragg response can be attributed to changes in the embedding conditions of the optical fibre. This points then to a shift to a new reference point. Hence, the change in Bragg wavelength due to RT filling should not be taken into account in the analysis of the process-induced and residual strains.

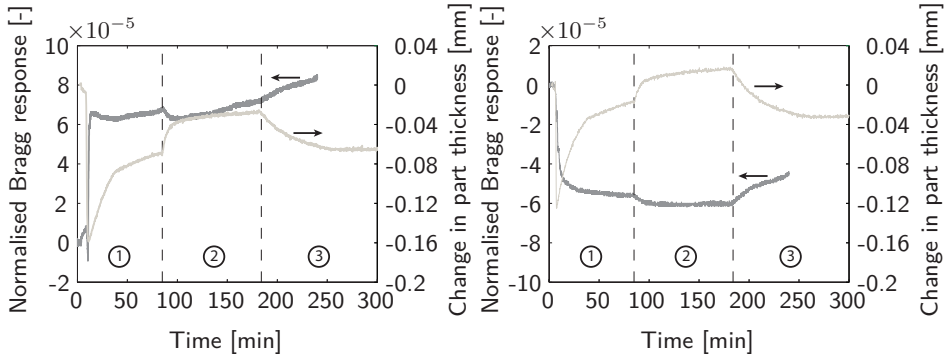


Figure 8.8: Normalised Bragg responses and variation in part thickness. LHS: FBG parallel to flow-front, line 1. RHS: FBG perpendicular to flow-front, line 2.

8.4.2 GFR EP04908: Effect of resin flow for the double-sided tooling concept

How FBG sensors react on the resin flow in the double-sided tooling concept was already touched on in the introduction. In Fig. A.3 the lines *i* and *ii* indicate the start of the infusion and the decrease in compaction pressure to 500 *mbar*, respectively. The cure cycle starts about a minute later, after closing the inlet. Hence, the third segment cannot be distinguished. Concerning the second segment, the decrease in normalised change in Bragg wavelength may be explained on the basis of the analysis presented in the previous section. The Bragg responses in the first segment differ completely. ‘FBG 1’ and ‘FBG 2’ show a similar type of spike, whereas ‘FBG 3’ has only a single peak. These spikes seem, nevertheless, to indicate the arrival of the resin at the FBG sensors. It is believed that the displacement of the top plate, due to the local variation in preform thickness, interacts with the embedded FBG sensors. This may explain why all three sensors react immediately at the start of the filling stage. The presence of thermocouples might also have influenced the compaction behaviour. For such a simple test, the Bragg response gets already quite complicated to unravel. Similar tests performed in studying the effect of the cure regime confirmed this (Chapter 6). For the 5 (+ 3) FBG sensors embedded in those GFR EP04908 laminates, the normalised change in Bragg response is in the range of -1.05×10^{-5} and 7.25×10^{-5} . None of the data sets matches the ‘clean’ behaviour as observed for the single-sided tooling concept. The effect of the filling stage on the Bragg response is fortunately small in most of the cases.

Based on the learning in the previous sections and the difficulties observed in analysing the double-sided tooling concept it is concluded that digital image correlation may not be as fruitful. Apart from thermal fluctuations⁶, changes in the Bragg response should be attributed to changing embedding conditions of the optical fibre during RT filling.

8.4.3 GFR RTM6: Effect of non-isothermal filling at elevated temperatures

In case of the RTM6 resin system, the non-isothermal filling takes place at an elevated temperature. This causes a temporary drop in temperature during (Fig. 6.12a). In addition, a permanent drop in thermal strain is observed of about 40-60 $\mu\epsilon$ (see Fig. 6.12b and Tables 6.9 and C.2). In Section 6.5.1 it was speculated that the effect of the local change in temperature on the thermal strain is reversible. There may have been some tool-part interaction in case the tooling temperature changes as well (see Chapter 7), but this will be difficult to isolate. It is therefore assumed that the temperature fluctuation is not the cause of the permanent change in thermal strain. Out-of-plane deformation of the preform, as observed in the filling stage of the GFR EP04908 laminates, may be held responsible for the drop in thermal strain. Confirming this statement by using the digital image correlation technique is impossible because of the elevated temperature. Though, the interaction between the Bragg response and variation in preform thickness is expected to be of a smaller order because of the lower compaction pressure and the stretched optical fibre (less microbends). It is therefore unlikely that the total drop in strain can be attributed solely to this phenomenon.

It is believed that a sudden change in compacting conditions may have caused the stretched optical fibre to contract. From Section 8.4.1, it is learnt that a drop in preform thickness may occur as soon as the resin arrives. In case of double-sided tooling, the preform would experience locally a temporary loss of compaction pressure instead of this drop. This loss may have resulted in the sudden contraction of the optical fibre. To support this idea, a similar test is performed as described in the previous chapter. That is, a dry preform is ramped to about 180 °C and subsequently cooled down. Instead of keeping the compaction pressure constant at 500 *mbar*

⁶Ignoring the thermal fluctuations on the Bragg response in the filling stage may form a source for the scatter in the pre-cure tool-part interaction (see Fig. 6.16).

throughout the test, the vacuum is suddenly released during heating to mimic the local loss of compaction pressure. In Fig. 8.9 the thermal strain is plotted as a function of temperature. The solid dots represent the states in which the preform is not compacted. At about 100 °C, an instant drop in thermal strain is observed due to the loss of compaction pressure. Upon reapplying the compaction pressure, the pre-cure tool-part interaction reappears. Although both the effect of debulking, indicated by the arrows, and pre-cure tool-part interaction are similar to the ones observed at RT conditions, an offset of about $110 \mu\epsilon$ is clearly present. This seems to prove that a sudden loss in compaction pressure may result in a permanent drop in thermal strain. That the value is higher than the ones observed filling may be explained by the fact that the compaction pressure does not perish completely and/or that the fluid present in the impregnated preforms acts as a damper. It is expected that for a higher compaction pressures this effect would diminish. For the compaction pressure applied in curing GFR RTM6 laminates, it forms nevertheless a problem in the determination of the process-induced and residual strains. The contraction of the optical fibre itself would only shift the reference point, but it seems logical that the adjacent reinforcing fibres to which the optical fibre is attached may become affected as well. Whether the contraction of the optical fibre has a broader impact cannot be assessed at the moment.

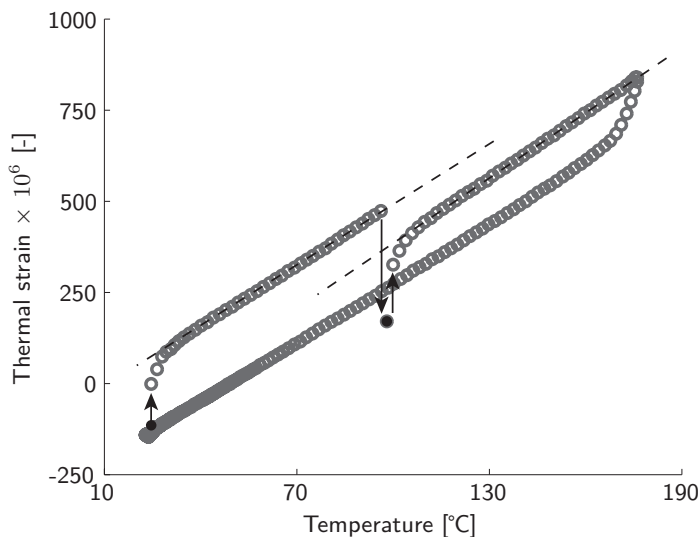


Figure 8.9: Mimicking loss of compaction pressure by sudden release of vacuum for a dry preform.

8.5 Conclusions

The analysis on the effect of the flow-front propagation on the Bragg response illustrates how difficult the interactions can be. The following can be concluded:

- For the single-sided tooling concept, digital image correlation has revealed that the Bragg response is inversely proportional to the variation in preform thickness after resin arrival for RT filling. This may relate to the already present microbends introduced by debulking.
- In the double-sided tooling concept, this trend is less clear. Spikes, which are not always observed, seem to relate to the moment the resin arrives at the FBG sensors. A clear separation of the different segments of the RT filling stage cannot be made. Since the changes are relatively small, fluctuations in ambient temperature become more dominant.
- In non-isothermal filling at elevated temperatures, the Bragg response can get affected by another phenomenon as well. At least for double-sided tooling, resin arrival may create a temporary loss of compaction pressure. As such, the tensioned optical fibre would instantly contract.

Based on the analyses presented in this chapter, it is concluded that the resin flow seems to act as a disturbing factor in determining the process-induced and residual strains in the reinforcing fibres. For the moment, this shift can best be interpreted as a change of the reference point.

9

EFFECT OF THE FIBRE VOLUME FRACTION ON THE FORMATION OF STRAINS IN RTM LAMINATES

9.1 Introduction

In previous chapters, the influence of several parameters on the formation of process-induced and residual strains in VI laminates is demonstrated. To consider the effect of the fibre volume fraction as well a switch to another LCM process, *i.e.* the (vacuum-assisted) RTM process, is required. For a constant mould cavity depth, the fibre volume fraction can be adjusted by the stack size. A typical pressure-thickness curve of a fabric under compaction is shown in Fig. 9.1. Reduction of pores and gaps among the fibres and yarns is initially the primary source of preform compaction. In the third stage the linear relation between the preform thickness and the compaction pressure is attributed to the bending (elastic) deformation of the yarns [176]. As the compaction pressure may be increased in (vacuum-assisted) RTM applications, it becomes possible to end up in the third stage.

The objective of this chapter is to discuss the effect of the fibre volume fraction on the strain formation by monitoring thin laminates manufactured by vacuum-assisted RTM process. In this manner, the chapter contributes also to the assessment of whether FBG sensors are useful for typical LCM processes.

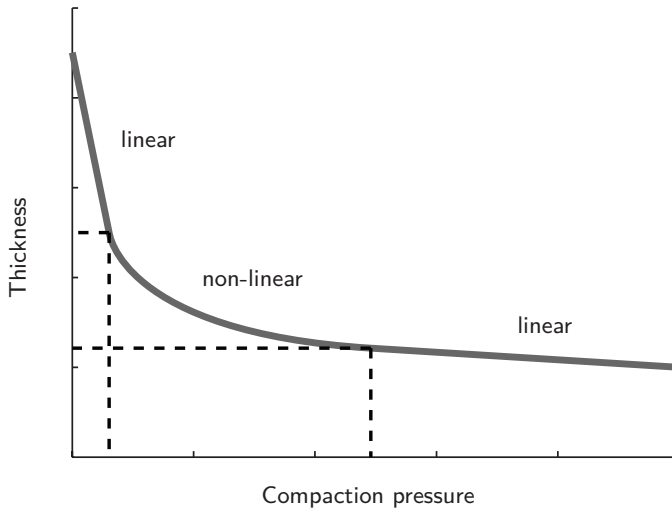


Figure 9.1: Typical pressure-thickness curve of a fabric under compaction (based on [176]).

9.2 Experimental

9.2.1 Vacuum-assisted RTM

The experimental setup for the vacuum-assisted RTM experiments was already discussed in Section 4.4.2. Three series of tests are performed here: (i) dry thermal cycling, (ii) the manufacturing of GFR EP04908 laminates, and (iii) the manufacturing of GFR RTM6 laminates. The stack size varies between: 8, 10, and 12 plies. Typical layouts of the sensors, embedded according to the procedure described in Section 4.5.3, are shown in Figure 9.2. The distance d between the sensors is about 15-20 mm . The configuration on the right-hand side is used only in the manufacturing of the GFR EP04908 laminates due to availability. In the other series a single FBG sensor is used. The position of the FBG sensors is such that the flow-front would arrive parallel to their longitudinal axis.

In the first series of tests, dry preforms are subjected to a thermal cycle ($3\text{ }^{\circ}\text{C}/\text{min}$ between RT and $180\text{ }^{\circ}\text{C}$). Due to the limited cooling capability of the oil heating unit the cooling rate drops near ambient conditions. Each preform is subjected twice to such a thermal cycle without intermediate changing any of the settings. In the second series of tests, the manufacturing of several GFR EP04908 laminates is monitored. The injection pressure is stepwise increased to achieve complete filling. After filling,

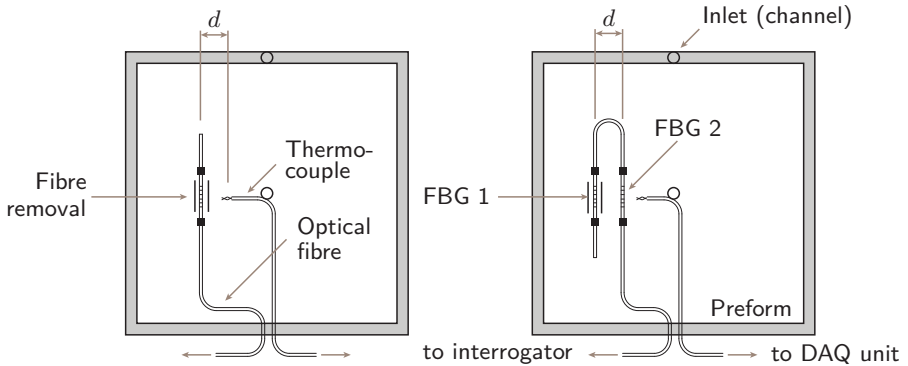


Figure 9.2: Schematics of the embedded sensors in the middle of the RTM preforms - LHS: dry preforms and GFR RTM6 laminates, RHS: GFR EP04908 laminates.

the tooling is subjected to a one-step thermal cycle to cure the impregnated preform. The cure cycle is almost identical to the one described for the vacuum-infused GFR EP04908 laminate cured at 60 °C (Section 6.4). The heating ramp is about 1 °C/*min*. Cooling is done as fast as possible, but its rate never exceeded the one of heating. In the last series of tests, a similar strategy is followed in the manufacturing of the GFR RTM6 laminates. Though, the lower viscosity of RTM6 requires a lower pressure difference between inlet and vent. To this end, the vacuum level is reduced. Obviously, the cure cycle has to be adapted as well. The dry preform is ramped to the first dwell at 120 °C at a rate of about 3 °C/*min*¹. After filling, the heating is continued at a rate of 1 °C/*min* to the cure temperature. The second dwell is extended to 133% of the recommended cure time to guarantee a sufficient cure at the inlet. The initial cooling rate is about 3 °C/*min*. After demoulding, the laminates are machined carefully (see Section 4.4.2). To prevent breaking of the optical fibre, the egress point is reinforced with a metal mesh in later testing.

9.2.2 Thermal annealing

The laminates that survived the removal of the resin-rich edges are thermally annealed according to the procedure described in Section 6.2.2.

¹Keeping the rate constant at 1 °C/*min* is not opted for, because it would make the process more lengthy.

9.2.3 Data analysis

Equation 5.1 is used to convert the Bragg responses to strains (see Section 5.4.3).

9.3 Results

9.3.1 First series: tool-part interaction in dry preforms

That tool-part interaction is an important process phenomenon was already discussed for the VI process in Chapter 7. In Figure 7.10 it was shown that a linear relation exists between the compaction pressure and the strain difference $\Delta\epsilon$. Whether this relation would still hold for higher compaction pressures is of interest here. Figures 9.3, 9.4, and 9.5 show the (T, ϵ) -plots after post-processing the data collected during thermal cycling of the dry preforms. Table 9.1 lists the estimated CTEs of the four stages, for which their definitions can be found in Fig. 7.8.

The behaviour of the preform with the lowest fibre content agrees well with the behaviour as observed in VI testing. However, extrapolating the last stage to RT reveals a gap of $108 \mu\epsilon$, which is 42% of the strain difference $\Delta\epsilon$, for which three reasons can be mentioned. First of all, a sudden release of strains at the start of the second cycle seems to confirm the existence of compressive strains. Perhaps less noticeable in the graph for the 8-ply preform, but the encircled data in the graph of the 10-ply preform indicates clearly this sudden release of strain. For the 8-ply preform this strain measures about $48 \mu\epsilon$. Secondly, in Table 9.1 it can be seen that the first stage deviates from other tooling-dominated stages. The high compaction of the preform favours a non-optimal arrangement of the reinforcing fibres. As the optical fibre is affected by this through microbending, a rearrangement of the reinforcing fibres has a direct influence on the measured CTE. Last but not least, the gap is influenced by the difference in measured CTEs of the second and fourth stage. That the measured CTE in the third stage differs for the 8-ply preform cannot be explained for the moment.

The 10-ply preform behaves similarly compared to the 8-ply preform. Though, the difference $\Delta\epsilon$ is significantly larger. Typical stick-slipping behaviour, *i.e.* a sawtooth response, is observed in the second stage of the heating segment. The preform tries to follow the expansion of the tooling, but the friction forces are insufficient. The average slope of this stage matches well with E-glass. This stick-slipping behaviour implies that the reinforcing fibres are in tension. As mentioned before, a sudden release in

strain occurs at the start of the second thermal cycle. For the 10-ply preform, the contribution of this phenomenon is about $90 \mu\epsilon$. Hence, the difference $\Delta\epsilon$ must be a combination of tensile strains introduced during heating, yarn straightening, and compressive strains introduced during cooling.

For the 12-ply, the difference $\Delta\epsilon$ cannot be determined for the given temperature range. The first stage shows a slightly different behaviour (see encircled data). The preform seems to resist or counteract somehow the thermal expansion of the tooling for a while. It is believed that mould closing may have stretched the preform. The monitoring of the manufacturing of GFR EP04908 laminates seems to confirm this statement (see next section). Furthermore, an unusual high value is found for that what is presumed the CTE of E-glass for the second stage. A small temperature range in combination with the averaging of the stick-slip behaviour may have resulted in this overestimation.

Using the slopes of the best fits to relate the difference $\Delta\epsilon$ to the compaction pressure (Table 7.1 and the average of slopes presented in Fig. 7.12), estimates might be given for the compaction pressures based on the measured strain differences in the 8-ply and 10-ply preforms (Fig. 9.6). At first sight, the results agree fairly well. Though, points that have not been addressed in this study are the effects of the preform size and the position of the FBG sensors with respect to the edges of the preform². It is known that the length of the preform influences the measured strain related to tool-part interaction [205]. More research is thus inevitable.

9.3.2 Second series: strain in GFR EP04908 laminates

The GFR EP04908 laminates are manufactured with two different stack sizes: 8 and 10 plies. Due to the relatively high viscosity of the EP04908 resin system, some minor dry spots are observed at the corners of the 10-ply laminate. Their presence is assumed to be marginal on the formation of strains. Figure 9.7 shows the Bragg responses during the filling stage. The graph on the right-hand side shows the fluid pressure as measured by a pressure cell on the inlet line. At $t = 0 \text{ min}$ the filling is started. The first couple of minutes are spent on filling the inlet tubing and the injection channel surrounding the preform. For the 8-ply laminate, the time to reach the outlet is about 15 min , whereas the time triples for the 10-ply laminate. The temperature remains fairly constant. Despite the stepwise increase in fluid pressure

²In the vacuum-assisted RTM setup the preform is about 1.5 times larger in the measuring direction of the FBG sensors compared to the VI preforms.

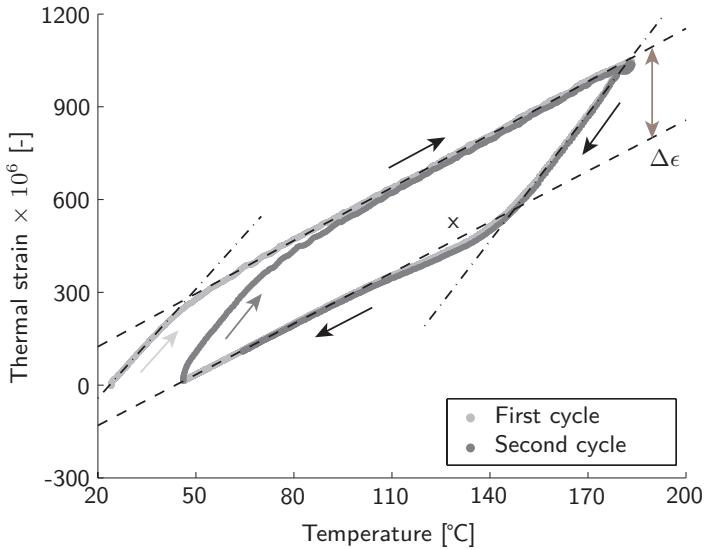


Figure 9.3: Thermal cycling of the 8-ply preform in dry state.

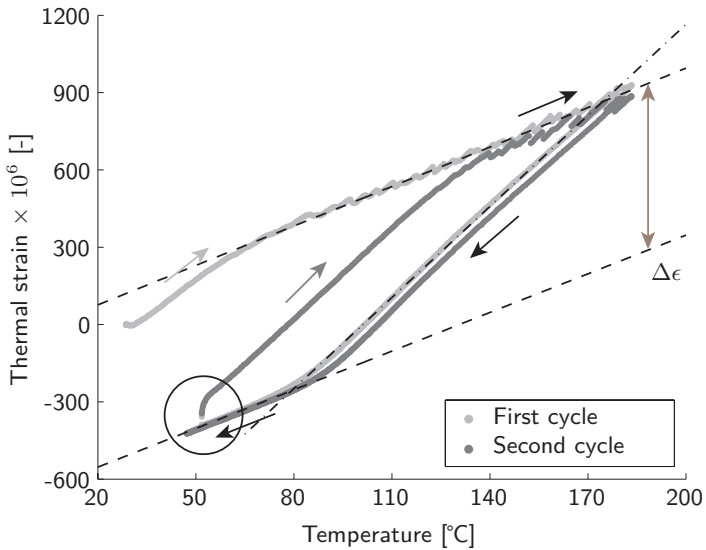


Figure 9.4: Thermal cycling of the 10-ply preform in dry state.

having no effect on the Bragg response, the FBG sensors record a steep drop for the 8-ply preform. This drop may be linked to the resin arrival at the sensors' location. In fact, the Bragg response of FBG 1 drops first, because it is closer to the

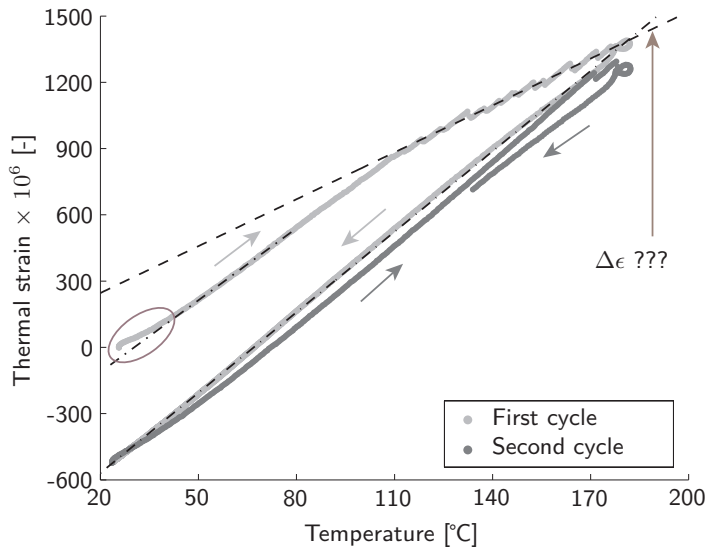


Figure 9.5: Thermal cycling of the 12-ply preform in dry state.

Table 9.1: Linear fitting to stages I-IV (defined in Fig. 7.8) for multiply preforms

Name	Estimated CTE [$\mu\epsilon/^\circ\text{C}$] for temperature zone [$^\circ\text{C}$]				
	Stage I-II	Stage II-III	Stage III-IV	Stage IV-I	
8-ply preform	1 st cycle	(26-36) 11.76	(80-180) 5.72	(175-160) 13.73	(100-48) 5.49
	2 nd cycle	(48-63) 13.21	(100-180) 5.84	(175-160) 14.21	(100-65) 5.34
10-ply preform	1 st cycle	(35-50) 9.68	(100-180) 5.10	(175-100) 11.78	(65-52) 5.00
	2 nd cycle	(60-120) 11.7	(140-180) 5.18	(175-100) 11.81	(80-50) 5.02
12-ply preform	1 st cycle	(60-100) 11.02	(140-180) 7.08	(140-25) 12.14	(-) -
	2 nd cycle	(80-160) 12.58	(-) -	(-) -	(-) -

injection channel. Loss of compaction pressure because of lubrication, mentioned in Section 8.4.2, in combination with a rearrangement of the yarns and optical fibre may have caused this drop. As the resin flows slower in the 10-ply preform due to the lower permeability, the steep drop in Bragg response occurs later. However, a steady decrease in the Bragg responses is noted several minutes after starting. At this time,

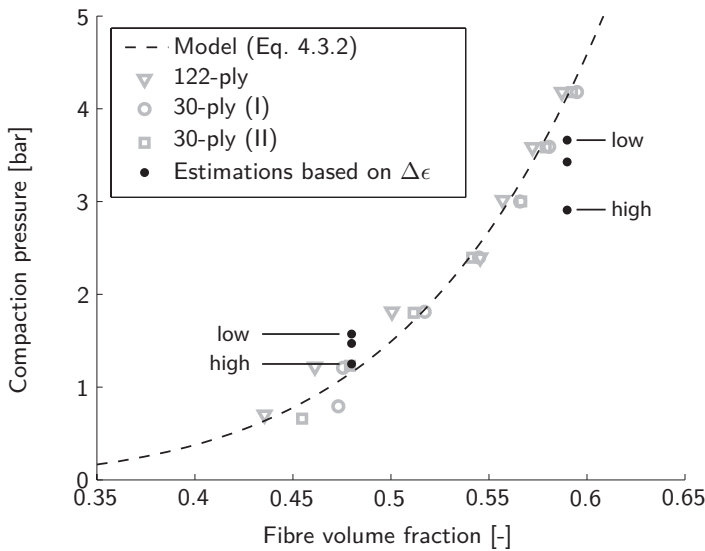


Figure 9.6: Estimations of compaction pressure based on measured $\Delta\epsilon$ and $(p, \Delta\epsilon)$ -relation for the 8-ply and 10-ply preforms.

the 10-ply preform can be assumed to be almost entirely dry. This points to the presence of tensile strains introduced during debulking. The drop in the in the Bragg response is thus likely a combination of the released tensile strain at the start and the rearrangement of adjacent yarns and the optical fibre at the moment of resin arrival. After resin arrival, most of the tensile strains in the preform seems to have released implying a stress-free state. The difference in embedding the FBG sensors, *i.e.* with or without fibre removal (FBG 1 or FBG 2, respectively), has not a significant impact.

Figure 9.8 shows the thermal strains as observed by FBG 2 in curing and subsequent thermal annealing. Tables 9.2 and 9.3 present an overview of the main features. For the 8-ply laminate is almost identical to the vacuum-infused 60 °C-cured laminate (Fig. 6.5). Though, the tool-part interaction is now dictated by the steel tooling. The black marker indicates the state of the laminate after demoulding. The removal of the resin-rich edges has a minimal impact on the strain level, because the sensors are close to/on the neutral line/surface of the laminate. Again, the impregnated preform appears to be expanding under a stress-free condition. That the first stage of the heating segment is smaller compared to dry testing may perhaps be attributed to lubrication. Furthermore, the difference between the two embedding strategies is minimal. The ultimate glass transition temperature seems lower than seen before in

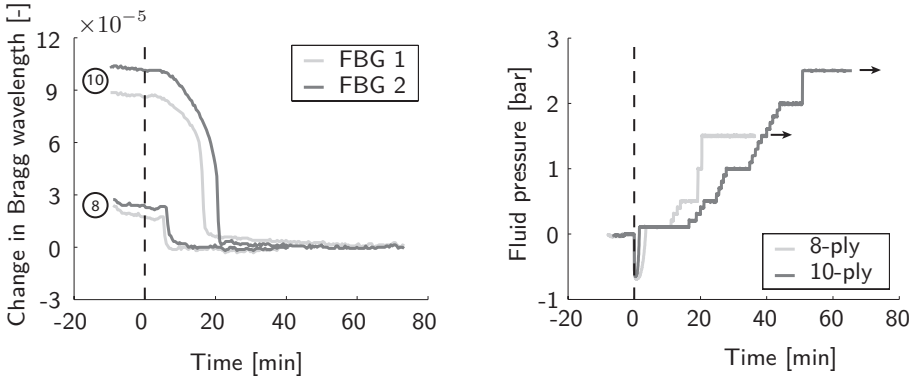


Figure 9.7: Effect of flow-front propagation. LHS: Normalised change in Bragg wavelength, RHS: Fluid pressure measured in inlet tubing.

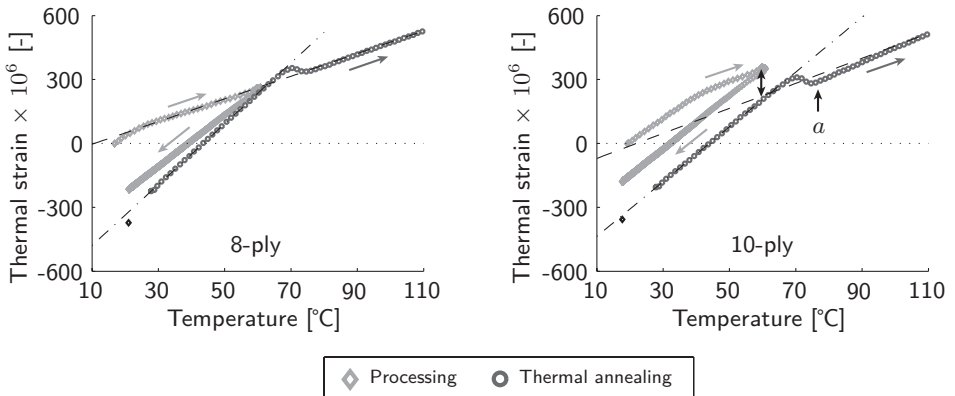


Figure 9.8: Thermal strains in 8-ply and 10-ply GFR preforms / GFR EP04908 laminates.

VI laminates (Chapter 6). The higher fibre volume content results in a lower CTE of the laminate and, therefore, less residual strain in the reinforcing fibres. The lower cure temperature lowers, of course, also the residual strain level. The latter is nullified by thermal annealing.

Concerning the 10-ply laminate, a significant change in the plot of the combined responses is observed. The LoZS indicates that the impregnated preform is under tension after reaching the cure temperature. That the impregnated preform is in a stress-free condition at the start of the cure cycle, an aforementioned assumption,

Table 9.2: Data extracted for the multi-ply GFR EP04908 laminates.

Name	Fibre removal	Temperatures [°C]			Estimated CTE [$\mu\epsilon/^\circ\text{C}$]			
		Cure	Initial	Ultimate	Fabric (LoZS)	Tooling ¹	Laminate	
			stress-free	glass transition			before TA ²	after TA
8-ply	no	60.3	63.0	85.4	5.32	12.08	14.29	14.38
	yes		63.0	85.3	5.27	12.36	14.55	14.54
10-ply	no	60.3	62.4	94.4	5.87	12.45	12.86	13.24
	yes		64.1	92.9	5.84	13.00	13.52	13.85

¹ See note in Table 6.3. ² TA = thermal annealing.

Table 9.3: Measured strains at room temperature conditions ($T = 25^\circ\text{C}$) for multi-ply GFR EP04908 laminates.

Name	Fibre removal	Strains $\times 10^6$ [-]	
		<i>Change due to</i>	
		<i>Residual</i>	<i>thermal annealing</i>
8-ply	no	-341	-206
	yes	-352	-207
10-ply	no	-261	-250
	yes	-300	-244

seems to be confirmed by the LoZS as well. Removal of the resin-rich edges has again a negligible influence on the strain level. The ultimate glass transition temperature seems to be slightly overestimated³. The higher fibre volume content lowers the CTE of the laminate. Hence, a smaller change in strain due to thermal annealing is theoretically expected. However, the significant change in the measured CTEs of the laminate before and after thermal annealing and the unusually high ultimate glass transition temperature may have contributed to the opposed behaviour.

At the cure temperature, the tensile strain in the impregnated preform measures 126 $\mu\epsilon$. Apparently, this does not affect the shape of the (T, ϵ)-curve measured during thermal annealing such as in [183]. A theoretical study based on the CLT may help

³The overestimation was observed before in high-temperature curing of vacuum-infused GFR EP04908 laminates (Table 6.5).

to explain this. To introduce this strain a normal force has to be present⁴. The load-deformation relations can be used to determine the normal forces, $[N]_{x,y}$, due to the biaxial straining in the impregnated stage:

$$\begin{bmatrix} N_x \\ N_y \end{bmatrix}_{\text{impr}} = \begin{bmatrix} A_{xx} & A_{xy} \\ A_{yx} & A_{yy} \end{bmatrix}_{\text{impr}} \begin{bmatrix} \epsilon_x^o \\ \epsilon_y^o \end{bmatrix}_{\text{impr}} \quad (9.1)$$

where

$$A_{ij} = \sum_{k=1}^n Q_{ij}^k (h_k - h_{k-1}) \quad (9.2)$$

with $i, j = x, y$. The parameter Q_{ij}^k is the transformed stiffness matrix for the k^{th} layer⁵. Parameters h_k and h_{k-1} are the z -coordinates of the upper and lower surfaces of this layer. Upon theoretically removing the constraints imposed by the tooling, these normal forces would disappear. By substituting these forces in the force-deformation relation of the laminate, their effect on the strain state in the laminate can be determined. Thus,

$$\begin{bmatrix} \epsilon^o \end{bmatrix}_{\text{lam}} = \begin{bmatrix} a \end{bmatrix}_{\text{lam}} \begin{bmatrix} N \end{bmatrix}_{\text{lam}} = \begin{bmatrix} a \end{bmatrix}_{\text{lam}} \begin{bmatrix} A \end{bmatrix}_{\text{impr}} \begin{bmatrix} \epsilon^o \end{bmatrix}_{\text{impr}} \quad (9.3)$$

where $[a]_{\text{lam}}$ is the laminate's compliance matrix. Using the values from Table 6.4 and a fibre volume fraction of 59% and setting the reference plane strains $[\epsilon^o]_{x,y}$ of the impregnated preform to unity, results in a prestrain releasing of about 76%, which is 96 $\mu\epsilon$ in case of the 10-ply GFR EP04908 laminate. In Fig. 9.9 a part of the (T, ϵ) -plot is enlarged. Due to the fluctuations in the measured CTEs, see Section 6.8, and the unexplained lump, a in Fig. 9.8, observed after passing the initial glass-to-rubber transition (in this figure denoted by $\Delta\epsilon_a$), it is difficult to confirm the theoretical prediction, but the order of magnitude agrees. This explanation may also clarify why there is no big difference observed in case the resin gels before the cure temperature is reached (Section 6.6.2).

9.3.3 Third series: strain formation in GFR RTM6 laminates

Figures 9.10, 9.11, and 9.12 show the thermal strains observed during the manufacturing and thermal annealing of the GFR RTM 6 laminates. Thermal annealing is

⁴In Chapter 7 it was suggested that the compaction pressure results in frictional forces when the preform is ramped to a higher temperature. As such, the preform follows the thermal expansion of the tooling.

⁵In computing the stiffness matrix of the impregnated preform, the matrix has still a negligible stiffness. There is no curvature. Shear stresses are assumed to be absent.

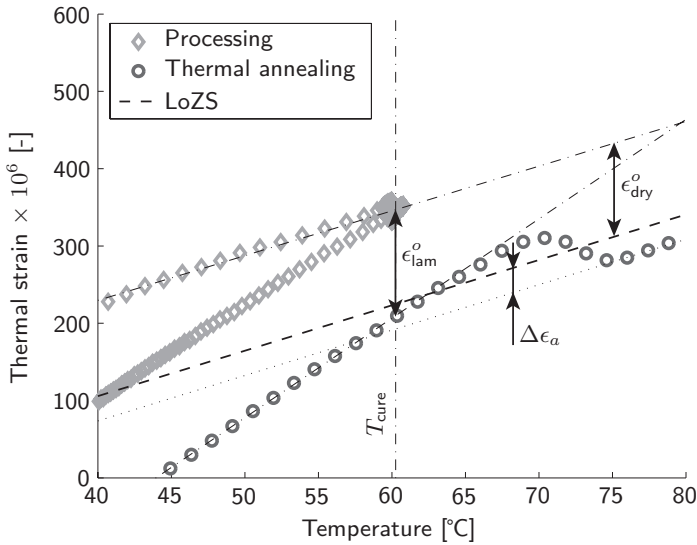


Figure 9.9: Enlargement of (T, ϵ) -plot for 10-ply laminate (Fig. 9.8).

performed twice. The first time the standard procedure is followed precisely. Based on the analysis of the GFR EP04908 laminates, it is expected that the impregnated preforms are no longer in a stress-free state. Hence, it is essential to find the LoZS by thermal annealing. Consequently, the second time that the laminates are annealed the temperature is raised to 250°C. Care is taken in determining the LoZS for the reasons mentioned in Section 5.4.4⁶. In the summary given in Table 9.4 four more entries can be found that relate to two identical tests in which two parallel embedded FBG sensors measure the influence of in-mould Post-Curing (PC) (see also Fig. 9.15). Data from thermal annealing are missing, because the optical fibres broke at the unreinforced egress points. In the following six categories the main results are briefly described.

1. Pre-cure tool-part interaction;

Tool-part interaction is, in general, comparable to what have been observed before in testing dry preforms. That is, the 8-ply preform does not show stick-slip behaviour, whereas the other two do. Some minor differences may perhaps be explained by the mould closing procedure, *i.e.* the way and the applied torque to fasten the twenty bolts.

⁶Rapid degassing of the adhesive on the fixation tapes made the experimental data after reaching 240 °C unreliable.

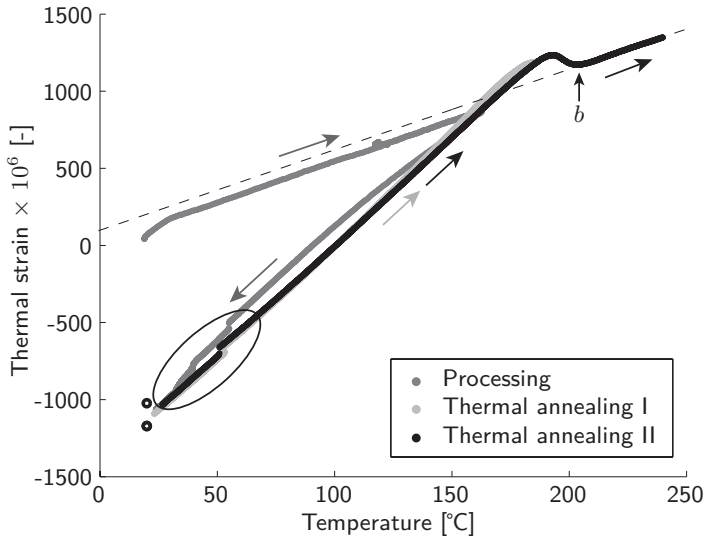


Figure 9.10: Manufacturing and thermal annealing of the 8-ply GFR RTM6 laminate.

2. Non-isothermal filling;

A temperature drop due to non-isothermal filling is not detected. The high volumetric heat capacity of the steel tooling heats the resin quickly. A thermal contribution to the Bragg response is thus not expected. Furthermore, a decrease in thermal strain, as observed in testing EP04908, is not observed in the 8-ply preform. Straightening (and stretching) of the less optimal arranged yarns may have reduced microbending to which the FBG sensor is susceptible. In contrast, the impregnation of the other two preforms results in a significant drop in thermal strain. The higher fibre volume fractions makes the explanation given in Section 8.4.3 less plausible⁷. Figure 9.14 shows three plots in which the first dwell at about 120 °C is shown. The dashed lines indicate the starting time and end time of mould filling. Directly after filling, the pressure is increased (RHS plot) for purging. In this particular stage, two jumps in the Bragg response, indicated by 1 and 2 in the upper left-hand plot, occurred. Neither the stepwise increasing of the fluid pressure nor the temperature fluctuations seem

⁷In Section 8.4.3 it is stated that a temporary loss of compaction pressure may result in contraction of the prestrained optical fibre.

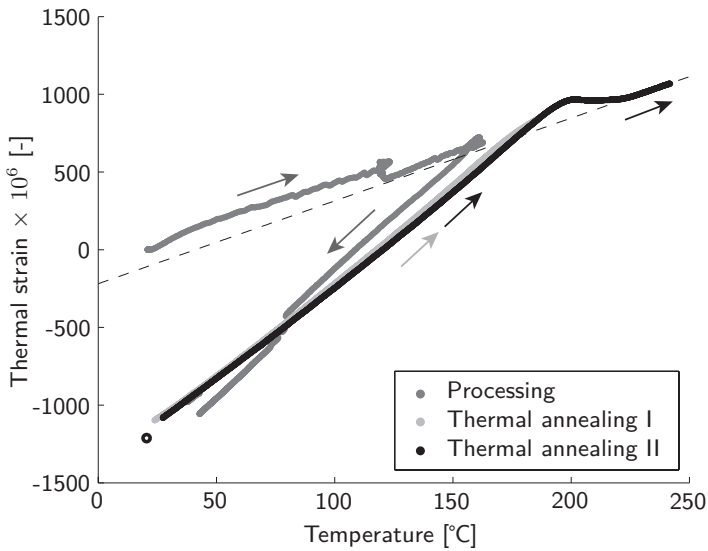


Figure 9.11: Manufacturing and thermal annealing of the 10-ply GFR RTM6 laminate.

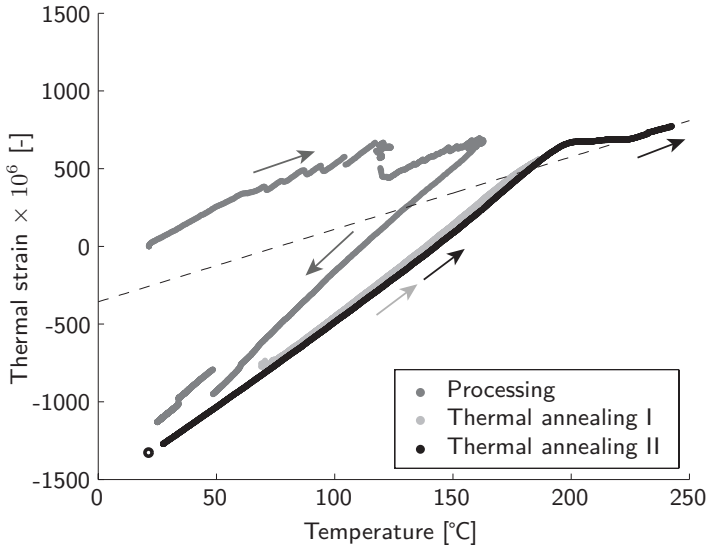


Figure 9.12: Manufacturing and thermal annealing of the 12-ply GFR RTM6 laminate.

the source. More plausible is the sudden contraction of the entire preform, which is supported by observations from the PC laminates (Fig. 9.15).

Table 9.4: Data extracted for the multi-ply GFR RTM6 laminates.

Name	Estimated CTE [$\mu\epsilon/^\circ\text{C}$] for temperature zones ¹ [$^\circ\text{C}$]						
	Processing				TA ² I	TA II	
	a (80-118)	b (125-160)	c (155-130)	c' (100-80)	Laminate (100-150)	Laminate (100-150)	Fabric (LoZS) (230-240)
8-ply	5.25 ³	5.34	11.10	13.83	14.94	13.48	5.22 ⁴
10-ply (1)	4.61	5.96	13.33	14.39	12.60	12.27	5.33
10-ply (2) ⁵	4.37	5.77	12.73	14.01 ⁶	12.52	12.09	5.29
10-ply PC ⁷ (1a)	4.93	6.21	12.78	14.09	-	-	-
10-ply PC (1b)	4.95	5.86	11.37	13.97	-	-	-
10-ply PC (2a)	5.03	6.90	14.59	13.11	-	-	-
10-ply PC (2b)	4.80	6.36	14.18	13.03	-	-	-
12-ply	5.29	6.15	12.74	14.91	11.81	11.44	4.66

¹ In Figure 6.10 the temperature zones for processing were defined by the letters a-e;

² TA = thermal annealing; ³ (60-118); ⁴ (210-240); ⁵ Not discussed in this chapter; ⁶ (97-80);

⁷ PC = postcure (cure was followed by a postcure at 180 °C for 120 min).

3. Cooling after cure;

In accordance with Fig. 6.7.2, the mismatch in CTEs of the tooling and the laminate appears to be insufficient to induce debonding⁸. Except for the second 10-ply PC laminate, the measured CTE seems to increase when cooling down (comparing zones *c* and *c'* in Table 9.4) despite of the fairly constant CTE of the steel tooling. As the effective CTE of the laminate decreases with increasing fibre content, this behaviour seems rather strange. However, the transverse stresses that build up during cooling may have broadened the reflected spectrum, *i.e.* increasing of the FWHM, for which the reduction in intensity of the peak wavelength is a good indicator (Fig. 9.13). This broadening may have lead to an additional shift in the Bragg wavelength and, therefore, in the laminate's CTE. That the second 10-ply PC laminate does not fit to this theory remains, however, unexplained by this theory.

Peak splitting is again the source of the sudden jumps in thermal strain towards the end of cooling (see encircled data in Fig. 9.10). Strangely, split peaks are not observed in the reflected spectra after demoulding of the 10-ply and 12-ply laminates, whereas the thermal strain measured during cooling seems to suspect this behaviour. The sudden jump in intensity, see Fig. 9.13, indicates that the software settings for peak recognition may also have played a role (see

⁸Clamping by the resin-rich edges may have resisted the sudden contraction of the laminate anyhow.

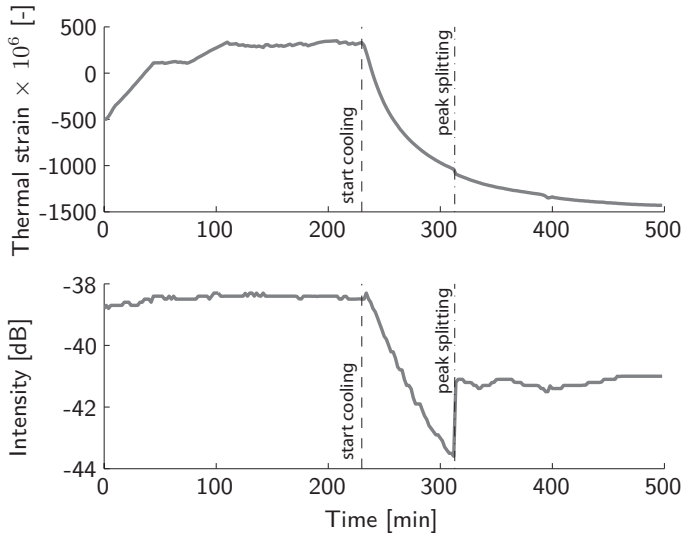


Figure 9.13: Thermal strain and the intensity of the recorded peak wavelength during manufacturing of the 8-ply laminate.

Section 4.5.1).

4. Thermal annealing;

The second thermal annealing cycles correspond well with the first ones. The small offset in thermal strain and effective CTE of the laminate may be explained by the additional curing during the first cycle. In case of the 8-ply preform, the mixing seems less perfect because of the slightly lower end temperature of the glass-to-rubber transition zone (indicated by *b* in Fig. 9.10).

5. Comparison of monitoring the manufacturing process and subsequent thermal annealing;

In contrast with the 8-ply GFR EP04908 laminate, the impregnated 8-ply RTM6 preform appears not to be in a stress-free state. Initially, it was thought that the LoZS may have obscured the analysis due to the problems mentioned in Section 5.4.4. However, the slope corresponds well with the measured CTE of the preform in both the dry and impregnated state. That the yarns are perhaps not fully straightened⁹ is in contradiction with the assumption that a higher

⁹This assumption was used in Chapter 6 to clarify a similar offset observed in the laminate with wrongly-mixed RTM6.

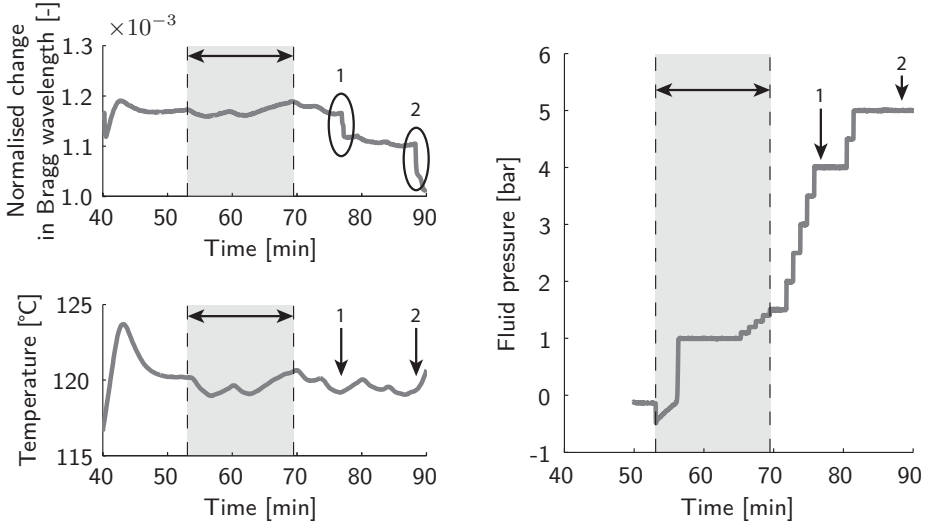


Figure 9.14: Jumping in thermal strain during first 'isothermal' dwell for the 12-ply GFR RTM6 laminate.

compaction pressure eases the straightening. In the laminates with higher fibre volume content, a similar behaviour compared to the 10-ply GFR EP04908 laminate is observed. That is, the reinforcing fibres seems to be loaded in tension, while the resin is curing. Again, it is difficult to prove the amount of prestrain released, because the slope of the LoZS of the 12-ply preform seems a bit on the low side. Moreover, the release of the compaction pressure may have resulted in a secondary contribution.

6. Miscellaneous;

The 8-ply preform expands almost identical in the dry and impregnated states. There is, however, a clear difference between the two zones for the ones with a higher fibre volume content. At least partially, a contribution is expected from the averaging problems for the CTE in the stick-slip behaviour dominated stage. In-mould post-curing does not alter the thermal strain state at RT. Upon finishing the cure stage at 160 °C, the laminates are given a post cure at 180 °C for 120 min. The cured laminates follow the expansion/contraction of the tooling. Whether the postcure has an effect on the residual strain in the reinforcing fibres cannot be assessed due to fibre breaking.

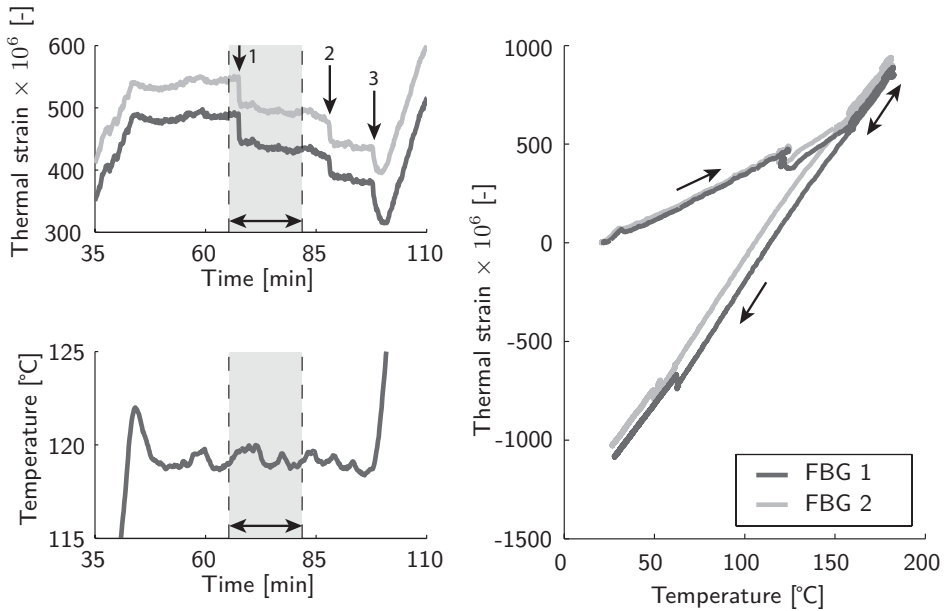


Figure 9.15: Effect of post cure in mould - RHS: jumping in thermal strain during first 'isothermal' dwell for the 10-ply GFR RTM6 laminate (PC 2). LHS: Thermal strain versus temperature for 10-ply GFR RTM6 laminate (PC 1).

9.4 Conclusions

The aim of this chapter was to investigate the influence of the fibre volume content on the formation of process-induced and residual strains in GFR laminates by using the vacuum-assisted RTM process. In general, the following can be concluded:

- For low fibre volume content (less than 50%), a similar behaviour, including pre-cure tool-part interaction and a near stress-free state of the impregnated preform, is observed compared with testing VI laminates.
- For higher fibre volume content, dry testing revealed that the tooling configuration can introduce tensile strains in the preform during heating. Typical stick-slip behaviour can occur in case of insufficient friction. That the preform can already be in a tensile strain state after closing the mould is concluded from filling experiments at RT conditions. Mould filling can, however, reduce these tensile strains. An offset with the LoZS can confirm the existence of tensile

strains at the moment of curing.

- Calculations based on CLT reveals that about 75% of the prestrain in the reinforcing fibres should be released upon removing the constraints. A similar order of magnitude is found, but a precise verification of the released prestrain has not been possible with the concise set of experimental data. This release explains, nevertheless, why the (T, ϵ) -plot of the prestrained laminate is almost identical to the one in which reinforcing fibres of the preform are in a stress-free state.
- The analysis shows that FBG sensors can be successfully applied in an RTM environment, but care has to be taken when post-processing the data collection. A useful statement about the process-induced and residual strains in laminates manufactured by LCM processes can only be given after having determined the LoZS of the reinforcing fibres.

10

EXPLORATORY INVESTIGATION OF STRAINS IN THICKER LAMINATES

10.1 Introduction

In conventional curing of thick composite parts, through-thickness thermal and cure gradients may develop due to the exothermic nature of the reaction. The progression of the through-thickness curing front is important in the formation of process-induced stresses (see also Section 2.2.1) [38]. In general, stress gradients get accentuated with increasing laminate thickness [24, 72]. The development of a hybrid solution, which combines the cure simulation and online process monitoring by means of FBG sensors, has been proposed here as one of the research goals. The predicted internal temperature can be used to discriminate between thermal and strain effects in the Bragg response. Foreign bodies such as embedded thermocouples (or an encapsulated FBG sensor) become then superfluous. Realistic cure modelling relies, however, on the full-scale characterisation of numerous parameters (Chapter 2). In combination with the high accuracy of FBG sensors, the slightest difference may have a detrimental effect on the interpretation of the (T, ϵ) -plot of online monitored thick composites manufacturing processes. Nevertheless, the first step towards the hybrid solution has already been taken by introducing the cure kinetics model of the RTM6-2 resin system (Section 4.3.1).

This chapter forms an exploratory investigation that highlights some of the addi-

tional issues in monitoring LCM processes (for thick laminates) by FBG sensors^{1,2}. To this end the cure kinetics model is employed to improve the understanding. The presentation of the hybrid solution is, however, left for future work.

10.2 Intermezzo: degree of cure at gelation

To support the analysis on monitoring thick composites, the degree of cure at gelation is estimated. There are two ways that lead to the detection of resin's gelation in a (T, ϵ) -plot: either due to the external heating or due to the exothermic reaction. In both cases, a mismatch in CTE between the tooling and the impregnated preform is a prerequisite. An example of the former was shown before in Fig. 6.16. Figure 10.1 shows a magnification of the (T, ϵ) -plot given by Fig. 6.10. Clearly visible is the presence of a similar transition just before reaching the peak temperature caused by the exothermic reaction (see Fig. 6.9 as well). At first sight, the impregnated preform seems to behave as a cured laminate³. However, it is more likely that, although the tooling temperature is not recorded directly, the tooling does not reach the peak temperature because of heat diffusion⁴. As tool-part interaction is expected to occur, the apparent CTE of the host structure has to be lower than the one quoted for the aluminium alloy (as observed in zone *c* (Fig. 6.10)). Table 10.1 lists the measured CTEs for the four 2-mm RTM6 laminates in the second column. Both the second and fourth test seem to prove this. In Test II, the higher CTE may perhaps relate to poor heat diffusion such that the tooling temperature is closer to the laminate temperature. At least for steel tooling in Test IV, the measured slope is significantly lower than the free-standing laminate's CTE.

Table 10.2 lists the gelation temperatures for the six thin GFR RTM6 laminates

¹In order to compare eventually the cure modelling (output in stress) with the experimental data from the FBG sensing technique (output in strain), the generalised Hooke's law may be considered.

²Monitoring thin laminates being manufactured by vacuum-assisted RTM can result in complex Bragg responses due to prestraining and stick-slip behaviour (Chapter 9). Adding the handleability issues during demoulding and poor design of the sensor throughput channel as problems, the experimental setup for this manufacturing process is not suitable for evaluating strains in thick laminates.

³The CTE measures $15.75 \mu\epsilon/^\circ\text{C}$ ($164.5^\circ\text{C} - 162^\circ\text{C}$), which is close to $15.86 \mu\epsilon/^\circ\text{C}$, the value determined for zone *e* in which the laminate is no longer bonded to the tooling (Table 6.2).

⁴At the surfaces of a thick GFR RTM6 laminate produced under similar conditions the temperature is found to be lower (Fig. 1.2).

Table 10.1: Estimated CTE [$\mu\epsilon/^\circ\text{C}$] at the end of the thermal spike by an FBG sensor embedded in the middle of the laminate.

Laminate thickness [mm]	2	5	10	15	20
Temperature zone [$^\circ\text{C}$]	(164-162)	(165-162)	(168-162)	(149-143)	(150-144)
Test I	15.75 ¹	20.45	17.82	15.89	14.69 (18.64) ²
Test II	18.02 ³	19.65	-	-	-
Test III	15.36 ⁴	-	-	-	-
Test IV	9.63 ⁵	-	-	-	-

¹ Laminate 'GFR RTM6 I'; ² Between plies 1-2; ³ Laminate 'GFR RTM6 II'; ⁴ Laminate 'GFR RTM6 III';
⁵ Laminate 'GFR RTM6 - steel'.

discussed in Chapter 6⁵. To this end, the gelation temperature is linked to the degree of cure via the cure kinetics model of RTM6-2 (Table 10.2). Estimations are based on two points: (i) resin arrival at the FBG sensor and (ii) start of second heating segment. The latter is used to highlight the consequences of the filling stage on the evolution of the degree of cure. Preheating of the resin system is ignored in the analysis. Taking resin arrival at the sensors' locations as the initial point, the average conversion of laminates 'I', 'II', 'III', and 'steel plates' is about 0.5, which agrees with literature⁶. However, the smallest miscalculation of the gelation temperature may lead to a significant difference in the degree of cure. Secondly, an extrapolation of the cure kinetics model is necessary to capture the first part of curing. That a significant higher conversion is predicted for the laminates in which gelation occurs before reaching the cure temperature can only be partially explained by this. To this end, rheological analysis would be required.

⁵The first four entries correspond to the laminates that are conventionally cured at 160 $^\circ\text{C}$. That is, 'I' is the laminate extensively discussed in Section 6.5. Laminates 'II' and 'III' are the ones used for addressing reproducibility (Section 6.7.3 and Appendix C). The fourth one, 'Steel plates', has its tooling made of steel (Section 6.7.2). The 'Slow cure' and 'High temperature' laminates have a lower heating rate, 0.25 $^\circ\text{C}/\text{min}$ and a higher cure temperature, 180 $^\circ\text{C}$, respectively (Section 6.6.2).

⁶Gelation is said to occur at a conversion of about 0.5 for epoxy-amine resin systems [89]. For RTM6-1, rheological analysis shows an average of 0.53 ± 0.02 for isothermal cure [166].

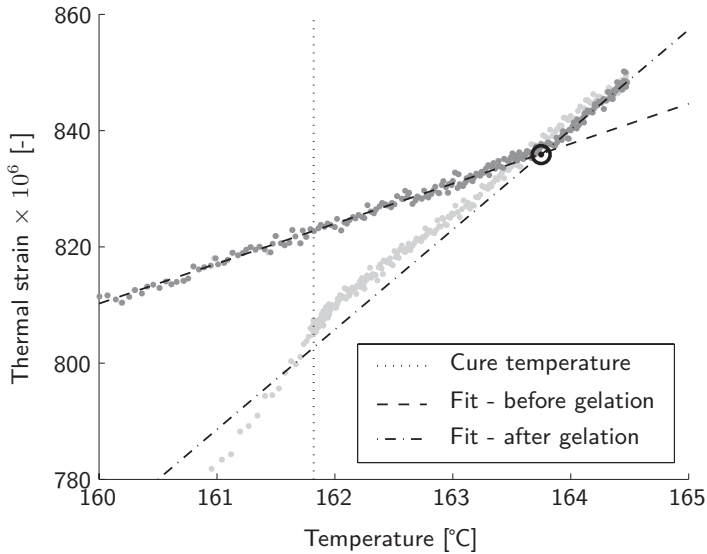


Figure 10.1: Gelation point in thin vacuum-infused GFR RTM6 laminate.

10.3 Cure of a thick GFR EP04908 laminate

10.3.1 Experimental

As an introduction to monitoring thick vacuum-infused GFR laminates, a single GFR EP04908 laminate is manufactured according to the procedure in Section 4.4.1. In this test, 60 plies are symmetrically stacked resulting in a preform thickness of 15 mm. A single optical fibre is embedded between plies 30 and 31. One of the FBG sensors is oriented perpendicular to the resin flow. The other one, not discussed here in detail, has its orientation parallel to the resin flow. Thermocouples are embedded between plies 1-2 (bottom), 30-31 (middle), and 59-60 (top). Flow settings are unchanged. The cure is done conventionally, *i.e.* 80 °C for 8 hours with 1 °C/min. The procedure described in Section 5.5.1 is followed for thermal annealing.

10.3.2 Results and discussion

On the left-hand side of Fig. 10.2 the slightly unsymmetrical through-thickness temperature distribution is shown for the first 150 minutes. The right-hand side of the same figure shows the corresponding (T, ϵ) -plot. Besides the curve belonging to the manufacturing, the other two curves represent the thermal strain during the heating

Table 10.2: Estimated degree of cure at gelation point.

Laminate (GFR RTM6)	I	II	III	Steel plates	Slow cure	High temperature
Gelation temperature [°C]	163.77	163.71	163.99	163.80	151.14	178.29
Filling time ¹ [min]	23	32	26	95 ²	19	23
Degree of cure @ gelation						
α_0 @ resin arrival	0.45 (0.36, 0.56) ³	0.52 (0.41, -)	0.57 (0.47, 0.71)	0.47 (0.41, 0.57)	0.69 (0.66, 0.71)	0.65 (0.64, 0.67)
α_0 @ heating	0.35 (0.27, 0.46)	0.48 (0.37, -)	0.45 (0.36, 0.61)	0.33 (0.28, 0.42)	0.60 (0.57, 0.64)	0.56 (0.54, 0.58)

¹ Time between resin arrival at FBG sensor and start of second heating ramp.

² Inlet almost blocked by tacky-tape.

³ Degree of cure at gelation temperature ± 0.5 °C.

and cooling segment of the thermal annealing. Table 10.3 lists the main features. In analysing the results, the following is noted:

- Although the peak temperature in the middle of the laminate measures 108 °C (24 °C higher than the intended cure temperature), the through-thickness thermal gradient is small.
- Pre-cure tool-part interaction is hardly present in the mid-plane (only 14 $\mu\epsilon$ @ $T_0 = 23.3$ °C). Yarns seem not to have straightened; a behaviour that is observed in dry testing as well (Section 7.6).
- A transition due to gelation is not observed (up to the peak temperature the thermal expansion is fairly constant). The rapid increase in temperature due to the exothermic reaction may have shifted the gelation to a higher temperature⁷. An assumed inside-out progression of the curing front contributes to a higher temperature as well⁸.
- Thermal spiking causes a shift in thermal strain (denoted by a in the figure) (37 $\mu\epsilon$ @ $T_{\text{cure}} = 84$ °C). Figure 10.3 shows the temperature and thermal strain as

⁷For a heating rate of 1 °C/min, the gelation temperature was earlier found to be about 92 °C.

⁸Gelation at the mid-plane may have occurred earlier, but in order to become visible the tooling has to become effective as well. The latter can only be achieved by gelation of the resin at the interface(s)

a function of cycle time⁹. The time the internal temperature reaches the cure temperature for the first time is taken as reference. The Bragg wavelength, *i.e.* $x = \Delta\lambda_B/\lambda_B$, is added as the intermediate stage in determining the thermal strain. Peaking occurs at different times. Furthermore, the Bragg response and its derivative, thermal strain, do not return to the reference level. The small offset between the peak times of the two raw data series leads to an exaggeration in the (T, ϵ) -plot. In-plane thermal variations due to voids or local difference in fibre volume fraction may be reasons for this offset. However, both cannot clarify the offset with respect to the reference level at the end of cure. It is believed that (partial) cancellation of the absence of yarn straightening plays a role, but a sound proof is difficult to present at this stage.

- According to [206], the shear stress τ is related to the laminate mechanical strain ϵ_m by:

$$\tau = \frac{E_c \epsilon_m t}{L_0} \quad (10.2)$$

where E_c , t , and L_0 are the modulus of elasticity, the thickness, and the length of the laminate, respectively. When conditioning of the tooling dictates this maximum shear stress at the interface (calculated in [192]), the mechanical strain has to decrease for thicker laminates. As such, debonding occurs earlier compared to thinner laminates^{10,11}.

- An apparent offset is present between the contraction of the moulded laminate and the expansion of its ‘free-standing’ counterpart (denoted by b in Fig. 10.2) ($72 \mu\epsilon$ @ 50°C). The mutual difference in CTE is, however, too small for such an offset (see Table 10.3). Figure 10.4 shows the intensity of the Bragg wavelength versus temperature. The cause seems to relate to the first shift (at 34.4°C in Fig. 10.2). However, equal CTE before and after this shift excludes debonding. As the occurrence is global, *i.e.* the second FBG sensor recorded a similar shift, it is believed that the offset originates from friction and that slipping, *i.e.* strain release, occurred at 34.4°C .
- The impregnated plies in the mid-plane seem in a different state when compared to the (apparent) LoZS of the reinforcing fibres (denoted by c in Fig. 10.2

⁹To this end, the parameters are normalised according to:

$$\hat{x} = \frac{x - x_{\text{ref}}}{x_{\text{max}} - x_{\text{ref}}} \quad (10.1)$$

where x is one of the parameters.

¹⁰That debonding occurs in a single step is not uncommon (see Fig. 6.15).

¹¹The jump at 34°C is not an artefact of debonding.

(difference of $105 \mu\epsilon @ T_{cure}$). In Fig. 10.5 results of this thick laminate are compared with the ones collected for the thin GFR EP04908 laminate cured at similar conditions (see Sections 5.5 and 6.6.1). Taking the start of the cure cycle as the initial point results in two LoZSs having a mutual offset denoted by d for yet unknown reasons. To improve the understanding of yarn straightening effects seems thus inevitable.

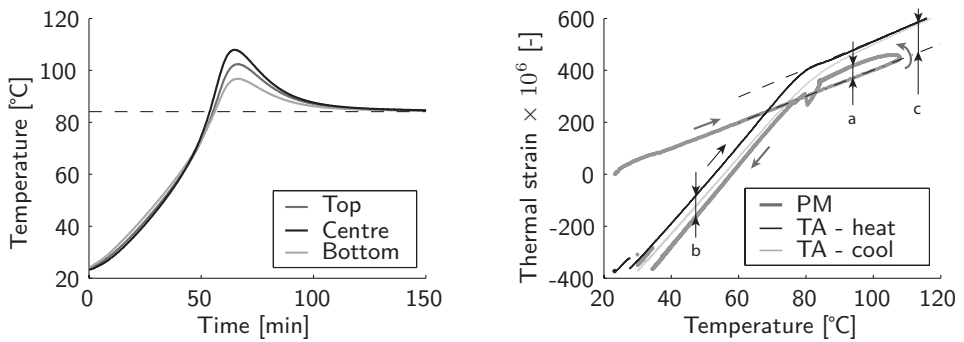


Figure 10.2: Cure of 60-ply GFR EP04908 laminate. LHS: effect of exothermic reaction on cure temperature - RHS: thermal strain during manufacturing and subsequent thermal annealing.

Table 10.3: Features of processing and thermal annealing of 60-ply and 8-ply GFR EP04908 laminates.

Laminate	CTE [$\mu\epsilon/^\circ\text{C}$]						
	Impr. Fabric			Tooling ¹	Laminate		
	<i>before peak</i>	<i>after peak</i>	<i>LoZS</i>		<i>in mould</i>	<i>TAH</i>	<i>TAC</i>
60-ply (thick)	(50-100)	(95-85)	(100-150)	(84-81)	(75-40)	(40-75)	(75-40)
	5.05	6.19	5.46	21.75	15.75	15.26	14.73
8-ply (thin) ²	(50-80)	-	(100-150)	(80-50)	-	(40-75)	(75-40)
	5.30	-	5.63	22.44	-	15.61	14.54

¹ In practice, these values represented a combined effect of tooling and laminate. The former dictated, however, the thermal contraction. Hence, the heading referred to tooling only.

² Discussed before in Section 6.6.1.

10.4 Cure of thicker GFR RTM6 laminates - thickness effect

Despite that yarn straightening in the fabric, or actually the absence of it, complicates the strain analysis, first attempts in studying the effect of the laminate's thickness are reported here.

10.4.1 Experimental

The test procedure for GFR RTM 6 laminates is given in Sections 4.4.1 and 6.2.1. As a starting point, 5 and 10 mm thick laminates are conventionally cured. As the post cure temperature of 180 °C serves as the upper limit, the 15 and 20 mm laminates are cured at 140 °C to avoid 'overcooking'. Vacuum settings are: 100 mbar during first heating stage and infusion and 500 mbar after the resin reached the vent. Afterwards, the cured laminates are thermally annealed. The upper limit is set to 190 °C, because the effects of material degradation and coating instability were still unknown at that time.

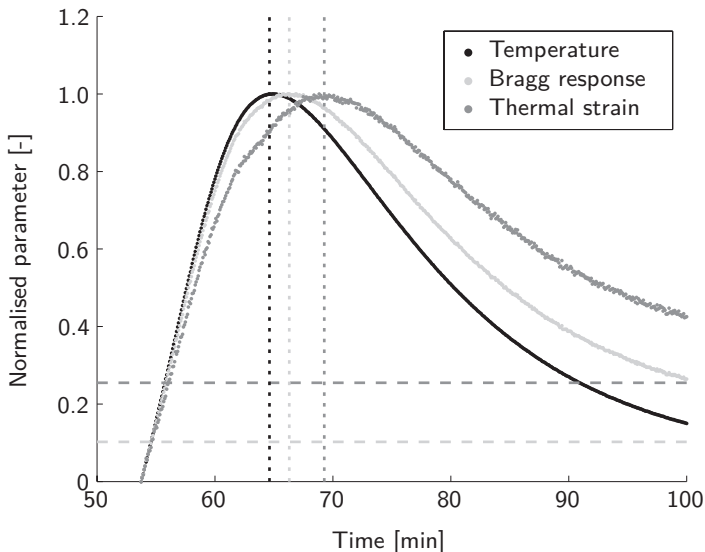


Figure 10.3: Comparison between data sets. The Bragg response is given as $\Delta\lambda_B/\lambda_B$. The dashed and dotted lines represent the values at the end of the dwell period and the times at which the peak occurred, respectively.

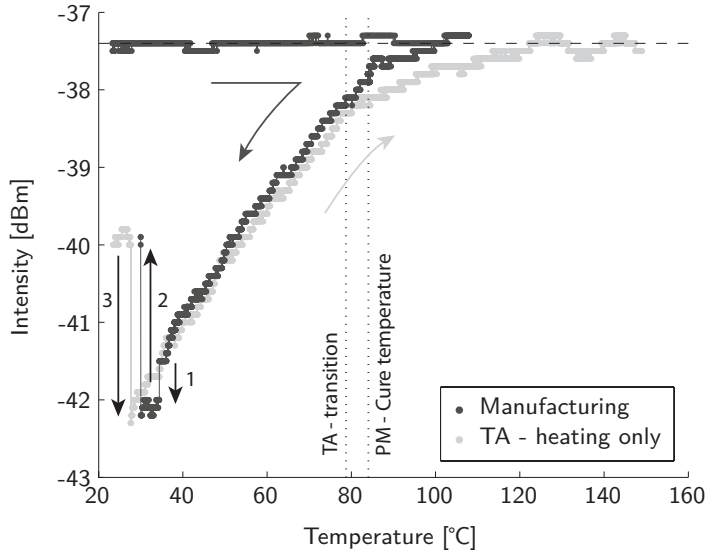


Figure 10.4: Intensity of measured peak wavelength during manufacturing and subsequent thermal annealing (heating only).

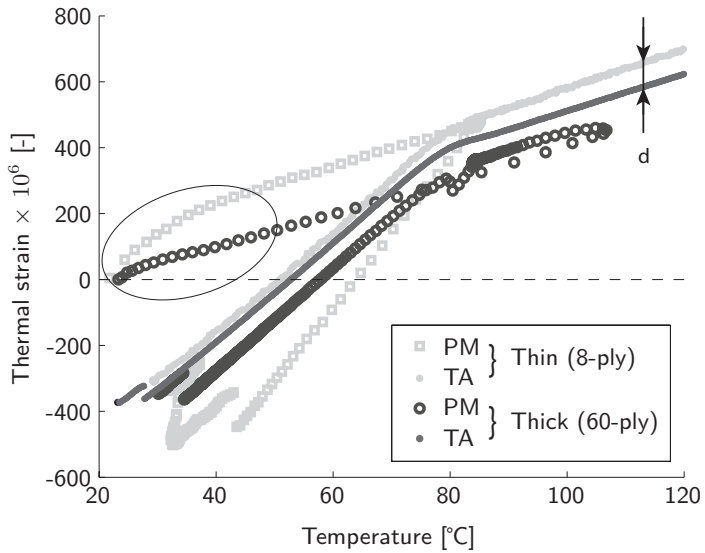


Figure 10.5: Comparison between 80 °C-cured thin (8-ply) and thick (60-ply) GFR EP04908 laminate.

10.4.2 Results

In a first step, a proof is given of the reproducibility of the thermal response (Fig. 10.6). The impact of the exothermic reaction is significant. As such, the thickness of a conventionally cured GFR RTM6 laminate in this particular VI setup is limited to about 10 mm. Figures 10.7 and 10.8 show the process-induced and residual strains for laminates with thickness of 2, 5, and 10 mm¹². Features of manufacturing and thermal annealing of these laminates are summarised in Table 10.4 (see last page of this chapter). Due to the change in vacuum settings, the recordings for the 5-mm-thick laminate show more yarn straightening in the early stage of heating compared to the 2-mm-thick laminate. Eventually, the increase in thickness minimises the pre-cure tool-part interaction in the mid-plane (see also Section 7.6). The effect of the resin arrival is consistent, but the magnitude of the drop fluctuates a bit. The measured CTEs in the dry and impregnated stages of the preform are in a similar order of magnitude and agree well with, for instance, Table 6.7. In case of the 10-mm-thick laminate, the exothermic reaction leads to significant thermal spiking in which, initially, the process-induced strain increases. As there is a similarity with the GFR EP04908 laminate, yarn straightening is again held responsible. That the increase is initiated prior to reaching the peak temperature might be attributed to gelation. Before returning back to the cure temperature, a strong decrease in process-induced strain is recorded. The latter is most likely due to vitrification, which increases the CTE of the host structure (see Table 10.1). The statement of earlier debonding for thicker laminates seems to hold here as well. It must be realised, however, that vitrification during thermal spiking may have created additional stresses at the tool-part interface. Overall, the differences in process-induced strains is marginal. The latter is also confirmed by the residual strain measured during thermal annealing. That the drop in strain due to thermal annealing is the largest for the thinnest laminate may be understood from the cure state (see also Figs. 5.8 and 6.22).

Figures 10.9 and 10.10 show the process-induced and residual strains for the 60- and 80-ply laminates¹³. An almost identical behaviour is observed compared to the 40-ply laminate cured at 160 °C (Fig. 10.7). Though, pre-cure tool-part interaction is vanished completely in the middle of the stack. On the left-hand side of Fig. 10.11 the unsymmetrical through-thickness temperature profile is shown for the 80-ply laminate. Using the cure kinetics model (Section 4.3.1), the cure front seems to have propagated inside-out (right-hand side of same figure). The effect of inside-out curing on the

¹²The 2 mm 160 °C-cured laminate corresponds to the one extensively discussed in Section 6.5.

¹³Here, the 2 mm 140 °C-cured laminate discussed in Section 6.6.2 is used as the reference.

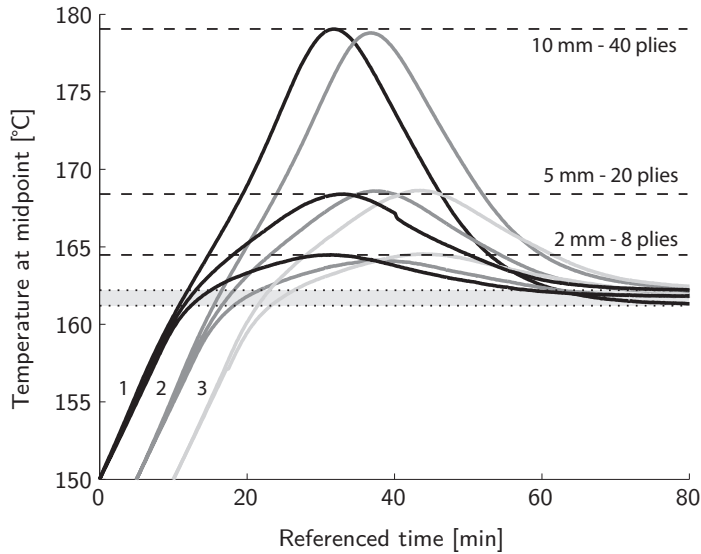


Figure 10.6: Development of exothermic peak in 2, 5, and 10 mm thick GFR RTM6 laminates. The referenced time has its starting point at the moment the internal temperature reached 150 °C. For convenience, the second and third tests are shifted by 5 and 10 min, respectively. The grey area reflects the bandwidth of the cure temperature at the end of the dwell.

thermal strain is highlighted in Fig. 10.12. The difference due to the pre-cure tool-part interaction at the surface and in the mid-plane of the laminate seems to sustain during subsequent curing and cooling down. Please note that the (ϵ, t) -plots are not that useful in this respect (Fig. 10.13). The difference is nonetheless too small to draw solid conclusions on the formation of strains due to the exothermic reaction. In thermal annealing, the FBG sensors respond almost identical (Fig. 10.14).

Two details in the (T, ϵ) -plot of Fig. 10.12, which are related to the FBG sensor near the interface, require further explanation. At the end of the first heating stage the thermal strain increases steadily (encirclement *a*). The CTE is about $11 \mu\epsilon/^\circ\text{C}$. In relation, the resin arrival at the sensor's location causes a larger drop in thermal strain. Secondly, the measured CTE is smaller than usual after the first debonding (encirclement *b*). Instead of finding a slope between the CTEs of aluminium and cured GFR laminate, its value is well below the cured GFR laminate (Table 10.4). For the latter, an analogy with expanding/contracting bimetal is found. Figure 10.15 shows the two paths after completing the cure dwell. Ideally, free conditions are preferred at

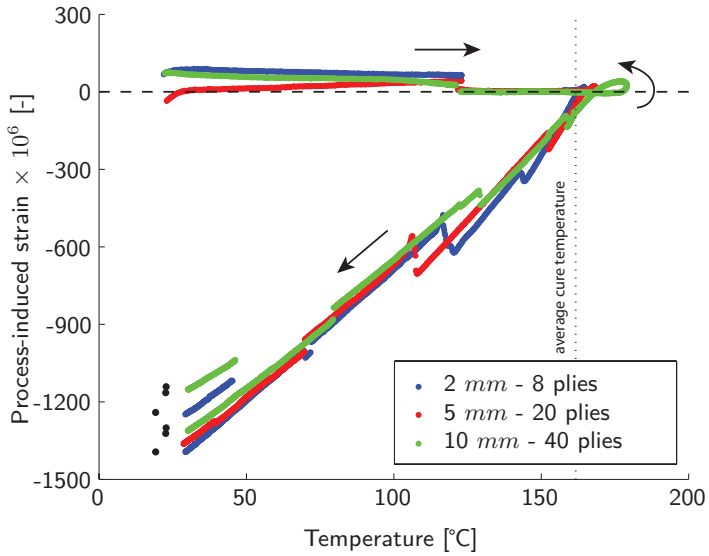


Figure 10.7: Process-induced strains in 2, 5, and 10 mm thick GFR RTM6 laminates cured at 160 $^{\circ}\text{C}$.

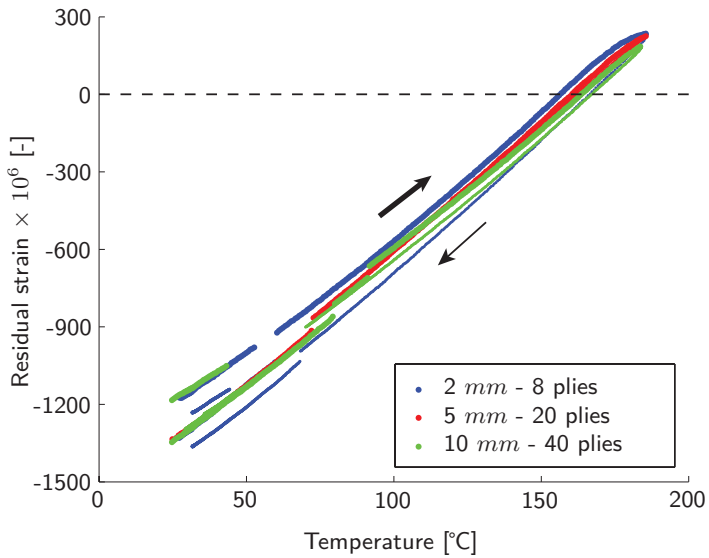


Figure 10.8: Residual strains in reinforcing fibres of 2, 5, and 10 mm thick GFR RTM6 laminates cured at 160 $^{\circ}\text{C}$.

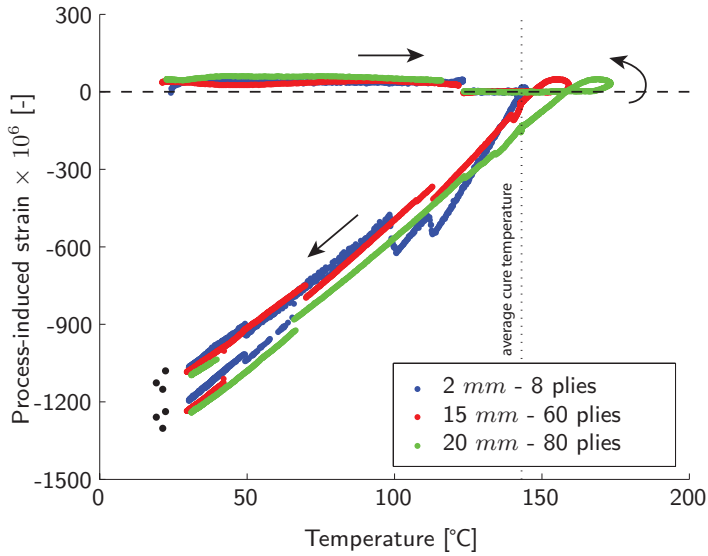


Figure 10.9: Process-induced strains in 2, 15, and 20 mm thick GFR RTM6 laminates cured at 140 °C.

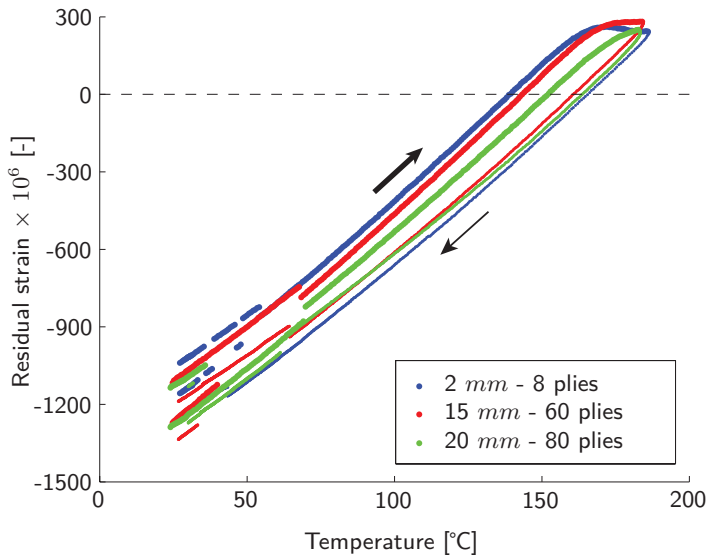


Figure 10.10: Residual strains in reinforcing fibres of 2, 15, and 20 mm thick GFR RTM6 laminates cured at 140 °C.

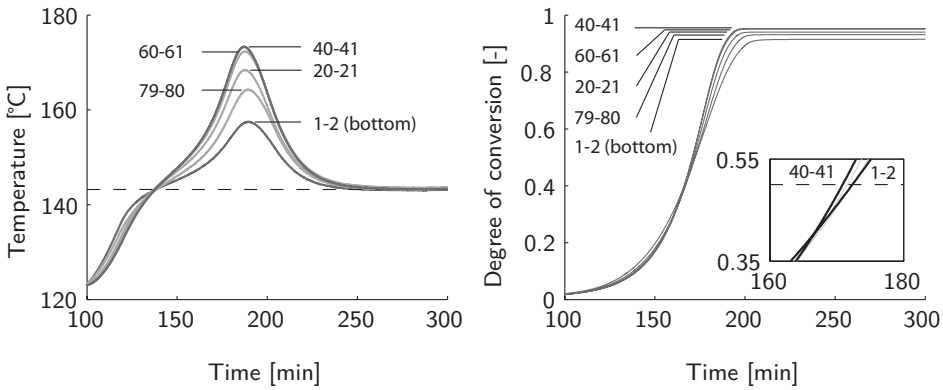


Figure 10.11: Measured through-thickness temperature distribution and estimated degree of cure for the 20 mm-thick GFR RTM6 laminates cured at 140 °C. Dashed line in the inset on the left-hand side is the assumed gelation level of $\alpha = 0.5$.

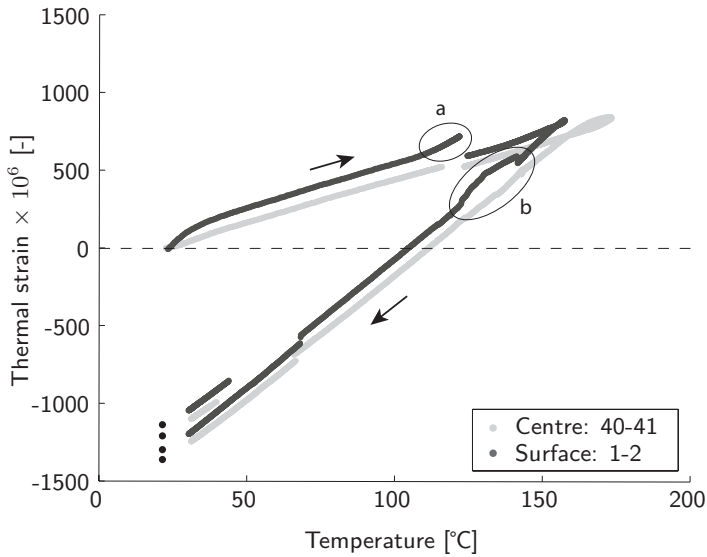


Figure 10.12: Measured thermal strain during processing close to the surface and in the centre of the 20 mm 80-ply GFR RTM6 laminate.

the two interfaces. In practice, the tooling plates are still bonded to the laminate after curing (stage A). After the first debonding, the mismatch in CTEs of both materials

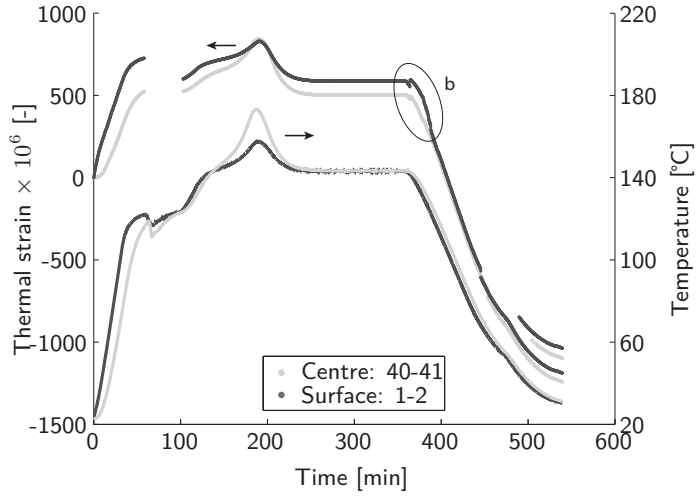


Figure 10.13: Thermal strain and temperature at the surface and in the midplane of the 20 mm 80-ply GFR RTM6 laminate.

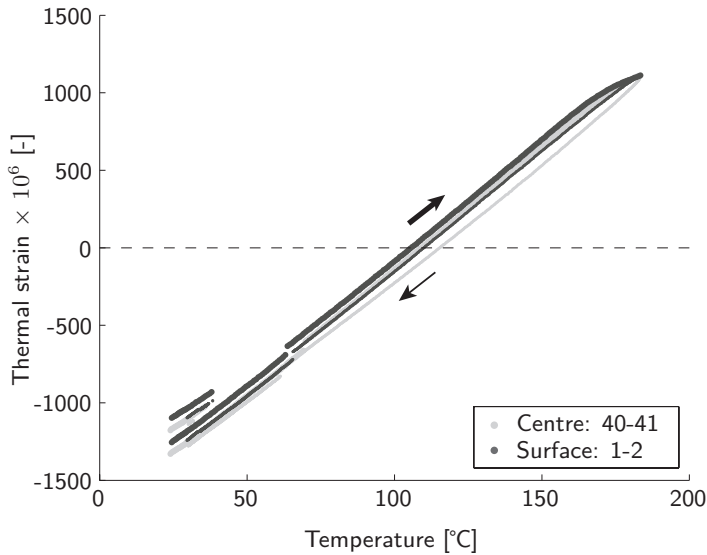


Figure 10.14: Measured thermal strain during thermal annealing close to the surface and in the centre of the 20 mm 80-ply GFR RTM6 laminate.

causes the assembly to bend (stage B). Hence, the measured CTE is lower, because bending introduces tensile mechanical strains that partially counteract the strains due to thermal contraction. After the second debonding, these tensile strains are released

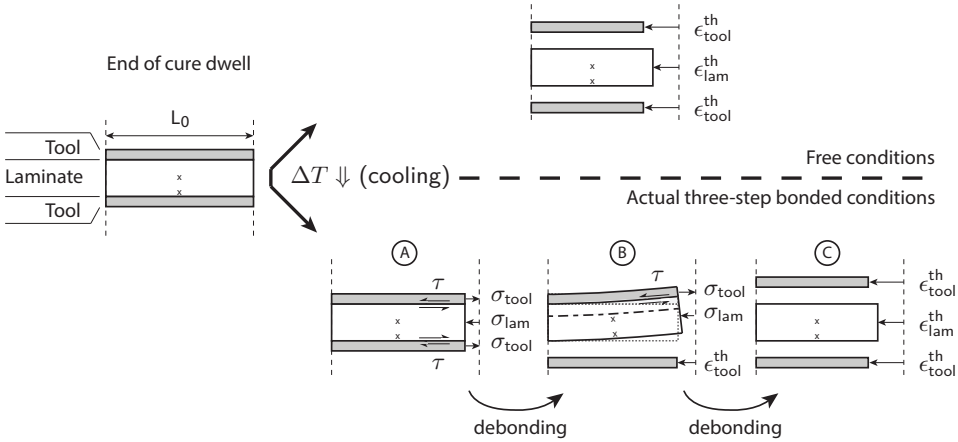


Figure 10.15: Effect of mismatch of CTEs between laminate and tooling during cooling (based on [192]).

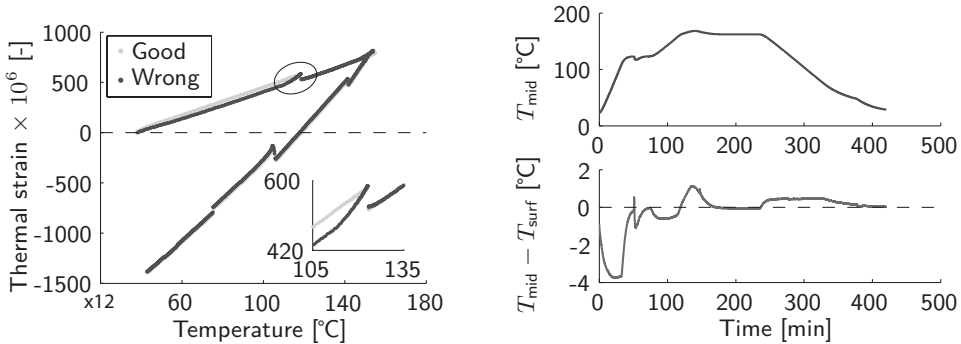


Figure 10.16: Effect of wrong temperature on the (T, ϵ) -plot.

again (under stick-slip conditions). The particular behaviour in the other observation was noted for the first time in Chapter 7. Speculations may point to renewed tool-part interaction due to the decreasing heating rate. Another plausible explanation is illustrated in Fig. 10.16. In addition to the 'good' data set, a 'wrong' data set is created in which the temperature profile comes from the thermocouple embedded near the interface. The temperature difference, which is smaller than 4 °C, results in an identical behaviour.

10.5 Concluding remarks

In this chapter, the Bragg response from embedded FBG sensors were analysed for thick laminates. To support the analysis, the transition in strain due to gelation is linked to the degree of cure in thin GFR RTM6 laminates. A reasonable agreement with literature values is obtained, but, as the reaction rate is relatively high during gelation for epoxy-amine resin systems, a small difference in temperature/time can influence the outcome significantly.

A series of tests for both resin systems, *i.e.* EP04908 and RTM6, were then discussed as part of the exploratory investigation. Pre-cure tool-part interaction seems to affect the Bragg response. The expansion of the dry/impregnated preforms is no longer 'stress-free', but seems to occur in a 'compressive' state. Debonding is found to occur earlier. Bending of the laminate is a source that affects the CTE measurement in further cooling. Scatter in the measured data and the effect of peak splitting make it, however, difficult to detect through-thickness differences in process-induced and residual strains. Some fundamental steps have, nevertheless, been taken in further improving the understanding of the FBG sensing technique in LCM processes. The presentation of a hybrid solution in which the through-thickness temperature is virtually determined while online measuring the strains is still a bridge too far.

Table 10.4: Features of processing and thermal annealing of thin and thick GFR RTM6 laminates.

Laminate	Estimated CTE [$\mu\epsilon/^\circ\text{C}$]					Strain [$\mu\epsilon$]					
	Manufacturing ¹					Thermal annealing		Tool-part interaction ²	Drop at infusion ³	Offset between PVI and TAH ⁵	Drop due to thermal annealing ⁴
	a	b	c	d	e	heat	cool				
8-ply - 140 °C	(95-115)	(130-140)	(140-120)	(111-101)	(98-70)	(70-100)	(100-70)	35	37	61	246
	5.74	5.65	24.21	19.38	15.72	15.72	14.89				
60-ply - 140 °C	(60-100)/(95-115)	(130-155)	(142.5-141)	(135-115)	(100-70)	(70-100)	(100-70)	-17	22 (52)	33	149
	5.61/4.76	5.22	30.51	17.45	15.29	15.48	14.54				
80-ply - 140 °C	(60-100)/(95-114)	(130-160)	(143.3-143)	(142-136)	(100-70)	(70-100)	(100-70)	19	43 (51)	36	86
	5.51/5.21	5.75	49.2	18.95	15.00	15.30	14.38				
80-ply - 140 °C (centre)	(60-100)/(116-122)	(130-150)	(143-142)	(141-131)	(100-70)	(70-100)	(100-70)	117	142 (91) ⁶	-25	66
	5.67/10.93	6.74	22.31	10.51	15.40	15.14	15.08				
8-ply - 160 °C	(95-115)	(130-150)	(161-146)	(142-122)	(100-75)	(70-100)	(100-70)	34	42	119	124
	5.98	5.64	25.09	19.48	15.86	14.68	15.17				
20-ply - 160 °C	(60-100)/(95-115)	(130-160)	(160-153)	(150-110)	(100-70)	(73-100)	(140-120) ⁷	7	63 (58)	69	-15
	5.52/5.69	5.78	24.72	18.11	15.13	15.34	15.27				
40-ply - 160 °C	(60-100)/(95-115)	(130-160)	(161-159)	(150-130)	(100-80)	(95-115)	(115-95)	-10	27 (44)	54	48
	5.73/5.00	5.89	28.68	17.28	15.01	14.58	14.90				

¹ Zones a-e were defined before in Fig. 6.10. ² Starting temperature ranged between 21.2 and 23.3 °C. ³ Infusion temperature ranged between 118.9 and 123 °C. ⁴ Offset determined at 100 °C.
⁵ Values between brackets were determined by using the CTE of the dry fabric measured between 60 and 100 °C. ⁶ Values based on CTE of 5.22 $\mu\epsilon/^\circ\text{C}$ (125 °C - 135 °C) instead of 6.74 $\mu\epsilon/^\circ\text{C}$ (130 °C - 150 °C).
⁷ Optical fibre broke during cooling.

11

CONCLUSIONS AND RECOMMENDATIONS

11.1 Introduction

The objective of this study, as formulated in a research question, was to evaluate whether the FBG sensing technique is an effective method for online monitoring of the formation of process-induced (and residual) strains in typical LCM processes. As such, the gap of verification may eventually be closed that has been caused by a lack of experimental studies on the formation of these strains in thicker composite parts.

This chapter summarises the conclusions and recommendations of this study. In Section 11.2, conclusions with respect to the background analyses are briefly repeated. The applicability of FBG sensors in LCM processes is discussed in Section 11.3. In Section 11.4 conclusions are drawn that are linked to the actual determination of the process-induced and residual strains. Evident by the many speculations and open ends in this study is the need for further research. Areas for future work are therefore outlined in Section 11.5.

11.2 Conclusions: background

In Chapter 1, LCM processes have been promoted for the manufacturing of complex-shaped, and even thicker composite parts. Conventional curing of these thick parts may result in excessively high localised temperatures. Verified simulation-based optimisation techniques are considered essential to suppress the negative effects of these hot spots, because trial-and-error approaches are time-consuming and expensive.

11.2.1 Cure modelling and optimisation of thick composite parts

Even the simplest cure simulation, a one-dimensional lumped model for the determination of the through-thickness thermochemical state, puts a high demand on material characterisation. Assuming constant parameters throughout the cure, this partial model requires still a dozen parameters to be evaluated *a priori*. This number grows rapidly when the model is extended to determine process-induced strains. Failed assumptions in the model, incorrect modelling of the occurring physical phenomena, and/or incorrect values for the parameters, can be sources that affect the quality of the simulation.

A wide variety of optimised cure cycles for thicker composite parts has been proposed. The classical way to reach a complete cure without material degradation due to the exothermic nature of the reaction is to cure slower by lowering the heating rate. Including the minimisation of processing time as a reasonable sub-objective results in shorter cure cycles with multiple dwells. Herein, cycles typically include a 'cooling and reheating' step or an intermediate dwell. Satisfying the objective function would result automatically in parts with theoretically the 'best' quality. An incorrect fitness function would, however, have a detrimental impact.

11.2.2 Monitoring composites manufacturing processes by FBG sensors

That experimental work must supplement the simulation tools is recognised as a bottleneck in studying the formation of process-induced and residual strains. To this end, optical fibre based techniques such as FBG sensing are seen as most adequate and promising for serving this particular purpose.

Many studies have demonstrated the potential of the FBG sensor by discussing results for a wide variety of neat resin and composite specimens and their manufacturing techniques. Careful interpretation appears to be mandatory because of the numerous process parameters influencing the Bragg response. For in-lab applications, the use of thermocouples is regularly advised to compensate for thermal influences on standard (uniform) FBG sensors despite the need for *a priori* calibration for thermal sensitivity. The presence of the coating appears crucial: not only does it attenuate non-uniform straining and birefringence, but, most of all, it also improves the handleability of the optical fibre. That the experimentally obtained process-induced strains have not been verified by other means is seen as a missing link in bringing them in more perspective.

11.3 Conclusions: applicability of FBG sensors in LCM

11.3.1 General statement

The high precision and sensitivity of FBG sensors form a threat when coupled to multiphysical processes such as VI and (vacuum-assisted) RTM. That is, a multitude of process parameters/steps influences the Bragg response. Deriving the actual strain state from a single FBG sensor can be imagined as solving a single equation with multiple unknowns. The contribution of each process step/parameter must be deliberately weighted before conclusions can be drawn with respect to the actual strain state. For LCM processes, this implies that this so-called decision-based analysis has to be carried out preferably by a multi-field expert-level operator.

11.3.2 Issues concerning the embedding

Several issues have to be addressed before the FBG sensor can even start fulfilling its actual purpose in LCM processes. Achieving a high survivability rate of the optical fibres and guaranteeing proper functioning of the FBG sensor asks for some level of experience. In this study, positioning and subsequent fixating to the underlying ply of the optical fibre is performed manually. Hence, scatter may have arisen due to poor visual control. Fixating the optical fibre on both sides of the FBG sensor is necessary to maintain the alignment (even more important for an array of FBG sensors), to avoid fibre slipping (at low compaction pressure) and to minimise strain transfer through the optical fibre. The proposed solution for embedding is, however, not yet ideal for industrialised LCM processes. Non-uniform straining may be levelled out by proper selection of the gauge length with respect to the tow width, but peak splitting due to transverse stresses remains problematic in determining the actual strain state. Finally, the coating on the optical fibre can be tolerated during testing even when the computational analysis is carried out using properties of the uncoated FBG sensor only.

11.3.3 Operator's experience

When the operator is still at a beginner's level, monitoring by means of FBG sensors is an excellent method to familiarise with the designated composites manufacturing process. In fact, every change in the Bragg response should trigger the person to identify the cause. In this study, in which solely LCM processes are evaluated, it has

been shown that (some) knowledge is required in the areas of: (i) preform compaction, (ii) thermal behaviour of (un)constrained preforms, (iii) (non-)isothermal resin flow, (iv) cure behaviour, *e.g.* kinetics and rheology of resin systems, and (v) debonding effects due to tool-part interaction. Thus the operator masters himself in different fields, while analysing the Bragg response. At this level, wrong conclusions may, however, easily be drawn. Considering the use of FBG sensors, extensive testing is, therefore, a prerequisite to confirm found solutions. Once more, only an experienced operator may be capable of retrieving useful data from the Bragg response in processes based on LCM.

11.4 Conclusions: determination of process-induced and residual strains

Two phenomena have been investigated in more detail: tool-part interaction in the early stage of the cure cycle and the effect of resin flow and its arrival at the sensor's location. Note here that most of the research has been conducted on vacuum-infused laminates with a small thickness. Some conclusions about monitoring of the vacuum-assisted RTM process are presented in the last paragraph.

11.4.1 The LoZS-method

Selecting a common point, *e.g.* the start of cure cycle, is not a proper choice for correlating the Bragg responses from different tests. Instead of this, a secondary technique is proposed in which the LoZS of the reinforcement is determined by thermal annealing. In this way, the Bragg response can be converted to process-induced strains in the reinforcing fibres¹. The method relies on the assumption that the reinforcement expands freely above the glass transition temperature. That the measurements during thermal annealing are carried out with the same embedded sensors (FBG and thermocouple) eases the comparison with manufacturing data. The choice of RTM6, or any other high-temperature curing resin system in general, as a reference resin system is debatable in investigating this approach. The high glass transition temperature leaves a small window for determining the LoZS². More fruitful attempts for gaining insight have been reported for the low-temperature curing matrix. A set of rules based on the latter is required for the former.

¹By using the generalised Hooke's law, the process-induced strains in the matrix can also be retrieved.

²The upper limit is dictated by material degradation.

11.4.2 Pre-cure tool-part interaction

In literature, the initially non-linear behaviour while heating, as expressed in a (T, ϵ) -plot, is attributed to resin flow. A dry run indicates, however, that the matrix has a negligible influence. Further testing points to pre-cure tool-part interaction due to the mismatch in CTEs of the tooling and preform. As a proof, different tooling material are used. Pre-cure tool-part interaction behaves linearly with the compaction pressure (up to 1 *bar*). The higher the compaction pressure the more 'tensile' straining is observed. In tests with single-sided tooling, pre-cure tool-part interaction reduces by 50%, because the frictional forces act only on one side. In thicker preforms, the pre-cure tool-part interaction vanishes towards the middle of the stack. The LoZS proofs, however, that the reinforcing fibres do not get loaded in tension, but are merely in a stress-free state.

Considering the fact that yarn straightening may have such a profound effect on the Bragg response, several speculations are currently needed for interpreting the LoZS. This is mainly because yarn straightening obscures the transition between reinforcing fibres being under compression and tension. Consequently, decision-based analysis is required to deal with the apparent strain associated to yarn straightening. In anticipating the section about recommendations, it would have been interesting here to make a direct comparison with cross-ply laminates for which crimp can be considered minimal (a simpler case).

11.4.3 Resin flow as a disturbing factor

Characteristically for all LCM processes is the filling stage. With respect to online monitoring by FBG sensors, resin flow, or more precisely, the resin arrival at the sensor's location seems to act as a disturbing factor in the analysis. For RT filling (and single-sided tooling), it is shown by digital image correlation that the Bragg response appears to be inversely proportional to the variation in preform thickness. In high-temperature filling (and double-sided tooling), the optical fibre becomes loaded in tension prior to filling. Upon resin arrival, the temporary loss of compaction pressure may result in sudden contraction of the optical fibre. Furthermore, the time-delayed response between the FBG sensor and the accompanying thermocouple makes the analysis of the filling stage in the (T, ϵ) -plot risky. In both cases, the changes in Bragg response cannot be linked to in-plane variations in strain in the reinforcing fibres.

11.4.4 Other trends in monitoring the curing of GFR laminates

Cure-induced straining occurs only for a low fibre volume fraction, because the reinforcing fibres act as a constraint³. Thermal influences dominate mostly the Bragg response. In studying the effect of the cure regime, the cure temperature (as long as it stays below the ultimate glass transition temperature) is the primary source for differences. The higher the cure temperature the more strains are introduced in the reinforcing fibres. As a secondary source, the gelation during heating should be mentioned. Thermal annealing cancel these differences. In thicker GFR laminates, the thermal spike does not only led to additional curing. Apparently, the reinforcing fibres get initially 'tensioned'. It is believed that yarn straightening, which is absent at the start, causes this apparent strain. Towards the end of the thermal spike, the rubber-to-glass transition, in which the resin's CTE changes, results in compressive straining. A single test with multiple embedded FBG sensors has not been able to confirm whether the through-thickness thermal (and cure) gradients lead to additional straining.

The effect of a higher fibre volume fraction becomes evident in monitoring thin laminates produced by vacuum-assisted RTM⁴. Apparently, mould closing puts the reinforcing fibres in tension. In addition, the higher compaction pressure (up to several bars) results in typical stick-slip behaviour in subsequent heating. At RT conditions, a peripheral injection strategy can reduce the tensile prestrain in the reinforcing fibres. Sudden strain releases have been recorded in high temperature mould filling. Neither the resin arrival nor the stepwise increase in injection pressure are identified as the trigger. Upon curing, CLT-calculations indicate that about 75% of the tensile prestrain in the reinforcing fibres should be released after demoulding. The concise set of experimental data does not allow to confirm this statement in detail, but there has been a clear offset with the LoZS⁵.

Overall, the LoZS-method helps in improving the determination of process-induced and residual strains in flat laminates manufactured by LCM processes. Some interesting trends have been distilled that have enlarged the understanding of the formation of these strains. The approach is, nevertheless, still open for further improvement.

³It has to be seen whether the cure-induced strain in the optical fibre can be translated to the reinforcing fibres on a one-to-one basis.

⁴Due to the poor design of the sensor's throughput channel, testing of thicker laminates has not been considered here.

⁵It is speculated that the out-of-plane elastic deformation of the preform during compaction can contribute to this offset as well.

11.5 Recommendations - conceptual foundation to proceed

11.5.1 Towards a hybrid solution for online process monitoring and cure modelling

Defined as one of the research goals, the development of a hybrid solution for online process monitoring and cure modelling has not been fully accomplished yet. Future researchers are encouraged to continue along this route. Ultimately, this solution may exclude the (intrusive) thermosensors from the list of embedded sensors. A verified cure model may then be extended towards the calculation of process-induced strains. In this field, a recent attempt has been reported by Khoun *et al.* [192] for thin CFRP laminates in an RTM application.

11.5.2 How FBG sensors can become useful in industrialised LCM processes

The LoZS-method is recognised as an important step towards industrialising the use of FBG sensors in composites manufacturing processes. Whether this method can be extended to other more complex-shaped parts, *e.g.* curved or L-shaped, has to be proven in the near future. Perhaps that a set of rules (knowledge-based driven) from simpler cases is needed to interpret the measured strains. Eventually, thermal annealing may even become superfluous. As such, the determination of process-induced and residual strains relies then solely on online process monitoring, but with an improved understanding.

At the current research level, FBG sensors are best described as decision-based monitoring tools, because each contribution to the Bragg response has to be weighted carefully. This implies that a fully quantitative analysis of the in-plane strains cannot be presented yet. In this study, speculations let the effect of preform compaction be ignored in evaluating the measured strains for low compaction pressure. Digital image correlation may be an interesting technique to verify this assumption. Similarly, the effect of resin flow on the Bragg response needs to be explored in more detail than presented in Chapter 8. The orthotropic nature of the composite material, which causes peak splitting in the Bragg response, may be added as another source for currently sticking to qualitative conclusions. In this respect, comparing the Bragg

responses of embedded sensors with aligned surface-mounted ones may reveal (an) interesting trend(s).

So far, the embedding procedure, which is another major concern in industrialising the FBG sensing technique, has not been touched upon in this discussion. It may be worth to reconsider the manual placement of sensors in view of reproducibility. A better control of the lay-up, *e.g.* by automation, may reduce the scatter in CTE values and allow then for proper comparison of different settings in manufacturing. To avoid artificial delaminations by the tapes, it is believed that, at least for high-temperature applications, binding with a thermoplastic glue may be a solution. Another interesting option may be co-weaving (by replacing a tow or by integrating into a tow), but the execution may be troublesome for an array of FBG sensors. No matter which technique is selected a closer look is needed to assess its effect on pre-cure tool-part interaction. Other remaining actions with respect to the embedding procedure are: presenting an industrially feasible concept for protecting the optical fibre at the egress point and assessing the level of intrusiveness of the embedded optical fibre.

11.5.3 Other steps guiding further investigation

The FBG sensing technique is interesting for studying the pre-cure tool-part interaction. Although simplification has been the keyword here in studying the Bragg response to LCM processes, the selection of a woven fabric as reinforcement complicates the analysis significantly due to yarn straightening. Comparing with a cross-ply, suggested in Section 11.4, may prove some of the assumptions. Correlating with tensile testing may also confirm that yarn straightening is important in pre-cure tool-part interaction^{6,7}.

In studying the effect of the compaction pressure, the amount of strain associated to pre-cure tool-part interaction has been determined for dry preforms only. The effect of the resin flow seems marginal, but this has not been proven for prepregs used in autoclaving processes. The stickiness of the resin can alter the slipping conditions and thus the amount of strain related to pre-cure tool-part interaction. The approach of modelling the tool-part interaction by an interface layer, as proposed in [205], can be verified then online.

⁶Thermal straining due to a mismatch in CTEs of the tooling and preform has an analogy with straining the same preform by a mechanical load.

⁷The presence of yarn straightening on the mechanical properties of the cured laminate is worthwhile to investigate as well. It can be imagined that non-fully straightened yarns, *e.g.* in thicker preforms, put a higher demand on the matrix during mechanical loading.

Another interesting point is the verification of the FBG-based method in measuring the strain during thermal annealing and the subsequent retrieving of the LoZS. Making a comparison with the method proposed in [183] has already been addressed in Chapter 5. The requirement of a smaller specimen size seems to obstruct a direct comparison. Digital image correlation may again be a good substitute in case an oven with an inspection window is available. There may be some practical issues, *e.g.* air circulation inducing swinging of the laminate or degradation of the paint, that need some attention, but these may not be stand-in-the-ways to do at least some preliminary testing.

A

RESPONSES OF GRATINGS IN DIFFERENT OPTICAL FIBRES

In a single experiment, three different optical fibres, each of them equipped with a single FBG sensor, are embedded in a glass woven preform. The characteristics of the optical fibres are: (1) standard optical fibre (OF) with coating (FBG1), (2) polyamide coated OF supplied by a third party (FBG2), and (3) standard OF without coating (FBG3). In the analysis, the properties of the uncoated OF are used to determine the process-induced and residual strains. Three thermocouples accompanied the optical fibres. The manufacturing of the GFR laminate follows the procedure described in Chapter 4. A picture of the laminate after demoulding as well as a schematic representation are shown in Figure A.1. Typical for the VI laminates produced with this set-up is the gradual variation in thickness from inlet to vent (Fig. A.2).

Embedding of the optical fibres and subsequent preform compaction by applying vacuum results in a fairly constant Bragg response among the three optical fibres (Table A.1). Spiking of the Bragg responses indicates apparently the arrival of the resin at the sensor's location (Fig. A.3). The flow propagates thus from left to right (see right-hand side of Fig. A.1). Remarkably, OF 3 reacts differently after resin arrival. According to the theory presented in Chap 8, in which the Bragg response are linked to the variation in preform thickness, it is speculated that the preform gets locally compacted. The Digital Image Correlation (DIC) technique has not been applied yet to verify this statement for this particular test set-up. The decrease in the compaction pressure at point *ii* causes a drop in Bragg response in all three FBGs,

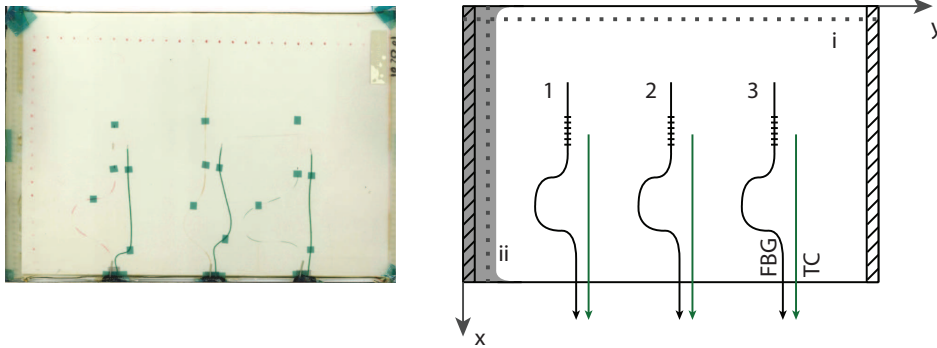


Figure A.1: LHS: Image of manufactured laminate, RHS: schematic representation.

which is probably due to the increase in preform thickness (see Chapter 8). The magnitude of the Bragg responses to the filling stage differs as well. That this does not influence the process-induced and residual strains in the reinforcing fibres, as shown in Figs. A.4 and A.5, is seen as a proof for leaving out the filling stage at RT in the strain analysis. The slopes of the LoZS are in the range of measured CTEs reported in Fig. 6.27. The influence of the thermocouples and their position on the scatter is marginal (Table A.2). Furthermore, the variation in laminate thickness can not be seen as the cause of the scatter.

In general, a good agreement is obtained with the 80 °C-cured laminate presented earlier (Figs. 5.8, 5.9 and 6.16). Please note that the uncoated optical fibre shows peak splitting during cooling down. In case of birefringence, the peak with the lowest Bragg wavelength seems to describe better the formation of process-induced strain. In the strain plots, the coating appears to have a marginal effect. Though, plotting the responses against each other in a pairwise fashion shows that the standard coated FBG sensor behaves slightly different during the initial part of heating the impregnated preform. In cooling down of the assembly, the Bragg responses are identical (ignoring the higher Bragg wavelength of the split peaks). In thermal annealing (Fig. A.8), the coated FBG sensors shows identical behaviour. A kink at the glass transition temperature is observed in comparing the standard coated and uncoated FBG sensor. Contributing effects are the difference in the slope of the LoZS and the transverse stresses causing peak splitting in the uncoated FBG sensor.

On a global level, all three FBG sensors measure similar straining in manufacturing irrespective of their differences in coating options and their position in the laminate.

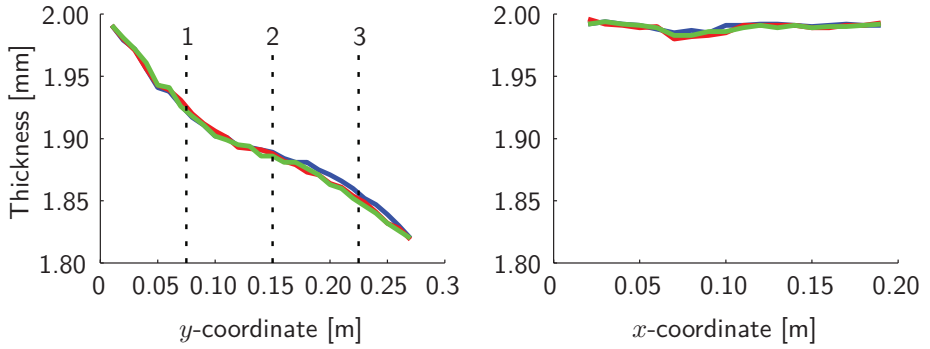


Figure A.2: Thickness profiles, measured three times, along lines *i* and *ii* (see Fig. A.1).

Table A.1: Effect of compacting preform on Bragg response.

Sensor	1	2	3
I - Wavelength [nm] - before	1549.914	1550.150	1542.301
II - Wavelength [nm] - after	1550.413	1550.620	1542.840
Apparent strain [$\mu\epsilon$]	404	381	439

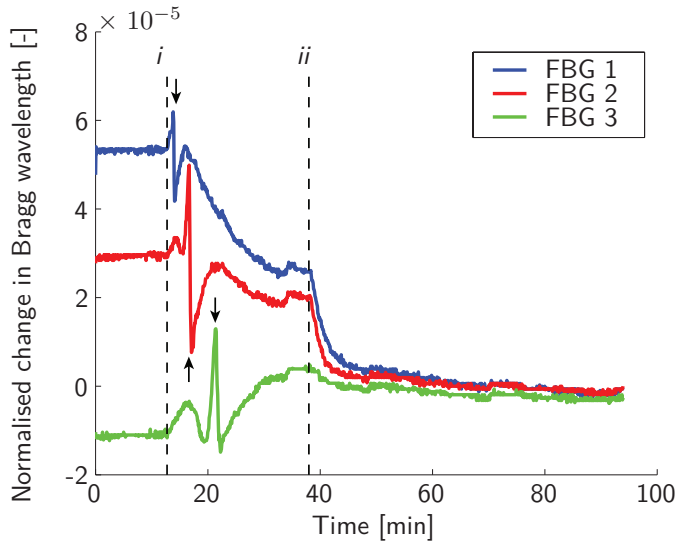


Figure A.3: Bragg response while infusing glass fibre preform.

Table A.2: Effect of interchanging thermocouple data in calculating CTE values of laminate above its glass transition temperature.

FBG sensor	1	2	3
CTE [$\mu\epsilon/^\circ\text{C}$] (TC 1)	5.339	5.250	5.677
CTE [$\mu\epsilon/^\circ\text{C}$] (TC 2)	5.353	5.263	5.692
CTE [$\mu\epsilon/^\circ\text{C}$] (TC 3)	5.350	5.260	5.688
<i>Mean</i>	5.347	5.258	5.686
<i>Standard deviation</i>	0.0071	0.0071	0.0077

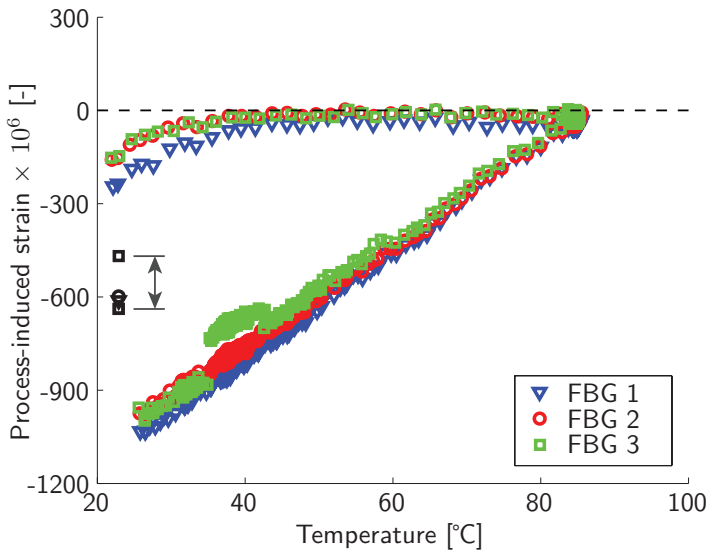


Figure A.4: Process-induced strains in GFR laminate.

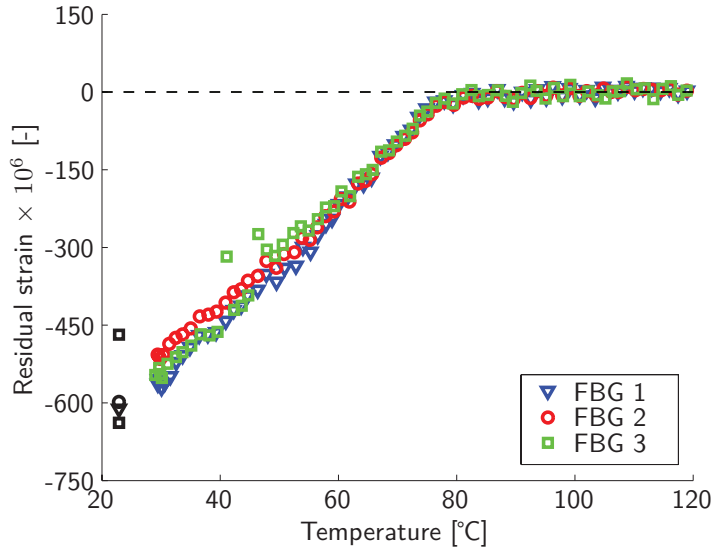


Figure A.5: Residual strains in GFR laminate.

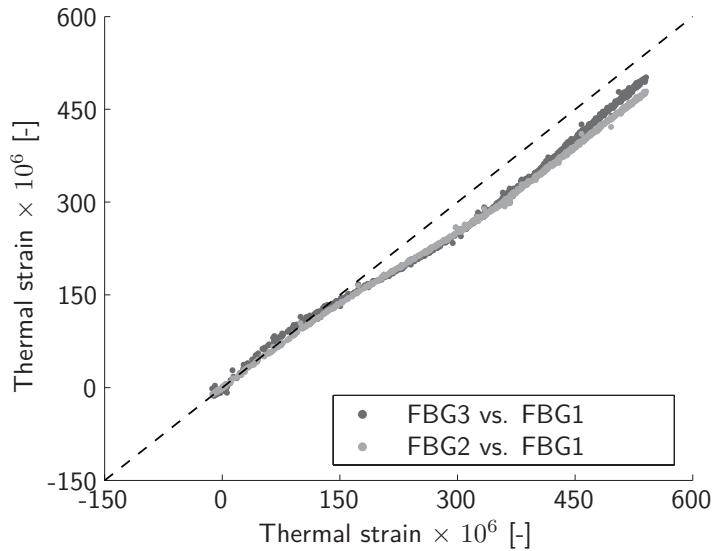


Figure A.6: Thermal straining - Comparison of Bragg responses (Heating up of mould assembly).

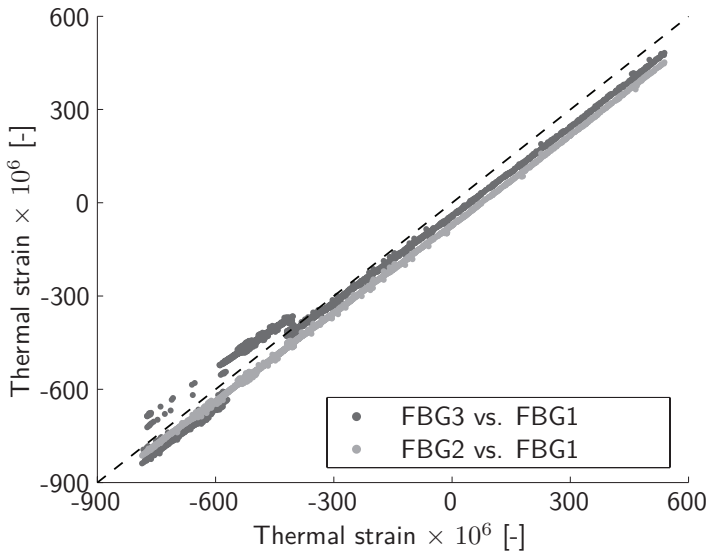


Figure A.7: Thermal straining - Comparison of Bragg responses (Cooling down of mould assembly).

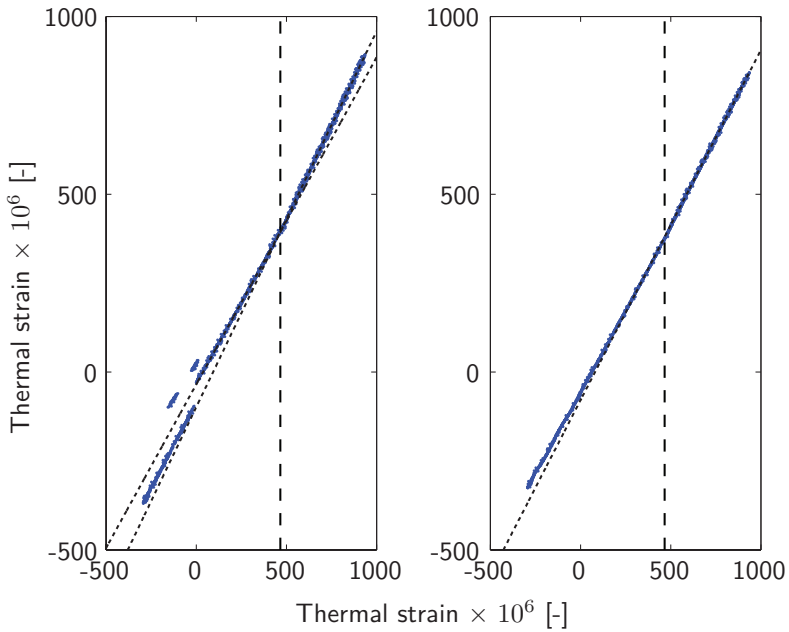


Figure A.8: Thermal annealing - comparison of Bragg responses - LHS: FBG3 vs. FBG1, RHS: FBG2 vs. FBG1.

B

EFFECT OF WRONG RTM6 RESIN MIXTURE

Mistakenly mixing the two components of the RTM6-2 resin system with a wrong ratio does affect the glass transition temperature (Fig. B.1 vs. Fig. 6.13). Due to the lower glass transition temperature, the process-induced and residual strains in the reinforcing fibres were less than usual (see again Fig. 6.13). Table B.1 lists the slopes for the different segments, as defined in Chapter 6. There is no significant deviation observed with other CTE values measured before (see Fig. 6.27 and Tables 6.7). Though, the slope of the LoZS, which is $5.17 \mu\epsilon/^\circ\text{C}$, is again significantly less than the CTEs recorded during heating up of the dry/impregnated preform. A possible explanation is given in Section 6.8.

The mistake allowed for a closer look at the LoZS, because the temperature range in which the matrix is now in a rubber state extends to a lower temperature. Consequently, a better approximation of the LoZS is found without risking material degradation. There is a clear offset between the LoZS and the line describing the thermal straining of the impregnated preform. Figure B.2, an enlarged version of Fig. B.1, highlights this offset. At the infusion, the drop in strain measures $53 \mu\epsilon$ (see point 1). The offset itself, indicated by point 2 in the same figure, is of similar order of magnitude: $45 \mu\epsilon$ at 155°C . As mentioned in Section 6.5.3, additional yarn straightening at the glass-to-rubber transition is likely a source.

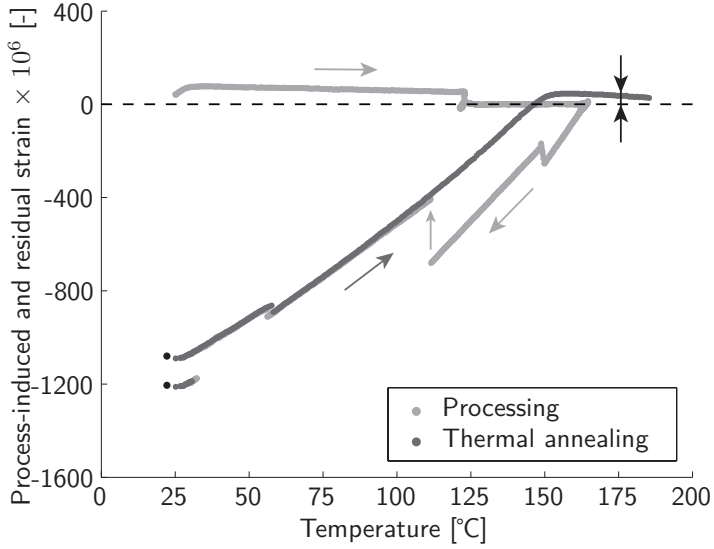


Figure B.1: Experimental data for GFR RTM6 laminate cured at 160 °C (Wrong resin mixture).

Table B.1: Linear fitting in temperature segments *a-e* (defined in Fig. 6.10).

Name	Estimated CTE [$\mu\epsilon/^\circ\text{C}$] for temperature zone [$^\circ\text{C}$]				
	<i>a</i>	<i>b</i>	<i>c</i>	<i>d</i>	<i>e</i>
	(95-115)	(130-150)	(162-156)	(142-122)	(110-90)
GFR RTM6 wrong	5.61	5.88	24.21	19.2	15.0

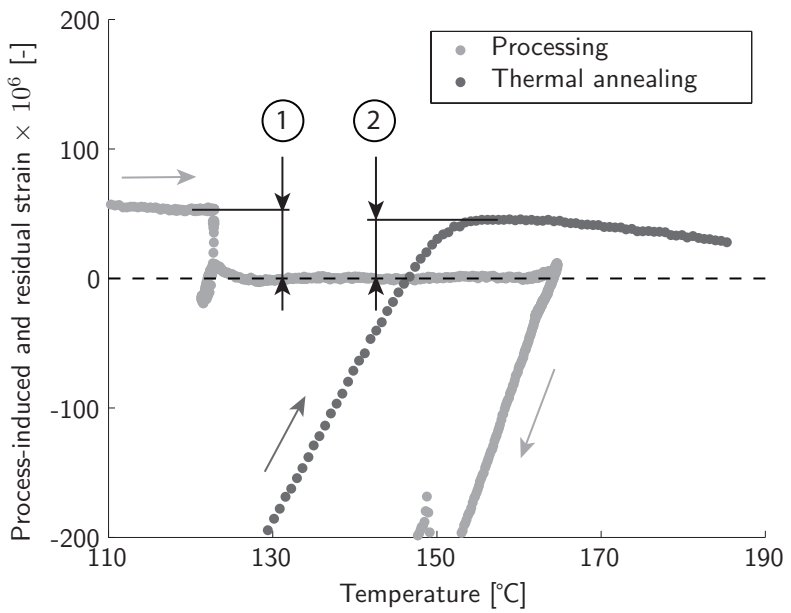


Figure B.2: Enlargement of Fig. B.1.

C

REPRODUCIBILITY: VACUUM-INFUSED GFR RTM6 LAMINATES

To assess the reproducibility, a series is conducted in which three GFR RTM6 laminates have been manufactured at nearly similar conditions¹. Evaluated data are listed and graphically presented in Tables C.1 and C.2 and Figures C.1, C.2 and C.3, respectively. Despite some minor fluctuations in CTE for the different segments and changes in thermal strain due to resin arrival and thermal annealing, it is concluded that there is a good mutual agreement on a global level. As the effectiveness of the release layer decreases for consecutive manufacturing, the postponement of debonding to lower temperature can be clarified. More strain is temporarily built up at the interface due to this 'better' adhesion. Since these strains are released as soon as debonding occurs, a significant difference in residual strain is not observed.

¹Filling is performed at a lower temperature in the third test, but this seems not to have influenced the comparison.

Table C.1: Linear fitting to curves a-e (defined in Fig. 6.10) for different GFR RTM6 laminates.

Name	Estimated CTE [$\mu\epsilon/^\circ\text{C}$] for temperature zone [$^\circ\text{C}$]				
	a (95-115)	b (130-150)	c (161-146)	d (142-122)	e (110-90)
GFR RTM6 I	5.98	5.64	25.09	19.48	15.81
GFR RTM6 II	5.64 ¹	5.99	24.97 ²	18.98 ³	15.39
GFR RTM6 III	5.74	5.98	25.06 ²	19.82 ⁴	15.61 ⁵

¹ (80-100) ² (161-141) ³ (134-122) ⁴ (130-115) ⁵ (102-82)

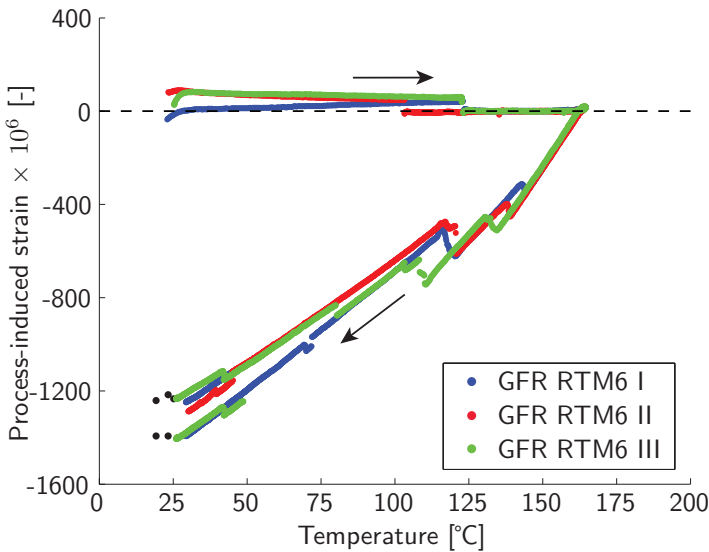


Figure C.1: Process monitoring of GFR RTM6 laminates - repetition.

Table C.2: Change in thermal strain due to resin arrival at FBG sensors and thermal annealing.

Name	Infusion temperature [$^\circ\text{C}$]	Drop in process-induced strain at infusion [$\mu\epsilon$]	Averaged drop in residual strain due to thermal annealing [$\mu\epsilon$] ¹
GFR RTM6 I	123	42	111 (1.7)
GFR RTM6 II	123	41	67 (3.2)
GFR RTM6 III	103	62	62 (1.9)

¹ Temperature range between 140 and 160 $^\circ\text{C}$ (stepsize of 5 $^\circ\text{C}$)

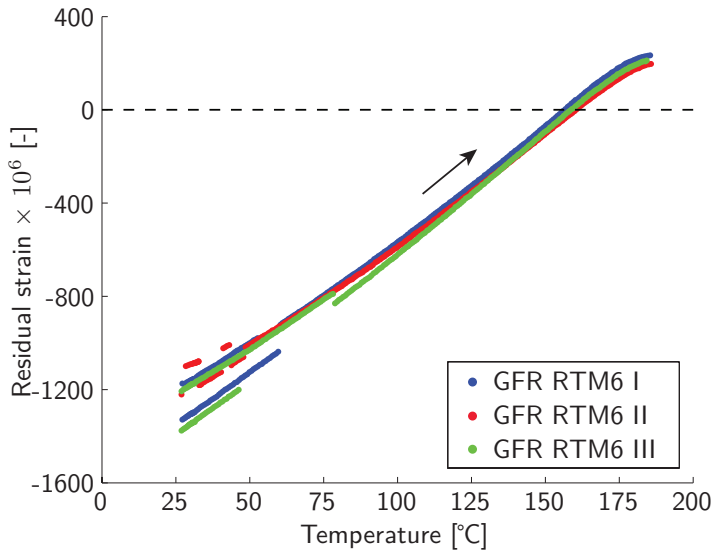


Figure C.2: Thermal annealing of GFR RTM6 laminates - repetition (heating only).

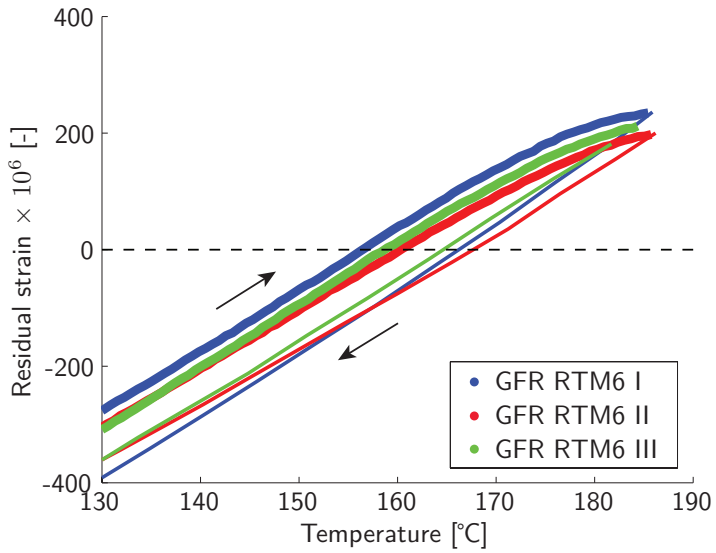


Figure C.3: Thermal annealing of GFR RTM6 laminates - repetition (zoom).

REFERENCES

- [1] J. Hale. Boeing 787 - from the ground up. *AERO Magazine*, 6(4):17–23, 2006.
- [2] C. Red. Aviation outlook: fuel pricing ignites demand for composites in commercial transports. *High-Performance Composites*, July 2008. Available from: <http://www.compositesworld.com/articles/aviation-outlook-fuel-pricing-ignites-demand-for-composites-in-commercial-transport>.
- [3] European Transport Research. Advanced low-cost aircraft structures. Available from: http://ec.europa.eu/research/transport/projects/article_3675_en.html.
- [4] G. Watson. ALCAS - advanced low-cost aircraft structures, February 2007. Available from: <http://uko.tubitak.gov.tr/Toplantidokumanlari/1ce6048b-d9d5-4aae-ab8a-9ffb069ea312.pdf>.
- [5] H. De Vries. Development of the ALCAS main landing gear attachment fitting. In *Proceedings of the SEICO 10, SAMPE Europe 31st International Technical Conference & Forum, Paris, France, April 12–14, 2010*, pages 501–507, 2010.
- [6] S. Topping. Resin transfer moulding of a wing inner rear spar. In *Proceedings of the SEICO 10, SAMPE Europe 31st International Technical Conference & Forum, Paris, France, April 12–14, 2010*, pages 495–500, 2010.
- [7] M. Siemetzki, K. Zimmermann, and P. Middendorf. Ultra-thick laminates - chances and limitations. In *Proceedings of the 17th International Conference on Composite Materials, Edinburgh, UK, July 27–31, 2009*, pages 1–10, 2009.
- [8] B. Berenberg. Liquid composite molding achieves aerospace quality. *High-Performance Composites*, November 2003. Available from: <http://www.compositesworld.com/articles/liquid-composite-molding-achieves-aerospace-quality>.
- [9] D. Brosius. Boeing 787 update. *High-Performance Composites*, May 2007. Available from: <http://www.compositesworld.com/articles/boeing-787-update>.
- [10] M. Jinno, S. Sakai, K. Osaka, and T. Fukuda. Smart autoclave processing of thermoset resin matrix composites based on temperature and internal strain monitoring. *Advanced Composite Materials*, 12(1):57–72, 2003.
- [11] E. Ruiz and F. Trochu. Multi-criteria thermal optimization in liquid composite molding to reduce processing stresses and cycle time. *Composites Part A: Applied Science and Manufacturing*, 37(6):913–924, 2006.

References

- Selected contributions from the 7th International Conference on Flow Processes in Composite Materials held at University of Delaware, USA.
- [12] D. J. Michaud, A. N. Beris, and Dhurjati P. S. Thick-sectioned RTM composite manufacturing: Part ii - robust cure cycle optimization and control. *J. of Comp. Mater.*, 36(10):1201–1231, 2002.
- [13] P. P. Parlevliet. *Residual strains in thick thermoplastic composites - An experimental approach*. PhD dissertation, Delft University of Technology, Delft, The Netherlands, 2010.
- [14] M. A. Seif, U. A. Khashaba, and R. Rojas-oviedo. Residual stress measurements in CFRE and GFRE composite missile shells. *Composite Structures*, 79(2):261–269, 2007.
- [15] V. Antonucci, M. Giordano, A. Cusano, J. Nasser, and L. Nicolais. Real time monitoring of cure and gelification of a thermoset matrix. *Composites Science and Technology*, 66(16):3273–3280, 2006. Manufacturing, Processing and Characterisations of Polymer Composites.
- [16] E. Chailleux, M. Salvia, N. Jaffrezic-Renault, V. Matejec, and I. Kasik. In situ study of the epoxy cure process using a fibre-optic sensor. *Smart Materials and Structures*, 10(9):194–202, 2001.
- [17] E. Chehura, A. A. Skordos, C. C. Ye, S. W. James, I. K. Partridge, and R. P. Tatam. Strain development in curing epoxy resin and glass fibre/epoxy composites monitored by fibre Bragg grating sensors in birefringent optical fibre. *Smart Materials and Structures*, 14(9):354–362, 2005.
- [18] D. J. Michaud. *Simulation-based design optimization and control of thick composite laminates manufactured by resin transfer molding*. PhD dissertation, University of Delaware, Delaware, United States of America, 2000.
- [19] R. S. Parnas. *Liquid composite molding*. Carl Hanser Verlag, Munich, Germany, 2000.
- [20] A. B. Strong. *Fundamentals of composite manufacturing - Materials, methods, and applications*. Society of Manufacturing Engineers, Michigan, United States of America, 2008.
- [21] S. G. Advani and E. M. Sozer. *Process modeling in composites manufacturing*. Marcel Dekker AG, Switzerland, 2003. in Manufacturing engineering and materials processing - A series of reference books and textbooks.
- [22] A. C. Loos and G. S. Springer. Curing of epoxy matrix composites. *Journal of Composite Materials*, 17(2):135–169, 1983.
- [23] T. A. Bogetti and J. W. Gillespie. Two-dimensional cure simulation of thick thermosetting composites. *J. of Comp. Mater.*, 25(3):239–273, 1991.
- [24] T. A. Bogetti and J. W. Gillespie. Process-induced stress and deformation in thick-section thermoset composite laminates. *J. of Comp. Mater.*, 26(5):626–660, 1992.
- [25] P. R. Ciriscioli, Q. Wang, and G. S. Springer. Autoclave curing - comparisons of model and test results. *J. of Comp. Mater.*, 26(1):90–102, 1992.
- [26] L. N. Hjellming and J. S. Walker. Thermal curing cycles for composite cylinders with thick walls and thermoset resins. *Journal of Composite Materials*, 23:1048–1064, 1989.

- [27] G. M. Martinez. Fast cures for thick laminated organic matrix composites. *Chemical Engineering Science*, 46(2):439–450, 1991.
- [28] T. E. Twardowski, S. E. Lin, and P. H. Geil. Curing in thick composite laminates: Experiment and simulation. *J. of Comp. Mater.*, 27(3):216–250, 1993.
- [29] S. R. White and C. Kim. A simultaneous lay-up and in situ cure process for thick composites. *Journal of Reinforced Plastics and Composites*, 12(5):520–535, 1993.
- [30] R. J. J. Williams, M. A. Benavente, R. A. Ruseckaite, M. S. Churio, and H. G. Hack. Criteria for selecting cure cycles in autoclave processing of graphite/epoxy composites. *Polymer Engineering & Science*, 30(18):1140–1145, 1990.
- [31] D. H. Lee, S. K. Kim, W. I. Lee, S. K. Ha, and S. W. Tsai. Smart cure of thick composite filament wound structures to minimize the development of residual stresses. *Comp. Part A: Appl. Sci. and Manuf.*, 37(4):530–537, 2006.
- [32] X. L. Liu, I. G. Crouch, and Y. C. Lam. Simulation of heat transfer and cure in pultrusion with a general-purpose finite element package. *Composites Science and Technology*, 60(6):857–864, 2000.
- [33] K. S. Olofsson. Temperature predictions in thick composite laminates at low cure temperatures. *Applied Composite Materials*, 4(1):1–11, 1997.
- [34] V. Antonucci, M. Giordano, K.-T. Hsiao, and S. G. Advani. A methodology to reduce thermal gradients due to the exothermic reactions in composites processing. *International Journal of Heat and Mass Transfer*, 45(8):1675–1684, 2002.
- [35] K.-T. Hsiao, R. Little, O. Restrepo, and B. Minaie. A study of direct cure kinetics characterization during liquid composite molding. *Comp. Part A: Appl. Sci. and Manuf.*, 37(6):925–933, 2006.
- [36] D. J. Michaud, A. N. Beris, and Dhurjati P. S. Curing behavior of thick-sectioned RTM composites. *J. of Comp. Mater.*, 32(14):1273–1296, 1998.
- [37] D. Rouison, M. Sain, and M. Couturier. Resin transfer molding of natural fiber reinforced composites: cure simulation. *Composites Science and Technology*, 64(5):629–644, 2004.
- [38] E. Ruiz and F. Trochu. Numerical analysis of cure temperature and internal stresses in thin and thick RTM parts. *Comp. Part A: Appl. Sci. and Manuf.*, 36(6):806–826, 2005.
- [39] V. A. F. Costa and A. C. M. Sousa. Modeling of flow and thermo-kinetics during the cure of thick laminated composites. *International Journal of Thermal Sciences*, 42(1):15–22, 2003.
- [40] P. Olivier and M. Cavarero. Comparison between longitudinal tensile characteristics of thin and thick thermoset composite laminates: influence of curing conditions. *Computers and Structures*, 76:125–137, 2000.
- [41] M. Li, Q. Zhu, P. H. Geubelle, and C. L. Tucker. Optimal curing for thermoset matrix composites: Thermochemical considerations. *Polymer Composites*, 22(1):118–131, 2001.
- [42] V. Pillai, A. N. Beris, and P. Dhurjati. Intelligent curing of thick composites using a knowledge-based system. *J. of Comp. Mater.*, 31(1):22–51, 1997.

- [43] J. M. Kenny. Application of modeling to the control and optimization of composites processing. *Comp. Struc.*, 27(1-2):129–139, 1994.
- [44] T. W. Secord, K. A. Stelson, and S. C. Mantell. Scaling analysis and a critical thickness criterion for thermosetting composites. In *Proceedings of the ASME 2006 International Mechanical Engineering Congress and Exposition (IMECE2006)*, 2006.
- [45] H.-T. Chiu, B. Yu, S. C. Chen, and L. J. Lee. Heat transfer during flow and resin reaction through fiber reinforcement. *Chem. Eng. Sci.*, 55(17):3365–3376, 2000.
- [46] A. Shojaei, S. R. Ghaffarian, and S. M. H. Karimian. Three-dimensional process cycle simulation of composite parts manufactured by resin transfer molding. *Composite Structures*, 65(3-4):381–390, 2004.
- [47] M. Hojjati and S. V. Hoa. Curing simulation of thick thermosetting composites. *Comp. Manuf.*, 5(3):159–169, 1994.
- [48] D. C. Blest, B. R. Duffy, S. McKee, and A. K. Zulkifl. Curing simulation of thermoset composites. *Comp. Part A: Appl. Sci. and Manuf.*, 30(11):1289–1309, 1999.
- [49] M.-H. Chang, C.-L. Chen, and W.-B. Young. Optimal design of the cure cycle for consolidation of thick composite laminates. *Polymer Composites*, 17(5):743–750, 1996.
- [50] M. I. Naji and S. V. Hoa. Curing of thick angle-bend thermoset composite part: curing process modification for uniform thickness and uniform fiber volume fraction distribution. *Journal of Composite Materials*, 34(20):1710–1755, 2000.
- [51] J. H. Oh and D. G. Lee. Cure cycle for thick glass/epoxy composite laminates. *J. of Compos. Mater.*, 36(1):19–45, 2002.
- [52] D. D. Shin and H. T. Hahn. Compaction of thick composites: simulation and experiment. *Polymer Composites*, 25(1):49–59, 2004.
- [53] W.-B. Young. Compacting pressure and cure cycle for processing of thick composite laminates. *Comp. Sci. and Technol.*, 54(3):299–306, 1995.
- [54] M. Li and L. Tucker. Optimal curing for thermoset matrix composites: thermochemical and consolidation considerations. *Polymer composites*, 23(5):739–757, 2002.
- [55] Z.-S. Guo, S. Du, and B. Zhang. Temperature field of thick thermoset composite laminates during cure process. *Comp. Sci. and Technol.*, 65(3-4):517–523, 2005.
- [56] S. C. Joshi, X. L. Liu, and Y. C. Lam. A numerical approach to the modeling of polymer curing in fibre-reinforced composites. *Comp. Sci. and Technol.*, 59(7):1003–1013, 1999.
- [57] S. Joncas. *Thermoplastic composite wind turbine blades - An integrated design approach*. PhD dissertation, Delft University of Technology, Delft, The Netherlands, 2010.
- [58] T. J. Corden, I. A. Jones, D. T. Jones, and V. Middleton. The mechanisms of interlaminar cracking in thick resin transfer moulded composite cylinders. *Comp. Part A: Appl. Sci. and Manuf.*, 29(4):455–464, 1998.

- [59] J. D. Reuss, A. J. Fowler, Y. K. Kim, and A. Lewis. Manufacture of thick cross-section composites using a pre-catalysed fabric technique. *Journal of Composite Materials*, 36(11):1367–1379, 2002.
- [60] Y. Jiang and S. V. Hoa. A novel method for the manufacturing of thick composites. *Journal of Composite Materials*, 40(5):433–453, 2006.
- [61] S. R. White and Y. K. Kim. Staged curing of composite materials. *Comp. Part A: Appl. Sci. and Manuf.*, 27(3):219–227, 1996.
- [62] L. Zhu and R. Pitchumani. Analysis of a process for curing composites by the use of embedded resistive heating elements. *Composites Science and Technology*, 60(14):2699–2712, 2000.
- [63] W. L. Lee and G. S. Springer. Microwave curing of composites. *Journal of Composite Materials*, 18(4):387–409, 1984.
- [64] V. Tanrattanakul and D. Jaroendee. Comparison between microwave and thermal curing of glass fiber-epoxy composites: effect of microwave-heating cycle on mechanical properties. *Journal of Applied Polymer Science*, 102(2):1059–1070, 2006.
- [65] F. Guasti and E. Rosi. Low energy electron beam curing for thick composite production. *Composites Part A: Applied Science and Manufacturing*, 28(11):965–969, 1997.
- [66] J. Raghavan. Evolution of cure, mechanical properties, and residual stress during electron beam curing of a polymer composite. *Composites Part A: Applied Science and Manufacturing*, 40(3):300–308, 2009.
- [67] E. Ruiz and F. Trochu. Comprehensive thermal optimization of liquid composite molding to reduce cycle time and processing stresses. *Polymer Composites*, 26(2):209–230, 2005.
- [68] H. W. Yu and W. B. Young. Optimal design of process parameters for resin transfer molding. *Journal of Composite Materials*, 31(11):1113–1140, 1997.
- [69] J. S. Kim and D. G. Lee. Development of an autoclave cure cycle with cooling and reheating steps for thick thermoset composite laminates. *J. of Comp. Mater.*, 31(22):2264–2282, 1997.
- [70] J. W. Kim, J. H. Lee, H. G. Kim, H. S. Kim, and D. G. Lee. Reduction of residual stresses in thick-walled composite cylinders by smart cure cycle with cooling and reheating. *Comp. Struc.*, 75(1-4):261–266, 2006.
- [71] S. Yi and H. H. Hilton. Effects of thermo-mechanical properties of composites on viscosity, temperature and degree of cure in thick thermosetting composite laminates during curing process. *Journal of Composite Materials*, 32(7):600–622, 1998.
- [72] Y. K. Kim and S. R. White. Viscoelastic analysis of processing-induced residual stresses in thick composite laminates. *Mechanics of Advanced Materials and Structures*, 4(4):361–387, 1997.
- [73] S. P. Kinsey, A. Haji-Sheikh, and D. Y. S. Lou. A thermal model for cure of thermoset composites. *Journal of Materials Processing Technology*, 63:442–449, 1997.
- [74] A. Cheung, Y. Yu, and Pochiraju K. Three-dimensional finite element simulation of curing of polymer composites. *Finite Elements in Analysis and Design*, 40(8):895–912, 2004.

References

- [75] D. J. Michaud, A. N. Beris, and Dhurjati P. S. Thick-sectioned RTM composite manufacturing: Part i - in situ cure model parameter identification and sensing. *J. of Comp. Mater.*, 36(10):1175–1200, 2002.
- [76] H. C. Park, N. S. Goo, K. J. Min, and K. J. Yoon. Three-dimensional cure simulation of composite structures by the finite element method. *Comp. Struct.*, 62(1):51–57, 2003.
- [77] H. C. Park and S. W. Lee. Cure simulation of thick composite structures using the finite element method. *J. of Comp. Mater.*, 35(3):188–201, 2001.
- [78] S. Yi, H. H. Hilton, and M. F. Ahmad. A finite element approach for cure simulation of thermosetting matrix composites. *Computers & Structures*, 64(1-4):383–388, 1997.
- [79] T. Behzad and M. Sain. Finite element modeling of polymer curing in natural fiber reinforced composites. *Composites Science and Technology*, 67(7-8):1666–1673, 2007.
- [80] X. Yan. Finite element simulation of cure of thick composites: formulations and validation verification. *Journal of Reinforced Plastics and Composites*, 27(4):339–355, 2008.
- [81] Q. Zhu, P. H. Geubelle, M. Li, and C. L. Tucker. Dimensional accuracy of thermoset composites: simulation of process-induced residual stresses. *Journal of Composite Materials*, 35(24):2171–2205, 2001.
- [82] X. Huang, J. W. Gillespie, and T. Bogetti. Process induced stress for woven fabric thick section composite structures. *Composite Structures*, 49(3):303–312, 2000.
- [83] S. Parthasarathy, S. C. Mantell, and K. A. Stelson. Estimation, control and optimization of curing in thick-sectioned composite parts. *ASME Journal of Dynamic Systems, Measurement, and Control*, 126:824–833, 2004.
- [84] D. E. Kranbuehl, P. Kingsley, S. Hart, G. Hasko, B. Dexter, and A. C. Loos. In situ sensor monitoring and intelligent control of the resin transfer molding process. *Polymer Composites*, 15(4):299–305, 1994.
- [85] N. D. Ngo, R. V. Mohan, P. W. Chung, K. K. Tamma, and D. R. Shires. Recent developments encompassing non-isothermal/isothermal liquid composite molding process modeling/analysis: physically accurate, computationally effective, and affordable simulations and validations. *Journal of Thermoplastic Composite Materials*, 11(6):493–532, 1998.
- [86] R. B. Dessenberger and C. L. Tucker. Thermal dispersion in resin transfer molding. *Polymer Composites*, 16(6):495–506, 1995.
- [87] P. J. Halley and M. E. Mackay. Chemorheology of thermosets - an overview. *Polymer Engineering & Science*, 36(5):593–609, 1996.
- [88] W. I. Lee, A. C. Loos, and G. S. Springer. Heat of reaction, degree of cure, and viscosity of Hercules 3501-6 resin. *Journal of Composite Materials*, 16:510–520, 1982.
- [89] P. I. Karkanis, I. K. Partridge, and D. Attwood. Modelling the cure of a commercial epoxy resin for applications in resin transfer moulding. *Polymer International*, 41(2):183–191, 1996.
- [90] J. E. K. Schawe. A description of chemical and diffusion control in isothermal kinetics of cure kinetics. *Thermochemica Acta*, 388(1-2):299–312, 2002.

-
- [91] I. M. Daniel and O. Ishai. *Engineering Mechanics of Composite Materials*. Oxford University Press, Inc., United States of America, Second edition, 2006.
- [92] G. S. Springer and S. W. Tsai. Thermal conductivities of unidirectional materials. *Journal of Composite Materials*, 1:166–173, 1967.
- [93] S. Sihm and A. K. Roy. Micromechanical analysis for transverse thermal conductivity of composites. *Journal of Composite Materials*, 11(18):1–11, 2010.
- [94] E. Ruiz and F. Trochu. Thermomechanical properties during cure of glass-polyester RTM composites: elastic and viscoelastic modeling. *Journal of Composite Materials*, 39(10):881–916, 2005.
- [95] D. H. Lee, W. I. Lee, and M. K. Kang. Analysis and minimization of void formation during resin transfer molding process. *Composites Part A: Applied Science and Manufacturing*, 66(16):3281–3289, 2006.
- [96] E. Ruiz, V. Achim, S. Soukane, F. Trochu, and J. Bréard. Optimization of injection flow rate to minimize micro/macro-voids formation in resin transfer molded composites. *Composites Science and Technology*, 66(3-4):475–486, 2006.
- [97] E. T. Thostenson and T.-W. Chou. Microwave and conventional curing of thick-section thermoset composite laminates: Experiment and simulation. *Polymer Composites*, 22(2):197–212, 2001.
- [98] M. Harsch, J. Karger-Kocsis, and F. Herzog. Influence of cure regime on the strain development in an epoxy resin as monitored by a fiber Bragg grating sensor. *Macromolecular Materials and Engineering*, 292(4):474–483, 2007.
- [99] P. Ferdinand, S. Magne, V. Dewynter-Marty, S. Rougeault, and L. Maurin. Applications of fiber Bragg grating sensors in the composite industry. *Material Research Society*, pages 400–407, 2007.
- [100] G. F. Fernando. Fibre optic sensor systems for monitoring composite structures. *Reinforced Plastics*, 49(11):41–49, 2005.
- [101] K. O. Hill, Y. Fujii, D. C. Johnson, and B. S. Kawasaki. Photosensitivity in optical fiber waveguides: Application to reflection filter fabrication. *Applied Physics Letters*, 32(10):647–649, 1978.
- [102] C. Ambrosino, A. Iadicicco, S. Campopiano, A. Cutolo, M. Giordano, and A. Cusano. Fiber Bragg grating sensors: industrial applications. In *An Introduction to Optoelectronic Sensors (Series in Optics and Photonics - Vol. 7)*, pages 34–76. World Scientific Publishing Co. Pte. Ltd., Singapore, 2009.
- [103] G. Meltz, W. W. Morey, and W. H. Glenn. Formation of Bragg gratings in optical fibers by a transverse holographic method. *Optics Letters*, 14(15):823–825, 1989.
- [104] K. O. Hill, B. Malo, F. Bilodeau, D. C. Johnson, and J. Albert. Bragg gratings fabricated in monomode photosensitive optical fiber by UV exposure through a phase mask. *Applied Physics Letters*, 62(10):1035–1037, 1993.
- [105] A. Mendéz. Fiber bragg grating sensors: a market overview. In *Proceedings of SPIE*, volume 6619, 2007.
- [106] M. J. O'Dwyer, G. M. Maistros, S. W. James, R. P. Tatam, and I. K. Partridge. Relating the state of cure to the real-time internal strain development in a curing composite using in-fibre Bragg gratings and dielectric sensors. *Measurement Science and Technology*, 9(8):1153–1158, 1998.

References

- [107] V. Dewynter-Marty, P. Ferdinand, E. Bocherens, R. Carbone, H. Beranger, S. Bourasseau, M. Dupont, and D. Balageas. Embedded fiber Bragg grating sensors for industrial composite cure monitoring. *Journal of Intelligent Material Systems and Structures*, 9(10):785–787, 1998.
- [108] J. Leng and A. Asundi. Structural health monitoring of smart composite materials by using EFPI and FBG sensors. *Sensors and Actuators A: Physical*, 103(11):330–340, 2003.
- [109] W. Du, X. M. Tao, H. Y. Tam, and C. L. Choy. Fundamentals and applications of optical fiber Bragg grating sensors to textile structural composites. *Composite Structures*, 42(3):217 – 229, 1998.
- [110] J. Botsis, L. Humbert, F. Colpo, and P. Giaccari. Embedded fiber Bragg grating sensor for internal strain measurements in polymeric materials. *Optics and Lasers in Engineering*, 43(3-5):491 – 510, 2005. Optics in Switzerland.
- [111] R. Kashyap. *Fiber Bragg Gratings*. Academic Press, 2009.
- [112] W. De Waele. *Structural monitoring of composite elements using optical fibres with Bragg-sensors*. PhD dissertation, Ghent University, Ghent, Belgium, 2001 - 2002.
- [113] M. J. O'Dwyer, C.-C. Ye, S. W. James, and R. P. Tatam. Thermal dependence of the strain response of optical fibre Bragg gratings. *Measurement Science and Technology*, 15(8):1607–1613, 2004.
- [114] Z.-S. Guo. Strain and temperature monitoring of asymmetric composite laminate using FBG hybrid sensors. *Structural Health Monitoring*, 6(3):191–197, 2007.
- [115] M. Harsch, J. Karger-Kocsis, and F. Herzog. Strain development in a filled epoxy resin curing under constrained and unconstrained conditions as assessed by fibre Bragg grating sensors. *Express Polymer Letters*, 1(4):217–225, 2007.
- [116] M. Harsch, J. Karger-Kocsis, and F. Herzog. Monitoring of cure-induced strain of an epoxy resin by fiber Bragg grating sensor. *Journal of Applied Polymer Science*, 107(2):719–725, 2008.
- [117] K. Jung and T. J. Kang. Cure monitoring and internal strain measurement of 3-D hybrid braided composites using fiber Bragg grating sensor. *Journal of Composite Materials*, 41(12):1499–1519, 2007.
- [118] T. Kosaka, H. Kurimoto, K. Osaka, A. Nakai, T. Osada, H. Hamada, and T. Fukuda. Strain monitoring of braided composites by using embedded fiber-optic strain sensors. *Advanced Composite Materials*, 13(3-4):157–170, 2004.
- [119] K. S. C. Kuang, R. Kenny, M. P. Whelan, W. J. Cantwell, and P. R. Chalker. Residual strain measurement and impact response of optical fibre Bragg grating sensors in fibre metal laminates. *Smart Materials and Structures*, 10(9):338–346, 2001.
- [120] K. S. C. Kuang, L. Zhang, W. J. Cantwell, and I. Bennion. Process monitoring of aluminum-foam sandwich structures based on thermoplastic fibre-metal laminates using fibre Bragg gratings. *Composites Science and Technology*, 65(3-4):669–676, 2005.
- [121] H.-J. Yoon, D. M. Costantini, H. G. Limberger, R. P. Salathé, C.-G. Kim, and V. Michaud. In situ strain and temperature monitoring of adaptive composite materials. *Journal of Intelligent Material Systems and Structures*, 17(12):1059–1067, 2006.

- [122] M. Mulle, R. Zitoune, F. Collombet, P. Olivier, and Y.-H. Grunevald. Thermal expansion of carbon-epoxy laminates measured with embedded FBGS - Comparison with other experimental techniques and numerical simulation. *Composites Part A: Applied Science and Manufacturing*, 38(5):1414–1424, 2007.
- [123] J. A. Balta, F. Bosia, V. Michaud, G. Dunkel, J. Botsis, and J.-A. Manson. Smart composites with embedded shape memory alloy actuators and fibre Bragg grating sensors: activation and control. *Smart Materials and Structures*, 14(4):457, 2005.
- [124] H. Hernández-Moreno, F. Collombet, B. Douchin, D. Choqueuse, P. Davies, and J. González Velázquez. Entire life time monitoring of filament wound composite cylinders using Bragg grating sensors: I. adapted tooling and instrumented specimen. *Applied Composite Materials*, 16(3):173–182, 2009.
- [125] H. Hernández-Moreno, F. Collombet, B. Douchin, D. Choqueuse, P. Davies, and J. González Velázquez. Entire life time monitoring of filament wound composite cylinders using Bragg grating sensors: II. process monitoring. *Applied Composite Materials*, 16(4):197–209, 2009.
- [126] P. P. Parlevliet, H. E. N. Bersee, and A. Beukers. Measurement of (post-)curing strain development with fibre Bragg gratings. *Polymer Testing*, 29(3):291–301, 2010.
- [127] M. Mulle, F. Collombet, P. Olivier, and Y.-H. Grunevald. Assessment of cure residual strains through the thickness of carbon-epoxy laminates using FBGs, Part I: Elementary specimen. *Composites Part A: Applied Science and Manufacturing*, 40(1):94–104, 2009.
- [128] L. Sorensen, T. Gmur, and J. Botsis. Residual strain development in an AS4/PPS thermoplastic composite measured using fibre Bragg grating sensors. *Composites Part A: Applied Science and Manufacturing*, 37(2):270–281, 2006. CompTest 2004.
- [129] M. Mulle, F. Collombet, P. Olivier, R. Zitoune, C. Huchette, F. Laurin, and Y.-H. Grunevald. Assessment of cure residual strains through the thickness of carbon-epoxy laminates using FBGs part II: Technological specimen. *Composites Part A: Applied Science and Manufacturing*, 40(10):1534–1544, 2009.
- [130] F. Colpo, L. Humbert, P. Giaccari, and J. Botsis. Characterization of residual strains in an epoxy block using an embedded FBG sensor and the OLCR technique. *Composites Part A: Applied Science and Manufacturing*, 37(4):652–661, 2006. Internal Stresses in Polymer Composites.
- [131] H.-K. Kang, D.-H. Kang, H.-J. Bang, C.-S. Hong, and C.-G. Kim. Cure monitoring of composite laminates using fiber optic sensors. *Smart Materials and Structures*, 11(9):279–287, 2002.
- [132] H.-K. Kang, D.-H. Kang, C.-S. Hong, and C.-G. Kim. Simultaneous monitoring of strain and temperature during and after cure of unsymmetric composite laminate using fibre-optic sensors. *Smart Materials and Structures*, 12(1):29–35, 2003.
- [133] F. Colpo, L. Humbert, and J. Botsis. Characterisation of residual stresses in a single fibre composite with FBG sensor. *Composites Science and Technology*, 67(9):1830–1841, 2007.
- [134] K. S. C. Kuang, R. Kenny, M. P. Whelan, W. J. Cantwell, and P. R. Chalker. Embedded fibre Bragg grating sensors in advanced composite materials. *Composites Science and Technology*, 61(10):1379–1387, 2001.
- [135] J. S. Leng and A. Asundi. Real-time cure monitoring of smart composite materials using extrinsic Fabry-Perot interferometer and fiber Bragg grating sensors. *Smart Materials and Structures*, 11(7):249–255, 2002.

References

- [136] R. Montanini and L. D'Acquisto. Simultaneous measurement of temperature and strain in glass fiber/epoxy composites by embedded fiber optic sensors: II. Post-cure testing. *Smart Materials and Structures*, 16(5):1727–1735, 2007.
- [137] V. M. Murukeshan, P. Y. Chan, L. S. Ong, and L. K. Seah. Cure monitoring of smart composites using fiber Bragg grating based embedded sensors. *Sensors and Actuators A: Physical*, 79(2):153–161, 2000.
- [138] V. Antonucci, A. Cusano, M. Giordano, J. Nasser, and L. Nicolais. Cure-induced residual strain build-up in a thermoset resin. *Composites Part A: Applied Science and Manufacturing*, 37(4):592–601, 2006. Internal Stresses in Polymer Composites.
- [139] M. Giordano, A. Laudati, J. Nasser, L. Nicolais, A. Cusano, and A. Cutolo. Monitoring by a single fiber Bragg grating of the process induced chemo-physical transformations of a model thermoset. *Sensors and Actuators A: Physical*, 113(2):166–173, 2004.
- [140] A. Cusano, P. Capoluongo, A. Cutolo, and M. Giordano. Chirped fiber-Bragg grating as self-temperature referenced strain sensor in nonisothermal thermoset processing. *Sensors Journal, IEEE*, 6(1):111–117, 2006.
- [141] R. de Oliveira, S. Lavanchy, R. Chatton, D. Costantini, V. Michaud, R. Salathé, and J.-A. E. Månson. Experimental investigation of the effect of the mould thermal expansion on the development of internal stresses during carbon fibre composite processing. *Composites Part A: Applied Science and Manufacturing*, 39(7):1083–1090, 2008.
- [142] R. Montanini and L. D'Acquisto. Simultaneous measurement of temperature and strain in glass fiber/epoxy composites by embedded fiber optic sensors: I. Cure monitoring. *Smart Materials and Structures*, 16(5):1718 – 1726, 2007.
- [143] D. Karalekas, J. Cugnoni, and J. Botsis. Monitoring of process induced strains in a single fibre composite using FBG sensor: A methodological study. *Composites Part A: Applied Science and Manufacturing*, 39(7):1118 – 1127, 2008.
- [144] Y. Wang, B. Han, D. Kim, A. Bar-Cohen, and P. Joseph. Integrated measurement technique for curing process-dependent mechanical properties of polymeric materials using fiber Bragg grating. *Experimental Mechanics*, 48(1):107–117, 2008.
- [145] C. A. Ramos, R. De Oliveira, and A. T. Marques. Design of an optical fibre sensor patch for longitudinal strain measurement in structures. *Materials & Design*, 30(7):2323–2331, 2009.
- [146] T. Erdogan. Fiber grating spectra. *Journal of Lightwave Technology*, 15(8):1277–1294, 1997.
- [147] T. A. Dawood, R. A. Sheno, and M. Sahin. A procedure to embed fibre Bragg grating strain sensors into GFRP sandwich structures. *Composites Part A: Applied Science and Manufacturing*, 38(1):217–226, 2007.
- [148] J. A. Guemes and J. M. Menéndez. Response of Bragg grating fiber-optic sensors when embedded in composite laminates. *Composites Science and Technology*, 62(7-8):959–966, 2002.
- [149] D. H. Kang, C. U. Kim, and C. G. Kim. The embedment of fiber Bragg grating sensors into filament wound pressure tanks considering multiplexing. *NDT & E International*, 39(2):109–116, 2006.

- [150] J.-R. Lee, H. Tsuda, and B.-Y. Koo. Single-mode fibre optic Bragg grating sensing on the base of birefringence in surface-mounting and embedding applications. *Optics & Laser Technology*, 39(1):157–164, 2007.
- [151] S. Lebid, W. Habel, and W. Daum. How to reliably measure composite-embedded fibre Bragg grating sensors influenced by transverse and point-wise deformations? *Measurement Science and Technology*, 15(8):1441–1447, 2004.
- [152] Y. Okabe, S. Yashiro, R. Tsuji, T. Mizutani, and N. Takeda. Effect of thermal residual stress on the reflection spectrum from fiber Bragg grating sensors embedded in CFRP laminates. *Composites Part A: Applied Science and Manufacturing*, 33(7):991–999, 2002.
- [153] M. Giordano, A. Laudati, M. Russo, J. Nasser, G. V. Persiano, and A. Cusano. Advanced cure monitoring by optoelectronic multifunction sensing system. *Thin Solid Films*, 450(1):191–194, 2004. Proceedings of Symposium M on Optical and X-Ray Metrology for Advanced Device Materials Characterization, of the E-MRS 2003 Spring Conference.
- [154] S. H. Eum, K. Kageyama, H. Murayama, K. Uzawa, I. Ohsawa, M. Kanai, S. Kobayashi, H. Igawa, and T. Shirai. Structural health monitoring using fiber optic distributed sensors for vacuum-assisted resin transfer molding. *Smart Materials and Structures*, 16(6):2627–2635, 2007.
- [155] A. Vieira, R. De Oliveira, O. Frazão, J. M. Baptista, and A. T. Marques. Effect of the recoating and the length on fiber Bragg grating sensors embedded in polymer composites. *Materials & Design*, 30(5):1818–1821, 2009.
- [156] A. L. Kalamkarov, S. B. Fitzgerald, and D. O. MacDonald. The use of Fabry Perot fiber optic sensors to monitor residual strains during pultrusion of FRP composites. *Composites Part B: Engineering*, 30(2):167–175, 1999.
- [157] X. D. Jin, J. S. Sirkis, J. K. Chung, and V. S. Venkat. Embedded in-line fiber etalon/Bragg grating hybrid sensor to measure strain and temperature in a composite beam. *Journal of Intelligent Material Systems and Structures*, 9(3):171–181, 1998.
- [158] X. Shu, Y. Liu, D. Zhao, B. Gwandum, F. Floreani, L. Zhang, and I. Bennion. Dependence of temperature and strain coefficients on fiber grating type and its application to simultaneous temperature and strain measurement. *Optics Letters*, 27(9):701–703, 2002.
- [159] G. F. Fernando and B. Degamber. Process monitoring of fibre reinforced composites using optical fibre sensors. *International Materials Reviews*, 51(2):65–106, 2006.
- [160] D. H. Kang, S. O. Park, C. S. Hong, and C. G. Kim. The signal characteristics of reflected spectra of fiber Bragg grating sensors with strain gradients and grating lengths. *NDT & E International*, 38(8):712 – 718, 2005.
- [161] Hexcel Composites Ltd. Industry breakthroughs in carbon fiber and aerospace prepregs launched by Hexcel at JEC 2010, April 2010. Available from: <http://www.hexcel.com/News/Market+News/INDUSTRY+BREAKTHROUGHS+IN+CARBON+FIBER+AND+AEROSPACE+PREPREGS+LAUNCHED+BY+HEXCEL+AT+JEC+2010.html>.
- [162] Hexcel. HexFlow® RTM 6. In product data sheet, 2010.

References

- [163] HEXION™ Specialty Chemicals. EPIKOTE™ resin 04908, EPIKURE™ curing agent 04908. In product data sheet, 2006.
- [164] J. M. Balvers, J. Chen, M.-A. Oceau, H. E. N. Bersee, and A. Yousefpour. Through-thickness cure monitoring of thick advanced composites using dielectric sensors. In *Proceedings of the 17th International Conference on Composite Materials (ICCM-17), Edinburgh, Scotland, 2009*, 2009.
- [165] J. M. Balvers, M.-A. Oceau, J. Chen, H. E. N. Bersee, and A. Yousefpour. Comparison of sensing techniques for process monitoring in thick advanced composites. In *Proceedings of the Society for the Advancement of Material and Process Engineering (SAMPE Seattle 2010), Seattle, USA, 2010*, 2010.
- [166] R. J. Varley. Reaction kinetics and phase transformations during cure of a thermoplastic-modified epoxy thermoset. *Macromolecular Materials and Engineering*, 292(1):46–61, 2007.
- [167] P. I. Karkanis and Partridge. Cure modeling and monitoring of epoxy/amine resin systems. i. cure kinetics modeling. *Journal of Applied Polymer Science*, 77(7):1419–1431, 2000.
- [168] P. I. Karkanis and Partridge. Cure modeling and monitoring of epoxy/amine resin systems. ii. network formation and chemoviscosity modeling. *Journal of Applied Polymer Science*, 77(10):2178–2188, 2000.
- [169] Q. Govignon, S. Bickerton, and P. A. Kelly. Simulation of the reinforcement compaction and resin flow during the complete resin infusion process. *Composites Part A: Applied Science and Manufacturing*, 41(1):45–57, 2010.
- [170] R. A. Saunders, C. Lekakou, and M. G. Bader. Compression and microstructure of fibre plain woven cloths in the processing of polymer composites. *Composites Part A: Applied Science and Manufacturing*, 29(4):443–454, 1998.
- [171] B. Chen, E. J. Lang, and T.-W. Chou. Experimental and theoretical studies of fabric compaction behavior in resin transfer molding. *Materials Science and Engineering A*, 317(1-2):188–196, 2001.
- [172] T. Kruckenberg, L. Ye, and R. Paton. Static and vibration compaction and microstructure analysis on plain-woven textile fabrics. *Composites Part A: Applied Science and Manufacturing*, 39(3):488–502, 2008.
- [173] R. A. Saunders, C. Lekakou, and M. G. Bader. Compression in the processing of polymer composites 1. a mechanical and microstructural study for different glass fabrics and resins. *Composites Science and Technology*, 59(7):983–993, 1999.
- [174] F. Robitaille and R. Gauvin. Compaction of textile reinforcements for composites manufacturing. II: compaction and relaxation of dry and h_2O -saturated woven reinforcements. *Polymer Composites*, 19(5):543–557, 1998.
- [175] B. Chen, A. H. D. Cheng, and T.-W. Chou. A nonlinear compaction model for fibrous preforms. *Composites Part A: Applied Science and Manufacturing*, 32(5):701–707, 2001.
- [176] B. Chen and T.-W. Chou. Compaction of woven-fabric preforms in liquid composite molding processes: single-layer deformation. *Composites Science and Technology*, 59(10):1519–1526, 1999.
- [177] Zyx Inc. Waterworks aerospace release, [cited November 17th, 2010]. Available from: <http://www.waterworks4.com>.

- [178] J. B. Layman. Technical laboratory project report, TSR-043. Personal communication, February 19th, 2009. Recipient: Balvers, J.M.
- [179] FOS&S. Instruction manual FBG-Scan (version 2.02). On CD, 2007.
- [180] I. De Baere, E. Voet, W. Van Paepegem, J. Vlekken, V. Cnudde, B. Masschaele, and J. Degrieck. Strain monitoring in thermoplastic composites with optical fiber sensors: embedding process, visualization with micro-tomography, and fatigue results. *Journal of Thermoplastic Composite Materials*, 20(5):453–472, 2007.
- [181] J. M. Balvers, H. E. N. Bersee, and A. Beukers. Integration of fiber bragg gratings in woven fabrics: Influences of preform compaction and flow-front propagation. In *Proceedings of the 9th International Conference on Flow Processes in Composite Materials (FPCM-9)*, Montreal, Canada, July 8–10, 2008, 2008.
- [182] P. P. Parlevliet, H. E. N. Bersee, and A. Beukers. Residual stresses in thermoplastic composites—A study of the literature—Part II: Experimental techniques. *Composites Part A: Applied Science and Manufacturing*, 38(3):651–665, 2007.
- [183] R. G. Reid and R. Paskaramoorthy. A novel method to measure residual stresses in unidirectional grp. *Composite Structures*, 88(3):388–393, 2009.
- [184] W. D. Callister. *Materials science and engineering: an introduction*. John Wiley & Sons, Inc., United States of America, Fifth edition, 2000.
- [185] J. D. Muzzy. Thermoplastics—properties. In A. Kelly and C. Zweben, editors, *Comprehensive Composite Materials*, pages 57–76. Pergamon Press, Oxford, UK, 2000.
- [186] N. G. Pantelelis. Towards the dynamic optimisation for the cure control of thermoset-matrix composite materials. *Composites Science and Technology*, 65(7-8):1254–1263, 2005.
- [187] L. F. M. Da Silva and R. D. Adams. Stress-free temperature in a mixed-adhesive joint. *J. of Adh. Sci. and Technol.*, 20(15):1705–1726, 2006.
- [188] J. M. Balvers, H. E. N. Bersee, and A. Beukers. Integration of fiber bragg gratings in woven fabrics: Influences of preform compaction and flow-front propagation. In *Proceedings of the 9th International Conference on Flow Processes in Composite Materials (FPCM-9)*, Montreal, Canada, July 2008.
- [189] P. A. Kelly, R. Umer, and S. Bickerton. Viscoelastic response of dry and wet fibrous materials during infusion processes. *Composites Part A: Applied Science and Manufacturing*, 37(6):868–873, 2006.
- [190] S. Bickerton, M. J. Buntain, and A. A. Somashekar. The viscoelastic compression behavior of liquid composite molding preforms. *Composites Part A: Applied Science and Manufacturing*, 34(5):431–444, 2003.
- [191] W. Martienssen and H. Warlimont (Eds.). *Springer Handbook of Condensed Matter and Materials Data*. Springer Berlin Heidelberg, Germany, 2005.
- [192] L. Khoun, R. De Oliveira, V. Michaud, and P. Hubert. Investigation of process-induced strains development by fibre bragg grating sensors in resin transfer moulded composites. *Composites Part A: Applied Science and Manufacturing*, 42(3):274 – 282, 2011.

References

- [193] R. A. Schapery. Thermal expansion coefficients of composite materials based on energy principles. *Journal of Composite Materials*, 2:390–404, 1968.
- [194] P. H. Verburg. *Development of techniques for polymer shrinkage measurement*. MSc thesis, Delft University of Technology, Delft, The Netherlands, 2008.
- [195] ASTM International: D3171-99. Standard test methods for constituent content of composite materials, 2004. ASTM International: 100 Barr Harbor Drive, PO Box C700, West Conshohocken, PA 19428-2959, United States of America.
- [196] J. P. Hernandez, T. Raush, A. Rios, S. Strauss, and T. A. Osswald. Theoretical analysis of fiber motion and loads during flow. *Polymer Composites*, 25(1):1 – 11, 2004.
- [197] V.B.C. Tan, V.P.W. Shim, and X. Zeng. Modelling crimp in woven fabrics subjected to ballistic impact. *International Journal of Impact Engineering*, 32(1-4):561 – 574, 2005. Fifth International Symposium on Impact Engineering.
- [198] R. G. Lerner and G. L. Trigg. *Encyclopedia of physics*. VCH Publishers, Inc., 2009.
- [199] Q. Govignon, S. Bickerton, J. Morris, and P. A. Kelly. Full field monitoring of the resin flow and laminate properties during the infusion process. *Composites Part A: Applied Science and Manufacturing*, 39(9):1412–1426, 2008.
- [200] B. Yenilmez, M. Senan, and E. M. Sozer. Variation of part thickness and compaction pressure in vacuum infusion process. *Composites Science and Technology*, 69(11-12):1710–1719, 2009.
- [201] C. D. Williams, S. M. Grove, and J. Summerscales. The compression response of fibre-reinforced plastic plates during manufacture by the resin infusion under flexible tooling method. *Composites Part A: Applied Science and Manufacturing*, 29(1-2):111–114, 1998.
- [202] Germany LIMESS Messtechnik & Software GmbH. Camera based measurement systems. Accessed by: <http://www.limess.com>.
- [203] H. M. Andersson, T. S. Lundstrom, B. R. Gebart, and P. Synnergren. Application of digital speckle photography to measure thickness variations in the vacuum infusion process. *Polymer composites*, 24(3):448–455, 2007.
- [204] Germany LIMESS Messtechnik & Software GmbH. Course material on digital image correlation.
- [205] G. Twigg, A. Poursartip, and G. Fernlund. Tool-part interaction in composites processing. Part I: experimental investigation and analytical model. *Composites Part A: Applied Science and Manufacturing*, 35(1):121–133, 2004.
- [206] G. Twigg, A. Poursartip, and G. Fernlund. An experimental method for quantifying tool-part shear interaction during composites processing. *Composites Science and Technology*, 63(13):1985–2002, 2003.

NOMENCLATURE

Symbols

Greek

α	Coefficient of thermal expansion [$1/^\circ\text{C}$]
α	Degree of cure/conversion [-]
α_n	Thermo-optic coefficient [$1/^\circ\text{C}$]
β	Moisture expansion coefficient [-]
Δc	Moisture concentration [-]
ϵ	Strain [-]
ϵ_{flux}	Strain due to resin flow [-]
γ	Chemical expansion coefficient [-]
γ_{chem}	Chemical shrinkage coefficient [-]
λ	Structural parameter in DiBenedetto equation [-]
λ_B	Bragg wavelength [m]
λ_{chem}	Total chemical shrinkage [-]
Λ	Grating period [m]
ν	Poisson's ratio [-]
ρ	Density [kg/m^3]
σ	Stress [Pa]
τ	Shear stress [Pa]
ϕ	Porosity [-]

Latin

A	Pre-exponential factor in cure kinetics [$1/s$]
A_{ij}	Component of laminate stiffness matrix [Pa]
A_w	Areal weight [kg/m^2]
C	Condition number [-]
c_p	Specific heat capacity [$J/kg-^\circ\text{C}$]
d	Cavity length in an EFPI sensor [m]
d	Minimum distance between sensors [m]

Nomenclature

Da	Damköhler number [-]
e	Hygrothermochemical strain [-]
E	Activation energy [J/mol]
Ge	Gelling ratio [-]
h	Heat transfer coefficient [$W/m^2-^{\circ}C$]
H_U	Ultimate enthalpy [J/g]
I	Intensity [-]
k	Thermal conductivity [$W/m-^{\circ}C$]
k	Rate constant [$1/s$]
L	Gauge length [mm]
L_0	Length of the laminate [m]
m	Reaction order in cure kinetics [-]
n	Number of plies [-]
n	Reaction order in cure kinetics [-]
n	Refractive index [-]
N	Force [N]
p	Pressure [Pa]
P	Effective photo-elastic coefficient [-]
\dot{Q}	Heat source [J/s]
Q_{ij}	Component of reduced stiffness matrix [Pa]
R	Universal gas constant [$J/mol-^{\circ}C$]
R_{α}	Rate of reaction [$1/s$]
S_{ϵ}	Strain sensitivity [-]
S_p	Pressure sensitivity [$1/Pa$]
S_T	Thermal sensitivity [$1/^{\circ}C$]
t	Thickness [m]
t	Time [s]
T	Temperature [$^{\circ}C$]
$T_{g,\infty}$	Ultimate glass transition temperature [$^{\circ}C$]
$T_{g,0}$	Initial glass transition temperature [$^{\circ}C$]
T_g	Glass transition temperature [$^{\circ}C$]
v	Volume fraction [-]
V	Volume [m^3]
\vec{V}	Velocity [m/s]
x	Position of the flow-front [m]

Sub- and superscripts

Subscripts

0	initial	lam	laminate
1	axial	liq	liquid
ϵ	strain	m	mechanical
c	composite	r	resin
c	kinetic	ref	reference
d	diffusion	s	slow
eff	effective	s	surface
f	fast	T	temperature
f	(optical) fibre	TC	thermocouple
gel	gelled	tot	total
H	host	vit	vitrified
impr	impregnated		

Superscripts

HTC	hygrothermochemical	o	reference
-----	---------------------	---	-----------

Acronyms

AGP	After Gel Point
ALCAS	Advanced Low-Cost Aircraft Structures
CFR	Carbon Fibre Reinforced
CFRP	Carbon Fibre Reinforced Plastic
CLT	Classical Lamination Theory
COTS	Commercial Off-The-Shelf
CTE	Coefficient of Thermal Expansion
DIC	Digital Image Correlation
DOC	Direct Operating Cost
DPCS	Design and Production of Composite Structures
DSC	Differential Scanning Calorimetry
DMA	Dynamic Mechanical Analyser

EFPI	Extrinsic Fabry-Perot Interferometry
FBG	Fibre Bragg Grating
FE	Finite Element
FML	Fibre Metal Laminate
FWHM	Full Width at Half Maximum
GFR	Glass Fibre Reinforced
GFRP	Glass Fibre Reinforced Plastic
HiBi	High Birefringence
LCM	Liquid Composite Moulding
LoZS	Line of Zero Stress
MRCC	Manufacturer's Recommended Cure Cycle
NDT	Non Destructive Testing
PDS	Product Data Sheet
OF	optical fibre
OFDR	Optical Frequency Domain Reflectometry
OLCR	Optical Low-Coherence Reflectometry
PC	Post-Curing
RHS	right-hand side
RT	Room Temperature
RTM	Resin Transfer Moulding
SHM	Structural Health Monitoring
SM	Single Mode
SSI	Structural Significant Item
TMA	Thermal Mechanical Analyser
UD	uni-directional
VI	Vacuum Infusion

ACKNOWLEDGEMENTS

The writing and completion of this thesis would not have been possible without the assistance, support and guidance of a few very special people. I would like to show my gratitude to the following:

- My supervisor Harald Bersee and promoter Adriaan Beukers for offering me a position as a PhD student in the pioneering DPCS group in the first place, but also for being patient with me when the perfectionist in me was taking over or when I was exploring the dark side of doing a PhD.
- AgentschapNL (formerly NIVR), Stork SP Aerospace B.V., Stork Fokker AESP B.V. (all located in the Netherlands) and FOS&S (Belgium), which partially funded this work. I gratefully acknowledge their support, but most of all the freedom they offered me during the research.
- All of my students I supervised along the road. A special thanks to two of them: Marina and Catherine. Their hard-working capabilities and their never ending curiosity and hunger for knowledge contributed significantly to the creation of this book.
- My colleagues and technical staff of the DPCS group, but especially my roomies Giovanni, Carlos, Huajie and Adrian, for the good chats & fruitful discussions, lunches, travels to conferences and sharing my mood when science was playing a prank on me. Lisette & Gemma: thanks for taking care of the administrative work! To Patricia who mentioned once in a long phone call that taking one step back can eventually bring you two steps forward. And to Paola who helped me in the last phase of getting the dissertation ready to print.
- The technicians Sebastiaan, Fred and all the others of the 'vliegtuighal' for their support in carrying out numerous experiments and moving tons of steel and equipment "again and again" during the two-year of rebuilding activities in the lab.

Acknowledgements

- The people of the National Research Council Canada in Montreal for helping me with the material characterization & testing.
- My “Delft friends” who helped me refreshing my mind / forgetting about daily work by playing endlessly card and board games, organising BBQs, drinks and weekends or longer trips across the world. Thanks for staying a bit longer student such that I enjoyed even more the first years of my PhD in Delft ;-)
- My home-town friends for putting everything into perspective while having a beer in the hand.
- My father, mother, sister & brother-in-law (Peter, Elly and Marit & Steven). Thank you for always wanting the best for me. Your unconditional love, concern, good advices, care, interest and trust in me has made me definitely a stronger person.
- Last but not least, my love goes to my girlfriend Janine. More than happy to have you around me!!!

ABOUT THE AUTHOR

Johannes Mattheus Balvers was born on 9th April 1983 in Alkmaar, the Netherlands. After graduating in 2001 from the Christelijke Scholengemeenschap Jan Arentsz in Alkmaar, he was enrolled as a student at the Faculty of Aerospace Engineering of the Delft University of Technology, the Netherlands. During these years, he developed a strong interest in manufacturing processes and the optimisation thereof. After completion of his Bachelor's degree, he specialised himself in composite manufacturing at the chair Design and Production of Composite Structures. In his four month internship at Universidad de Concepción in Chile he developed both his engineering and lecturing skills. He completed his Master's degree in 2007 by investigating and modelling the cure behaviour in thick composite structures. As the interest was there to perform a more detailed analysis, he decided to take a position as a PhD with the same chair. His four-year research, aimed at exploring the capabilities of process monitoring by fibre Bragg grating sensors in liquid composite moulding, led to those results found in this thesis. Since October 2011 he is employed by Airbus Helicopters in Donauwörth, Germany. In his daily activities, he is a project engineer / manager in composite manufacturing technologies. His focus is on developing and implementing new tools and methods such as compensation for process-induced deformation by manufacturing process simulation. For this job, he moved to Munich, Germany.

PUBLICATIONS

This thesis is based on the following publications:

- **Balvers, J.M.**, Bersee, H.E.N., *Comparing flow-front propagation sensed by FBGs with PAM-RTM simulation*. Proceeding of the 10th International Conference on Flow Processes in Composite Materials (FPCM-10), Ascona, Switzerland, 2010.
- **Balvers, J.M.**, Octeau, M.-A., Chen, J., Bersee, H.E.N., Yousefpour, A., *Comparison of sensing techniques for process monitoring in thick advanced composites*. Proceeding of the Society for the Advancement of Material and Process Engineering (SAMPE Seattle 2010), Seattle, WA. USA, 2010.
- **Balvers, J.M.**, Selezneva, M.A., Bersee, H.E.N., *Determination of residual strain in (partially) cured composites using FBG sensors*. Proceeding of the SAMPE Europe 31st International Technical Conference & Forum (SEICO 10), Paris, France, 2010.
- **Balvers, J.M.**, Chen, J., Octeau, M.-A., Bersee, H.E.N., Yousefpour, A., *Through-thickness cure monitoring of thick advanced composites using dielectric sensors*. Proceeding of the 17th International Conference on Composite Materials (ICCM-17), Edinburgh, United Kingdom, 2009.
- **Balvers, J.M.**, Bersee, H.E.N., Beukers, A., *Settling of glass woven fabric in steel RTM mould: impact on residual stress?* Proceeding of the 17th International Conference on Composite Materials (ICCM-17), Edinburgh, United Kingdom, 2009.
- **Balvers, J.M.**, Bersee, H.E.N., Beukers, A., *Integration of fiber Bragg gratings in woven fabrics: influences of preform compaction and flow-front propagation*. Proceeding of the 9th International Conference on Flow Processes in Composite Materials (FPCM-9), Montreal, Canada, 2008.

- **Balvers, J.M.**, Bersee, H.E.N., Beukers, A., Jansen, K.M.B., *Determination of cure dependent properties for curing simulation of thick-walled composites*. Proceeding of the 49th AIAA/ASME/ASCE/AHS/ACS Structures, Structural Dynamics, and Material Conference, Schaumburg, IL. USA, 2008.

Others:

- Bel, S., Margossian, A., **Balvers, J.M.**, Leutz, D., Freitas, R., Hinterhoelzl, R., *Finite element forming simulation of locally stitched non-crimp fabrics*. Manuscript submitted to Composites Part A: Applied Science and Manufacturing.
- Wille, T., Hein, R., Horn, M., Knotte, A., Opitz M., Mayer, N., Prowe, J., **Balvers, J.M.**, Apmann, H., *Development, implementation and demonstration of a composite tool chain for concurrent engineering*. Proceeding of the NAFEMS World Congress 2013, Salzburg, Austria, 2013.